



HAL
open science

Improvement of high-resolution air quality predictions : Focus on urban and peri-urban areas and specific pollution episodes in France

Lei Jiang

► **To cite this version:**

Lei Jiang. Improvement of high-resolution air quality predictions : Focus on urban and peri-urban areas and specific pollution episodes in France. Ocean, Atmosphere. Sorbonne Université, 2021. English. NNT : 2021SORUS024 . tel-03521004

HAL Id: tel-03521004

<https://theses.hal.science/tel-03521004v1>

Submitted on 11 Jan 2022

HAL is a multi-disciplinary open access archive for the deposit and dissemination of scientific research documents, whether they are published or not. The documents may come from teaching and research institutions in France or abroad, or from public or private research centers.

L'archive ouverte pluridisciplinaire **HAL**, est destinée au dépôt et à la diffusion de documents scientifiques de niveau recherche, publiés ou non, émanant des établissements d'enseignement et de recherche français ou étrangers, des laboratoires publics ou privés.



Improvement of high-resolution air quality predictions - Focus on urban and peri-urban areas and specific pollution episodes in France

Amélioration des prévisions de la qualité de l'air à haute résolution - Focus sur les zones urbaines et périurbaines et les épisodes de pollution spécifiques en France

Thèse de doctorat de l'Université de la Sorbonne
École doctorale n°129, Sciences de l'environnement d'Ile-de-France
Météorologie, océanographie physique de l'environnement

Thèse présentée et soutenue à Verneuil en Halatte, le 21 Juin 2021, par

M. Lei JIANG

Composition du Jury :

Philippe Thunis (PhD)	Joint Research Centre (IT)	Rapporteur
Jean-Baptiste Renard (DR)	LPC2E/CNRS (FR)	Rapporteur
Solène Turquety (Prof.)	IPSL/Sorbonne Université (FR)	Examinatrice
Alma Hodzic (HDR)	LA/OMP (FR) – NCAR (USA)	Examinatrice
Karine Sartelet (HDR)	CEREA/ENPC (FR)	Examinatrice
Cécile Mari (DR)	LA/OMP-IRD (FR)	Examinatrice
Frédéric Tognet (Ing.)	INERIS (FR)	Encadrant INERIS
Bertrand Bessagnet (HDR)	INERIS/Sorbonne Université (FR)	Directeur de Thèse

Résumé

De nos jours, plus de la moitié de la population mondiale vit dans des zones urbaines. La prévision et l'analyse de la qualité de l'air dans les zones urbaines est un sujet d'actualité. L'amélioration des modèles de transport chimique à méso-échelle passe généralement par le développement de paramétrisations plus avancées en termes de dynamique et mécanismes chimiques. Dans la première partie de l'étude, trois configurations du coefficient de diffusion verticale (K_z) basées sur la théorie de fermeture de premier ordre (*k-theory*) sont testées avec le modèle CHIMERE alimenté par les données Européennes météorologiques IFS pendant une année. Ces configurations, bien que jugées efficaces pour les simulations de qualité de l'air à méso-échelle, montrent une surestimation significative du mélange vertical dans les zones urbaines avec des différences faibles entre les trois schémas. Il convient de noter que le modèle ainsi configuré a surestimé le rapport PM_{2.5}/PM₁₀ d'environ 20% quelle que soit la saison. L'étude de l'impact de la paramétrisation de la diffusion verticale confirme bien que la modélisation météorologique est d'une importance majeure pour la modélisation de la qualité de l'air. Par la suite, le modèle Weather Research and Forecast (WRF) couplé au modèle de transport de la chimie (CTM) CHIMERE a été utilisé pour comprendre l'impact des paramétrisations physiques sur la simulation de la qualité de l'air sur épisode de pollution en la région parisienne. Les différents schémas de canopée testés montrent des différences importantes avec une surestimation globale des concentrations pendant l'épisode de pollution. Les tests de sensibilité des schémas de la couche limite montrent une sous-estimation de la hauteur de la couche limite qui a pour conséquence une forte surestimation de la concentration des polluants pendant l'épisode de pollution. Le schéma de Boulac-BEP montre des performances significativement meilleures que les autres schémas pour la simulation de cette hauteur de couche limite ainsi que pour les concentrations en polluants, ce qui confirme bien que les schémas de canopée urbaine et de couche limite ont un effet critique sur la modélisation de la qualité de l'air dans la région urbaine. La troisième partie de ce travail porte sur l'impact de la résolution verticale de la grille et la hauteur de la première couche qui jouent également un rôle très important dans la modélisation du transport. Les trois configurations testées démontrent les capacités du modèle à simuler des journées normales hors épisodes de pollution. Cependant, lors d'un épisode de pollution, l'affinement de la résolution verticale et de la hauteur de la première couche entraîne une nette amélioration des résultats de modélisation en comparaison avec la configuration

initiale du modèle. La simulation et la prévision de la qualité de l'air en région urbaine sont donc influencées par les caractéristiques de la canopée urbaine, la couche limite et les conditions de diffusion, le modèle de surface terrestre ayant un léger impact sur la simulation météorologique et la qualité de l'air. Dans la dernière partie de ce travail, la diffusivité turbulente de WRF issue d'un schéma de fermeture de la diffusivité d'ordre 1.5 basé sur l'énergie cinétique de la turbulence est intégré dans CHIMERE afin de représenter un mélange vertical plus réaliste près de la surface pour les applications de pollution urbaine. Une simulation haute résolution de 15 jours en hiver a été réalisée sur Paris, Lyon et Bordeaux avec des résolutions horizontale et verticale fines de 1,67km et 12m respectivement. Il est à noter que la nouvelle diffusion verticale (NED) a amélioré la simulation du NO₂ pour chaque site urbain par rapport à la diffusion K_z initiale (IKD). Les améliorations moyennes en termes de RMSE sont de 18,77%, 24,51% et 9,52% à Paris, Lyon et Bordeaux, respectivement. La simulation des PM_{2.5} et PM₁₀ a donné les mêmes résultats que celle du NO₂, avec des améliorations de 13,47% et 19,08% respectivement dans la zone urbaine de Paris. La simulation avec un coefficient de diffusion turbulente plus réaliste est meilleure qu'avec le K_z initial utilisé dans le CTM.

Outre l'analyse de paramétrisations à l'échelle urbaine et leur influence sur la qualité de l'air à l'échelle urbaine, Ce travail de thèse permet donc à l'utilisateur d'identifier plus facilement les paramètres essentiels pour la configuration des modèles atmosphériques dans l'objectif d'une utilisation opérationnelle optimisée afin de simuler la qualité de l'air pendant les épisodes de pollution ou pour des analyses sur le long terme en zone urbaine.

Mots-clés : *Qualité de l'air ; modélisation ; urbain ; diffusion ; haute résolution*

Abstract

Nowadays, more than half of the world's population lives in urban areas, air quality prediction in urban areas is therefore flagship topic. The improvement of mesoscale chemical transport models generally focused on the dynamics, physical parameterization processes, and chemical reaction mechanisms. In the first part of the study, three configurations of vertical diffusion coefficient (K_z) based on first order closure K -theory are tested within CHIMERE model fed by IFS meteorology over one year. Although, all these K_z configurations are known to be efficient for mesoscale air quality simulations and the results show small differences between the three schemes, they all overestimated vertical mixing in urban areas. It is worth noting that the model used overestimates the ratio of $PM_{2.5}/PM_{10}$ by approximately 20% for all seasons. Discrepancies on emission inventories could be a relevant explanation. Many studies on the impact of physical parameterizations indicates the need of more accurate simulations of meteorological conditions for air quality modeling at urban scale. Also, for the second part of this work, the Weather Research and Forecast (WRF) model coupled with the chemistry transport model (CTM) CHIMERE has been used to understand the impact of physics parameterizations on air quality simulation during a short-term pollution episode on the Paris region. Large differences were found between different canopy schemes, showing an overall overestimation of concentrations during the pollution episode. The boundary layer schemes sensitivity tests display an underestimation of the boundary layer height which leads to a strong overestimations of pollutants concentration. The Boulac-BEP scheme had significantly better performances than the other schemes for the simulation of both the PBL height and the pollutants concentrations, indicating that both the canopy schemes and boundary layer schemes have a critical effect on air quality prediction in the urban region. The third part of this work focuses on the vertical resolution of the grid and the height of the first layer which also plays a very important role in the transport modeling. The three configurations tested demonstrate the model's ability to simulate regular days without pollution episodes. However, during a pollution episode, the refinement of the vertical resolution and of the height of the first layer leads to a clear improvement of the modeling results compared to the initial configuration of the model. The air quality predictions in urban regions are mainly influenced by the urban canopy, the boundary layer and the diffusion conditions. The land surface model had a slight impact for both meteorological and air quality simulation. In the last part of this work, the eddy diffusion of WRF from a 1.5 order diffusivity closure scheme based on the kinetic energy of turbulence is directly integrated into CHIMERE in order to represent a more realistic vertical mixing near the surface for urban pollution applications. A two weeks high resolution simulation was performed in Paris, Lyon and Bordeaux with finest horizontal and vertical resolution of 1.67km and 12m respectively. The new eddy diffusion (NED) integrated in this research improves NO_2 simulations at all urban site compared to the original K_z diffusion (IKD) on board CHIMERE. The average improvements in terms of RMSE are

18.77%, 24.51% and 9.52% in Paris, Lyon and Bordeaux, respectively. PM_{2.5} and PM₁₀ simulation provided similar results with NO₂, 13.47% and 19.08% improvements were found in the urban area of Paris. The simulation with more realistic eddy viscosities is better than initial K_z parameterization which has been widely used in CTM. This work illuminates the user to identify the best settings of atmospheric models for appropriate operational uses to simulate the air quality during pollution episodes or for long term analyses in urban areas.

Keywords: *Air quality; modeling; urban; diffusion; high-resolution*

Acknowledgement

First and foremost, I would like to thank my supervisor Dr. Bertrand Bessagnet for providing me with valuable opportunities and continuous guidance during my Ph.D. From the selection of the topic to the final draft, His careful guidance is indispensable. His extensive professional knowledge, rigorous academic attitude has benefited me a lot from my Ph.D. study, and this wealth will surely benefit me throughout my life.

Thanks to my co-supervisor Frédéric Tognet, Frédéric Meleux, Florian Couvidat. They put forward many valuable suggestions on the specific implementation of my research work and the difficulties encountered in the experiment process, these have laid a good foundation for the smooth development and completion of my thesis. The discussions on Friday afternoon benefited me a lot. The growth of my research and mindset is inseparable from their help.

I would like to sincerely thank all the team members of MOCA, Augustin, Jean-Maxime, Adrien, Florian, Gael, Alicia, Palmira-Valentina, Blandine, Hugo, Antonio, Frédéric, Elsa, Frédéric, Anthony, Florence and Vincent. They let me experience a good working atmosphere and teamwork spirit. In particular, I would like to thank you for the various delicacies provided during work breaks. The weight I have gained in the past three years is inseparable from their help.

Thanks to my friends Deep, Yunjiang, Grazia, Camille, Alexander, Adrien, Helene, Audrey, Suize, Boris and all other lost friends. You are brothers and sisters. We spent a lot of good time together, which is unforgettable. I will always remember our every party, every trip.

I am very grateful to the Sorbonne University for providing me with the doctoral program, and I am grateful to INERIS for providing me with a good working environment and financial support.

Finally, thank my beloved family, thank you for sharing the hard work and joy with me on this road of life, and for giving me unselfish love and unconditional support and encouragement.

The Ph.D. study is coming to an end. The past three-year is a precious experience and wealth in my life. Thank you to everyone I have met along the way.

Acronyms, Variables and Abbreviations

AQS	Air Quality monitoring Stations
ARW-WRF	Advanced Research Weather Research and Forecasting model
BEP	Building Effect Parameterization scheme
BL	Boundary layer
Boulac	Bougeault and Lacarrere scheme
CAAR	Consolidated Annual Activity Report
CAMx	the Comprehensive Air-quality Model with extensions
CFD	Computational Fluid Dynamics
CMAQ	Community Multiscale Air Quality Model
CO	Carbon monoxide
CO ₂	Carbon dioxide
CTM	Chemical Transport Model
ECMWF	European Centre for Medium-Range Weather Forecasts
EEA	European Environment Agency
EKMA	Empirical Kinetic Modeling Approach
EMEP	European Monitoring and Evaluation Program
EPA	Environmental Protection Agency
EU28	28 countries Europe Union
FALL3D	three-dimensional Eulerian model
GAINS	Greenhouse gas - Air pollution Interactions and Synergies
GFS	Global Forecasting System
<i>h</i>	Boundary layer height
IARC	International Agency for Research on Cancer
IFS	Integrated Forecasting System
IKD	Initial K Diffusion scheme
INS	The French National Spatialized Inventory
ISC	Industrial Source Complex model
K	diffusion coefficient
<i>k</i>	von Karman constant

Kz	Vertical diffusion coefficient
L	Monin–Obukhov length
LSM	Land surface model
LW	Longwave radiation
MB	Mean bias
MO	Monin–Obukhov scheme
MOS	Meteorological observation stations
MYJ	Mellor–Yamada–Janjic scheme
NCAR	National Center for Atmospheric Research
NCEP	National Centers for Environmental Prediction
NED	New Eddy Diffusion scheme
NH ₃	<i>Ammonia</i>
NO	Nitric oxide
NO ₂	Nitrogen dioxide
NO _x	Nitrogen oxides
NWP	Numerical Weather Prediction
O ₃	Ozone
PBL	Planetary boundary layer
PBLH	Planetary boundary layer height
PE	Pollution Episode
PM	Particulate Matter
PM10	Particulate Matter that have a diameter of less than 10 micrometers
PM2.5	Particulate Matter that have a diameter of less than 2.5 micrometers
PREV’AIR	the French national air quality forecasting platform
R	Mean linear correlation coefficient
RADM	Regional Acid Deposition Model
RB	Relative bias
RD	Regular days
RF	Radiative forcing
RH	Relative humidity

RMSE	Root mean square error
RRTMG	Rapid radiative transfer model for GCMs scheme
SHERPA	Screening for High Emission Reduction Potential on Air
SHF	Surface heat flux
SL	Surface layer
SO ₂	<i>Sulfur dioxide</i>
SO _x	Sulfur oxides
SR	Sunrise
SS	Sunset
SW	Shortwave radiation
T2	2m temperature
TKE	Turbulent Kinetic Energy
u^*	Friction velocity
UAM	Urban Air shed Model
UCM	Single layer urban canopy scheme
UHI	Urban heat island
URB	Urban canopy
URBAN-PAM	Urban parameterization
VOCs	Volatile organic compounds
w^*	Convective velocity
W10	10m windspeed
WHO	World Health Organization
WP	Whole period
WRF	Weather Research and Forecast model
YSU	YonSei University scheme
z	Altitude

Contents

Chapter I: Introduction	1
1.1 Air pollutants in the Atmosphere	2
1.2 Effects of air pollution on climate	3
1.3 Health effect of air pollution	6
1.4 The development of atmospheric models.....	8
1.5 Urbanization and air quality	12
1.6 Objectives and outline of the PhD thesis	16
References	20
Chapter II: Meteorology and atmospheric dispersion in the urban canopy– One-year air quality simulations in France using IFS/CHIMERE modeling system.....	31
2.1 General principle of the chemical transport model	32
2.2 Urban meteorology	34
2.3 Urban canopy modeling	36
2.4 The basic equations and dispersion in the urban canopy layer	38
2.5 Preliminary study – Model setup	42
2.6 Results and Discussions	44
2.7 Conclusions	53
References	54
Chapter III: Impact of physics parameterizations on high-resolution air quality simulations over urban region	59
Abstract	60
Résumé.....	61
3.1 Introduction	62
3.2 Model Description and Experiment Design	64
3.2.1 WRF Model Description	64
3.2.2 Description of the CHIMERE Model.....	66
3.2.3 Domains Setup and Observations Data	68
3.3. Results and Discussions	69
3.3.1 Urban Parameters and Nudging Tests	69

3.3.2 Impact of the Urban Canopy Model.....	70
3.3.3 Impact of Mixing Boundary Layer Height.....	79
3.3.4 Impact of Land surface model.....	87
3.4 Conclusions	89
References	91
Chapter IV: On the impact of WRF-CHIMERE vertical grid resolution and first layer height on mesoscale meteorological and chemistry transport modelling	
Abstract	97
Résumé.....	98
4.1 Introduction	98
4.2 Method	99
4.3. Results and Discussion.....	101
4.3.1 Surface meteorological and pollutants concentration	101
4.3.2 Vertical profiles.....	104
4.3.3 Comparison of model results with observations	105
4.4 Conclusions	112
References	114
Chapter V: Improvement of the vertical mixing in chemistry transport modelling based on a 1.5 order turbulence kinetic energy-based eddy diffusivity closure scheme	
Abstract	120
Résumé.....	121
5.1 Introduction	121
5.2 Model Description and Experiment Design	124
5.2.1 WRF and CHIMERE Model Description	124
5.2.2 Domains Setup and Observations Data.....	128
5.3 Results and Discussions	129
5.3.1 Impact of the first layer height on NED modelling.....	129
5.3.2 NO ₂ and O ₃ Simulations over Paris region	131
5.3.3 PM _{2.5} and PM ₁₀ Simulations over Paris region	139
5.3.4 Study in Lyon and Bordeaux regions	142

5.4 Conclusions	154
References	156
Conclusions and Perspectives	160
List of Figures	165
List of Tables.....	170
Annex A	172
Annex B.....	184

Chapter I: Introduction

1.1 Air pollutants in the Atmosphere

The atmosphere of Earth is schematically divided into four different sub layers: the troposphere, the stratosphere, the mesosphere, and the thermosphere, each of them with different chemical and physical properties (Mohanakumar, 2008; Williams and Avery, 1992). The troposphere is the lowest layer of the atmosphere which extends approximately up to 10 to 15km from the surface of Earth and contains most of the atmosphere's mass and human activities. Fossil fuels such as oil and coal have been powering the industrial development and daily life since the first industrial revolution (Najjar, 2011). Anthropogenic emissions of gaseous and particulate matters changed the share of many species in the atmosphere, causing air pollution, climate change and other environmental issues (Meng et al., 2009). Gaseous pollutants can be divided into primary pollutants and secondary pollutants (Nazaroff and Weschler, 2004). Primary pollutants refer to the original pollutants discharged directly from the pollution source into the atmosphere (Fisher, 2017). Secondary pollutants refer to a series of chemical or photochemical reactions between primary pollutants and existing components in the atmosphere, or several primary pollutants (Jenkin and Clemitshaw, 2000). Primary pollutants that have received general attention in air pollution control include sulfur oxides, nitrogen oxides, carbon oxides and organic compounds; secondary pollutants include sulfuric acid and photochemical compounds (WHO, 2006).

The presence in the atmosphere of particles with different sizes, which are usually defined as aerosols with their specific chemical composition, is of particular interest. They are ubiquitous in the Earth's atmosphere, but their distribution patterns are extremely variable, due to complex cycles of different aerosol types from various sources and with different lifetimes from a few days to a few weeks (Seinfeld and Pandis, 2016). Some aerosols can be directly emitted from both anthropogenic emissions (traffic emissions, industrial activities, biomass burning, etc.) and natural sources (vegetation, volcanoes, oceans, deserts, etc.) which are called primary particles, or later formed by physical and chemical mechanisms like the condensation of low-volatility gases, nucleation or chemical reactions, described as secondary particles (Hallquist et al., 2009). The size and chemical composition of an aerosol mixture present in the atmosphere is determined by its source and formation pathways (Colbeck and

Lazaridis, 2010). As shown in Figure 1.1, particles with an aerodynamic diameter greater than $2.5\mu\text{m}$ are usually produced by mechanical processes (coarse mode) whereas for nucleation mode particles (less than 10nm) homogeneous nucleation is the main source (Xu et al., 2011). In between these size ranges, at $10\text{-}100\text{nm}$ (Aitken mode) and $0.1\text{-}2.5\mu\text{m}$ (accumulation mode), particles are generated via coagulation from the nucleation mode which can further grow through condensation (Finlayson-Pitts and Pitts, Jr, 1999).

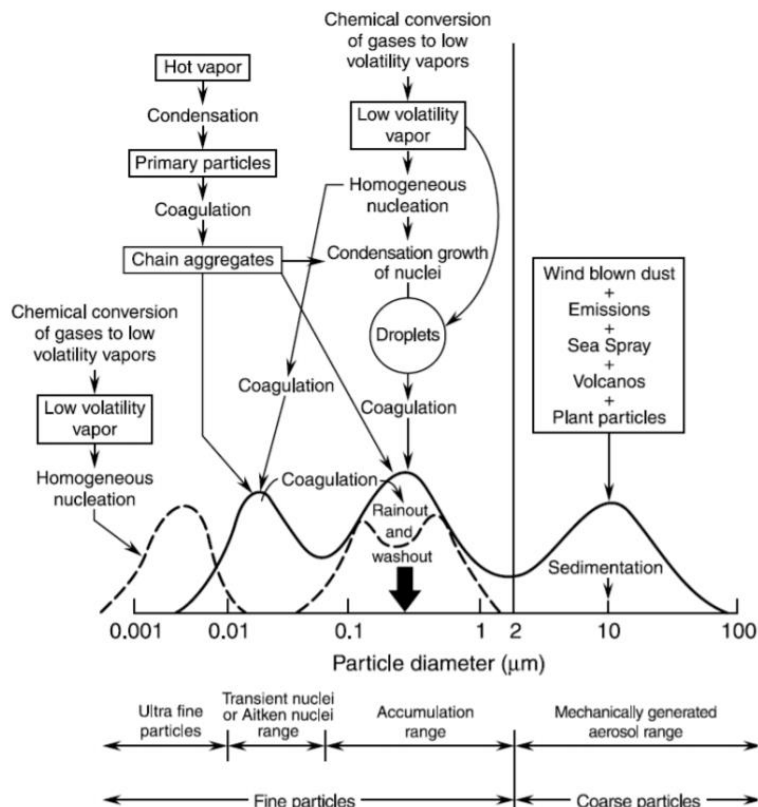


Figure 1.1 Typical sources, formation, removal pathways and size distributions of atmospheric aerosol (Finlayson-Pitts and Pitts, Jr, 1999).

1.2 Effects of air pollution on climate

Human activities, particularly fuel combustion increase the concentration of greenhouse gases, leading to global warming. This has also led to rising sea levels and melting of glaciers caps. As the temperature continues to rise, more environmental changes will inevitably occur (Bai et al., 2018). Studies have demonstrated that the average global temperature is expected to rise by $2\text{ }^{\circ}\text{C}$ to $4.5\text{ }^{\circ}\text{C}$ while the sea levels will increase about 28 cm until 2100 (Desonie, 2007; Kemp et al., 2011). Aerosols also have significant impacts in climate change (Prather,

2009). These impacts are generally described in terms of radiative forcing (RF) (Bond et al., 2013; Charlson et al., 1992; IPCC 2013; Kok, 2011; Scott et al., 2018). Some pollutants mainly scatter solar radiation have a direct cooling effect, associated to negative RF (Myhre et al., 2013). In contrast, absorbing pollutants have a direct warming effect, it could darken the surface of snow and ice, reducing their albedo then hastening melting (Hansen et al., 2005). The largest contribution to RF is caused by increasing fossil fuel combustion, mostly of carbon dioxide (Andres et al., 2012). Those greenhouse gases and particles increased as a result of human activities especially in the past century. As illustrated by Figure 1.2, semi-direct and indirect effects are also important processes on climate changes. The semi-direct effect corresponds to rapid adjustments induced by aerosol radiative effects on the surface energy. It enhances the heating of the surrounding air while reducing the amount of solar radiation reaching the ground that can stabilize the atmosphere and reduce convection, it could also increase the atmospheric temperature which reduce the relative humidity, inhibit cloud formation, and enhance the evaporation of existing clouds (Myhre et al., 2013).

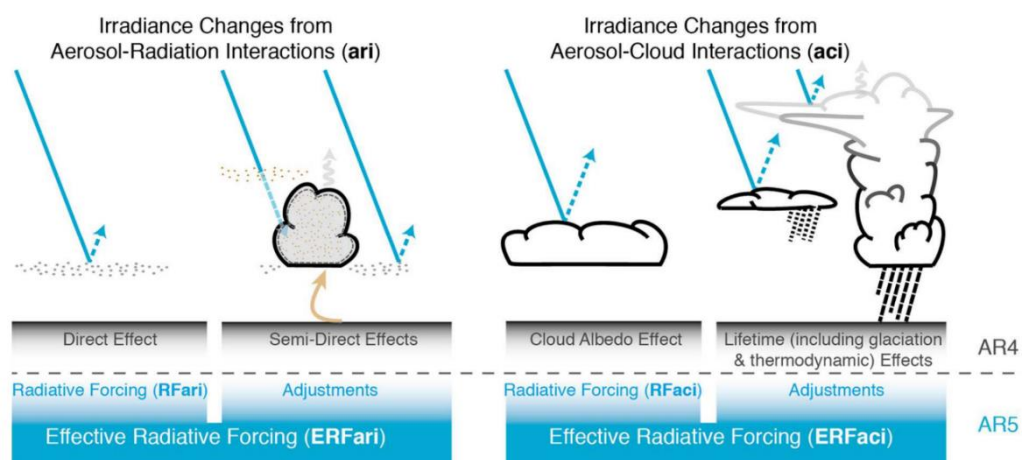


Figure 1.2 Direct, semi-direct and indirect effects of aerosols on climate (IPCC, 2013).

Figure 1.3 summarizes the mean net RF estimated for the major air pollutants with uncertainty levels - as compared to reference conditions prevailing before the industrial age. Gaseous species globally display an increase of positive RF, uncertainties remains low (Shindell et al., 2009). In contrast, climate change effects caused by aerosols are strongly associated with their chemical composition, with opposite influences, as well as much higher uncertainties. For example, inorganic species like nitrate and sulfate, globally exhibit negative RF, while black

carbon shows a strong positive RF through aerosol - radiation interactions organic aerosol are associated with a net negative RF at global scale (Corbera et al., 2016). However, it could also participate in local to regional positive RF due to brown carbon light absorption (Liu et al., 2017). Overall, with the breakthrough in observation measurements and atmospheric model, researchers made a great improvement in the understanding of characteristics of atmospheric aerosols and their climate effect over the last decades, uncertainty in the total direct aerosol effect is reduced based on a combination of global aerosol models and observation-based methods. But for a single component of particulate matter, especially the influence of carbonaceous aerosol, the effect on RF remains uncertain. Meanwhile, as shown in Figure 1.4, aerosols optical depth obtained from remote sensing is highly inhomogeneous, and the global aerosol composition varies greatly in space and time (Remer et al., 2008). Therefore, the regional differences in the impact of aerosols on climate change and the propagation process are also worthy of more in-depth study. Overall, effective climate change mitigation and adaptation strategies depend on the enhancement of our understanding of their sources and optical properties.

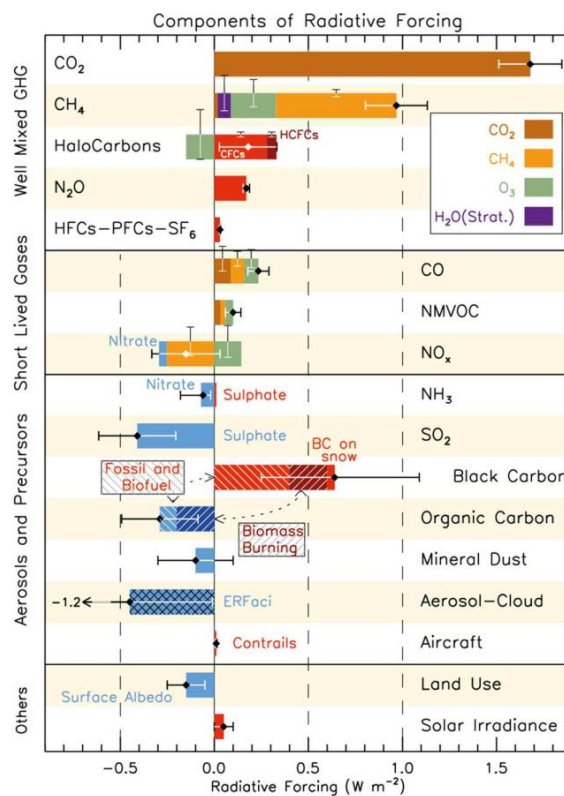


Figure 1.3 Change in RF effects caused by atmospheric pollutants for the period 1750–2011, associated with individual confidence range (IPCC, 2013)

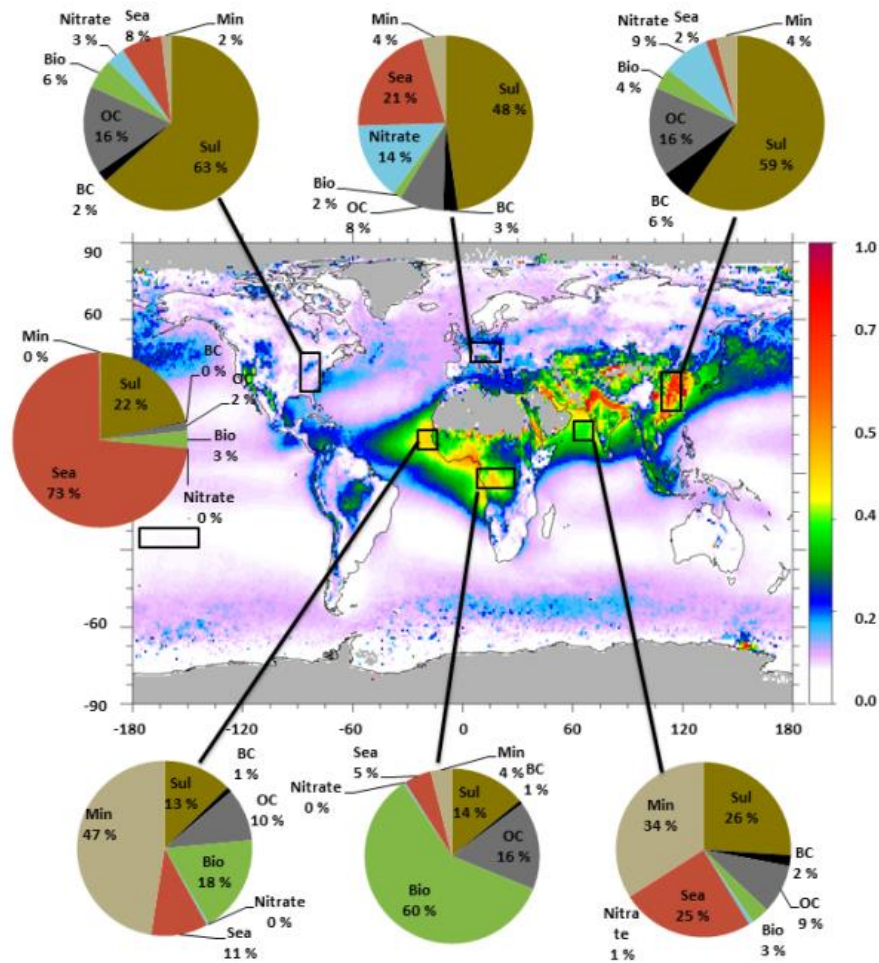


Figure 1.4 MODIS aerosol optical depth averaged over the 10-year period 2001–2010. Pie charts show the contribution of different aerosols to the total aerosol optical depth for different regions (Myhre et al., 2013).

1.3 Health effect of air pollution

Ambient air pollution is a complex mixture of aerosols and gases. PM_{2.5} and ozone are two important indicators for air quality (White, 2009; You et al., 2018). PM_{2.5} is a consistent and robust predictor for health effects from studies of long-term exposure to air pollution (Danesh Yazdi et al., 2020; Kloog et al., 2013). Studies indicate that a 10 $\mu\text{g}/\text{m}^3$ increase in ambient PM_{2.5} was expected to increase admissions in hospitals by 4.5% (Kwon et al., 2019). Ozone has been associated with increased respiratory mortality (Zhang et al., 2019)

According to the World Health Organization (WHO), air pollution represents one of the greatest risks to public health (WHO., 2016), it attributes 3.7 million premature deaths to

outdoor air pollution and 4.3 million to indoor air pollution. Formation of air pollution episodes is caused by the harmful emission or excessive quantities of air pollutants combined with a lack of atmospheric dispersion (Florentina and Io, 2011; Watson et al., 1988a). This association between air pollution exposure and the risks to human health has been a public health concern for over 700 years (Yin et al., 2020). Despite this early recognition of the health risks associated with poor air quality it has only become a global topic over the last 80 years (Manisalidis et al., 2020). Issues related to air quality has emerged in the human conscious with severe events like such as the Los Angeles smog in 1949, the Great London fog in 1952, and the Beijing haze in 2013 (Huang, 2018; Li and Svarverud, 2018; McNeill and Engelke, 2016; Xiao, 2015). Chronic exposure also remaining risks, with air pollution leading to premature death of about 3 million population per year over the world (Anderson et al., 2012; Fang et al., 2013). In Europe, aerosols are assessed as the most worrying atmospheric pollutants along with nitrogen oxides and ozone (“Consolidated Annual Activity Report 2018 (CAAR) - EEA annual report — European Environment Agency,” n.d.). Health effects include difficulty in breathing, wheezing, coughing, asthma and worsening of existing respiratory and cardiac conditions (Kim et al., 2013; Levy et al., 2006). These effects result in increased medication use and premature death (Liu et al., 2018). Some studies are also showing air pollution impacts on fertility, pregnancy, premature birth, dementia, and/or obesity (Koman et al., 2018; Olsson et al., 2013).

The various biological mechanisms beyond pollutants health effects still remains uncertainties (Samet and Krewski, 2007), but it also has been generally recognized that particle size and chemical composition are major factors determining their health effects (Lighty et al., 2000; Natusch and Wallace, 1974). Exposure to fine particulate matter has largest health risk (Bell et al., 2010; Power et al., 2015), since those small particles could join into the deepest regions of the lungs and transport the toxic compounds into the bloodstream. For instance, Quan et al (2010) indicated that PM_{2.5} was responsible for plaque exacerbation, causing vascular inflammation and atherosclerosis. (Feng et al., 2016) reported that PM_{2.5} promotes the initiation and progression of diabetes and driving adverse birth outcomes. Recognizing the dangers of air pollutants to public health, the European Commission has proposed to fix the ceiling of the annual average concentration of 25µg/m³ for PM_{2.5}. The European Union

member states shall comply with this value since 2015 and the is reflecting to adopt more stringent standards in line with WHO guidelines. Furthermore, some compounds such as black carbon are suspected to be carcinogenic which have been recently classified in the 2A (probably carcinogenic to human) and 2B (possibly carcinogenic to human) groups by IARC (International Agency for Research on Cancer)(Baan, 2007; Lauby-Secretan et al., 2016). Air pollution is one of the greatest social and environmental problems, with terrible consequences (Koolen and Rothenberg, 2019a). Therefore, an efficient air quality simulation and forecast model especially in urban region can be a key tool to assess health risks for humans exposed to airborne pollutants.

1.4 The development of atmospheric models

Atmospheric models are mathematical representations based on a complete set of dynamic equations that can generate physical and numerical data of climate and chemical parameters (Li et al., 2016). Today, an atmospheric model becomes an essential tool in a variety of atmospheric sciences applications. Early in 1904, the Norwegian scientist Vilhelm Bjerknes listed seven basic variables (temperature; pressure; air density; humidity; the three components of wind velocity) and set down a two-step scientific viewpoint for the weather prediction: (i) the initial state of the atmosphere is determinates by observation giving the distribution of the variables at different levels in the diagnostic step first, (ii) then the changes over time calculated using the law of motion in the prognostic step (Lynch, 2008). By about 1922, the British scientist Lewis Fry Richardson presaged the numerical weather prediction after the advent of electronic computers in his book *Weather Prediction by Numerical Process* (Inness and Dorling, 2012; Somerville, 2011). In those days, the weather forecasting was a haphazard process, the forecaster used rough techniques of extrapolation based on their knowledge of local climatology and intuition, but the principles of theoretical physics played little role in practical forecasting, weather forecasting was more an art than a science (Lynch, 2002, 2008). Since the 1960s, with the development of computers and network communication techniques, the atmospheric model arises at the historic moment (Hersbach et al., 2015; Paine, 2019). For the past half century, with the rapid development of

high-performance computers, satellite detection and the continuous in-depth research of numerical prediction theory, numerical prediction has achieved great success and has become an important symbol of the atmospheric science and the main methods of weather forecasting operations (Meng et al., 2019). Although the processes of climate change are of global proportions, there are significant differences in its specific manifestations between regions (temperature; precipitation and land-use changes). Thus, atmospheric mesoscale models are being embedded to provide specific guidance to policy makers at all administrative levels. The development of mesoscale models goes back to the 1960's, in which with a grid size of tens of kilometers to simulate regional weather over a few days (Dudhia, 2014). With the evolution of dynamics and physical representations and the availability of cheaper computing resources, high resolution simulation and forecast became possible and various "local customized" models began to emerge. For example, a mesoscale meteorological model coupled with a chemical transport model (CTM) is an essential tool to provide the regional airshed information to help government develop strategies for manage regional air quality. In the past two decades, those models have been used to provide information for integrated models like GAINS (Greenhouse gas - Air pollution Interactions and Synergies) for key negotiations on the air pollution control agreements (Amann et al., 2011). New approaches based on statistics are in use or under development like the Screening for High Emission Reduction Potential on Air (SHERPA) tool. In SHERPA (Pisoni et al., 2017; Thunis et al., 2016a), a different approach is undertaken that reproduces the grid-cell-to-grid-cell approach but does not require anywhere near as many CTM runs. SHERPA assumes that the unknown parameters vary on a cell-by-cell basis but are no longer independent of each other.

According to the model design concepts and parameters, the development of CTM is roughly divided into three generations (Casado, 2013). The first generation of CTM originated in the 1970's which mainly include the box model based on the law of conservation of mass (Seinfeld, 1988) such as Empirical Kinetic Modeling Approach (EKMA), the Gaussian dispersion model based on the statistical theory of turbulence diffusion (Atkinson et al., 1997) like Industrial Source Complex model (ISC). These models use simple, parameterized linear mechanisms to describe complex atmospheric physical processes, which are suitable for simulating the long-term average concentration of inert pollutants (Watson et al., 1988b). In

the early 1980s, with the study of the turbulence characteristics of the atmospheric boundary layer, researchers found that the Gaussian model could not answer many questions, which gradually promoted the development of the second generation. The second generation of CTM considers nonlinear response mechanism and incorporates the treatment of gas and aqueous phase chemistry. These models divide the simulated domain into many three-dimensional grid cells, the cloud, fog and precipitation scavenging processes are calculated in each cell (Carey Jang et al., 1995; Liu et al., 1984; Stockwell et al., 1990). Representative models in this category include the Urban Air shed Model (UAM), the Regional Acid Deposition Model (RADM), etc. The second generation CTM are only designed to address individual pollutant issues such as ozone and acid deposition, which does not fully consider the mutual transformation and mutual influence of various pollutants (Reis et al., 2005). However, the physical and chemical reaction processes among various pollutants are complex in the real atmosphere. In 1990's, the US Environmental Protection Agency (EPA) developed the third-generation air quality simulation platform Models-3 based on the concept of "one atmosphere" (Byun and Schere, 2006a). At present, the most widely used are the third-generation comprehensive CTM in clouding WRF-Chem, the Comprehensive Air-quality Model with extensions (CAMx), Community Multiscale Air Quality Model (CMAQ), CHIMERE, etc.

The WRF-Chem is a regional atmospheric dynamic-chemical coupling model developed by the US National Center for Atmospheric Research (NCAR), which is integrated with the atmospheric chemistry module in the mesoscale Weather Research and Forecast model (WRF) (Grell et al., 2005). The WRF provides online large airflow fields for CTM, simulating pollutant transportation, dry and wet deposition, gas phase chemistry, aerosol formation, radiation, biological radiation, etc. (Lin et al., 2020). The advantage of WRF-Chem is that the meteorology mode and the chemical transport mode are fully coupled in time and space resolution to achieve true online feedback. The CAMx model is a comprehensive CTM developed by ENVIRON on the basis of the UAM model. In addition to the typical features of the third-generation air quality model, the most famous features of CAMx include: two-way nesting and flexible nesting, grid plume module, ozone source allocation technology, particulate source allocation technology (Bove et al., 2014; Pepe et al., 2016). The CMAQ,

emission inventory processing model (SMOKE), mesoscale meteorological model (MM5 or WRF.) together constitute the Models-3 platform, of which CMAQ is the core of the entire system (Hanna, 2008). The CMAQ was originally designed to comprehensively deal with complex air pollution problems such as tropospheric ozone, acid deposition, and visibility. For this reason, the design concept of CMAQ can systematically simulate various scales and various complicated air pollution issues. The CMAQ model has become a quasi-regulatory model used by the US EPA in environmental planning, management and decision-making. The characteristics of this model are: simultaneously simulate the behavior of a variety of air pollutants, including ozone, PM, acid deposition, and visibility and other air quality problems in different spatial scales; make full use of the latest Computer hardware and software technologies, such as high-performance computing, modular design, visualization technology, etc., make air quality simulation technology more efficient and accurate, and the application fields tend to be diversified. Since CMAQ 5.0, the model has realized the on-line coupling of meteorological model, absorbing the advantages of WRF-CHEM model (Kong et al., 2015). CHIMERE is a three-dimensional CTM driven by meteorological drivers like MM5 or WRF. More than 80 kinds of species more than 300 reactions are described in the model. Processes include chemistry, transportation, vertical diffusion, photochemistry, dry deposition, absorption in and below clouds, and SO₂ oxidation. Clouds are included in the process model. It can simulate processes including gas-phase chemistry, vertical diffusion, photochemistry, aerosol formation, deposition and transport at regional and urban scales (Bessagnet et al., 2004; Vautard et al., 2005). A new version CHIMERE-V2019 has realized the online coupling of meteorological model like WRF-Chem and CMAQ (Bessagnet et al., 2020). Compare to the first and second generation CTM, the third generation CTM has distinct advances in:

- (i) full consideration of various atmospheric physical processes, chemical reactions between pollutants and gas-solid two-phase transformation process (San José et al., 2009);
- (ii) based on nested grid design, it can be used as a multi-scale atmospheric simulation and prediction tool (Xue et al., 2001);

- (iii) simultaneously simulate the variety of air pollutants, including ozone, PM, acid deposition, visibility and other environmental pollution problems;
- (iv) make full use of the latest computer technologies, such as high-performance computing, modular design, visualization technology to make air quality simulation technology more efficient and accurate (Reis et al., 2005).

Today, around ninety nations run their own mesoscale models until 2016 either for specific regions or for specific applications such as local air quality, dust transport, agricultural production, airport weather, solar ultraviolet radiation and hydrology according to World Meteorological Organization technical progress report (<https://www.wmo.int/pages/prog/www/DPFS/GDPFS-Progress-Reports.html>). Despite the remarkable advances of atmospheric model over the past decades, formidable challenges remain. The effective coupling between the dynamical processes and physical parameterizations during the short-term weather changes and extremes is still a significant challenge. Under the background of global warming, the chaotic nature of the atmosphere becomes stronger, which puts forward higher requirements for long-term accurate forecasting, a stronger fusion between model and observations for its data assimilation and bias corrections are needed. Maybe the next-generation model with a focus on chemical and physical processes, neural networks, machine learning are the ways in the future model evolution.

1.5 Urbanization and air quality

In recent decades, air pollution in urban areas, especially megacities, have aroused people's attention (Baklanov et al., 2016b). With the accelerating process of industrialization and urbanization, an increasing number of people will be affected by such process especially in developing regions (Beirle et al., 2011; Fang et al., 2015; Hopke et al., 2008). Urbanization was positively related to global health in the short term and long term. In the short run, 1% increase in urbanization was associated with reduced mortality, under-five mortality, and infant mortality of 0.05%, 0.04%, and 0.04%, respectively, as well as increased life expectancy of 0.01 year (Wang, 2018). However, the process of urbanization has also made

important contributions to regional climate changes and has caused a bad effect on ecosystem and extreme climate significantly increased (Changnon et al., 1996; Semenza et al., 1996). Since the end of World War II, the world's population has grown from 2.5 billion to about 7 billion today, the urban pollution has risen from below 30% to 58% in the past seventy years. Air pollution in cities is exacerbated by increased human activity in urban areas due to population growth (Miranda et al., 2015). The recent global lockdown events response to COVID-19 pandemic have reduced the NO₂ concentrations and particulate matter levels by about 60% and 31% respectively by using satellite data and a network of more than 10000 air quality observation stations in 34 countries (Venter et al., 2020), the NO₂ and PM_{2.5} concentration in China was reduced by around 20% and 17% for 30–50 days (Z. Liu et al., 2020; Zinke, 2020). Using the mesoscale meteorological and chemical transport model, Menut et al.(2020) noted a decrease of -30% to -50% for NO₂ and -5% to -15% for particulate matter in all western Europe counties during the lockdown events. In general, air pollution is positively correlated with the initial and acceleration stages of urbanization, with pollution in major cities tending to increase during the construction phase, passing through a maximum pollution level and then again decreased at the end of the urbanization process as abatement strategies are developed (Fenger, 1999). In the industrialized Europe countries, urban air pollution is in some respects in the last stage with effectively reduced levels of many pollutants such as Sulphur dioxide, carbon monoxide and lead (Fenger, 2002). Figure 1.5 shows that ground - level concentrations of almost all pollutants have declined steadily since 2000 in 28 countries Europe Union (EU28). The two notable results concerning emission reductions are the total SO_x from the EU28 member states were cut by 69 % since 2000 and the almost no changes of total ammonia (Koolen and Rothenberg, 2019).

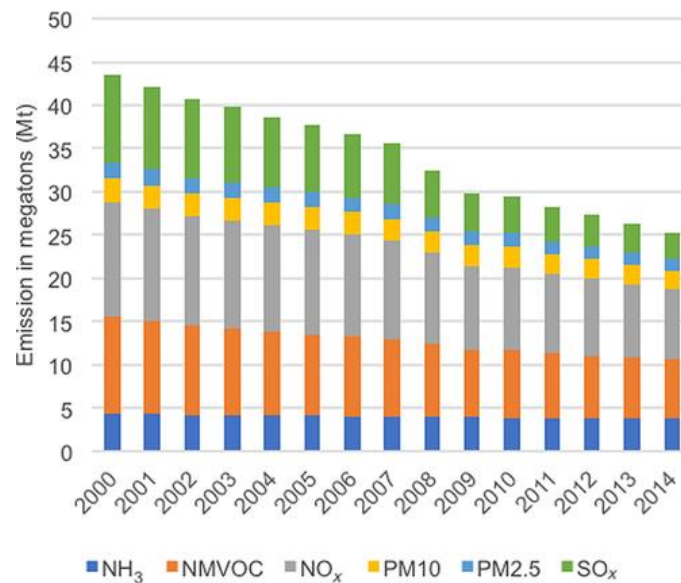


Figure 1.5 Emission trends in the EU28 on the basis of fuel sold (Koolen and Rothenberg, 2019)

Besides, geographical condition also plays an important role in transportation and dispersion of pollutants. Pollutants dispersion processes over the valley-basin city are much more complicated than over flat areas. Therefore, pollution episodes have been frequently witnessed over complex terrain, especially in wintertime (Chen et al., 2019; Sabatier et al., 2020). In coastal cities, shipping emissions contribute to air quality degradation. Viana et al. (2014) found that shipping emissions contribute with 1% to 7% for PM10, with 1% to 20% for PM2.5, and with 7% to 24% for NO₂ annual mean concentrations in European coastal areas. In addition, continuing urbanization has resulted in cities that are almost always warmer than the surround, which are known as urban heat island (UHI). A recent research shows that urban region has higher heat index than rural areas by a difference of about 1.5–2 °C (Bhati and Mohan, 2018). Compared with the natural vegetation canopy, the city has its unique features: taking buildings as an example, different buildings have different functions, shapes, heights, orientations, styles, etc. (Wong and Chen, 2008). Figure 1.6 shows the differences in surface temperature between buildings and vegetation canopy. Meanwhile, UHI can significantly exacerbate building energy consumption (Palme et al., 2017). The growing cooling energy consumption caused by UHI will increase CO₂ emissions by up to five times in 2050 than in 2000 for buildings in cities (Y. Liu et al., 2020). Besides, there are various types of artificial surfaces in urban areas, such as asphalt roads, concrete sidewalks, glass

curtain walls, parking lots, and green spaces which have impact on urban air quality (Wise, 2016). For example, computational fluid dynamics studies indicated that the flow resistance of tree crowns decreased wind speed and the dispersion of pollutants is limited in the ground level and the particulate matter concentrations accumulate within the canyon (Gromke and Blocken, 2015). These diversified types of artificial areas appear alternately, leading to complex, diverse, and non-uniform urban canopy characteristics, which give more complex turbulent airflows in urban region, increased the difficulty of air quality simulation and forecast in cities than in other regions. The urban canopy, urban street canopy and urban boundary layer consist of the urban micro environment. The boundary layer is the atmospheric structure closest to the underlying surface. The meteorological conditions within the boundary layer play an important role in the formation of air pollution (Bianco et al., 2008). The wind field determines the regional transportation of pollutants. The height of the atmospheric boundary layer determines the amount of ventilation and the dilution capacity of pollutants. Heavy pollution episodes are always accompanied by a low boundary layer height (Quan et al., 2014; Yin et al., 2019). In cities, urbanization causes thermodynamic perturbations and facilitates the development of the boundary layer (Miao et al., 2019). Moreover, some aerosols like black carbon can warm the upper PBL which help to stabilize the boundary layer height and weaken turbulent mixing, resulting in a decrease of the boundary layer height (BLH), which enhances the accumulation of air pollutants (Ding et al., 2016; Li et al., 2017).

Overall, cities are highly sensitive to the impact of meteorological disasters. How to be efficient in extreme climates risk analysis and early warning, firmly keeping the bottom line of city safe operation and ecological environment protection is a concern of scientists and politicians. The impact of the accelerated urbanization process on the regional climate and atmospheric environment mainly includes the following aspects:

- (1) The urban underlying surface is defined as the part of the city in direct exchange with the atmosphere (Y. Li et al., 2020), the changes of the urban underlying surface have changed the environmental properties of the natural underlying surface;

- (2) The urban canopy has a "shading effect" on solar radiation, which reduces the solar radiation reaching the surface. At the same time, there is the exchange and storage of radiation energy between the buildings in the canopy, which affects the surface energy balance;
- (3) Human activities will increase atmospheric pollutants and artificial heat generation. In short, in addition to bringing economic and social benefits to humanity, urbanization has also brought many problems to the urban climate and atmospheric environment Statement.

The climate effect brought by urbanization and its impact on the atmospheric environment is becoming one of the key issues of the world.

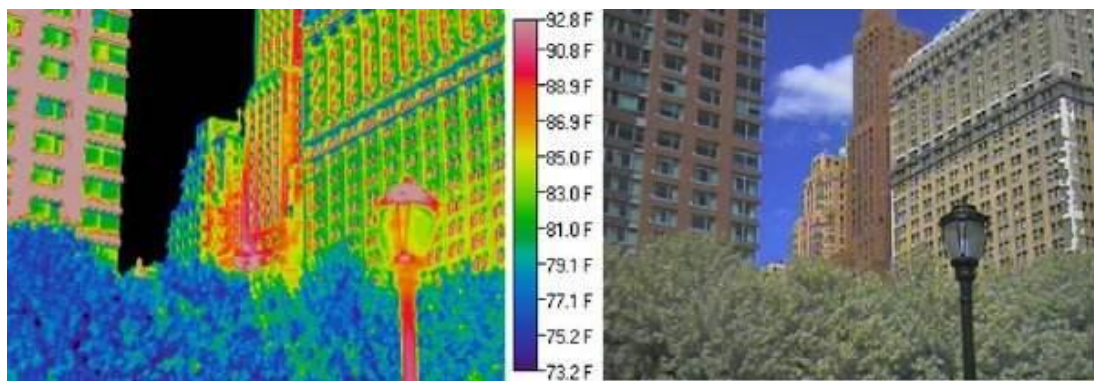


Figure 1.6 Urban heat island in cities.

1.6 Objectives and outline of the PhD thesis

The main goal of this PhD work is to improve the air quality simulation and forecast in France especially in urbanized areas. For its operational requirements, the system requires continuous improvements, particularly the ability to better predict certain types of episodes and exceedances of limit values for criteria pollutants. Patterns of urban air pollution are rather variable and spatially heterogeneous. Turbulence plays an important role on the vertical mixing of physical parameters and pollutants. Understanding the impact of multiple parameterization schemes on air quality simulation can help improve model configuration to address local areas.

The third generation of CTM system generally has three basic modules: a meteorological process module (input information from mesoscale meteorological models), emission inventory pre-processor and the core air quality simulation module. Studies indicate that the physics parameterizations play the key role in both meteorological and air quality simulation particularly in urban areas. The buildings and cement pavement form the urban canopy layers and surface roughness, therefore change thermal and dynamic characteristics of the surface layer. These changes will significantly influence the surface heat accumulation that has a negative effect of the planetary boundary layer (PBL) height and surface wind speed which affect the transport and dispersion of pollutants. The PBL height is a key factor on the formation and evolution of pollutants. A low boundary layer height is regarded as a major meteorological process for haze formation. Thus, a smart selection of physics parameterizations plays a crucial role in urban air quality prediction.

With the development of computer performances, high resolution meteorological and air quality simulations become possible. However, studies demonstrate that the higher resolution does not represent better simulation results, horizontal resolution below 1km is not necessary. Meanwhile, the building clusters modified surface roughness and zero-plane displacement height, an overestimated vertical resolution can cause unreasonable wind flows near surface.

The *K*-theory shows certain advantages in dealing with the dispersion of air pollution at the mesoscale. It can use the observed wind speed profile data to obtain the concentration distribution of pollutants without assuming a certain form of distribution. However, high pollutants concentrations are frequently found under stable and cold weather conditions, such conditions are characterized by a stratified lower atmosphere and weak turbulent diffusion. In cities, traffic, residential and local industrial emissions have a major share of the pollutants; those emissions can accumulate and have longer residence times near the ground level due to the inefficient transport and mixing. The transient turbulent flow plays an important role on the transportation and deposition of pollutants, thus, an advanced vertical eddy coefficient may helpful to provide an accurate prediction of pollution during the short-term episode. It is noteworthy that meteorological sciences have focused on extreme events to forecast heavy precipitations, thunderstorms, high wind speed conditions while air quality is mainly driven

by stable and calm meteorological situations and these latter conditions are difficult captured by meteorological models.

Different geographical areas will be investigated in France, especially mainly for short-term pollution episodes. The ability of models to assess air quality management strategies is also important, it will be appropriate during this study to perform the diffusion and dispersion of main pollutants and possibly improve the vertical diffusion coefficient in the selected CTM (CHIMERE here) (Menut et al., 2013; Mailler et al., 2017).

The objectives of this work are to provide clues and answers to the following questions:

- 1) Which formulae for computing the vertical diffusion coefficient based on K-theory gives the best performances on air quality simulation?*
- 2) How well do physics parameterizations impact the urban air quality simulation and forecast?*
- 3) How does vertical grid resolution and first layer height impact the meteorological and chemistry transport modelling?*
- 4) Can we improve the vertical mixing through the use of turbulence kinetic energy sub-grid eddy coefficient?*

To tackle these issues, the present work has been breakdown in four main steps detailed in the various chapters.

Chapter II addresses the results of the one-year air quality simulation that was determined by three *K*-theory vertical diffusion coefficient. Inter-annual trends, seasonal and daily variations of main pollutants concentrations are presented. Here, it has been chosen to focus both on cities and surroundings over the whole France.

In **Chapter III**, the impact of physics parameterizations on high-resolution meteorological and air quality simulations over the urban region will be analyzed, with a focus on a winter pollution episode in Paris region. Three canopy schemes, three boundary layer schemes, two land surface schemes will be tested in this part. Benefits as well as drawbacks and specific issues of the considered approaches are discussed and compared. Finally, the most reasonable physics parameterizations will be used in the subsequent chapters.

In **Chapter IV**, the impact of vertical grid resolution and first layer height on meteorological and chemistry transport modelling will be analyzed; three vertical resolution configurations and three first layer height will be applied in a fifteen days winter episode including a pollution event.

In **Chapter V**, we use a 1.5-order turbulence kinetic energy-based eddy diffusivity closure scheme from WRF defined as NED on the urban air quality context to assess consequences of surface-level pollutants concentrations in Paris, Lyon and Bordeaux regions.

References

- Amann, M., Bertok, I., Borken-Kleefeld, J., Cofala, J., Heyes, C., Höglund-Isaksson, L., Klimont, Z., Nguyen, B., Posch, M., Rafaj, P., Sandler, R., Schöpp, W., Wagner, F., and Winiwarter, W.: Cost-effective control of air quality and greenhouse gases in Europe: Modeling and policy applications, *Environmental Modelling & Software*, 26, 1489–1501, <https://doi.org/10.1016/j.envsoft.2011.07.012>, 2011.
- Anderson, J. O., Thundiyil, J. G., and Stolbach, A.: Clearing the Air: A Review of the Effects of Particulate Matter Air Pollution on Human Health, *J. Med. Toxicol.*, 8, 166–175, <https://doi.org/10.1007/s13181-011-0203-1>, 2012.
- Andres, R. J., Boden, T. A., Breon, F.-M., Ciais, P., Davis, S., Erickson, D., Gregg, J. S., Jacobson, A., Marland, G., Miller, J., Oda, T., Oliver, J. G. J., Raupach, M. R., Rayner, P., and Treanton, K.: A synthesis of carbon dioxide emissions from fossil-fuel combustion, 2012.
- Anon: AR5 Climate Change 2013: The Physical Science Basis — IPCC, n.d.
- Consolidated Annual Activity Report 2018 (CAAR) - EEA annual report — European Environment Agency: <https://www.eea.europa.eu/publications/consolidated-annual-activity-report-2018>, last access: 13 January 2021.
- WHO | World Malaria Report 2016: <http://www.who.int/malaria/publications/world-malaria-report-2016/report/en/>, last access: 13 January 2021.
- Atkinson, D., Bailey, D., Irwin, J., and Touma, J.: Improvements to the EPA Industrial Source Complex Dispersion Model, *Journal of Applied Meteorology - J APPL METEOROL*, 36, 1088–1095, [https://doi.org/10.1175/1520-0450\(1997\)036<1088:ITTEIS>2.0.CO;2](https://doi.org/10.1175/1520-0450(1997)036<1088:ITTEIS>2.0.CO;2), 1997.
- Baan, R. A.: Carcinogenic Hazards from Inhaled Carbon Black, Titanium Dioxide, and Talc not Containing Asbestos or Asbestiform Fibers: Recent Evaluations by an IARC Monographs Working Group, 19, 213–228, <https://doi.org/10.1080/08958370701497903>, 2007.
- Bai, L., Wang, J., Ma, X., and Lu, H.: Air Pollution Forecasts: An Overview, *Int J Environ Res Public Health*, 15, <https://doi.org/10.3390/ijerph15040780>, 2018.
- Baklanov, A., Molina, L. T., and Gauss, M.: Megacities, air quality and climate, *Atmospheric Environment*, 126, 235–249, <https://doi.org/10.1016/j.atmosenv.2015.11.059>, 2016.
- Beirle, S., Boersma, K. F., Platt, U., Lawrence, M. G., and Wagner, T.: Megacity Emissions and Lifetimes of Nitrogen Oxides Probed from Space, 333, 1737–1739, <https://doi.org/10.1126/science.1207824>, 2011.

- Bell, M. L., Belanger, K., Ebisu, K., Gent, J. F., Lee, H. J., Koutrakis, P., and Leaderer, B. P.: Prenatal Exposure to Fine Particulate Matter and Birth Weight, *Epidemiology*, 21, 884–891, <https://doi.org/10.1097/EDE.0b013e3181f2f405>, 2010.
- Bessagnet, B., Hodzic, A., Vautard, R., Beekmann, M., Cheinet, S., Honoré C., Liousse, C., and Rouil, L.: Aerosol modeling with CHIMERE—preliminary evaluation at the continental scale, *Atmospheric Environment*, 38, 2803–2817, <https://doi.org/10.1016/j.atmosenv.2004.02.034>, 2004.
- Bessagnet, B., Menut, L., Lapere, R., Couvidat, F., Jaffrezo, J.-L., Mailler, S., Favez, O., Pennel, R., and Siour, G.: High Resolution Chemistry Transport Modeling with the On-Line CHIMERE-WRF Model over the French Alps—Analysis of a Feedback of Surface Particulate Matter Concentrations on Mountain Meteorology, *Atmosphere*, 11, 565, <https://doi.org/10.3390/atmos11060565>, 2020.
- Bhati, S. and Mohan, M.: WRF-urban canopy model evaluation for the assessment of heat island and thermal comfort over an urban airshed in India under varying land use/land cover conditions, *Geosci. Lett.*, 5, 27, <https://doi.org/10.1186/s40562-018-0126-7>, 2018.
- Bond, T. C., Doherty, S. J., Fahey, D. W., Forster, P. M., Berntsen, T., DeAngelo, B. J., Flanner, M. G., Ghan, S., Kärcher, B., Koch, D., Kinne, S., Kondo, Y., Quinn, P. K., Sarofim, M. C., Schultz, M. G., Schulz, M., Venkataraman, C., Zhang, H., Zhang, S., Bellouin, N., Guttikunda, S. K., Hopke, P. K., Jacobson, M. Z., Kaiser, J. W., Klimont, Z., Lohmann, U., Schwarz, J. P., Shindell, D., Storelvmo, T., Warren, S. G., and Zender, C. S.: Bounding the role of black carbon in the climate system: A scientific assessment, 118, 5380–5552, <https://doi.org/10.1002/jgrd.50171>, 2013.
- Bove, M. C., Brotto, P., Cassola, F., Cuccia, E., Massabò D., Mazzino, A., Piazzalunga, A., and Prati, P.: An integrated PM_{2.5} source apportionment study: Positive Matrix Factorisation vs. the chemical transport model CAMx, *Atmospheric Environment*, 94, 274–286, <https://doi.org/10.1016/j.atmosenv.2014.05.039>, 2014.
- Byun, D. and Schere, K. L.: Review of the Governing Equations, Computational Algorithms, and Other Components of the Models-3 Community Multiscale Air Quality (CMAQ) Modeling System, *Applied Mechanics Reviews*, 59, 51–77, <https://doi.org/10.1115/1.2128636>, 2006.
- Carey Jang, J.-C., Jeffries, H. E., Byun, D., and Pleim, J. E.: Sensitivity of ozone to model grid resolution—I. Application of high-resolution regional acid deposition model, *Atmospheric Environment*, 29, 3085–3100, [https://doi.org/10.1016/1352-2310\(95\)00118-I](https://doi.org/10.1016/1352-2310(95)00118-I), 1995.
- Casado, R.: The three generations of Big Data processing, 2013.
- Changnon, S. A., Kunkel, K. E., and Reinke, B. C.: Impacts and Responses to the 1995 Heat Wave: A Call to Action, 77, 1497–1506, [https://doi.org/10.1175/1520-0477\(1996\)077<1497:IARTTH>2.0.CO;2](https://doi.org/10.1175/1520-0477(1996)077<1497:IARTTH>2.0.CO;2), 1996.

- Charlson, R. J., Schwartz, S. E., Hales, J. M., Cess, R. D., Coakley, J. A., Hansen, J. E., and Hofmann, D. J.: Climate Forcing by Anthropogenic Aerosols, 255, 423–430, <https://doi.org/10.1126/science.255.5043.423>, 1992.
- Chen, Z., Zhuang, Y., Xie, X., Chen, D., Cheng, N., Yang, L., and Li, R.: Understanding long-term variations of meteorological influences on ground ozone concentrations in Beijing During 2006–2016, *Environmental Pollution*, 245, 29–37, <https://doi.org/10.1016/j.envpol.2018.10.117>, 2019.
- Colbeck, I. and Lazaridis, M.: Aerosols and environmental pollution, *Naturwissenschaften*, 97, 117–131, <https://doi.org/10.1007/s00114-009-0594-x>, 2010.
- Corbera, E., Calvet-Mir, L., Hughes, H., and Paterson, M.: Patterns of authorship in the IPCC Working Group III report, 6, 94–99, <https://doi.org/10.1038/nclimate2782>, 2016.
- Danesh Yazdi, M., Kuang, Z., Dimakopoulou, K., Barratt, B., Suel, E., Amini, H., Lyapustin, A., Katsouyanni, K., and Schwartz, J.: Predicting Fine Particulate Matter (PM_{2.5}) in the Greater London Area: An Ensemble Approach using Machine Learning Methods, 12, 914, <https://doi.org/10.3390/rs12060914>, 2020.
- Desonie, D.: *Atmosphere: Air Pollution and Its Effects*, Infobase Publishing, 209 pp., 2007.
- Dudhia, J.: A history of mesoscale model development, *Asia-Pacific J Atmos Sci*, 50, 121–131, <https://doi.org/10.1007/s13143-014-0031-8>, 2014.
- Fang, C., Liu, H., Li, G., Sun, D., and Miao, Z.: Estimating the Impact of Urbanization on Air Quality in China Using Spatial Regression Models, 7, 15570–15592, <https://doi.org/10.3390/su71115570>, 2015.
- Fang, Y., Mauzerall, D. L., Liu, J., Fiore, A. M., and Horowitz, L. W.: Impacts of 21st century climate change on global air pollution-related premature mortality, *Climatic Change*, 121, 239–253, <https://doi.org/10.1007/s10584-013-0847-8>, 2013.
- Feng, S., Gao, D., Liao, F., Zhou, F., and Wang, X.: The health effects of ambient PM_{2.5} and potential mechanisms, *Ecotoxicology and Environmental Safety*, 128, 67–74, <https://doi.org/10.1016/j.ecoenv.2016.01.030>, 2016.
- Fenger, J.: Urban air quality, *Atmospheric Environment*, 33, 4877–4900, [https://doi.org/10.1016/S1352-2310\(99\)00290-3](https://doi.org/10.1016/S1352-2310(99)00290-3), 1999.
- Fenger, J.: Chapter 1 Urban air quality, in: *Developments in Environmental Science*, vol. 1, edited by: Austin, J., Brimblecombe, P., and Sturges, W., Elsevier, 1–52, [https://doi.org/10.1016/S1474-8177\(02\)80004-3](https://doi.org/10.1016/S1474-8177(02)80004-3), 2002.
- Finlayson-Pitts, B. J. and Jr, J. N. P.: *Chemistry of the Upper and Lower Atmosphere: Theory, Experiments, and Applications*, Elsevier, 993 pp., 1999.
- Fisher, M. R.: 10.1 Atmospheric Pollution, in: *Environmental Biology*, Open Oregon Educational Resources, 2017.
- Florentina, I. and Io, B.: The Effects of Air Pollutants on Vegetation and the Role of Vegetation in Reducing Atmospheric Pollution, in: *The Impact of Air Pollution on*

- Health, Economy, Environment and Agricultural Sources, edited by: Khallaf, M., InTech, <https://doi.org/10.5772/17660>, 2011.
- Grell, G., Peckham, S., Schmitz, R., McKeen, S., Frost, G., Skamarock, W., and Eder, B.: Fully coupled “online” chemistry in the WRF model, *Atmospheric Environment*, 39, 6957–6975, <https://doi.org/10.1016/j.atmosenv.2005.04.027>, 2005.
- Gromke, C. and Blocken, B.: Influence of avenue-trees on air quality at the urban neighborhood scale. Part II: Traffic pollutant concentrations at pedestrian level, *Environmental Pollution*, 196, 176–184, <https://doi.org/10.1016/j.envpol.2014.10.015>, 2015.
- Hallquist, M., Wenger, J. C., Baltensperger, U., Rudich, Y., Simpson, D., Claeys, M., Dommen, J., Donahue, N. M., George, C., Goldstein, A. H., Hamilton, J. F., Herrmann, H., Hoffmann, T., Iinuma, Y., Jang, M., Jenkin, M. E., Jimenez, J. L., Kiendler-Scharr, A., Maenhaut, W., McFiggans, G., Mentel, T. F., Monod, A., Prévôt, A. S. H., Seinfeld, J. H., Surratt, J. D., Szmigielski, R., and Wildt, J.: The formation, properties and impact of secondary organic aerosol: current and emerging issues, 9, 5155–5236, <https://doi.org/10.5194/acp-9-5155-2009>, 2009.
- Hanna, A.: Modelin the Transport and Chemical Evolution of Onshore and Offshore Emissions and Their Impact on Local and Regional Air Quality Using a Variable-Grid-Resolution Air Quality Model, Univ. of North Carolina, Chapel Hill, NC (United States), <https://doi.org/10.2172/962694>, 2008.
- Hansen, J., Sato, M., Ruedy, R., Nazarenko, L., Lacis, A., Schmidt, G. A., Russell, G., Aleinov, I., Bauer, M., Bauer, S., Bell, N., Cairns, B., Canuto, V., Chandler, M., Cheng, Y., Genio, A. D., Faluvegi, G., Fleming, E., Friend, A., Hall, T., Jackman, C., Kelley, M., Kiang, N., Koch, D., Lean, J., Lerner, J., Lo, K., Menon, S., Miller, R., Minnis, P., Novakov, T., Oinas, V., Perlwitz, J., Perlwitz, J., Rind, D., Romanou, A., Shindell, D., Stone, P., Sun, S., Tausnev, N., Thresher, D., Wielicki, B., Wong, T., Yao, M., and Zhang, S.: Efficacy of climate forcings, 110, <https://doi.org/10.1029/2005JD005776>, 2005.
- Hersbach, H., Peubey, C., Simmons, A., Berrisford, P., Poli, P., and Dee, D.: ERA-20CM: a twentieth-century atmospheric model ensemble, 141, 2350–2375, <https://doi.org/10.1002/qj.2528>, 2015.
- Hopke, P. K., Cohen, D. D., Begum, B. A., Biswas, S. K., Ni, B., Pandit, G. G., Santoso, M., Chung, Y.-S., Davy, P., Markwitz, A., Waheed, S., Siddique, N., Santos, F. L., Pabroa, P. C. B., Seneviratne, M. C. S., Wimolwattanapun, W., Bunprapob, S., Vuong, T. B., Duy Hien, P., and Markowicz, A.: Urban air quality in the Asian region, *Science of The Total Environment*, 404, 103–112, <https://doi.org/10.1016/j.scitotenv.2008.05.039>, 2008.
- Huang, S.: Air pollution and control: Past, present and future, *Chin. Sci. Bull.*, 63, 895–919, <https://doi.org/10.1360/N972017-01271>, 2018.

- Inness, P. M. and Dorling, S.: *Operational Weather Forecasting*, John Wiley & Sons, 211 pp., 2012.
- Jenkin, M. E. and Clemitshaw, K. C.: Ozone and other secondary photochemical pollutants: chemical processes governing their formation in the planetary boundary layer, *Atmospheric Environment*, 34, 2499–2527, [https://doi.org/10.1016/S1352-2310\(99\)00478-1](https://doi.org/10.1016/S1352-2310(99)00478-1), 2000.
- Kemp, A. C., Horton, B. P., Donnelly, J. P., Mann, M. E., Vermeer, M., and Rahmstorf, S.: Climate related sea-level variations over the past two millennia, *Proceedings of the National Academy of Sciences*, 108, 11017–11022, <https://doi.org/10.1073/pnas.1015619108>, 2011.
- Kim, K.-H., Jahan, S. A., and Kabir, E.: A review on human health perspective of air pollution with respect to allergies and asthma, *Environment International*, 59, 41–52, <https://doi.org/10.1016/j.envint.2013.05.007>, 2013.
- Kloog, I., Ridgway, B., Koutrakis, P., Coull, B. A., and Schwartz, J. D.: Long- and Short-Term Exposure to PM_{2.5} and Mortality, *Epidemiology*, 24, 555–561, <https://doi.org/10.1097/EDE.0b013e318294beaa>, 2013.
- Kok, J. F.: A scaling theory for the size distribution of emitted dust aerosols suggests climate models underestimate the size of the global dust cycle, *PNAS*, 108, 1016–1021, <https://doi.org/10.1073/pnas.1014798108>, 2011.
- Koman, P. D., Hogan, K. A., Sampson, N., Mandell, R., Coombe, C. M., Tetteh, M. M., Hill-Ashford, Y. R., Wilkins, D., Zlatnik, M. G., Loch-Caruso, R., Schulz, A. J., and Woodruff, T. J.: Examining Joint Effects of Air Pollution Exposure and Social Determinants of Health in Defining “At-Risk” Populations Under the Clean Air Act: Susceptibility of Pregnant Women to Hypertensive Disorders of Pregnancy, *World Med Health Policy*, 10, 7–54, <https://doi.org/10.1002/wmh3.257>, 2018.
- Kong, X., Forkel, R., Sokhi, R. S., Suppan, P., Baklanov, A., Gauss, M., Brunner, D., Barò, R., Balzarini, A., Chemel, C., Curci, G., Jiménez-Guerrero, P., Hirtl, M., Honzak, L., Im, U., Pérez, J. L., Pirovano, G., San Jose, R., Schlünzen, K. H., Tsegas, G., Tuccella, P., Werhahn, J., Žabkar, R., and Galmarini, S.: Analysis of meteorology–chemistry interactions during air pollution episodes using online coupled models within AQMEII phase-2, *Atmospheric Environment*, 115, 527–540, <https://doi.org/10.1016/j.atmosenv.2014.09.020>, 2015.
- Koolen, C. D. and Rothenberg, G.: Air Pollution in Europe, 12, 164–172, <https://doi.org/10.1002/cssc.201802292>, 2019.
- Kwon, O. K., Kim, S.-H., Kang, S.-H., Cho, Y., Oh, I.-Y., Yoon, C.-H., Kim, S.-Y., Kim, O.-J., Choi, E.-K., Youn, T.-J., and Chae, I.-H.: Association of short- and long-term exposure to air pollution with atrial fibrillation, *Eur J Prev Cardiol*, 26, 1208–1216, <https://doi.org/10.1177/2047487319835984>, 2019.

- Lauby-Secretan, B., Loomis, D., Baan, R., El Ghissassi, F., Bouvard, V., Benbrahim-Tallaa, L., Guha, N., Grosse, Y., and Straif, K.: Use of mechanistic data in the IARC evaluations of the carcinogenicity of polychlorinated biphenyls and related compounds, *Environ Sci Pollut Res*, 23, 2220–2229, <https://doi.org/10.1007/s11356-015-4829-4>, 2016.
- Levy, M. L., Fletcher, M., Price, D. B., Hausend, T., Halbert, R. J., and Yawn, B. P.: International Primary Care Respiratory Group (IPCRG) Guidelines: Diagnosis of respiratory diseases in primary care, 15, 20–34, <https://doi.org/10.1016/j.pcrj.2005.10.004>, 2006.
- Li, H. and Svarverud, R.: When London Hit the Headlines: Historical Analogy and the Chinese Media Discourse on Air Pollution, 234, 357–376, <https://doi.org/10.1017/S0305741017001400>, 2018.
- Li, J., Liu, K., and Huang, Q.: Chapter 17 - Utilizing Cloud Computing to Support Scalable Atmospheric Modeling: A Case Study of Cloud-Enabled ModelE, in: *Cloud Computing in Ocean and Atmospheric Sciences*, edited by: Vance, T. C., Merati, N., Yang, C., and Yuan, M., Academic Press, 347–364, <https://doi.org/10.1016/B978-0-12-803192-6.00017-7>, 2016.
- Li, Y., Zhang, X., Zhu, S., Wang, X., Lu, Y., Du, S., and Shi, X.: Transformation of Urban Surfaces and Heat Islands in Nanjing during 1984–2018, 12, 6521, <https://doi.org/10.3390/su12166521>, 2020.
- Lighty, J. S., Veranth, J. M., and Sarofim, A. F.: Combustion Aerosols: Factors Governing Their Size and Composition and Implications to Human Health, 50, 1565–1618, <https://doi.org/10.1080/10473289.2000.10464197>, 2000.
- Lin, H., Feng, X., Fu, T.-M., Tian, H., Ma, Y., Zhang, L., Jacob, D. J., Yantosca, R. M., Sulprizio, M. P., Lundgren, E. W., Zhuang, J., Zhang, Q., Lu, X., Zhang, L., Shen, L., Guo, J., Eastham, S. D., and Keller, C. A.: WRF-GC: online coupling of WRF and GEOS-Chem for regional atmospheric chemistry modeling, Part 1: description of the one-way model (v1.0), *Climate and Earth System Modeling*, <https://doi.org/10.5194/gmd-2019-333>, 2020.
- Liu, D., Whitehead, J., Alfarra, M. R., Reyes-Villegas, E., Spracklen, D. V., Reddington, C. L., Kong, S., Williams, P. I., Ting, Y.-C., Haslett, S., Taylor, J. W., Flynn, M. J., Morgan, W. T., McFiggans, G., Coe, H., and Allan, J. D.: Black-carbon absorption enhancement in the atmosphere determined by particle mixing state, 10, 184–188, <https://doi.org/10.1038/ngeo2901>, 2017.
- Liu, H.-Y., Dunea, D., Iordache, S., and Pohoata, A.: A Review of Airborne Particulate Matter Effects on Young Children’s Respiratory Symptoms and Diseases, 9, 150, <https://doi.org/10.3390/atmos9040150>, 2018.

- Liu, M.-K., Morris, R. E., and Killus, J. P.: Development of a regional oxidant model and application to the northeastern United States, *Atmospheric Environment* (1967), 18, 1145–1161, [https://doi.org/10.1016/0004-6981\(84\)90146-X](https://doi.org/10.1016/0004-6981(84)90146-X), 1984.
- Liu, Y., Li, Q., Yang, L., Mu, K., Zhang, M., and Liu, J.: Urban heat island effects of various urban morphologies under regional climate conditions, *Science of The Total Environment*, 743, 140589, <https://doi.org/10.1016/j.scitotenv.2020.140589>, 2020a.
- Liu, Z., Ciais, P., Deng, Z., Lei, R., Davis, S. J., Feng, S., Zheng, B., Cui, D., Dou, X., He, P., Zhu, B., Lu, C., Ke, P., Sun, T., Wang, Y., Yue, X., Wang, Y., Lei, Y., Zhou, H., Cai, Z., Wu, Y., Guo, R., Han, T., Xue, J., Boucher, O., Boucher, E., Chevallier, F., Wei, Y., Zhong, H., Kang, C., Zhang, N., Chen, B., Xi, F., Marie, F., Zhang, Q., Guan, D., Gong, P., Kammen, D. M., He, K., and Schellnhuber, H. J.: COVID-19 causes record decline in global CO₂ emissions, 2020b.
- Lynch, P.: Weather forecasting From woolly art to solid science, in: *International Geophysics*, vol. 83, edited by: Pearce, R. P., Academic Press, 106–119, [https://doi.org/10.1016/S0074-6142\(02\)80160-7](https://doi.org/10.1016/S0074-6142(02)80160-7), 2002.
- Lynch, P.: The origins of computer weather prediction and climate modeling, *Journal of Computational Physics*, 227, 3431–3444, <https://doi.org/10.1016/j.jcp.2007.02.034>, 2008a.
- Lynch, P.: The origins of computer weather prediction and climate modeling, *Journal of Computational Physics*, 227, 3431–3444, <https://doi.org/10.1016/j.jcp.2007.02.034>, 2008b.
- Mailler, S., Menut, L., Khvorostyanov, D., Valari, M., Couvidat, F., Siour, G., Turquety, S., Briant, R., Tuccella, P., Bessagnet, B., Colette, A., L  inois, L., Markakis, K., and Meleux, F.: CHIMERE-2017: from urban to hemispheric chemistry-transport modeling, 10, 2397–2423, <https://doi.org/10.5194/gmd-10-2397-2017>, 2017.
- Manisalidis, I., Stavropoulou, E., Stavropoulos, A., and Bezirtzoglou, E.: Environmental and Health Impacts of Air Pollution: A Review, *Front Public Health*, 8, <https://doi.org/10.3389/fpubh.2020.00014>, 2020.
- McNeill, J. R. and Engelke, P.: *The Great Acceleration: An Environmental History of the Anthropocene Since 1945*, Harvard University Press, 284 pp., 2016.
- Meng, Z., Zhang, F., Luo, D., Tan, Z., Fang, J., Sun, J., Shen, X., Zhang, Y., Wang, S., Han, W., Zhao, K., Zhu, L., Hu, Y., Xue, H., Ma, Y., Zhang, L., Nie, J., Zhou, R., Li, S., Liu, H., and Zhu, Y.: Review of Chinese atmospheric science research over the past 70 years: Synoptic meteorology, *Sci. China Earth Sci.*, 62, 1946–1991, <https://doi.org/10.1007/s11430-019-9534-6>, 2019.
- Meng, Z. Y., Xu, X. B., Yan, P., Ding, G. A., Tang, J., Lin, W. L., Xu, X. D., and Wang, S. F.: Characteristics of trace gaseous pollutants at a regional background station in Northern China, 9, 927–936, <https://doi.org/10.5194/acp-9-927-2009>, 2009.

- Menut, L., Bessagnet, B., Khvorostyanov, D., Beekmann, M., Blond, N., Colette, A., Coll, I., Curci, G., Foret, G., Hodzic, A., Mailler, S., Meleux, F., Monge, J.-L., Pison, I., Siour, G., Turquety, S., Valari, M., Vautard, R., and Vivanco, M. G.: CHIMERE 2013: a model for regional atmospheric composition modelling, *Geosci. Model Dev.*, 6, 981–1028, <https://doi.org/10.5194/gmd-6-981-2013>, 2013.
- Menut, L., Bessagnet, B., Siour, G., Mailler, S., Pennel, R., and Cholakian, A.: Impact of lockdown measures to combat Covid-19 on air quality over western Europe, *Science of The Total Environment*, 741, 140426, <https://doi.org/10.1016/j.scitotenv.2020.140426>, 2020.
- Miranda, A., Silveira, C., Ferreira, J., Monteiro, A., Lopes, D., Relvas, H., Borrego, C., and Roebeling, P.: Current air quality plans in Europe designed to support air quality management policies, *Atmospheric Pollution Research*, 6, 434–443, <https://doi.org/10.5094/APR.2015.048>, 2015.
- Mohanakumar, K.: *Stratosphere Troposphere Interactions: An Introduction*, Springer Science & Business Media, 424 pp., 2008.
- Myhre, G., Lund Myhre, C., Samset, B. H., and Storelvmo, T.: Aerosols and their Relation to Global Climate and Climate Sensitivity, *Nature Education Knowledge*, 4, 7, 2013.
- Najjar, Y.: *Gaseous Pollutants Formation and Their Harmful Effects on Health and Environment*, Ashdin Publishing Innovative Energy Policies, 1, <https://doi.org/10.4303/iep/E101203>, 2011.
- Natusch, D. F. S. and Wallace, J. R.: Urban Aerosol Toxicity: The Influence of Particle Size, 186, 695–699, <https://doi.org/10.1126/science.186.4165.695>, 1974.
- Nazaroff, W. W. and Weschler, C. J.: Cleaning products and air fresheners: exposure to primary and secondary air pollutants, *Atmospheric Environment*, 38, 2841–2865, <https://doi.org/10.1016/j.atmosenv.2004.02.040>, 2004.
- Olsson, D., Mogren, I., and Forsberg, B.: Air pollution exposure in early pregnancy and adverse pregnancy outcomes: a register-based cohort study, 3, e001955, <https://doi.org/10.1136/bmjopen-2012-001955>, 2013.
- Organization, W. H.: *Air Quality Guidelines: Global Update 2005 : Particulate Matter, Ozone, Nitrogen Dioxide, and Sulfur Dioxide*, World Health Organization, 497 pp., 2006.
- Paine, S.: The am atmospheric model, <https://doi.org/10.5281/zenodo.3406483>, n.d.
- Palme, M., Inostroza, L., Villacreses, G., Lobato-Cordero, A., and Carrasco, C.: From urban climate to energy consumption. Enhancing building performance simulation by including the urban heat island effect, *Energy and Buildings*, 145, 107–120, <https://doi.org/10.1016/j.enbuild.2017.03.069>, 2017.
- Pepe, N., Pirovano, G., Lonati, G., Balzarini, A., Toppetti, A., Riva, G. M., and Bedogni, M.: Development and application of a high resolution hybrid modelling system for the evaluation of urban air quality, *Atmospheric Environment*, 141, 297–311, <https://doi.org/10.1016/j.atmosenv.2016.06.071>, 2016.

- Pisoni, E., Clappier, A., Degraeuwe, B., and Thunis, P.: Adding spatial flexibility to source-receptor relationships for air quality modeling, *Environmental Modelling & Software*, 90, 68–77, <https://doi.org/10.1016/j.envsoft.2017.01.001>, 2017.
- Power, M. C., Kioumourtzoglou, M.-A., Hart, J. E., Okereke, O. I., Laden, F., and Weisskopf, M. G.: The relation between past exposure to fine particulate air pollution and prevalent anxiety: observational cohort study, *BMJ*, 350, h1111, <https://doi.org/10.1136/bmj.h1111>, 2015.
- Prather, K. A.: Our Current Understanding of the Impact of Aerosols on Climate Change, 2, 377–379, <https://doi.org/10.1002/cssc.200900037>, 2009.
- Quan, C., Sun, Q., Lippmann, M., and Chen, L.-C.: Comparative effects of inhaled diesel exhaust and ambient fine particles on inflammation, atherosclerosis, and vascular dysfunction, 22, 738–753, <https://doi.org/10.3109/08958371003728057>, 2010.
- Reis, S., Nitter, S., and Friedrich, R.: Innovative approaches in integrated assessment modelling of European air pollution control strategies – Implications of dealing with multi-pollutant multi-effect problems, *Environmental Modelling & Software*, 20, 1524–1531, <https://doi.org/10.1016/j.envsoft.2004.07.019>, 2005.
- Remer, L. A., Kleidman, R. G., Levy, R. C., Kaufman, Y. J., Tanré D., Mattoo, S., Martins, J. V., Ichoku, C., Koren, I., Yu, H., and Holben, B. N.: Global aerosol climatology from the MODIS satellite sensors, 113, <https://doi.org/10.1029/2007JD009661>, 2008.
- Sabatier, T., Paci, A., Lac, C., Canut, G., Llargeron, Y., and Masson, V.: Semi-idealized simulations of wintertime flows and pollutant transport in an Alpine valley: Origins of local circulations (Part I), 146, 807–826, <https://doi.org/10.1002/qj.3727>, 2020.
- Samet, J. and Krewski, D.: Health Effects Associated With Exposure to Ambient Air Pollution, 70, 227–242, <https://doi.org/10.1080/15287390600884644>, 2007.
- San José R., Pérez, J. L., Morant, J. L., and González Barras, R. M.: The Use of Modern Third-Generation Air Quality Models (MM5-EMIMO-CMAQ) for Real-Time Operational Air Quality Impact Assessment of Industrial Plants, *Water Air Soil Pollut: Focus*, 9, 27–37, <https://doi.org/10.1007/s11267-008-9196-4>, 2009.
- Scott, C. E., Arnold, S. R., Monks, S. A., Asmi, A., Paasonen, P., and Spracklen, D. V.: Substantial large-scale feedbacks between natural aerosols and climate, 11, 44–48, <https://doi.org/10.1038/s41561-017-0020-5>, 2018.
- Seinfeld, J. H.: Ozone Air Quality Models, *JAPCA*, 38, 616–645, <https://doi.org/10.1080/08940630.1988.10466404>, 1988.
- Seinfeld, J. H. and Pandis, S. N.: *Atmospheric Chemistry and Physics: From Air Pollution to Climate Change*, John Wiley & Sons, 1146 pp., 2016.
- Semenza, J. C., Rubin, C. H., Falter, K. H., Selanikio, J. D., Flanders, W. D., Howe, H. L., and Wilhelm, J. L.: Heat-Related Deaths during the July 1995 Heat Wave in Chicago, *N Engl J Med*, 335, 84–90, <https://doi.org/10.1056/NEJM199607113350203>, 1996.

- Shindell, D. T., Faluvegi, G., Koch, D. M., Schmidt, G. A., Unger, N., and Bauer, S. E.: Improved Attribution of Climate Forcing to Emissions, 326, 716–718, <https://doi.org/10.1126/science.1174760>, 2009.
- Somerville, R.: *The Development of Atmospheric General Circulation Models: Complexity, Synthesis and Computation*, Cambridge University Press, 289 pp., 2011.
- Stockwell, W. R., Middleton, P., Chang, J. S., and Tang, X.: The second generation regional acid deposition model chemical mechanism for regional air quality modeling, 95, 16343–16367, <https://doi.org/10.1029/JD095iD10p16343>, 1990.
- Thunis, P., Degraeuwe, B., Pisoni, E., Ferrari, F., and Clappier, A.: On the design and assessment of regional air quality plans: The SHERPA approach, *Journal of Environmental Management*, 183, 952–958, <https://doi.org/10.1016/j.jenvman.2016.09.049>, 2016.
- Vautard, R., Bessagnet, B., Chin, M., and Menut, L.: On the contribution of natural Aeolian sources to particulate matter concentrations in Europe: Testing hypotheses with a modelling approach, *Atmospheric Environment*, 39, 3291–3303, <https://doi.org/10.1016/j.atmosenv.2005.01.051>, 2005.
- Venter, Z. S., Aunan, K., Chowdhury, S., and Lelieveld, J.: COVID-19 lockdowns cause global air pollution declines with implications for public health risk, 2020.04.10.20060673, <https://doi.org/10.1101/2020.04.10.20060673>, 2020.
- Viana, M., Hammingh, P., Colette, A., Querol, X., Degraeuwe, B., Vlieger, I. de, and van Aardenne, J.: Impact of maritime transport emissions on coastal air quality in Europe, *Atmospheric Environment*, 90, 96–105, <https://doi.org/10.1016/j.atmosenv.2014.03.046>, 2014.
- WANG, Q.: Urbanization and Global Health: The Role of Air Pollution, *Iran J Public Health*, 47, 1644–1652, 2018.
- Watson, A. Y., Bates, R. R., and Kennedy, D.: *Atmospheric Transport and Dispersion of Air Pollutants Associated with Vehicular Emissions*, National Academies Press (US), 1988a.
- Watson, A. Y., Bates, R. R., and Kennedy, D.: *Mathematical Modeling of the Effect of Emission Sources on Atmospheric Pollutant Concentrations*, National Academies Press (US), 1988b.
- White, W. H.: Considerations in the use of ozone and PM_{2.5} data for exposure assessment, *Air Qual Atmos Health*, 2, 223–230, <https://doi.org/10.1007/s11869-009-0056-9>, 2009.
- Williams, C. R. and Avery, S. K.: Analysis of long-period waves using the mesosphere-stratosphere-troposphere radar at Poker Flat, Alaska, 97, 20855–20861, <https://doi.org/10.1029/92JD02052>, 1992.

- Wise, D. K. A. G. and D. S.: ICIE 2016 Proceedings of the 4th International Conference on Innovation and Entrepreneurship: ICIE2016, Academic Conferences and publishing limited, 439 pp., 2016.
- Wong, N. H. and Chen, Y.: Tropical Urban Heat Islands: Climate, Buildings and Greenery, Routledge, 276 pp., 2008.
- Xiao, Y.: The Experience to Abate Air Pollution : What Lessons can Beijing, China Draw from Developed Countries When Trying to Reduce Emissions?, 2015.
- Xu, M., Yu, D., Yao, H., Liu, X., and Qiao, Y.: Coal combustion-generated aerosols: Formation and properties, Proceedings of the Combustion Institute, 33, 1681–1697, <https://doi.org/10.1016/j.proci.2010.09.014>, 2011.
- Xue, M., Droegemeier, K. K., Wong, V., Shapiro, A., Brewster, K., Carr, F., Weber, D., Liu, Y., and Wang, D.: The Advanced Regional Prediction System (ARPS) – A multi-scale nonhydrostatic atmospheric simulation and prediction tool. Part II: Model physics and applications, Meteorol Atmos Phys, 76, 143–165, <https://doi.org/10.1007/s007030170027>, 2001.
- Yin, P., Brauer, M., Cohen, A. J., Wang, H., Li, J., Burnett, R. T., Stanaway, J. D., Causey, K., Larson, S., Godwin, W., Frostad, J., Marks, A., Wang, L., Zhou, M., and Murray, C. J. L.: The effect of air pollution on deaths, disease burden, and life expectancy across China and its provinces, 1990–2017: an analysis for the Global Burden of Disease Study 2017, 4, 13, 2020.
- You, C., Lin, D. K. J., and Young, S. S.: PM 2.5 and ozone, indicators of air quality, and acute deaths in California, 2004–2007, Regulatory Toxicology and Pharmacology, 96, 190–196, <https://doi.org/10.1016/j.yrtph.2018.05.012>, 2018.
- Zhang, J. (Jim), Wei, Y., and Fang, Z.: Ozone Pollution: A Major Health Hazard Worldwide, Front Immunol, 10, <https://doi.org/10.3389/fimmu.2019.02518>, 2019.
- Zinke, L.: Air quality during COVID-19, 1, 386–386, <https://doi.org/10.1038/s43017-020-0087-1>, 2020.

Chapter II: Meteorology and atmospheric dispersion in the urban canopy– One-year air quality simulations in France using IFS/CHIMERE modeling system

2.1 General principle of the chemical transport model

The chemical transport model (CTM) is a mathematical tool used for air quality research. It uses numerical methods to describe the dispersion, diffusion, chemical reactions and removal process of pollutants in the atmosphere (Karl, 2018). Emission sources, topography and meteorological data of the studied area are the key elements for an air quality simulation. In other words, the tool used for air quality simulation and forecast not only the CTM itself, but a simulation system with CTM as the core, including multiple related components. An air quality simulation system usually consists of five parts: meteorological field, pollutant emissions, boundary conditions, post-analysis procedures and the CTM core (Sarath K. Guttikunda et al., 2011). The framework of the system is shown in Figure2.1.

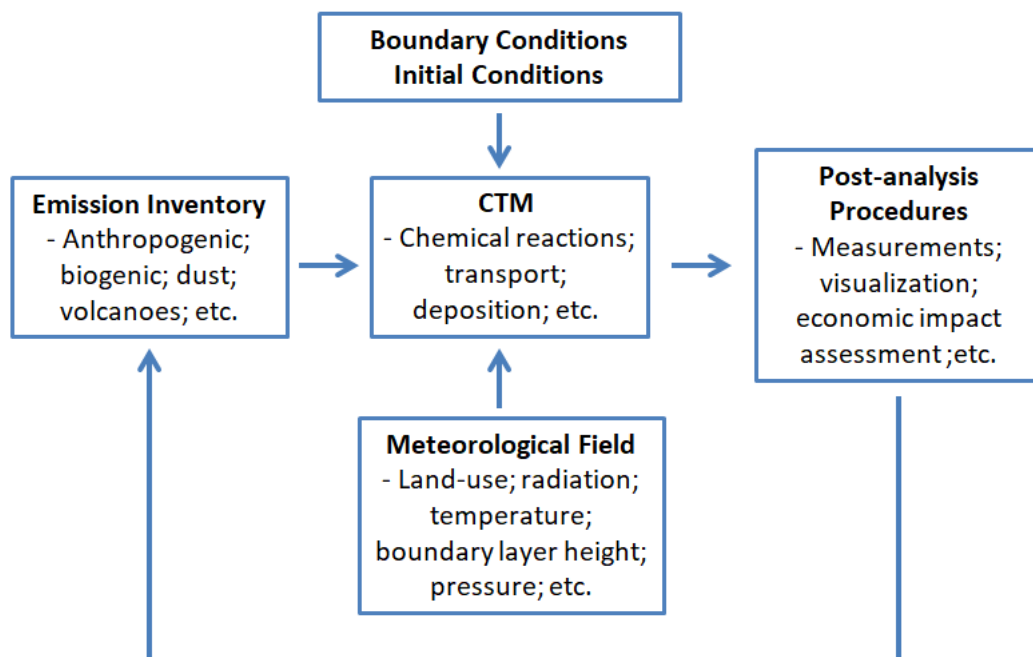


Figure2.1 General principle of the air quality simulation system

For a limited-area simulation, the model cannot solve for points on the edge of the grid because there are no points beyond the boundary to use for evaluating the derivative perpendicular to it (Warner, 2011). Therefore, the lateral-boundary condition need specified for the value of dependent variables at these boundary points. In addition, the upper and lower boundary conditions also must be specified in mesoscale model. For urban and regional scale

numerical simulations, the usual method for determining boundary conditions is to use the results of larger-scale regional models or global-scale models as boundary conditions. The meteorological field provides the meteorological data with a certain temporal and spatial resolution, such as wind field, temperature, mixed layer height, radiation, vertical diffusion coefficient, cloud characteristics, etc. (Rao et al., 2003). Usually, in air quality models, the atmospheric motion control equation is independent of the pollutant chemical dynamics equation. Thus, the formation of pollutants in the atmosphere will not significantly change the meteorological conditions and the simulation of meteorological field is independent of air quality simulation, this case is called as offline approach (Baklanov et al., 2016a; Seo et al., 2018). However, changes of pollutants concentrations have a non-negligible impact on meteorological conditions in some cases, in this case online approach is required. Study on the coupling of mesoscale meteorological models and CTM have shown that changes in pollutant concentration have slight impact on meteorological conditions (Bessagnet et al., 2020; Jacobson, 1997). Therefore, most air quality simulation systems use offline approach. Also, an identified drawback regarding the boundary conditions is a possible inconsistency of the model species and chemical regimes between the large-scale model and the nested regional model if they are different.

Accurate emission inventories play a crucial role in the simulation results. The list of species should satisfy the chemical reaction mechanism and temporal and spatial resolution of the model. For Eulerian models, gridded hourly emission data is usually required. The main pollutants include CO; NO_x; SO₂; NH₃; PM; VOCs; etc (Crippa et al., 2018). For practical applications to support decisions and policy making, the purpose of air quality modeling is to grasp the characteristics and laws of pollution, explore its causes, and finally provide scientific control countermeasures (Zhang and Na, 2018). The post-analysis program uses the observational data of the ground observation stations to analyze the simulation results which provide information to assess the impact on the environment and the economy and formulate corresponding control plans. In general, the principle of CTM should following those steps: (i) understand and determine the physical processes are needed for the simulation; (ii) choose a sufficiently small horizontal grid increment to resolve all the processes to be simulated on the

grid, numerically a finer resolution is supposed to be better; (iii) select the most suitable projection map for the range of the model grid, (iv) ensure the vertical resolution is reasonably compatible with the horizontal resolution, and can accurately define important vertical structures (Warner, 2011).

2.2 Urban meteorology

In the past centuries, humans are increasingly gathering in large settlements, as well as the urban population exceeded the rural (Morais et al., 2018). The population is concentrated in less than 3% of the Earth's land area (Baklanov et al., 2018). It is expected that two-thirds of the world's population will live in cities by 2050 (WUP 2014), therefore general knowledge of climatic characteristics of typical cities and differences with rural areas are becoming more and more crucial (Karlický et al., 2020).

Urbanization has a major impact on urban meteorology. It can change the atmospheric diffusion capacity thereby affecting the concentration of pollutants (Liu et al., 2015), weather and climate at local, regional and global scales (Baklanov et al., 2007). First, the urban surface are mostly characterized by buildings, roads and permeable natural surfaces, where various physical processes such as radiation trapping, atmospheric flow, turbulent heat exchange, and underground heat conduction occur, resulting in a unique local meteorology (Kim et al., 2020; Uehara et al., 2000). Second, changes in chemical emissions and feedbacks of atmospheric pollutants affect the weather and climate both locally and further afield (Reinmuth-Selzle et al., 2017). The main examples includes: (i) the distribution of rough elements which can affect the turbulence state, speed and flow direction; (ii) the extensive use of impervious materials which generally reduces vegetation coverage in urban areas thereby affecting the hydrological and meteorological conditions and the deposition of pollutants; (iii) the urban canopy affecting the flow and heat exchange between different land covers; (iv) the release and diffusion of pollutants can affects radiation transmission and the formation of clouds and precipitation (Baklanov et al., 2018). The most well-known urban meteorology is the so-called urban heat island (UHI), which was first described by Oke and Maxwell (Oke and Maxwell, 1975) in the year 1975 and has been extensively studied in the following

decades (Baklanov et al., 2016c; Karlický et al., 2020; KIM, 1992; Oke, 1982; Zhang et al., 2017). In short, it can be described as urban temperature is higher than in the countryside. UHI not only affects the microscale and mesoscale circulation to a large extent, but also cause the formation of convection (Dixon et al., 2003;). Several studies have demonstrated that the increase in the number of convection phenomena in cities were related to the increase in the convergence of the lower-level over urban areas (Fujibe, 2003). Theeuwes et al. (2019) found the cloud cover enhancement over urban region of Paris and London during summer because of increased convection caused by UHI. With the rapid improvement of computer capabilities and the widespread application of remote sensing technology in meteorology, geographic information on urban surfaces can be obtained with higher precision, which makes it possible to develop and apply high-resolution urban boundary layer models. Some studies indicate that meteorological variables are significantly affected by the urban canopy. For example, the impact of urban boundary layer structure causes changes in dispersion conditions (Karlický et al., 2018), which have considerable consequences for primary or secondary pollutant concentrations (Huszar et al., 2020; Li et al., 2019). Manola et al. (2020) found the overall precipitation increased in the urban areas of Amsterdam in comparison to rural surroundings.

In general, the relationship between meteorology and city is mutual: meteorology affects how urban space is used such as the different concerns between coastal cities and landlocked cities (Pelling and Blackburn, 2013) or tropical cities and boreal cities. In turn, the city has changed the regional meteorology conditions, resulting in differences in cloud cover, solar radiation, temperature and wind speed between the city and its surrounding areas thereby resulting the transport, diffusion, and chemical transformation of particulates and gases. Figure 2.2 summarized the main linkages between cities, air quality and climate. Specifically: (i) non-linear interaction and its feedback between emissions, land use, reaction and meteorology; (ii) complex spatial scales from local to global and time scales from minutes to centuries; (iii) mixing of pollutants from multiple pollution sources; (iv) interaction between city characteristics and emissions (Baklanov et al., 2010).

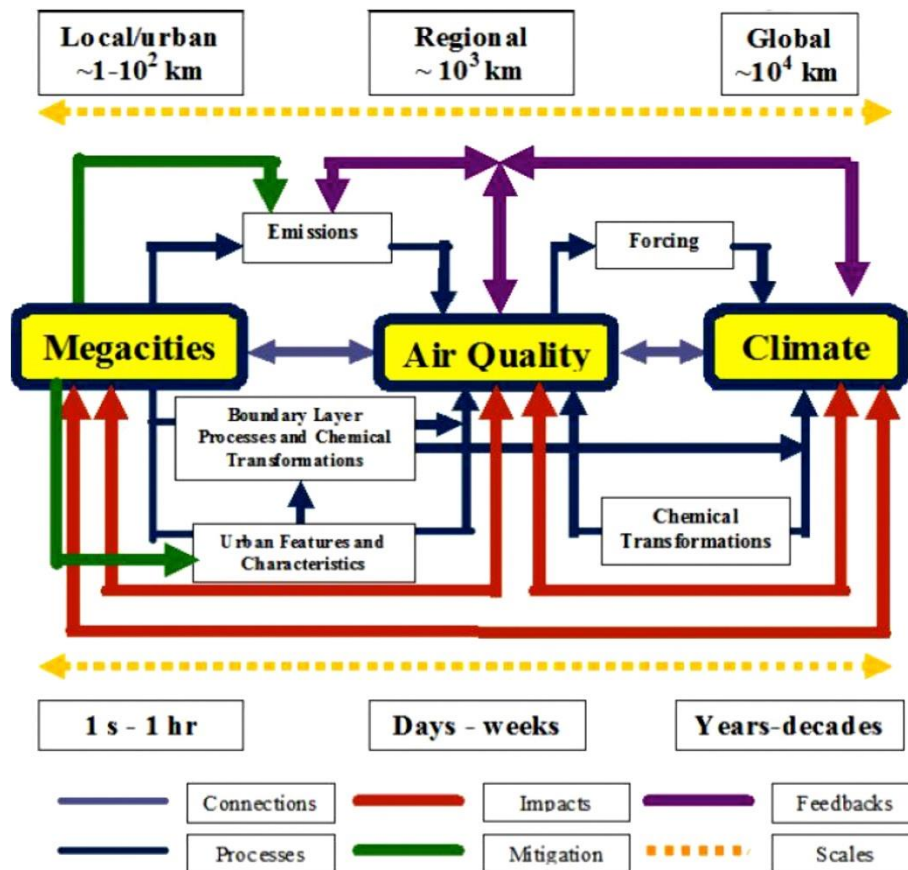


Figure 2.2 The main linkages between megacities, air quality and climate (Baklanov et al., 2010)

2.3 Urban canopy modeling

There are numbers of methods used to represent the dynamic and thermodynamic effects of urban areas on the atmosphere and each city has its unique spatial structure and urban metabolism characteristics (Ching, 2013). The smartest solution is to use a computational fluid dynamics (CFD) model, which clearly expresses the influence of each building on the atmospheric structure (Kirkil et al., 2012; Letzel et al., 2008). However, those fine-precision CFD models are extremely computationally luxurious to use. Based on the comprehensive consideration of model performance and computing resources, mesoscale meteorological and CTM models are increasingly being applied up to urban areas (Burian et al., 2007) with fine grids up to 1km resolutions (Tong et al., 2005).

In contrast to the fine-precision CFD models, for meteorological and air quality simulations in urban areas, all the normal mesoscale needed is the overall contribution of the bulk effects of

built-up areas on the mesoscale processes. The mesoscale model defines surface properties through adjusting parameter attributes associated with land use and other surface covers datasets to represent the altered morphological, reflective, and anthropogenic heating aspects so that they approximate the artificial surface conditions in cities (Beltran-Przekurat et al., 2012). For example, the roughness length can be used to indicate the resistance of the building. The albedo can be reduced to account for the existence of dark roofs and shortwave radiation capture in street canyons. The heat capacity and thermal conductivity of the substrate can be increased to solve the problem of heat storage in the walls of buildings; reduce the water capacity of the substrate to reflect the universality of impervious surfaces (Liu et al., 2006). The six key physical parameters of land-use categories are albedo, emissivity, surface thermal inertia, roughness length, soil moisture availability and soil heat capacity, respectively (H. Li et al., 2020). However, given the complexity of the urban system, those similarity frameworks may encounter problems when applied in the urban context (Roth, 2007), some other schemes are needed to represent more complex processes related to the presence of buildings and non-natural substrates. Oke (1988) provided a concept of the atmospheric regimes overlying urban areas for the first time. Since the flow convection and atmospheric processes respond to the heterogeneity of the urban surface, the boundary layer structure over urban areas are necessarily multi-scale (Klein et al., 2007). The varying buildings heights, distribution densities and varying street widths create a mean condition in the urban canopy. The layers above urban canopy is continuously adjusted by the vertical flux caused by the horizontal changes and gradients of the underlying land use and canopy structure. This situation produces countless internal boundary layers, and the turbulence generated in each boundary layer is balanced by dissipation. Urban canopy parameterizations with varying complexities were developed and coupled with the model to improve its skills in capturing fine-scale urban processes and in assessing the environmental issues (Kondo et al., 2005; Kusaka et al., 2001; Kusaka and Kimura, 2004; Liao et al., 2014). The single layer urban canopy scheme (UCM) parameterizes the aggregate effects of the urban morphology, but does not explicitly represent the effects of individual buildings and street canyons (Kusaka et al., 2001). The UCM considered radiation capture and wind shear in urban canopy affected by the geometry of buildings and roads (Huang et al., 2019). However, the UCM is a

single layer parameterization, which means moisture, heat and momentum fluxes are defined at the bottom boundary of the lowest atmosphere in the model (Warner, 2011). Thus, a multiple layer building effect parameterization scheme (BEP) was developed by (Martilli et al., 2002) in order to account for the three-dimensional nature of urban surfaces and the fact that buildings distribute sources and heat, moisture and momentum vertically throughout the urban canopy. The impact of urban canopy schemes will be discussed in the Chapter III of the manuscript.

2.4 The basic equations and dispersion in the urban canopy layer

In the atmospheric context, anthropogenic emissions are mainly influential on the lower urban atmosphere layers and communicated to regional, global, and smaller scales via transport and turbulence processes (Fernando et al., 2010). The understanding of the wind flows in an urban region and the concomitant dispersion of material released in that flow is gaining importance. Britter and Hanna, (2003) suggested that the dispersion in urban area should be classified in four scales of domain coverages: (i) 100km to 200km defined as regional scale; (ii) 10km to 20km defined as city scale; (iii) 1km to 2km defined as neighborhood scale; (iv) 100m to 200m defined as building scale.

Although there are a large diversity of Eulerian models, most of them are built on the same pollutant continuity equation as (4.1):

$$\begin{aligned} \frac{\partial \rho}{\partial t} + \frac{\partial(u\rho)}{\partial x} + \frac{\partial(v\rho)}{\partial y} + \frac{\partial(w\rho)}{\partial z} \\ = \frac{\partial}{\partial x} \left(K_x \frac{\partial \rho}{\partial x} \right) + \frac{\partial}{\partial y} \left(K_y \frac{\partial \rho}{\partial y} \right) + \frac{\partial}{\partial z} \left(K_z \frac{\partial \rho}{\partial z} \right) + R + S \end{aligned} \quad (1.1)$$

This general equation describes the chemical reaction, transport and diffusion, deposition and emission of pollutants. With ρ the concentration of gas; t the time; u , v , w the component of wind speed in x , y , z direction; K_x , K_y , K_z the horizontal and vertical diffusion coefficient; S the source and sink of pollutants; R chemical reaction term, determined by the chemical reaction mechanism of pollutants in the atmosphere. Figure 2.3 gives an example of mass conservation, taking the x direction as an example, the input and output wind speeds are u_1

and u_2 , respectively, the gas concentrations at the left and right boundaries of the cube are ρ_1 and ρ_2 . Then, the flux densities of the input and output cubes are $F_{x1} = u_1\rho_1$ and $F_{x2} = u_2\rho_2$, respectively.

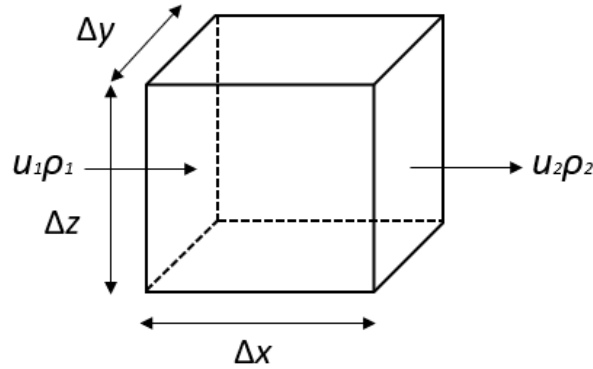


Figure 2.3 Example of mass conservation (Jacobson, 2005).

However, because atmospheric motion is a turbulent motion, that is, irregular motion. Therefore, it is difficult to characterize the transport flux density $F = u\rho$. Especially in the vertical direction, the turbulent motion causes the gas concentration and vertical wind speed to fluctuate rapidly over time.

In the simulation processes, what is interesting is not the instantaneous flux value, but the average flux over a certain period. Therefore, Reynolds decomposition can be used to deal with the problems caused by turbulence. Decompose the value of ρ and u, v, w into two parts: the average value and the disturbance value relative to the average value as the equation (1.2):

$$\begin{aligned}\rho(t) &= \bar{\rho} + \rho'(t) \\ u(t) &= \bar{u} + u'(t) \\ v(t) &= \bar{v} + v'(t) \\ w(t) &= \bar{w} + w'(t)\end{aligned}\tag{1.2}$$

With $\bar{\rho}, \bar{u}, \bar{v}, \bar{w}$ the average value of ρ, u, v, w in a certain period of time; $\rho'(t), u'(t), v'(t), w'(t)$ the disturbance value relative to the average value. According to the definition (1.3):

$$\bar{\rho}'=0, \bar{u}'=0, \bar{v}'=0, \bar{w}'=0\tag{1.3}$$

In x, y, z directions (1.4):

$$\begin{aligned}
\overline{F_x} &= \overline{u\rho} = \overline{u}\overline{\rho} + \overline{u'\rho'} = \overline{F_{x,A}} + \overline{F_{x,T}} \\
\overline{F_y} &= \overline{v\rho} = \overline{v}\overline{\rho} + \overline{v'\rho'} = \overline{F_{y,A}} + \overline{F_{y,T}} \\
\overline{F_z} &= \overline{w\rho} = \overline{w}\overline{\rho} + \overline{w'\rho'} = \overline{F_{z,A}} + \overline{F_{z,T}}
\end{aligned} \tag{1.4}$$

With $\overline{F_A}$ the advection flux, produced by the transport of average wind; $\overline{F_T}$ the turbulent flux, produced by the covariance of wind speed and concentration. In the vertical direction, the upward and downward motions caused by turbulence are generally close, the average wind speed often smaller than the disturbance value. This causes $\overline{F_T}$ to be usually greater than $\overline{F_A}$, which is the main part that affects the vertical transport. In the horizontal direction, it is the opposite (Jacobson, 2005).

In CTMs, empirical parameterization methods are required to estimate the turbulent fluxes (Dwivedi et al., 2020). One of the widely used methods is so called *K*-theory. Assuming that the diffusion process caused by turbulent motion is similar to molecular diffusion, analogy to the law of molecular diffusion defines an empirical diffusion coefficient *K*, as the equation (1.5):

$$\begin{aligned}
\overline{F_{x,T}} &= \overline{u'\rho'} = -K_x \frac{\partial \overline{\rho}}{\partial x} \\
\overline{F_{y,T}} &= \overline{v'\rho'} = -K_y \frac{\partial \overline{\rho}}{\partial y} \\
\overline{F_{z,T}} &= \overline{w'\rho'} = -K_z \frac{\partial \overline{\rho}}{\partial z}
\end{aligned} \tag{1.5}$$

With K_x , K_y , K_z the diffusion coefficient in *x*, *y*, *z* direction, respectively. Such scheme only retains the prognostic equations for the zero order mean variables like temperature, wind speed and humidity, which is also called first order local closure scheme (Stull, 1988). This scheme works well when the turbulent eddies are relatively small and locally generated.

This chapter addresses the results of the one-year air quality simulation that was performed with three different first order local closure scheme (*K*-theory scheme) to estimate the vertical diffusion coefficient (K_z) within the boundary layer. The initial K_z in CHIMERE is defined as the equation (1.6):

$$K_z = kw_s z \left(1 - \frac{z}{h}\right)^2 \quad (1.6)$$

where k is the von Karman constant set to 0.41 in the model, z is the altitude, h is the boundary layer height, and w_s is the vertical scale given by the similarity formulae. Convective turbulence driven by buoyancy dominates during the day, while turbulence driven by wind shear at night is more dominant (Warner, 2011). Figure 2.4 shows the typical diurnal variation of the boundary layer structure. The boundary layer height during the day is determined by vertical extent of the turbulent mixing. During the daytime, sunshine increases the surface temperature, buoyancy generates turbulence and extends to the troposphere, and the convective mixing layer increases. Usually the thickness is about 1000m. This period is called an unstable condition in the vertical mixing (Troen and Mahrt, 1986). At night, as the temperature decreases, the buoyancy gradually disappears. The energy of the turbulence near the surface can only be calculated from the vertical wind shear of the horizontal wind. Therefore, in most cases, the boundary layer is much higher during the day than at night, which is so-called stable condition in mixing process.

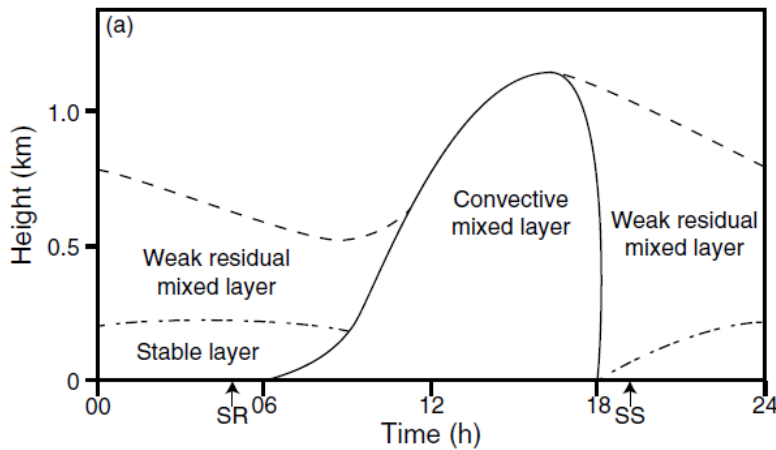


Figure 2.4 Typical diurnal variation of the boundary layer structure (Oke, 1982). Sunrise (SR), Sunset (SS).

In stable conditions ($h/L \geq 0$), the w_s is defined as (1.7):

$$w_s = \frac{u_*}{1 + 4.7 z/L} \quad (1.7)$$

In unstable conditions ($h/L < 0$), the w_s is defined as (1.8):

$$w_s = (u_*^3 + 2.8ew_*^3)^{1/3} \quad (1.8)$$

where $e = \max(0.1, z/h)$. The Monin–Obukhov similarity theory widely used in mesoscale CTM model and it has many expressions. For the k -theory in the Community Multiscale Air Quality Model (CMAQ), the K_z is defined by (Holtslag and Boville, 1993) as (1.9):

$$K_z = k \frac{u_*}{w_s} z \left(1 - \frac{z}{h}\right)^2 \quad (1.9)$$

In stable conditions, the w_s is defined as (1.10):

$$w_s = 1 + 5 \frac{z}{L} \quad (1.10)$$

In unstable conditions, the w_s is defined as (1.11):

$$w_s = \left(1 - 16 \frac{z}{L}\right)^{-\frac{1}{4}} \quad (1.11)$$

In a three-dimensional Eulerian model (FALL3D), K_z is defined as (Costa et al., 2006) (1.12):

$$K_z = k u_* w_s z \left(1 - \frac{z}{h}\right) \quad (1.12)$$

In stable conditions, the w_s is defined as (1.13):

$$w_s = \left(1 + 9.2 \frac{z}{L}\right)^{-1} \quad (1.13)$$

In unstable conditions, the w_s is defined as (4.1):

$$w_s = \left(1 - 13 \frac{z}{L}\right)^{\frac{1}{2}} \quad (1.14)$$

All three schemes use the friction velocity (u_*), convective velocity (w_*) and the Monin–Obukhov length (L) but in different configurations for stable and unstable conditions.

2.5 Preliminary study – Model setup

As a first analysis, a long-term simulation covering the entire year 2016 has been performed with three K_z parameterizations as previously mentioned. The K_z from CHIMERE, CMAQ and FALL3D are defined as K_{z1} , K_{z2} and K_{z3} respectively. The K_{z1} scheme is the initial vertical diffusion scheme of the CHIMERE model. The K_{z2} and K_{z3} schemes are the two most reasonable schemes selected on the basis of sensitivity experiments. A minimal K_z is setup to

$0.01\text{m}^2/\text{s}$ in the dry boundary layer and $1\text{m}^2/\text{s}$ in the cloudy boundary layer in three schemes to avoid unreasonable low mixing (Menut et al., 2013a).

The simulation is performed from 1st January to 31st December 2016 at 7km resolution over France. The domain is discretized vertically with 20 vertical levels from 999.5hPa to 500hPa, with the lowest level at about 4m and 14 levels below 1000m. Meteorological input data were taken from the Integrated Forecasting System (IFS) model from the European Centre for Medium-Range Weather Forecasts (ECMWF). Chemical boundary conditions were obtained from a lower (25km) resolution simulation performed on a European domain. The sector specific European Monitoring and Evaluation Program (EMEP) inventory (details can be found in <https://www.emep.int/>) has been used for anthropogenic emissions in the model, at a resolution of $0.1^\circ \times 0.1^\circ$.

The air quality monitoring data are taken from the French national air quality forecasting platform (PREV'AIR)(Honore et al., 2006). 57 urban background air quality monitoring stations and 15 rural background air quality monitoring stations includes the hourly surface concentrations of criteria pollutants (NO_2 , $\text{PM}_{2.5}$, and PM_{10}) are used to assess the performances of the models with the various K_z parameterizations, the locations of stations is shown in Figure2.5.

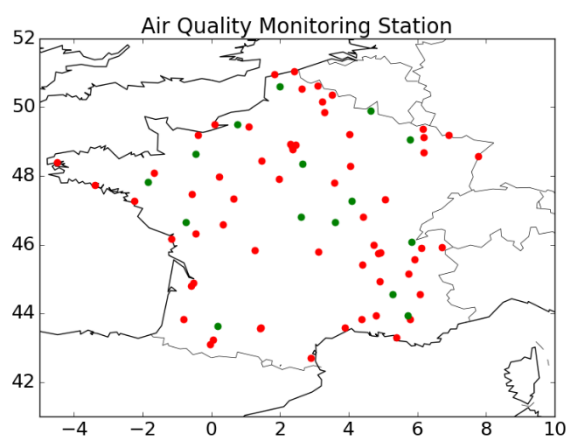


Figure2.5 Locations of air quality monitoring stations. Red points: urban background stations. Green points: rural background stations

To quantify the difference between model and instruments data, the relative bias (RB), mean bias (MB), mean linear correlation coefficient (R) and root mean square error (RMSE) is used as statistical estimation and calculated as:

$$RB(\%) = \frac{y_{mod} - y_{obs}}{y_{obs}} * 100 \quad (1.15)$$

$$MB = y_{mod} - y_{obs} \quad (1.16)$$

$$R = \frac{\sum(y_{mod} - \overline{y_{mod}})(y_{obs} - \overline{y_{obs}})}{\sqrt{\sum(y_{mod} - \overline{y_{mod}})^2 \sum(y_{obs} - \overline{y_{obs}})^2}} \quad (1.17)$$

$$RMSE = \sqrt{\frac{1}{N} \sum_{i=1}^N (y_{mod} - y_{obs})^2} \quad (1.18)$$

Where y_{mod} refers to the modelled value and y_{obs} refers to the results from instruments with $\overline{y_{mod}}$ and $\overline{y_{obs}}$ their mean values respectively. N is the number of the data.

2.6 Results and Discussions

A sensitivity test using the same model configurations, but different vertical diffusion coefficients was performed to understand the role of each Kz in stable and unstable conditions. As shown in Figure 2.6, three schemes display similar Kz at low levels in stable condition, with a relatively high surface diffusion rate in $Kz3$ and relatively low surface diffusion rate in $Kz2$, the $Kz1$ shows a slightly higher Kz in all levels. However, $Kz3$ has obviously stronger Kz since the fifth level than other two schemes. Under unstable conditions, the surface Kz shows a completely opposite trend to stable condition, with $Kz2 > Kz1 > Kz3$. In the middle levels, the difference between the different schemes is significantly higher than the stable condition, and the diffusion rates of $Kz2$ and $Kz3$ begin to reverse in the ninth level. According to this sensitivity test, three conclusions can be drawn: the differences between each scheme is small; the RB of pollutants concentrations from $Kz3$ will be higher than other two; and the RB of pollutants concentrations between three schemes will be higher in the nighttime than the daytime.

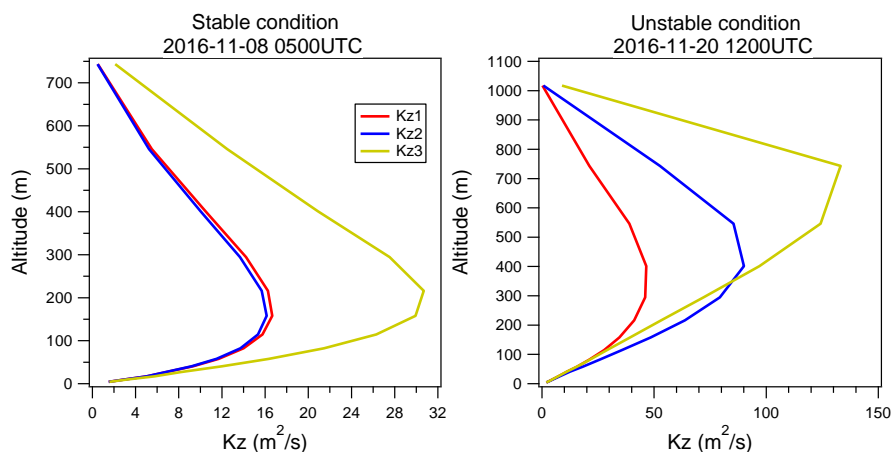


Figure 2.6 Sensitivity test of vertical profile of K_z (m^2/s) in stable and unstable conditions.

Figure 2.7 displays averaged vertical profiles of K_z , NO_2 , O_3 , $PM_{2.5}$ and PM_{10} for the year 2016. The K_z profiles show similar shapes from surface to the top, with an upward trend within 13 levels (approximately 550m). Table 2.1 lists detail information of K_z for the first 10 levels, the K_{z1} displays lowest K_z at all levels, K_{z2} and K_{z3} begin to reverse from the seventh level (approximately 82m). The vertical NO_2 , $PM_{2.5}$ and PM_{10} concentration profiles show that the increasing mass concentrations from surface to the top because of the anthropogenic emissions, highest concentrations are simulated in the K_{z1} at low levels. The average RB between K_{z1} and K_{z2} , K_{z1} and K_{z3} are 2.2% and 7.3% approximately. K_{z2} provides stronger diffusion rate than K_{z3} in the first layers, however, the pollutants concentrations at low levels are higher in K_{z2} . This indicates that surface pollutants concentrations are not only depend on the corresponding K_z . The transport also plays an important role in the low levels pollutants concentrations. The vertical profile of O_3 concentrations are different than for other pollutants, it shows lower concentrations in the surface than for upper layers. The vertical O_3 concentrations are different compared to other species, with the highest concentration in K_{z3} scheme at surface. The reason is the fast titration by NO_x and deposition processes close to the surface.

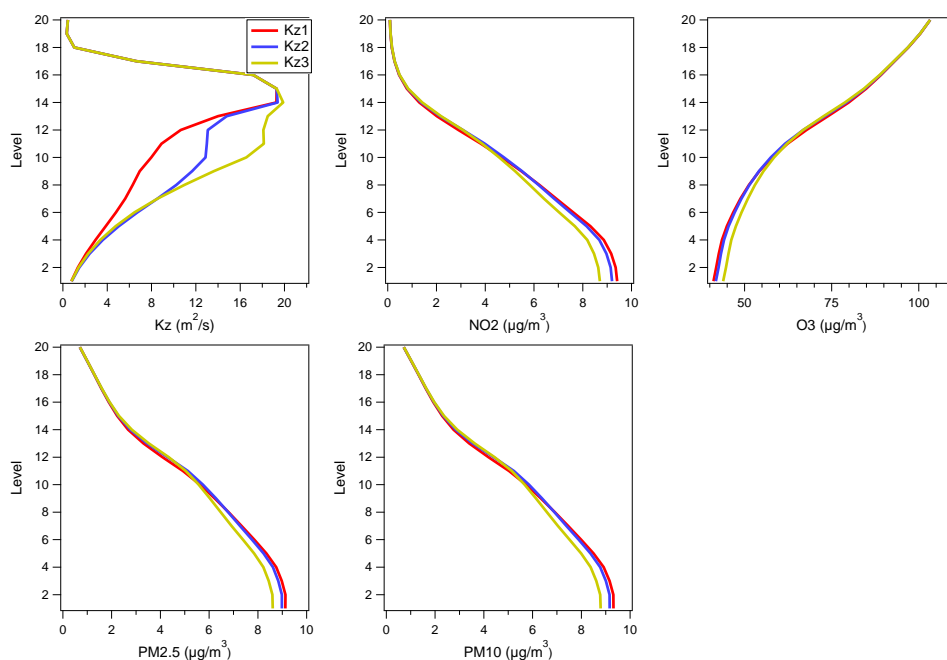


Figure 2.7 Vertical profiles of K_z (m^2/s); NO_2 ($\mu g/m^3$); O_3 ($\mu g/m^3$) $PM_{2.5}$ ($\mu g/m^3$) and PM_{10} ($\mu g/m^3$) over the France domain. The profiles are averaged from January 1st to December 31st, 2016.

Table 2.1 The K_z (m^2/s) values for the 10 levels.

Level	1	2	3	4	5	6	7	8	9	10
Kz1	0.76	1.35	2.09	2.94	3.86	4.78	5.61	6.29	6.93	7.97
Kz2	0.79	1.48	2.41	3.59	5.04	6.71	8.52	10.23	11.66	12.87
Kz3	0.77	1.41	2.27	3.37	4.75	6.45	8.53	10.95	13.63	16.55

Figure 2.8 displays the seasonal mean first layer K_z over France domain. Results show that the regional patterns are similar for three schemes. The K_{z1} shows a slightly higher surface K_z than K_{z3} at the Alps and the Pyrenees. However, K_{z3} gives a relative higher surface K_z than K_{z1} over mainland France in autumn and winter. In general, K_{z2} scheme has slightly higher vertical diffusion rate than other two schemes, the three schemes give the trend of spring > summer > autumn > winter of surface K_z in the France domain, and coastal areas are generally display higher K_z than inland areas, due to the sea breezes which enhance the dispersion of pollutants (Reid and Steyn, 1997). The seasonal profiles of surface NO_2 , $PM_{2.5}$ and PM_{10} concentrations between observation and simulation are illustrated in Figure 2.9. Model underestimated NO_2 concentrations whatever the season, but particularly during wintertime. The negative biases are $-6.05 \mu g/m^3$, $-6.16 \mu g/m^3$ and $-7.09 \mu g/m^3$ for K_{z1} , K_{z2} and

$Kz3$ in winter respectively. Compare with the model performances of PM simulations, the three schemes display higher biases for NO_2 simulations in spring, autumn and winter. NO_2 mainly comes from vehicle exhaust emission in cities, it can indicate the model may overestimate vertical diffusion rate in urban region. The model displays relatively better performance in $PM_{2.5}$ simulation, with slight negative biases in summer and positive biases in the rest of seasons. However, three schemes underestimated PM_{10} concentrations in every season. As shows in Table2.2, the observed PM_{10} concentrations are approximately the double of the simulation in summer. This could indicate the underestimation of coarse particles in the emission inventory.

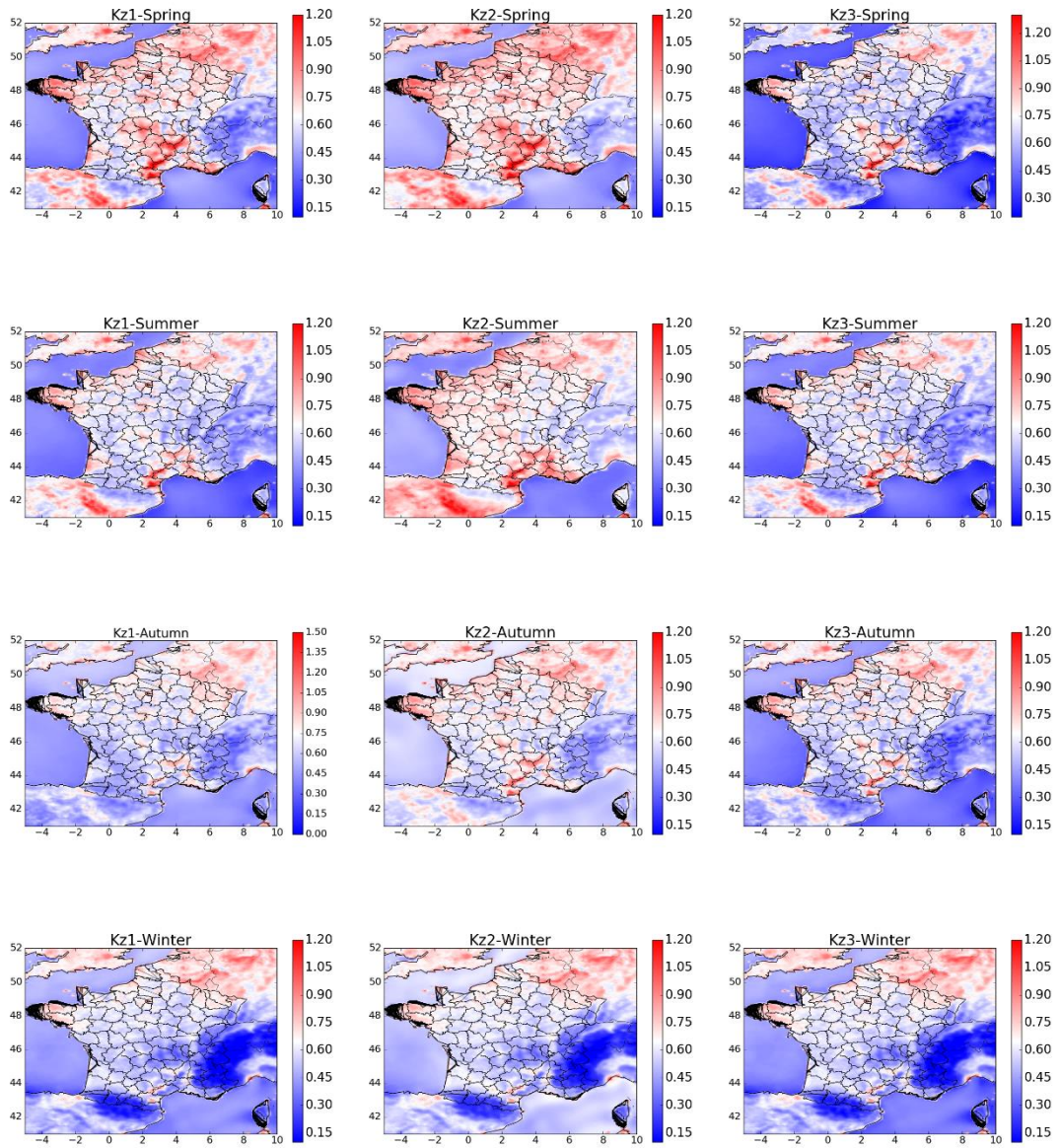


Figure 2.8 Maps of the seasonal mean vertical diffusion coefficient (m^2/s) over the France domain.

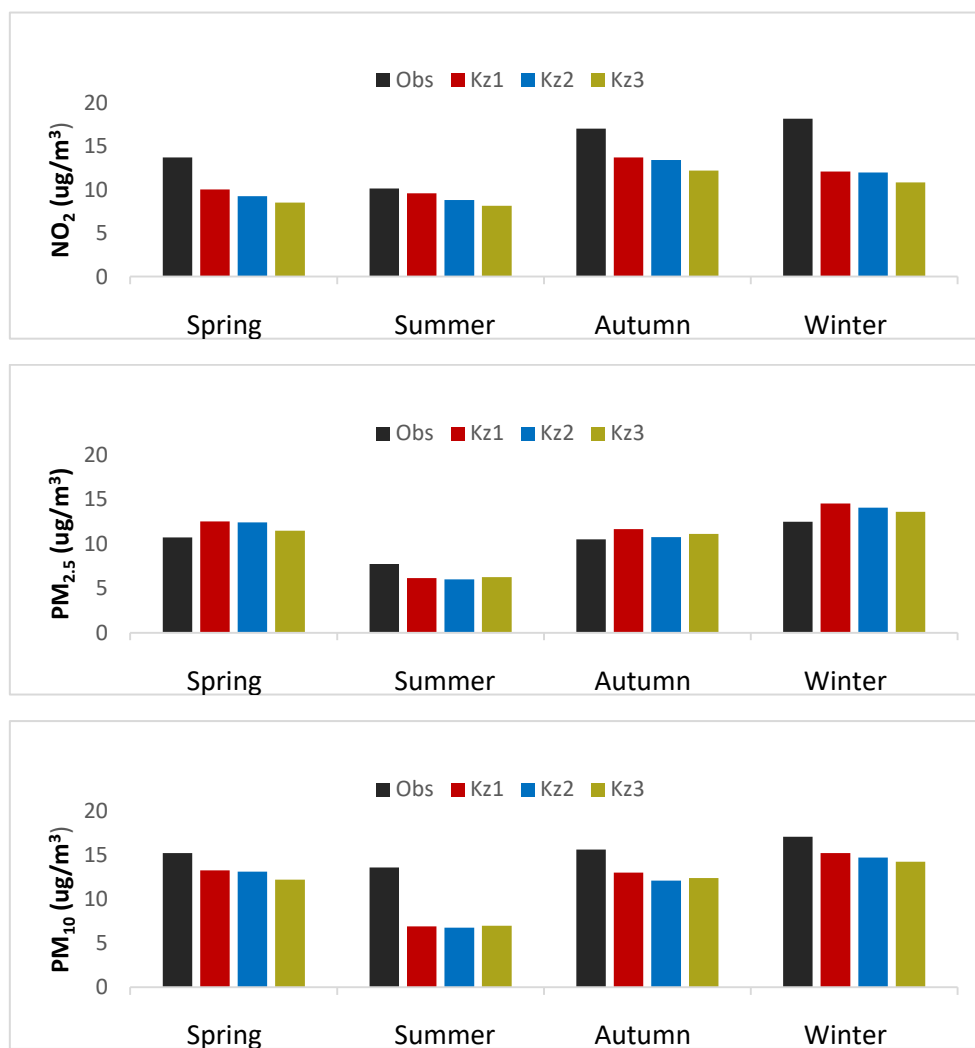


Figure 2.9 Seasonal changes between observed and modelled NO_2 , $\text{PM}_{2.5}$ and PM_{10} mass concentrations ($\mu\text{g}/\text{m}^3$) in France domain.

Table 2.2 Seasonal average mass concentration of NO_2 , $\text{PM}_{2.5}$ and PM_{10} ($\mu\text{g}/\text{m}^3$) between observation and three schemes.

		Spring	Summer	Autumn	Winter
NO₂	Obs	13.70	10.10	17.04	18.15
	Kz1	10.05	9.59	13.72	12.10
	Kz2	9.36	8.91	13.41	11.99
	Kz3	8.59	8.14	12.18	10.86
PM_{2.5}	Obs	10.75	7.76	10.52	12.49
	Kz1	12.55	6.14	11.69	14.58
	Kz2	12.42	6.02	10.79	14.09
	Kz3	11.51	6.26	11.13	13.62
PM₁₀	Obs	15.26	13.64	15.69	17.14
	Kz1	13.30	6.91	13.06	15.28
	Kz2	13.17	6.77	12.13	14.75

Kz3	12.25	6.99	12.41	14.29
-----	-------	------	-------	-------

In order to better evaluate the impact of vertical diffusion coefficients on the air quality predictions, modelled time series of the pollutants concentrations compared with the observations for urban and rural region are displayed in Figure 2.10. In urban areas, the models capture the time variability quite well for NO₂, PM_{2.5} and PM₁₀ simulations, particularly for the PM_{2.5}, model almost perfectly reproduced the seasonal variability. However, the model tends to underestimate the NO₂ and PM₁₀ concentrations of PM₁₀ in urban areas especially during wintertime for NO₂ and summertime for PM₁₀. Comparing the model performance of PM_{2.5} and PM₁₀ simulations, the model displays a slight negative bias of PM₁₀ concentration than PM_{2.5} for the whole period. The yearly average surface mass concentrations of PM_{2.5} and PM₁₀ are 10.37 µg/m³ and 15.41 µg/m³ from the observation over the France domain. PM_{2.5} comprised 67.30% of total PM₁₀. In the cases of simulations, PM_{2.5} surface concentrations are 10.79 µg/m³, 11.21 µg/m³, 10.60 µg/m³ and PM₁₀ surface concentrations are 11.66 µg/m³, 12.10 µg/m³, 11.45 µg/m³ from *Kz1*, *Kz2* and *Kz3*, respectively. The ratios of PM_{2.5}/PM₁₀ are almost the same which is approximately 92.5% for three schemes, the bias is approximately 25.3%. This result indicates the models could have a large overestimation of fine mode emissions or that coarse emissions are lacking. All three schemes in rural areas display a quite good reproduction of the evolution of pollutant concentrations and better capture the fluctuations of pollutants in the wintertime than urban areas. The model underestimate PM₁₀ concentration particularly in summertime. Table 2.3 provides an overall evaluation of three schemes in urban and rural areas including R, MB and RMSE. In general, the models present a better performance in rural than the model performances in urban areas. Concentrations of NO₂ and PM₁₀ are stronger underestimated in urban areas than for rural areas. This indicates the three schemes tend to overestimate the local vertical diffusivity in urban region compared to the rural areas. The value of exponent p is considered as 2 (the “square” in the equation) in equation (1.6) and (1.9). The range of this value has been considered from 1 to 3 by Troen and Mahrt (Troen and Mahrt, 1986), the vertical mixing varies considerably correspond to the range of p from 1 to 3 (Hu et al., 2010). Therefore, the results show that setting p value to 2 is applicable in rural areas, but the p value is

overestimated in urban areas. The easiest way to improve such a first order local closure scheme is to set p according to types of land use. Comparing the performances of three k -theory schemes and taking RMSE as the criterion for judging the ability of the model, in urban areas lead to the following outcomes on concentrations: $Kz1 > Kz2 > Kz3$ for NO_2 ; $Kz3 > Kz2 > Kz1$ for $\text{PM}_{2.5}$ and $Kz1 > Kz3 > Kz2$ for PM_{10} ; in rural areas, $Kz1 > Kz2 > Kz3$ for NO_2 , $Kz3 > Kz2 > Kz1$ for $\text{PM}_{2.5}$ and $Kz2 > Kz3 > Kz1$ for PM_{10} . However, the differences between the test results are low. Therefore, it cannot be expected to significantly improve the mesoscale model for air quality simulation and forecast through the modification of diffusion coefficient based on first order local closure scheme.

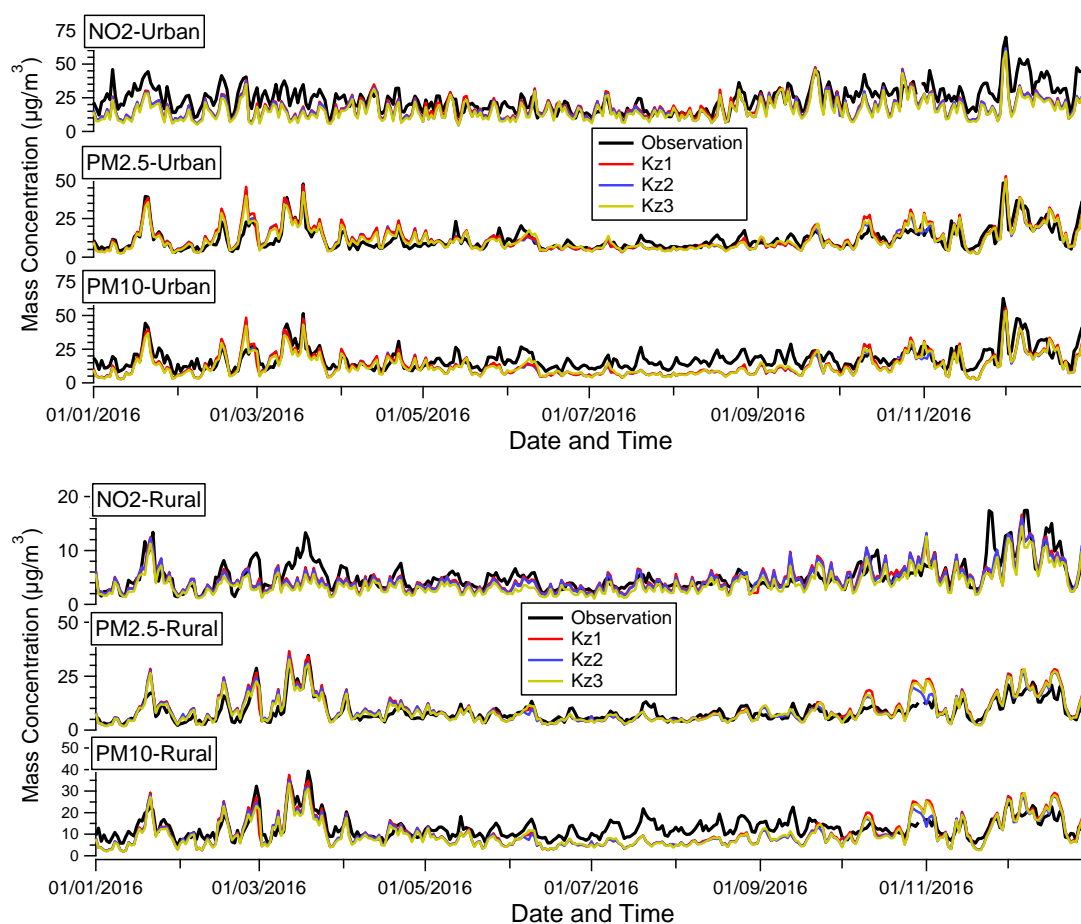


Figure 2.10 Time series between observed and modelled NO_2 , $\text{PM}_{2.5}$ and PM_{10} mass concentrations ($\mu\text{g}/\text{m}^3$) in Urban and Rural areas.

Table 2.3 Statistics of surface variables: mean linear correlation coefficient (R); mean bias (MB) and root mean square error ($RMSE$) between the simulations and observations of NO_2 , $\text{PM}_{2.5}$ and PM_{10} in Urban and Rural areas

		NO ₂			PM _{2.5}			PM ₁₀		
		Kz1	Kz2	Kz3	Kz1	Kz2	Kz3	Kz1	Kz2	Kz3
Urban	R	0.73	0.76	0.74	0.83	0.83	0.84	0.74	0.75	0.76
	MB	-6.39	-7.13	-8.38	0.56	0.16	-0.10	-4.31	-4.71	-5.01
	RMSE	9.32	9.58	10.64	4.77	4.50	4.32	7.42	7.62	7.50
Rural	R	0.72	0.73	0.73	0.88	0.88	0.87	0.78	0.77	0.77
	MB	-0.47	-0.62	-1.31	1.11	0.67	0.56	-2.35	-2.83	-2.95
	RMSE	2.07	2.10	2.36	3.68	3.29	3.26	5.18	5.13	5.17

In Figure 2.11 the results from urban and rural areas are illustrated for surface NO₂, PM_{2.5} and PM₁₀ concentrations. The diurnal cycles of NO₂, PM_{2.5} and PM₁₀ have a similar behavior at urban areas, with two peaks occurred in the morning and evening rush hours. In rural areas, the evening peak did not appear, with show a gradual accumulation at nighttime. Compared with observations, the simulation results have more significant diurnal differences for all pollutants, and the model significantly underestimates the NO₂ and PM₁₀ concentration during daytime. This indicates that the *K*-theory may overestimate the vertical diffusion rate under unstable conditions. The model performance between the three schemes shows higher biases in nighttime than for daytime, especially for the NO₂ simulation, which proved the conclusion in the sensitivity test that the RB between three schemes will be higher in absolute values in the nighttime than the daytime.

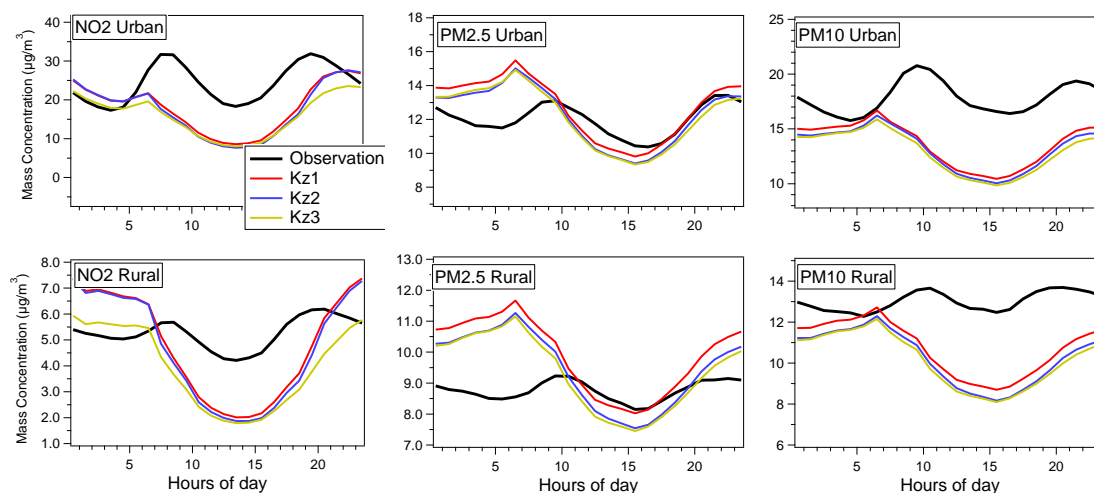


Figure 2.11 Diurnal cycles for surface concentrations ($\mu\text{g}/\text{m}^3$) of NO₂, PM_{2.5} and PM₁₀ in the year 2016

2.7 Conclusions

The micro meteorology over built-up areas differs from the non-urban landscape in many aspects: wind-flows, radiation, humidity, precipitation and air quality. The dispersion of pollutants in urban areas is an actual topic and the modelling approaches depend on the involved atmospheric processes. Initially we focused on the dispersion of pollutants in the urban canopy, three vertical diffusion coefficients based on first order local closure scheme have been investigated in a one-year simulation over France. Comparing the model performances of three scheme in urban and rural areas, it is found that the three schemes perform better in rural than in urban areas. The vertical mixing is relatively overestimated in urban areas. One idea is to decrease the p value (the “square” in the K_z equation) on urban land use. The results also indicate such simplest scheme is an effective way to reproduce the dispersion of pollutants both in urban canopy and surroundings in mesoscale chemistry transport model, but it cannot be expected to significantly improve the mesoscale model by this simple modification based on the first-order local closure Reynolds decomposition scheme. Further improvements should start with a more accurate turbulence process. Another problem to be solved is the ratio of PM_{2.5} / PM₁₀ that exceeds 90% in all seasons in the models, while the ratio is usually around 70% in the observations, the emission inventory requires notable improvements with probably a lack of coarse particles anthropogenic or biogenic in origins.

This first screening of usual K -theory diffusion parameterizations over a long-term simulation was a first step to identify limitations and possible improvements. The next chapter focuses at urban scale on pollution event in November-December 2016.

References

- Augustus, N. and Augustus, N.: Development and assessment of the second-generation National Building Statistics Database, Seventh Conference on Coastal Atmospheric and Oceanic Prediction and Processes joint with the Seventh Symposium on the Urban Environment (10-13 September 2007), 2007.
- Baklanov, A., Lawrence, M., Pandis, S., Mahura, A., Finardi, S., Moussiopoulos, N., Beekmann, M., Laj, P., Gomes, L., Jaffrezo, J.-L., Borbon, A., Coll, I., Gros, V., Sciare, J., Kukkonen, J., Galmarini, S., Giorgi, F., Grimmond, S., Esau, I., Stohl, A., Denby, B., Wagner, T., Butler, T., Baltensperger, U., Builtjes, P., van den Hout, D., van der Gon, H. D., Collins, B., Schlutzen, H., Kulmala, M., Zilitinkevich, S., Sokhi, R., Friedrich, R., Theloke, J., Kummer, U., Jalkinen, L., Halenka, T., Wiedensholer, A., Pyle, J., and Rossow, W. B.: MEGAPOLI: concept of multi-scale modelling of megacity impact on air quality and climate, in: *Advances in Science and Research*, 9th EMS Annual Meeting and 9th European Conference on Applications of Meteorology 2009 -, 115–120, <https://doi.org/10.5194/asr-4-115-2010>, 2010.
- Baklanov, A., Baldasano, J., Bouchet, V., Brunner, D., Ekman, A., Galmarini, S., Carmichael, G., Grell, G., Flemming, J., Forkel, R., Freitas, S., Gauss, M., Hegglin, M., Hov, Ø., Joffre, S., Makar, P., Mathur, R., Miranda, A., Moussiopoulos, N., and Zhang, Y.: Coupled Chemistry-Meteorology/ Climate Modelling (CCMM): status and relevance for numerical weather prediction, atmospheric pollution and climate research, <https://doi.org/10.13140/RG.2.1.4937.8169>, 2016a.
- Baklanov, A., Molina, L. T., and Gauss, M.: Megacities, air quality and climate, *Atmospheric Environment*, 126, 235–249, <https://doi.org/10.1016/j.atmosenv.2015.11.059>, 2016b.
- Baklanov, A., Grimmond, C. S. B., Carlson, D., Terblanche, D., Tang, X., Bouchet, V., Lee, B., Langendijk, G., Kolli, R. K., and Hovsepyan, A.: From urban meteorology, climate and environment research to integrated city services, *Urban Climate*, 23, 330–341, <https://doi.org/10.1016/j.uclim.2017.05.004>, 2018.
- Bessagnet, B., Menut, L., Lapere, R., Couvidat, F., Jaffrezo, J.-L., Mailler, S., Favez, O., Pennel, R., and Siour, G.: High Resolution Chemistry Transport Modeling with the On-Line CHIMERE-WRF Model over the French Alps—Analysis of a Feedback of Surface Particulate Matter Concentrations on Mountain Meteorology, *Atmosphere*, 11, 565, <https://doi.org/10.3390/atmos11060565>, 2020.
- Britter, R. E. and Hanna, S. R.: Flow and dispersion in urban areas, *Annu. Rev. Fluid Mech.*, 35, 469–496, <https://doi.org/10.1146/annurev.fluid.35.101101.161147>, 2003.
- Ching, J. K. S.: A perspective on urban canopy layer modeling for weather, climate and air quality applications, *Urban Climate*, 3, 13–39, <https://doi.org/10.1016/j.uclim.2013.02.001>, 2013.

- Costa, A., Macedonio, G., and Folch, A.: A three-dimensional Eulerian model for transport and deposition of volcanic ashes, *Earth and Planetary Science Letters*, 241, 634–647, <https://doi.org/10.1016/j.epsl.2005.11.019>, 2006.
- Crippa, M., Guizzardi, D., Muntean, M., Schaaf, E., Dentener, F., van Aardenne, J. A., Monni, S., Doering, U., Olivier, J. G. J., Pagliari, V., and Janssens-Maenhout, G.: Gridded emissions of air pollutants for the period 1970–2012 within EDGAR v4.3.2, *Earth Syst. Sci. Data*, 10, 1987–2013, <https://doi.org/10.5194/essd-10-1987-2018>, 2018.
- Dwivedi, Y. D., Nukala, V. B., Maddula, S. P., and Nair, K.: Prediction of Atmospheric Turbulence Characteristics for Surface Boundary Layer using Empirical Spectral Methods, *Rev. bras. meteorol.*, <https://doi.org/10.1590/0102-77863540083>, 2020.
- Fernando, H. J. S., Zajic, D., Di Sabatino, S., Dimitrova, R., Hedquist, B., and Dallman, A.: Flow, turbulence, and pollutant dispersion in urban atmospheres, *Physics of Fluids*, 22, 051301, <https://doi.org/10.1063/1.3407662>, 2010.
- Fujibe, F.: Long-term Surface Wind Changes in the Tokyo Metropolitan Area in the Afternoon of Sunny Days in the Warm Season., *JMSJ*, 81, 141–149, <https://doi.org/10.2151/jmsj.81.141>, 2003.
- Holtslag, B. and Boville, B.: Local Versus Nonlocal Boundary-Layer Diffusion in a Global Climate Model, *Journal of Climate*, 6, 1825–1842, [https://doi.org/10.1175/1520-0442\(1993\)006<1825:LVNBLD>2.0.CO;2](https://doi.org/10.1175/1520-0442(1993)006<1825:LVNBLD>2.0.CO;2), 1993.
- Honore, C., Menut, L., Bessagnet, B., Meleux, F., Rouil, L., Vautard, R., Beekmann, M., Poisson, N., and Peuch, V.-H.: PREV’AIR, a platform for air quality monitoring and forecasting, AGU Fall Meeting 2006, 2006.
- Hu, X.-M., Nielsen-Gammon, J. W., and Zhang, F.: Evaluation of Three Planetary Boundary Layer Schemes in the WRF Model, 49, 1831–1844, <https://doi.org/10.1175/2010JAMC2432.1>, 2010.
- Huang, M., Gao, Z., Miao, S., and Chen, F.: Sensitivity of urban boundary layer simulation to urban canopy models and PBL schemes in Beijing, *Meteorol Atmos Phys*, 131, 1235–1248, <https://doi.org/10.1007/s00703-018-0634-1>, 2019.
- Huszar, P., Karlický, J., Ďoubalová, J., Nováková, T., Šindelářová, K., Švábik, F., Belda, M., Halenka, T., and Žák, M.: The impact of urban land-surface on extreme air pollution over central Europe, *Atmos. Chem. Phys.*, 20, 11655–11681, <https://doi.org/10.5194/acp-20-11655-2020>, 2020.
- Jacobson, M. Z.: Development and application of a new air pollution modeling system—II. Aerosol module structure and design, *Atmospheric Environment*, 31, 131–144, [https://doi.org/10.1016/1352-2310\(96\)00202-6](https://doi.org/10.1016/1352-2310(96)00202-6), 1997.
- Jacobson, M. Z.: *Fundamentals of Atmospheric Modeling*, 2nd ed., Cambridge University Press, Cambridge, <https://doi.org/10.1017/CBO9781139165389>, 2005.

- Karl, M.: Development of the city-scale chemistry transport model CityChem-EPISODE and its application to the city of Hamburg, 1–60, <https://doi.org/10.5194/gmd-2018-8>, 2018.
- Karlický, J., Huszár, P., Halenka, T., Belda, M., Žák, M., Pišoft, P., and Mikšovský, J.: Multi-model comparison of urban heat island modelling approaches, *Atmos. Chem. Phys.*, 18, 10655–10674, <https://doi.org/10.5194/acp-18-10655-2018>, 2018.
- Karlický, J., Huszár, P., Nováková, T., Belda, M., Švábik, F., Ďoubalová, J., and Halenka, T.: The “urban meteorology island”: a multi-model ensemble analysis, 20, 15061–15077, <https://doi.org/10.5194/acp-20-15061-2020>, 2020.
- Kim, D.-J., Lee, D.-I., Kim, J.-J., Park, M.-S., and Lee, S.-H.: Development of a Building-Scale Meteorological Prediction System Including a Realistic Surface Heating, 11, 67, <https://doi.org/10.3390/atmos11010067>, 2020.
- KIM, H. H.: Urban heat island, 13, 2319–2336, <https://doi.org/10.1080/01431169208904271>, 1992.
- Kirkil, G., Mirocha, J., Bou-Zeid, E., Chow, F. K., and Kosović, B.: Implementation and Evaluation of Dynamic Subfilter-Scale Stress Models for Large-Eddy Simulation Using WRF*, 140, 266–284, <https://doi.org/10.1175/MWR-D-11-00037.1>, 2012.
- Klein, P., Leitl, B., and Schatzmann, M.: Driving physical mechanisms of flow and dispersion in urban canopies, 27, 1887–1907, <https://doi.org/10.1002/joc.1581>, 2007.
- Kondo, H., Genchi, Y., Kikegawa, Y., Ohashi, Y., Yoshikado, H., and Komiyama, H.: Development of a Multi-Layer Urban Canopy Model for the Analysis of Energy Consumption in a Big City: Structure of the Urban Canopy Model and its Basic Performance, *Boundary-Layer Meteorol.*, 116, 395–421, <https://doi.org/10.1007/s10546-005-0905-5>, 2005.
- Kusaka, H. and Kimura, F.: Coupling a Single-Layer Urban Canopy Model with a Simple Atmospheric Model: Impact on Urban Heat Island Simulation for an Idealized Case, 82, 67–80, <https://doi.org/10.2151/jmsj.82.67>, 2004.
- Kusaka, H., Kondo, H., Kikegawa, Y., and Kimura, F.: A Simple Single-Layer Urban Canopy Model For Atmospheric Models: Comparison With Multi-Layer And Slab Models, *Boundary-Layer Meteorology*, 101, 329–358, <https://doi.org/10.1023/A:1019207923078>, 2001.
- Letzel, M. O., Krane, M., and Raasch, S.: High resolution urban large-eddy simulation studies from street canyon to neighbourhood scale, *Atmospheric Environment*, 42, 8770–8784, <https://doi.org/10.1016/j.atmosenv.2008.08.001>, 2008.
- Li, H., Zhang, H., Mamtimin, A., Fan, S., and Ju, C.: A New Land-Use Dataset for the Weather Research and Forecasting (WRF) Model, 11, 350, <https://doi.org/10.3390/atmos11040350>, 2020.
- Li, X., Hu, X.-M., Ma, Y., Wang, Y., Li, L., and Zhao, Z.: Impact of planetary boundary layer structure on the formation and evolution of air-pollution episodes in Shenyang,

- Northeast China, *Atmospheric Environment*, 214, 116850, <https://doi.org/10.1016/j.atmosenv.2019.116850>, 2019.
- Liao, J., Wang, T., Wang, X., Xie, M., Jiang, Z., Huang, X., and Zhu, J.: Impacts of different urban canopy schemes in WRF/Chem on regional climate and air quality in Yangtze River Delta, China, *Atmospheric Research*, 145–146, 226–243, <https://doi.org/10.1016/j.atmosres.2014.04.005>, 2014.
- Liu, H., Ma, W., Qian, J., Cai, J., Ye, X., Li, J., and Wang, X.: Effect of urbanization on the urban meteorology and air pollution in Hangzhou, *J Meteorol Res*, 29, 950–965, <https://doi.org/10.1007/s13351-015-5013-y>, 2015.
- Manola, I., Steeneveld, G., Uijlenhoet, R., and Holtslag, A. A. M.: Analysis of urban rainfall from hourly to seasonal scales using high-resolution radar observations in the Netherlands, *Int J Climatol*, 40, 822–840, <https://doi.org/10.1002/joc.6241>, 2020.
- Martilli, A., Clappier, A., and Rotach, M. W.: An Urban Surface Exchange Parameterisation for Mesoscale Models, *Boundary-Layer Meteorology*, 104, 261–304, <https://doi.org/10.1023/A:1016099921195>, 2002.
- Menut, L., Bessagnet, B., Colette, A., and Khvorostiyarov, D.: On the impact of the vertical resolution on chemistry-transport modelling, *Atmospheric Environment*, 67, 370–384, <https://doi.org/10.1016/j.atmosenv.2012.11.026>, 2013.
- Morais, M. V. B. de, Freitas, E. D. de, Marciotto, E. R., Urbina Guerrero, V. V., Martins, L. D., and Martins, J. A.: Implementation of Observed Sky-View Factor in a Mesoscale Model for Sensitivity Studies of the Urban Meteorology, 10, 2183, <https://doi.org/10.3390/su10072183>, 2018.
- Oke, T. R.: The energetic basis of the urban heat island, *Q.J Royal Met. Soc.*, 108, 1–24, <https://doi.org/10.1002/qj.49710845502>, 1982.
- Oke, T. R. and Maxwell, G. B.: Urban heat island dynamics in Montreal and Vancouver, *Atmospheric Environment* (1967), 9, 191–200, [https://doi.org/10.1016/0004-6981\(75\)90067-0](https://doi.org/10.1016/0004-6981(75)90067-0), 1975.
- Pelling, M. and Blackburn, S. (Eds.): *Megacities and the coast: risk, resilience and transformation*, Routledge, London, 245 pp., 2013.
- Rao, S. T., Ku, J. Y., Berman, S., Zhang, K., and Mao, H.: Summertime Characteristics of the Atmospheric Boundary Layer and Relationships to Ozone Levels over the Eastern United States, *Pure and Applied Geophysics*, 160, 21–55, <https://doi.org/10.1007/s00024-003-8764-9>, 2003.
- Reid, K. H. and Steyn, D. G.: Diurnal variations of boundary-layer carbon dioxide in a coastal city—Observations and comparison with model results, *Atmospheric Environment*, 31, 3101–3114, [https://doi.org/10.1016/S1352-2310\(97\)00050-2](https://doi.org/10.1016/S1352-2310(97)00050-2), 1997.
- Reinmuth-Selzle, K., Kampf, C. J., Lucas, K., Lang-Yona, N., Fröhlich-Nowoisky, J., Shiraiwa, M., Lakey, P. S. J., Lai, S., Liu, F., Kunert, A. T., Ziegler, K., Shen, F., Sgarbanti, R., Weber, B., Bellinghausen, I., Saloga, J., Weller, M. G., Duschl, A.,

- Schuppan, D., and Pöschl, U.: Air Pollution and Climate Change Effects on Allergies in the Anthropocene: Abundance, Interaction, and Modification of Allergens and Adjuvants, *Environ. Sci. Technol.*, 51, 4119–4141, <https://doi.org/10.1021/acs.est.6b04908>, 2017.
- Roth, M.: Review of atmospheric turbulence over cities, *Q.J.R. Meteorol. Soc.*, 126, 941–990, <https://doi.org/10.1002/qj.49712656409>, 2007.
- Sarath K. Guttikunda, Calori, G., Lasry, F., and Ngo, R.: Air Quality Forecasting System for Cities: Modeling Architecture for Delhi, <https://doi.org/10.13140/RG.2.2.20285.92648>, 2011.
- Seo, J., Park, D.-S. R., Kim, J. Y., Youn, D., Lim, Y. B., and Kim, Y.: Effects of meteorology and emissions on urban air quality: a quantitative statistical approach to long-term records (1999–2016) in Seoul, South Korea, 18, 16121–16137, <https://doi.org/10.5194/acp-18-16121-2018>, 2018.
- Stull, R. B.: Turbulence Kinetic Energy, Stability and Scaling, in: *An Introduction to Boundary Layer Meteorology*, edited by: Stull, R. B., Springer Netherlands, Dordrecht, 151–195, https://doi.org/10.1007/978-94-009-3027-8_5, 1988.
- Theeuwes, N. E., Barlow, J. F., Teuling, A. J., Grimmond, C. S. B., and Kotthaus, S.: Persistent cloud cover over mega-cities linked to surface heat release, *npj Clim Atmos Sci*, 2, 15, <https://doi.org/10.1038/s41612-019-0072-x>, 2019.
- Tong, H., Walton, A., Sang, J., and Chan, J. C. L.: Numerical simulation of the urban boundary layer over the complex terrain of Hong Kong, *Atmospheric Environment*, 39, 3549–3563, <https://doi.org/10.1016/j.atmosenv.2005.02.045>, 2005.
- Troen, I. B. and Mahrt, L.: A simple model of the atmospheric boundary layer; sensitivity to surface evaporation, *Boundary-Layer Meteorol*, 37, 129–148, <https://doi.org/10.1007/BF00122760>, 1986.
- Uehara, K., Murakami, S., Oikawa, S., and Wakamatsu, S.: Wind tunnel experiments on how thermal stratification affects flow in and above urban street canyons, *Atmospheric Environment*, 34, 1553–1562, [https://doi.org/10.1016/S1352-2310\(99\)00410-0](https://doi.org/10.1016/S1352-2310(99)00410-0), 2000.
- Warner, T. T.: *Numerical weather and climate prediction*, Cambridge Univ. Press, Cambridge, 526 pp., 2011.
- Zhang, Y. and Na, S.: Research on the Topological Properties of Air Quality Index Based on a Complex Network, *Sustainability*, 10, 1073, <https://doi.org/10.3390/su10041073>, 2018.
- Zhang, Y., Miao, S., Dai, Y., and Bornstein, R.: Numerical simulation of urban land surface effects on summer convective rainfall under different UHI intensity in Beijing, 122, 7851–7868, <https://doi.org/10.1002/2017JD026614>, 2017.

Chapter III: Impact of physics parameterizations on high-resolution air quality simulations over urban region

Publication accepted and published in *Atmosphere*

Jiang, L.; Bessagnet, B.; Meleux, F.; Tognet, F.; Couvidat, F. Impact of Physics Parameterizations on High-Resolution Air Quality Simulations over the Paris Region. *Atmosphere* 2020, *11*, 618. <https://doi.org/10.3390/atmos11060618>

Supplementary material for the publication is provided in Annex A

Impact of physics parameterizations on high-resolution air quality simulations over the urban region

Lei Jiang^{1,2}, Bertrand Bessagnet¹, Frederik Meleux¹, Frederic Tognet¹, Florian Couvidat¹

¹ INERIS, National Institute for Industrial Environment and Risks, Parc Technologique ALATA, 60550 Verneuil-en-Halatte, France;

² Sorbonne University, UPMC Univ Paris 06, ED129, 75005 Paris, France

Abstract

The accurate simulation of meteorological conditions, especially within the planetary boundary layer (PBL), is of major importance for air quality modeling. In the present work, we have used the Weather Research and Forecast (WRF) model coupled with the chemistry transport model (CTM) CHIMERE to understand the impact of physics parameterizations on air quality simulation during a short-term pollution episode on the Paris region. A lower first model layer with a 4m surface layer could better reproduce the transport and diffusion of pollutants in a real urban environment. Three canopy models could better reproduce a 2m temperature (T2) in the daytime but present a positive bias from 1 °C to 5 °C during the nighttime; the multi-urban canopy scheme “building effect parameterization” (BEP) underestimates the 10m windspeed (W10) around 1.2m/s for the whole episode, indicating the city cluster plays an important role in the diffusion rate in urban areas. For the simulation of pollutant concentrations, large differences were found between three canopy schemes, but with an overall overestimation during the pollution episode, especially for NO₂ simulation, the average mean biases of NO₂ prediction during the pollution episode were 40.9 µg/m³, 62.2 µg/m³, and 29.7 µg/m³ for the Bulk, urban canopy model (UCM), and BEP schemes, respectively. Meanwhile, the vertical profile of the diffusion coefficients and pollutants indicated an important impact of the canopy model on the vertical diffusion. The PBL scheme sensitivity tests displayed an underestimation of the height of the PBL when compared with observations issued from the Lidar. The YonSei University scheme (YSU) and Boulac PBL schemes improved the PBL prediction compared with the Mellor–Yamada–Janjic (MYJ) scheme. All the sensitivity tests, except the Boulac–BEP, could not fairly reproduce the PBL height during the pollution episode. The Boulac–BEP scheme had significantly better performances than the other schemes for the simulation of both the PBL height and pollutants,

especially for the NO₂ and PM_{2.5} (particulate matter 2.5 micrometers or less in diameter) simulations. The mean bias of the NO₂, PM_{2.5}, and PM₁₀ (particulate matter 10 micrometers or less in diameter) prediction were $-5.1\mu\text{g}/\text{m}^3$, $1.2\mu\text{g}/\text{m}^3$, and $-8.6\mu\text{g}/\text{m}^3$, respectively, indicating that both the canopy schemes and PBL schemes have a critical effect on air quality prediction in the urban region. The air quality simulation and forecast in urban region mainly influenced by the urban canopy, boundary layer and diffusion conditions, land surface model had a slight impact for both meteorological and air quality simulation.

Résumé

La simulation précise des conditions météorologiques, en particulier dans la couche limite planétaire (PBL), est d'une importance majeure pour la modélisation de la qualité de l'air. Dans le présent travail, nous avons utilisé le modèle Weather Research and Forecast (WRF) couplé au modèle de transport de la chimie (CTM) CHIMERE pour comprendre l'impact des paramétrages de la physique sur la simulation de la qualité de l'air pendant un épisode de pollution de court terme sur la région parisienne. Un premier niveau vertical du modèle à 4m permettrait de mieux reproduire le transport et la diffusion des polluants dans un environnement urbain. Trois modèles de canopée pourraient mieux reproduire une température de 2m (T2) dans la journée mais présentent un biais positif de 1 °C à 5 °C pendant la nuit ; le schéma de canopée multi-urbain "building effect parameterization" (BEP) sous-estime la vitesse du vent à 10m (W10) d'environ 1.2m/s pour l'ensemble de l'épisode, indiquant que le cluster de la ville joue un rôle important dans la diffusion des polluants en zones urbaines. Pour la simulation des concentrations de polluants, de grandes différences ont été constatées entre les trois schémas de canopée, mais avec une surestimation globale pendant l'épisode de pollution, en particulier pour la simulation du NO₂, les biais moyens de la prédiction du NO₂ pendant l'épisode de pollution étaient de $40,9\mu\text{g}/\text{m}^3$, $62,2\mu\text{g}/\text{m}^3$ et $29,7\mu\text{g}/\text{m}^3$ pour les schémas Bulk, urban canopy model (UCM) et BEP, respectivement. Parallèlement, le profil vertical des coefficients de diffusion et des polluants indique un impact important du modèle de canopée sur la diffusion verticale. Les tests de sensibilité du schéma PBL ont montré une sous-estimation de la hauteur de la PBL par rapport aux observations fournies par le Lidar. Les schémas PBL de l'Université YonSei (YSU) et Boulac ont amélioré la prédiction de la PBL par rapport au schéma Mellor-Yamada-Janjic (MYJ). Tous les tests de sensibilité à l'exception du Boulac-BEP, n'ont pas pu reproduire fidèlement la hauteur de la PBL pendant l'épisode de pollution. Le schéma Boulac-BEP a eu des

performances significativement meilleures que les autres schémas pour la simulation de la hauteur de la CLP et des polluants, en particulier pour les simulations de NO₂ et PM2.5 (particules de 2,5 micromètres de diamètre ou moins). Le biais moyen des simulations de NO₂, PM2.5 et PM10 (particules de 10 micromètres ou moins de diamètre) était de -5,1 µg/m³, 1,2 µg/m³ et -8,6 µg/m³, respectivement, ce qui indique que les schémas de canopée urbaine et de PBL ont un effet critique sur la prévision de la qualité de l'air dans la région urbaine. La simulation et la prévision de la qualité de l'air dans la région urbaine sont principalement influencées par la canopée urbaine, la couche limite et les conditions de diffusion, le modèle de surface terrestre ayant un plus léger impact sur la simulation météorologique et la qualité de l'air.

Keywords: modeling; high resolution; air quality; urban canopy; surface layer

3.1 Introduction

Nowadays, around 55% of the world's population lives in urban areas, and this number is expected to increase by 68% by 2050. The European Environment Agency annual report has pointed out around 25% of the European urban population are exposed to air quality exceeding the European Union air quality standards (EEA, 2018), and air pollution is the leading preventable risk factors for premature death in Europe, being responsible for 400,000 deaths per year directly or indirectly. In addition, built-up surfaces that are mainly composed of artificial buildings and cement pavement which are clearly distinguished from natural surfaces favor heat accumulation (Sarrat et al., 2006; Coseo et al., 2015). Recent research shows that in urban regions, Urban Heat Island (UHI) can be observed by a difference of about 1.5–2 °C compared to rural area temperatures, and about 2.0–2.5 °C difference can be observed over densely built-up areas (Falasca et al., 2018). The UHI has a negative effect on the planetary boundary layer (PBL) height (Lin et al., 2008a) and surface wind speed, which affects the transport and dispersion of pollutants. Overall, the UHI changes the local atmospheric dynamic (Falasca et al., 2016), significantly influences local air pollution, reduces visibility, increases water usage, and enhances heat-related morbidity (Gedzelman et al., 2003; Lai et al., 2009). In modeling studies, detailed information on urban parameters is critical for the simulation of the UHI effect. Studies conducted in Taiwan have found that the urban canopy model can improve the prediction of UHI intensity, boundary layer development, land–sea breeze (Lin et al., 2008b), and precipitation (Lin et al., 2008a). Air pollution prediction is crucial in order to inform a large fraction of the population and take

adequate short- and long-term measures to improve air quality. The use of air quality modelling tools at high resolution is now common but remains a challenge, because buildings create local modifications in air flows and modify surface energy budgets and roughness, leading to very complex processes which make air quality simulation particularly difficult in the near-ground layers (Best et al., 2005; Liu et al., 2006; Bessagnet et al., 2014; Barlage et al., 2016). Chemical transport models usually require numerical weather prediction (NWP) models, which provide meteorological input data (Molteni et al., 1996; Tuccella et al., 2012). High-resolution urban canopy parameters databases are becoming more and more available for cities (Salamanca et al., 2009a; Salamanca et al., 2009b). NWP models with different physics parameterizations have been widely used in recent decades to simulate air quality over urban regions, especially the widely used community mesoscale Advanced Research Weather Research and Forecasting (ARW-WRF) model. Studies show that physics parameterizations play a critical role both in meteorological and air quality simulation or forecast (Miao et al., 2010; Fan et al., 2008; Liu et al., 2014; Valari et al., 2014; Markakis et al., 2016). For example, the Planetary Boundary Layer (PBL) height is determined by the heat and momentum exchanges between the PBL and the surface. In meteorological models, the PBL height is calculated by the PBL scheme. Therefore, the PBL scheme is a crucial factor in simulating the formation and evolution of air pollution (He et al., 2015; Wang et al., 2014; Wang et al., 2019). Studies on different PBL parameterization schemes have shown that an accurate description of the meteorological conditions within the PBL via an appropriate parameterization scheme is important for air pollution modeling (Hu et al., 2010). Some studies have presented the influences of meteorological models on pollutant concentrations; they estimate that uncertainties of PBL heights from the different models are one of the major sources of the differences in Particulate Matter (PM) concentrations (Hariprasad et al., 2014; Tyagi et al., 2018). Kleczek et al. compared three non-TKE (Turbulent Kinetic Energy) schemes and four TKE closures schemes; they found that non-TKE schemes tend to produce higher temperatures and wind speeds than in TKE schemes, especially during nighttime. Barlage et al. also had a similar result between TKE and non-TKE schemes at night and found that PBL schemes have little effect on model performances in urban locations during daytime. Some other studies indicate that most PBL schemes slightly overestimate near-ground wind speed (Borrego et al., 2013); a possible reason could be the omission of the effect of unresolved topographic features on the momentum flux (Anderson et al., 2010).

For the first time, the chemistry transport model CHIMERE model has been used with a very low first layer of about 4m to simulate the air quality. In order to understand the impact of physics parameterizations and improve high-resolution air quality simulation, various WRF configurations have been tested over the Paris region during a critical pollution episode occurring from 27th November to 4th December 2016. In this study, we examine three different PBL schemes: (1) the Mellor–Yamada–Janjic scheme (MYJ), (2) the YonSei University scheme (YSU), and (3) the Bougeault and Lacarrere scheme (Boulac); and three canopy schemes, (1) a reference scheme (Bulk) which does not consider urban canopy parameters, (2) a single urban canopy model (UCM) which simply defines the urban geometry as two-dimensional street canyons but considers the three-dimensional nature of urban morphologies, and (3) a multilayer urban canopy model considering building effect parameterization (BEP). BEP was developed by Martilli et al (2002). and allows the direct interaction between buildings and low atmospheric layers and therefore is more realistic in reproducing urban effects (Salamanca et al., 2009a). This work will inform the air quality community on our ability to assess and understand the atmospheric transport of air pollutants over cities for operational forecast with air quality models.

3.2 Model Description and Experiment Design

3.2.1 WRF Model Description

Several studies (Flaounas et al., 2010; Patricola et al., 2012; Vigaud et al., 2009) demonstrate the importance of physics parameterizations in driving air quality modelling outputs. As the first step of this work, the WRF model (Version 3.9.1) is used to simulate the meteorological conditions. The WRF model provides several options for the parameterizations (details can be found in the WRF user manual) of physical processes, including multiple longwave and shortwave radiation schemes, surface layer schemes, land surface schemes, urban canopy schemes, and boundary layer schemes. The initial and boundary conditions are issued from the Global Forecasting System (GFS) analysis data from the National Centers for Environmental Prediction (NCEP), available at a $0.25^\circ \times 0.25^\circ$ resolution at six-hourly time steps. The spectral nudging in WRF simulation is a way to constrain large-scale circulation and constrain the model to be more consistent with observations (Bowden et al., 2012). However, strong nudging may filter out extreme episodes, since nudging pushes the model toward a relatively smooth state (Glisan et al., 2013). Therefore, a weak spectral nudging

above PBL has been tested to improve the accuracy of the downscaled fields but not filter out the simulation of extreme episodes.

The experiment set includes 11 simulations, which are conducted for a winter period from 27th November to 4th December 2016 and are designed to test the sensitivity of the surface meteorological variables and pollutant concentrations at these different physics parameterizations.

Table3.1 Summary of the physics parameterizations used^a

	LW	SW	SL	LS	URB	BL
BULK	RRTMG	RRTMG	MO	Noah	No	MYJ
UCM	RRTMG	RRTMG	MO	Noah	UCM	MYJ
BEP	RRTMG	RRTMG	MO	Noah	BEP	MYJ
MYJ-BULK	RRTMG	RRTMG	MO	Noah	No	MYJ
YSU-BULK	RRTMG	RRTMG	MO	Noah	No	YSU
MYJ-UCM	RRTMG	RRTMG	MO	Noah	UCM	MYJ
YSU-UCM	RRTMG	RRTMG	MO	Noah	UCM	YSU
MYJ-BEP	RRTMG	RRTMG	MO	Noah	BEP	MYJ
BOULAC-BEP	RRTMG	RRTMG	MO	Noah	BEP	Boulac
NOAH	RRTMG	RRTMG	MO	Noah	BEP	Boulac
NOAH-MP	RRTMG	RRTMG	MO	Noah-MP	BEP	Boulac

^a LW= longwave radiation; SW= shortwave radiation; SL= surface layer; LS= land surface; URB= urban canopy; BL= boundary layer; RRTMG= rapid radiative transfer model for GCMs scheme; MO= Monin–Obukhov scheme; UCM= single-layer urban canopy scheme; BEP= multi-layer urban canopy scheme; MYJ= Mellor–Yamada–Janjic scheme; YSU= Yonsei University scheme; Boulac= Bougeault and Lacarrere scheme.

WRF provides several urban canopy schemes options, the UCM and BEP has been chosen in this study and its structure diagram is shown in Figure3.1. The UCM is a single urban canopy layer model used to consider the effects of urban geometry on the surface energy balance and wind shear for urban regions (Kusaka et al., 2001; Kusaka et al., 2004). This model includes shadows from buildings; canyon orientation; the diurnal variation in the azimuth angle; the reflection of short and long wave radiation; wind profiles in the canopy layer; anthropogenic heating associated with energy consumption by human activities; and multi-layer heat transfer equations for roof, wall, and road surfaces. The BEP is the multilayer canopy layer scheme. This scheme considers the sub-grid wall, roof, and road effects on radiation and fluxes but does not include the energy exchange between the inside and outside of buildings.

The MYJ PBL scheme uses the 1.5-order turbulence closure model of Mellor and Yamada (Mellor et al., 1982) to represent turbulence above the surface layer (Janjic et al., 1990; Janjic et al., 2002). The MYJ scheme determines eddy viscosity K -coefficients from prognostically calculated turbulent kinetic energy. The YSU PBL scheme is a first-order non-local scheme that uses a parabolic K -profile in an unstable mixed layer with the addition of an explicit term to treat the entrainment layer at the top of the PBL (Tyagi et al., 2018). Hong et al. enhanced mixing in the stable boundary layer by increasing the critical Bulk Richardson number from zero to 0.25. The Boulac PBL scheme was developed by Bougeault and Lacarrère (Bougeault et al., 1989) and is also a TKE prediction scheme and designed to work with a multi-layer urban model.

The Noah-mp land surface model (Niu et al., 2011) is the successor of the Noah model (Chen et al., 1996; Chen and Dudhia, 2001). There are multiple options for land-atmosphere interaction processes in Noah-mp, which users can select (Barlage et al., 2015). These options include a variety of formulations of processes such as stomatal conductance, runoff generation, snow and soil parameterizations, and radiative transfer in the canopy.

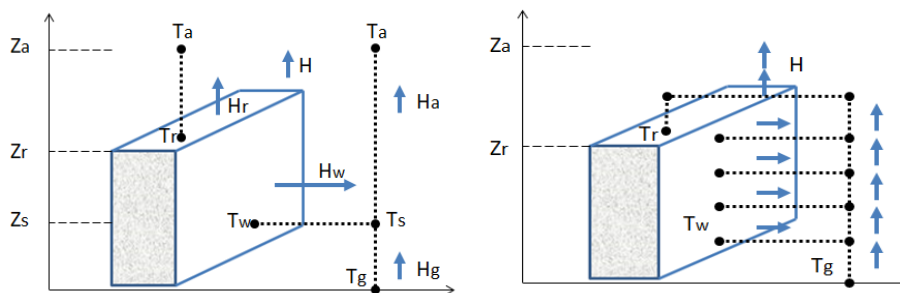


Figure 3.1 The structure diagram of UCM (left) and BEP (right) urban canopy scheme. T_a : Atmospheric temperature at Z_a meters height; T_g : Pavement temperature; H : Sensible heat exchange; T_r : Temperature of the roof; T_w : Temperature of the wall; T_g : Temperature of the street; T_s : Atmospheric temperature at Z_s meters height; H_a : Sensible heat flux from street canyon to atmosphere; H_w : Sensible heat flux from wall to street canyon; H_g : Sensible heat flux from road to street canyon; H_r : Sensible heat flux from roof to atmosphere.

3.2.2 Description of the CHIMERE Model

The chemistry transport model (CTM) CHIMERE (Version 2013) (Menut et al., 2013) is used for air quality modeling in the present study. CHIMERE is a state-of-the-art Eulerian offline CTM model; it requires pre-calculated boundary conditions, emission fluxes, and

meteorological variables. For the studied period, 27th November to 4th December 2016, an 8-day spin-up period is performed for initialization issues. The vertical turbulent mixing in CHIMERE takes place only within the boundary layer, which is calculated by meteorological parameters such as surface temperature and the wind speed issued from the WRF simulation. The first CHIMERE layer is set to 4 m. The vertical dispersion in CHIMERE is mostly controlled by the PBL height and a turbulent flux modeled by a vertical eddy diffusion coefficient (K_z). The horizontal diffusion is neglected in CHIMERE. The PBL height is directly taken from the WRF output and capped at a minimal value of 20m to avoid unrealistic simulations. In CHIMERE, the K_z is calculated using the parameterization of Troen and Mahrt (1986) in Equation (3.1):

$$K_z = kw_s z \left(1 - \frac{z}{h}\right)^2 \quad \#(3.1)$$

where k is the von Karman constant set to 0.41, z is the altitude, h is the boundary layer height, and w_s is the vertical scale given by the similarity formulae.

The emissions of pollutants include several different gaseous and aerosol species. Those emissions can be split into four parts: anthropogenic emissions, biogenetic emissions, mineral dust emissions, and fire emissions. The anthropogenic emissions play a critical role in the CTM model, since they include all human activities, especially in megacities, and they are the only source we can reduce. For Europe region studies, anthropogenic emissions of gases and PM are generated with the French National Spatialized Emission Inventory (INS) (Hamaoui-Lague et al., 2014), which is updated every six months. Biogenic emissions are estimated with the Model of Emissions and Gases and Aerosols from Nature (MEGAN). Mineral dust emissions are parameterized by Menut et al (2013). The resolution INS emission inventory is approximately 1×1 km, and the spatial resolutions of the emission data are recomputed from the INS emission inventory for each domain. Driven by those input data, CHIMERE provides the hourly concentrations of tens of species at a regional scale; detailed descriptions of the model can be found in several previous studies (Bessagnet et al., 2004; Menut et al., 2012; Bessagnet et al., 2017; Mailler et al., 2017). The aerosol module accounts for both inorganic and organic species, such as sulfate, nitrate, ammonium, primary organic matter, element carbon, secondary organic aerosol, sea salt, dust, and water. The aerosol size is assuming discrete aerosol size sections and that the particles are internally mixed. Nine diameter bins, from 10nm to 10 μ m, with 5 bins below 1 μ m, are used (Couvidat et al., 2018).

3.2.3 Domains Setup and Observations Data

In order to calculate realistic meteorological input variables and pollutant concentrations, the system is configured with four nested-grid domains (Figure3.2) over Europe, France, the north of France, and Ile-de-France, with cell sizes of 45 (d01), 15 (d02), 5 (d03), and 1.67km (d04), respectively. The finest grid domain (d04) used has 83×77 grid points and covers the whole Ile-de-France region, including urban, sub-urban, and rural areas. The WRF simulation is discretized vertically on 52 vertical levels from the surface to the top (50hPa), with 20 levels below 1000m and the lowest level at 2m. In order to take full advantage of the physical parameterizations, the CHIMERE simulation is performed with the same horizontal domains as the WRF; the 52 vertical levels from the WRF simulation are projected onto 20 levels in CHIMERE. The ground layer of the CHIMERE domains is at 999.5hPa from about 4m up to over 5000m, with 15 levels below 1000m. Such a low ground level could effectively reproduce the transport and diffusion of pollutants in a real urban environment.

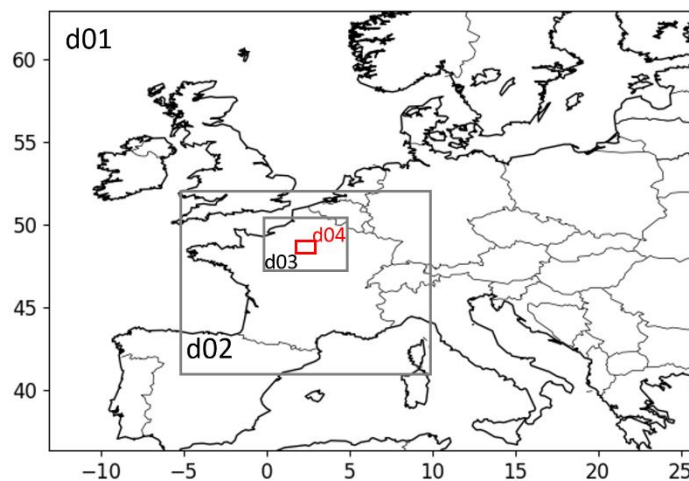


Figure3.2 Four nested domains—from d01, the largest one, at a low resolution to d04, the finest one, at a high resolution.

Two types of observation data are used in the present study: (i) three meteorological observation stations operated by METEO FRANCE and SIRTA were used to evaluate the simulated surface meteorological variables from the model; and (ii) the hourly surface concentrations of criteria pollutants (NO_2 , $\text{PM}_{2.5}$, and PM_{10}) issued from AIRPARIF, the official Paris air quality network. The location of the three meteorological observation stations (Montsouris, Roissy, Sirta) and the four air quality monitoring stations can be found in Figure3.3; they are urban or sub-urban background stations. The FR04143 air quality monitoring station is located in the city center. “Roissy” is a synoptic station of the Paris

international Airport; “Montsouris” is an historical meteorological station located within Paris, operating since 1869; “Sirta” is a recent station located in a suburban environment.

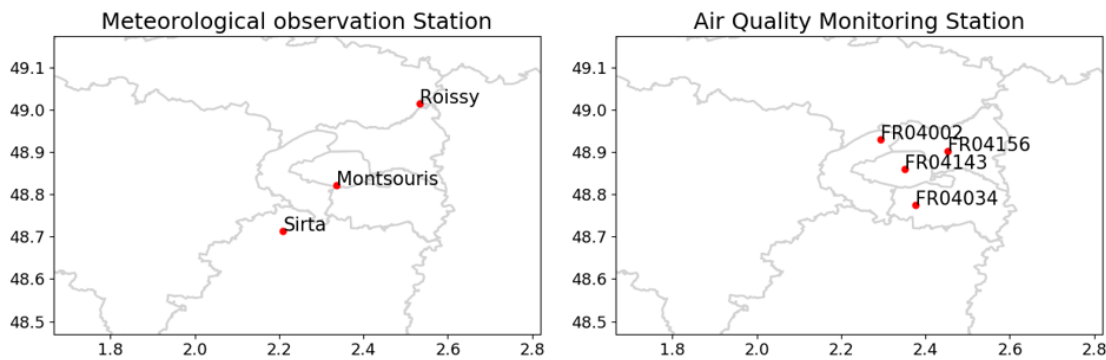


Figure 3.3 Maps of the meteorological and air quality monitoring stations.

3.3. Results and Discussions

3.3.1 Urban Parameters and Nudging Tests

The urban canopy model in the WRF simulation affects the modeling of several important meteorological variables for air quality issues (e.g., 10m wind speed W10, 2m surface temperature T2, and PBL height). It changes the vertical distribution of atmospheric pollutants by modifying the boundary layer height and mixing. Geometric and thermal parameters, including anthropogenic heat, thermal conductivities, and heat capacity, have a significant effect on the transfer of momentum between the atmosphere and urban surface (Kim et al., 2015). However, the representativeness of these parameters aggregated over a CTM grid cell remains highly uncertain, especially with a limited number of urban land-use types. The urban parameters (Table S1) used here are based on a previous study in Paris region (Allen et al., 2010; Kim et al., 2013) and default urban parameterization (URBAN-PAM). The TBL tables in the WRF code are defined as URBAN-PAM1 and URBAN-PAM2, respectively. The RRTMG shortwave and longwave radiation scheme, MO similarity surface layer scheme, Noah land surface model, BEP urban canopy model, and MYJ boundary layer scheme are used for all simulations in this section. Figure 3.4 presents the time series of hourly-averaged T2 and W10 at Sirta station. The results show that simply modifying the values of the parameters has a strong impact on the outputs. The T2 presents a more positive correlation (0.86 than 0.81) in URBAN-PAM1 than in URBAN-PAM2, while the W10 has a more negative bias (-1.51m/s than -1.42m/s) in URBAN-PAM1 than in

URBAN-PAM2. A weak spectral nudging above the boundary layer for all the domains is also tested in this part.

Figure3.5 indicates that the spectral nudging technique is effective in improving the model skills. The performance benefits in Paris from the assimilation of meteorological data at Roissy airport in the global meteorological fields. Thus, URBAN-PAM1 and spectral nudging are used for all our sensitivity tests, which are discussed in the following sections.

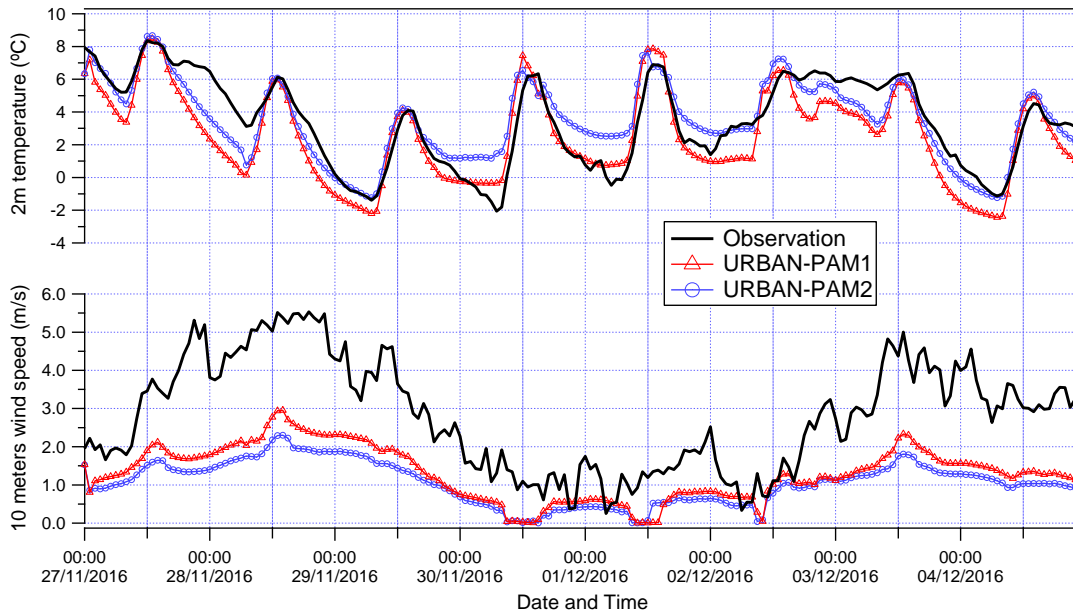


Figure3.4 Time series of 2m temperature and 10m wind speed at Sirta station.

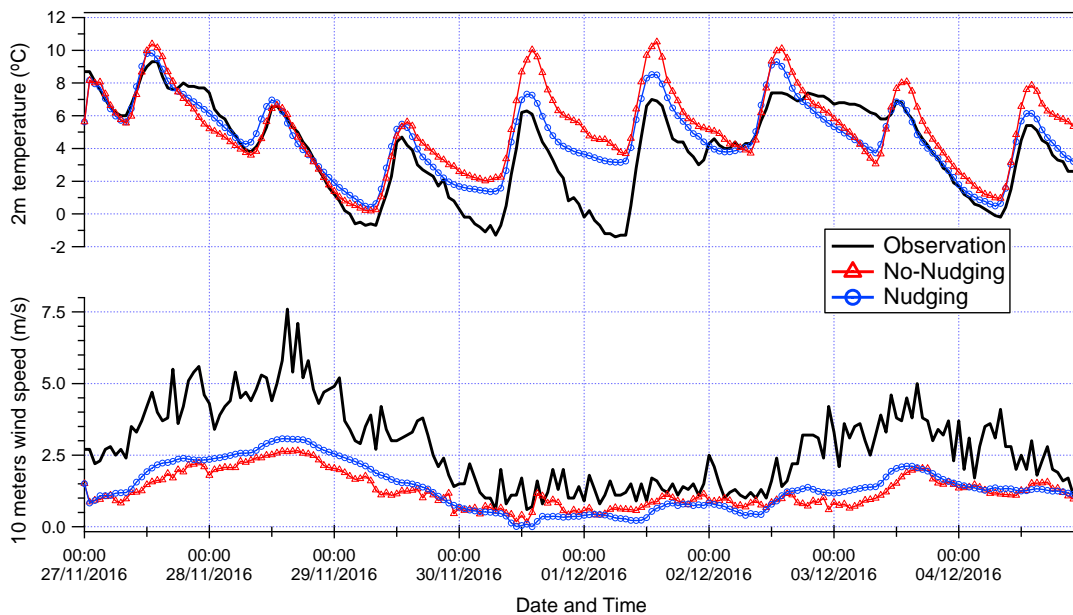


Figure3.5 Time series of 2m temperature and 10m wind speed at Montsouris station.

3.3.2 Impact of the Urban Canopy Model

3.3.2.1. Ground Meteorological Variables

The RRTMG shortwave and longwave radiation schemes, the MO similarity surface layer scheme, and the Noah land surface model are used for all the simulations in this section. The whole period (27th November to 4th December 2016) is divided into two periods: a pollution episode (PE) from 30th November to 2nd December; and other days than the PE, which are defined as regular days (RD). No rainfall occurred over both then PE and the RD. Figure3.6 presents the maps of averaged T2 simulated based on the Bulk, UCM, and BEP schemes in this period. All the schemes show a higher T2 in the urban region than the rural, and the BEP scheme displays the strongest UHI effect in the urban region, which gives a positive bias of up to 1 °C compared to the other two schemes. The Bulk and BEP schemes perform similarly in rural areas and display a negative bias (1–3 °C by Bulk and 1–4 °C by BEP) compared with urban areas, but the UCM scheme gives the highest T2 in rural areas, displaying a negative bias of about 0.5–1 °C compared with urban regions. A possible reason could be the overestimation of surface heat flux (SHF) in the rural areas. Figure3.7 presents the averaged SHF in this period. The Bulk and BEP schemes display obvious differences between urban and rural regions, with a negative bias (around -25W/m^2 to -35W/m^2) in rural compared to urban areas. The UCM scheme just produces a negative bias of -10W/m^2 and -15W/m^2 , respectively, in rural and urban areas, which could give an explanation of the overestimation of T2 in rural areas.

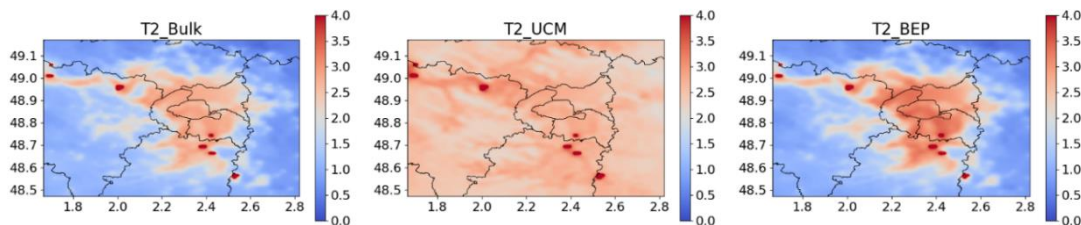


Figure3.6 Maps of the mean 2m temperature (°C) over the period from 27th November to 4th December.

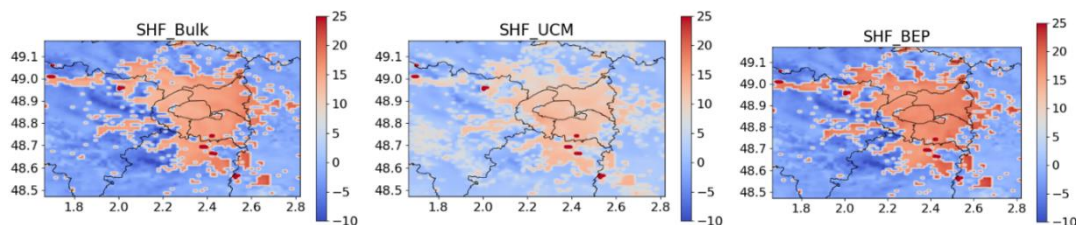


Figure3.7 Maps of the mean surface heat flux (W/m^2) over the period from 27th November to 4th December.

Results at the three meteorological stations are compared with the observations to evaluate the canopy scheme's performance. Figure 3.8 presents the time series of hourly-averaged T2 during the whole period. The observed T2 varies between $-1.4\text{ }^{\circ}\text{C}$ and $9.3\text{ }^{\circ}\text{C}$, $-3.9\text{ }^{\circ}\text{C}$ and $7.8\text{ }^{\circ}\text{C}$, and $-2.1\text{ }^{\circ}\text{C}$ to $8.4\text{ }^{\circ}\text{C}$, with an average of $4.0\text{ }^{\circ}\text{C}$, $2.6\text{ }^{\circ}\text{C}$, and $4.9\text{ }^{\circ}\text{C}$ at Montsouris, Roissy, and Sirta stations, respectively. Compared with the observations, all three schemes tended to underestimate the T2 during the period 16:00 pm–10:00 am UTC on the 27th and 28th for all stations, while higher positive values were observed around midnight of the 1st December for Montsouris and Roissy stations, especially at Roissy, with a positive bias from $1.8\text{ }^{\circ}\text{C}$ to $4.9\text{ }^{\circ}\text{C}$ during the PE. The BEP scheme simulates relatively higher T2 at PE for all the stations because the BEP scheme simulates a stronger UHI than the other two schemes. All the schemes have the best performance at the Sirta site. Compared with the observations from three stations, the differences in the modelled T2 are minimal between three stations during the PE. However, there are significant differences in the observed T2 between the stations. For example, the minimum observed T2 are $-1.4\text{ }^{\circ}\text{C}$, $-3.9\text{ }^{\circ}\text{C}$, and $-0.3\text{ }^{\circ}\text{C}$ during the midnight of 1st December at Montsouris, Roissy, and Sirta stations, respectively. A possible reason could be the use of a single urban category in our WRF simulations, but in the real environment Montsouris and Sirta stations are closer to commercial and residential areas and Roissy is a synoptic station close to the airport, which could be assimilated as a rural environment with a weaker UHI effect, especially during nighttime.

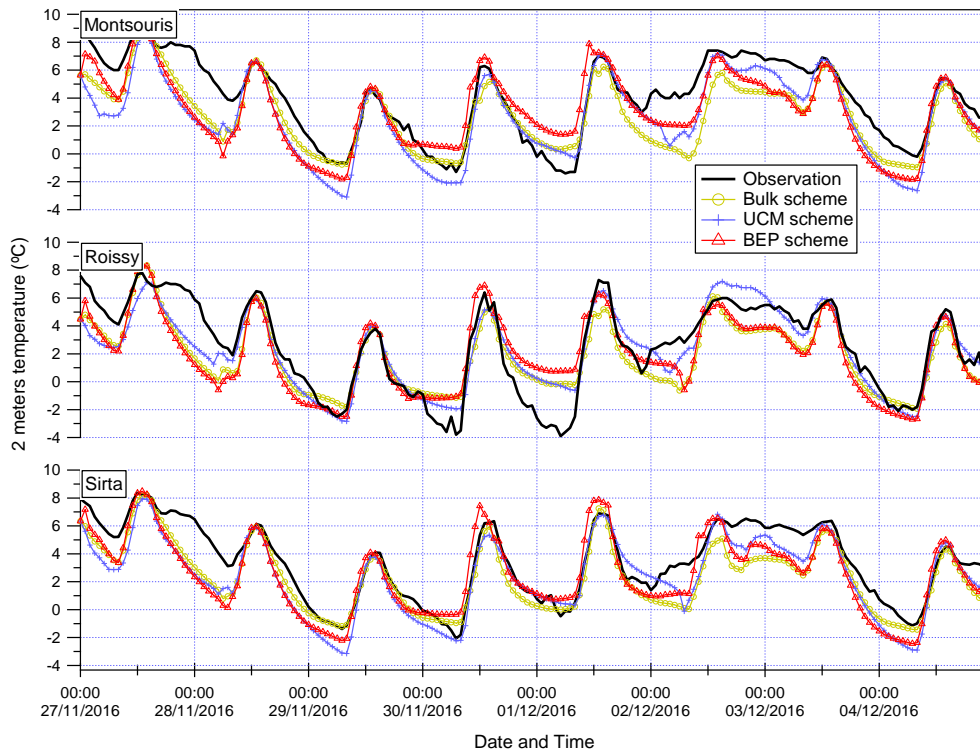


Figure 3.8 Time series of 2m temperature (°C) between observations and different urban schemes at Montsouris, Roissy, and Sirta stations.

Figure 3.9 shows the maps of the averaged W10 simulated for the Bulk, UCM, and BEP schemes in this period. All the schemes give a higher surface wind speed in rural areas than in urban regions; the Bulk scheme shows the weakest gradient from urban to rural areas, with a negative bias for 0.51m/s; UCM gives a relative higher negative bias than Bulk from 1m/s to 2m/s; and the BEP scheme had an obviously strongest impact from cities, displaying a negative bias around 3.5m/s. The comparison between the observations and models for W10 are displayed in Figure 3.10. The observed W10 varied between 0.6m/s to 7.6m/s, 0.1m/s to 9.4m/s, and 0.2m/s to 5.5m/s, with an average of 2.3m/s, 1.5m/s, and 2.8m/s in three meteorological observation stations (Montsouris, Roissy, Sirta), respectively. Both the observed and modelled W10 display much lower values during the PE than the RD. In contrast with the T2, the W10 does not display remarkable differences between stations. The BEP scheme tends to produce the lowest W10 throughout the whole period for all the stations. Bulk and UCM performed well for both the PE and RD. A possible reason could be due to the roughness length, which is not directly dependent on urban morphology for the UCM scheme, while the momentum sinks and drag force estimated by the BEP scheme depend on urban morphology in this study. Low wind speed leads to weak natural circulation and the accumulation of heat in the lower urban boundary layer, which in turn enhances the warming of the urban area (Wu et al., 2017). This would explain why BEP has a relative higher T2

simulation than the other schemes during the PE. This sensitivity test indicates that more realistic urban morphologies are needed to improve the model performance, because the parameters used in the urban canopy scheme (e.g., albedo, heat capacity, and roughness length) strongly influence the surface energy balance and heat absorption.

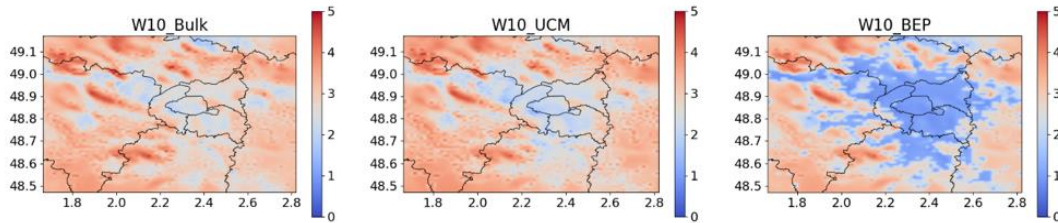


Figure 3.9 Maps of the mean 10m wind speed (m/s) over the period from 27th November to 4th December.

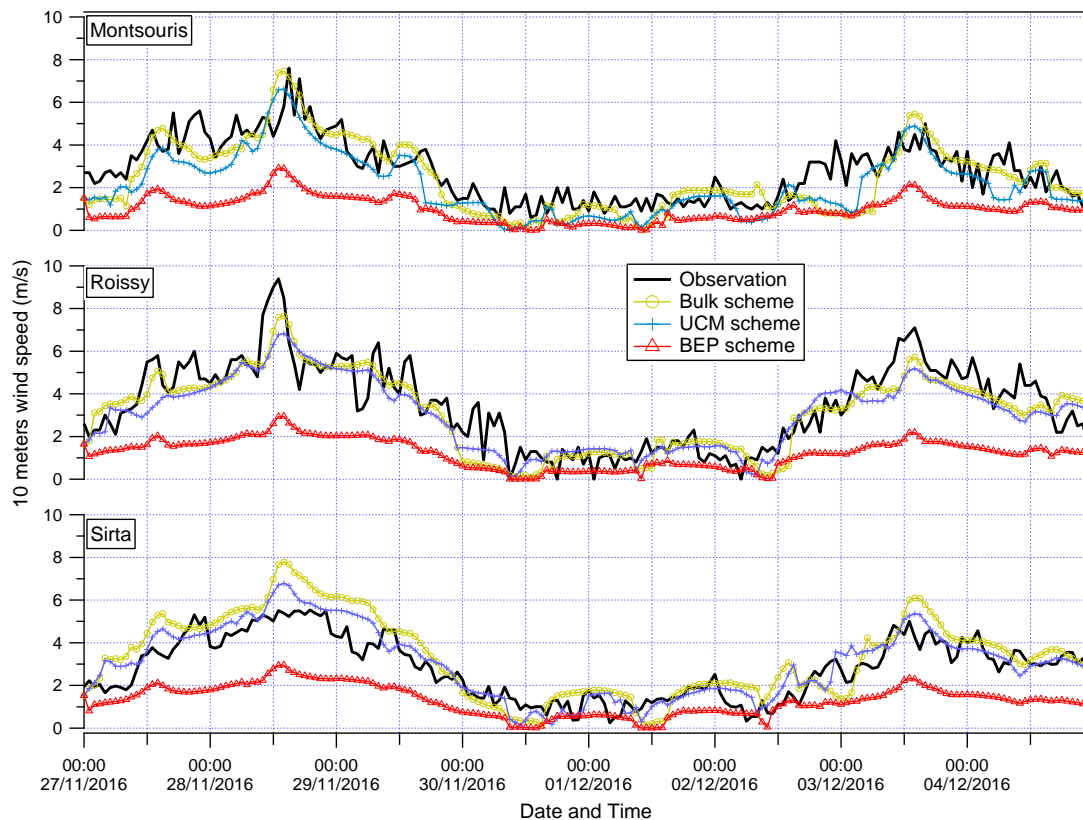


Figure 3.10 Comparison of the time series of 10 m wind speed (m/s) between the observations and different urban schemes at Montsouris, Roissy and Sirta stations.

3.3.2.2. Air Quality Modeling

In this study, NO_2 , $\text{PM}_{2.5}$, and PM_{10} concentrations are used to evaluate the impact of physics parameterizations on air quality simulations. NO_2 , which comes mainly from automobile exhaust emissions in cities, is selected to be an indicator of local pollution. Comparing the evolution and spatial patterns of NO_2 versus the $\text{PM}_{2.5}$ and PM_{10} gives an

indication of the local contribution during this episode. Figure 3.11 presents the differences in pollutants distribution between each canopy scheme. The results show that, compared to the Bulk scheme, the pollutant concentrations from the BEP scheme were lower in the city center, but displayed an opposite behavior compared to the UCM scheme. The UCM scheme displayed higher pollutant concentrations in the urban area and lower pollutant concentrations in rural areas. Figure 3.12 presents the time series of NO_2 mass concentrations for all the experiments compared to the observations for the four stations (the time series of $\text{PM}_{2.5}$ and PM_{10} mass concentrations can be found in Annex A Figure S1). The average biases of the four stations are given in Table 3.2, and the time series of the biases are displayed in Figure S2. The results show that the BEP scheme gives the best performance for almost the whole period, especially during the PE. All the schemes can effectively predict air pollution during the RD, but they usually overestimate pollutant concentrations for all the stations during the PE; all the schemes had their worst performance in NO_2 prediction, which means that the canopy schemes do not simulate well the emission of local air pollution. Figure 3.13 gives the vertical diffusion coefficient at daytime and nighttime in the RD and PE. The Bulk scheme has the highest vertical diffusion rate among the three schemes during the RD. Figure 3.14 presents the vertical profile of the NO_2 and $\text{PM}_{2.5}$ mass concentrations under 200m; both NO_2 and $\text{PM}_{2.5}$ show the lowest vertical mass concentrations at low layers by the Bulk scheme and the highest vertical mass concentrations by the BEP scheme during the RD, which agrees with the vertical profile of K_z in CHIMERE. At 06:00 UTC on 30th November, the K_z displays very low values at ground layers for all three schemes but rises rapidly in the BEP scheme from the third layer. Figure 3.14c also presents high pollutant concentrations at the ground layer for all three schemes but decreases rapidly in the BEP scheme from the third layer. Looking at the NO_2 concentrations, there is clearly an added value of using a low first model layer in the model to enhance the concentrations close to emission sources related to ground sources such as road traffic. In the models, it is more common to use a first layer of about 20m to 50m (Toll et al., 2000; Baklanov et al., 2008).

Figure S3 presents the hourly time series of NO_2 as an average of all the air quality monitoring stations between the observations and simulations, with first layers of about 4m, 18m, and 40m (based on the best physics parameterizations in this study). An extremely low vertical diffusion rate leads to high concentrations of pollutants, which is one reason for the strong overestimations at the surface layers at this time. In general, the BEP scheme has the best performance among the three schemes, but all the schemes strongly overestimate the

concentrations at the beginning of the PE, especially the UCM scheme. A low near-ground wind speed usually indicates low diffusion rates, which means the BEP scheme involves higher pollutant concentrations than for the other two schemes, but our study shows the pollutants concentrations is not found to be positively correlated with the W10. A possible explanation could be the underestimation of PBL height, which leads to a low diffusion rate at this period; a detail discussion about the impact of the PBL height is in the next section.

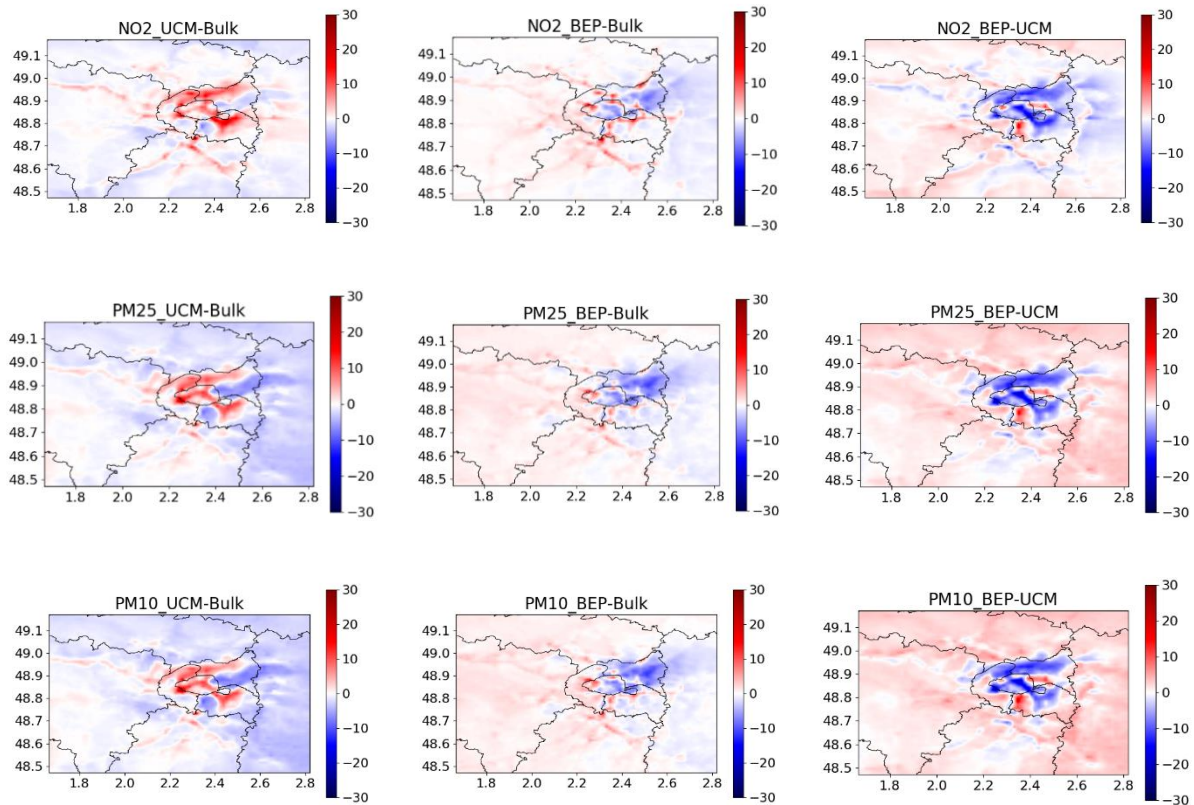


Figure 3.11 The differences in the daily averaged NO_2 ($\mu\text{g}/\text{m}^3$), $\text{PM}_{2.5}$ ($\mu\text{g}/\text{m}^3$), and PM_{10} ($\mu\text{g}/\text{m}^3$) between different schemes from 27th November to 4th December 2016.

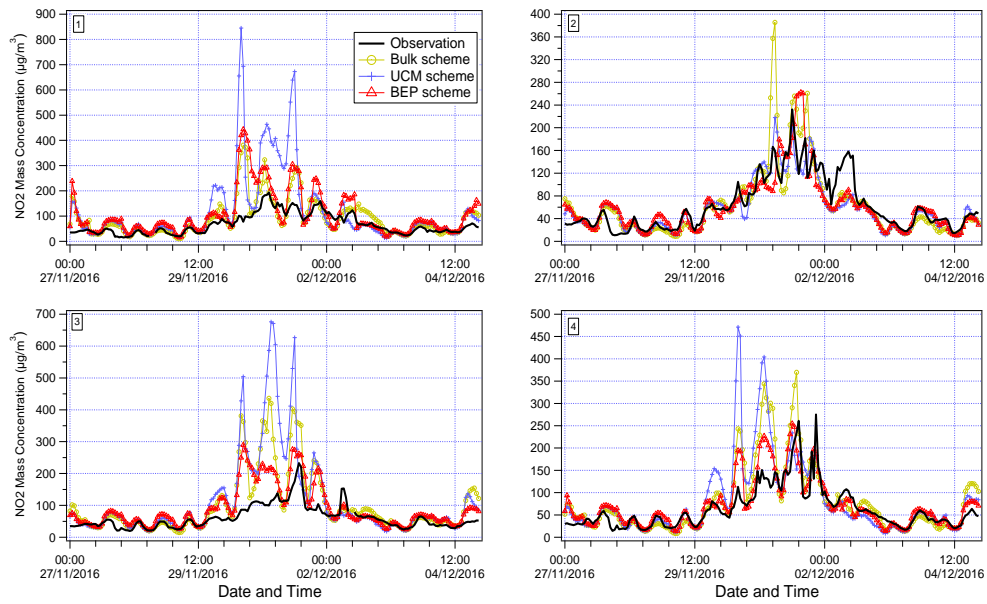


Figure 3.12 Time series of NO_2 mass concentrations ($\mu\text{g}/\text{m}^3$). No 1, 2, 3, 4 represent station FR04002, FR04034, FR04143, and FR04156, respectively.

Table 3.2 Statistics of surface pollutants: mean bias between the simulations and observations of NO_2 , $\text{PM}_{2.5}$, and PM_{10} during Whole Period (WP) and Pollution Episode (PE).

	Bulk		UCM		BEP	
	WP	PE	WP	PE	WP	PE
NO_2	21.5	40.9	29.8	62.2	18.4	29.7
$\text{PM}_{2.5}$	21.8	31.4	24.9	37.7	19.1	21.1
PM_{10}	12.6	13.7	15.2	18.9	10.1	4.2

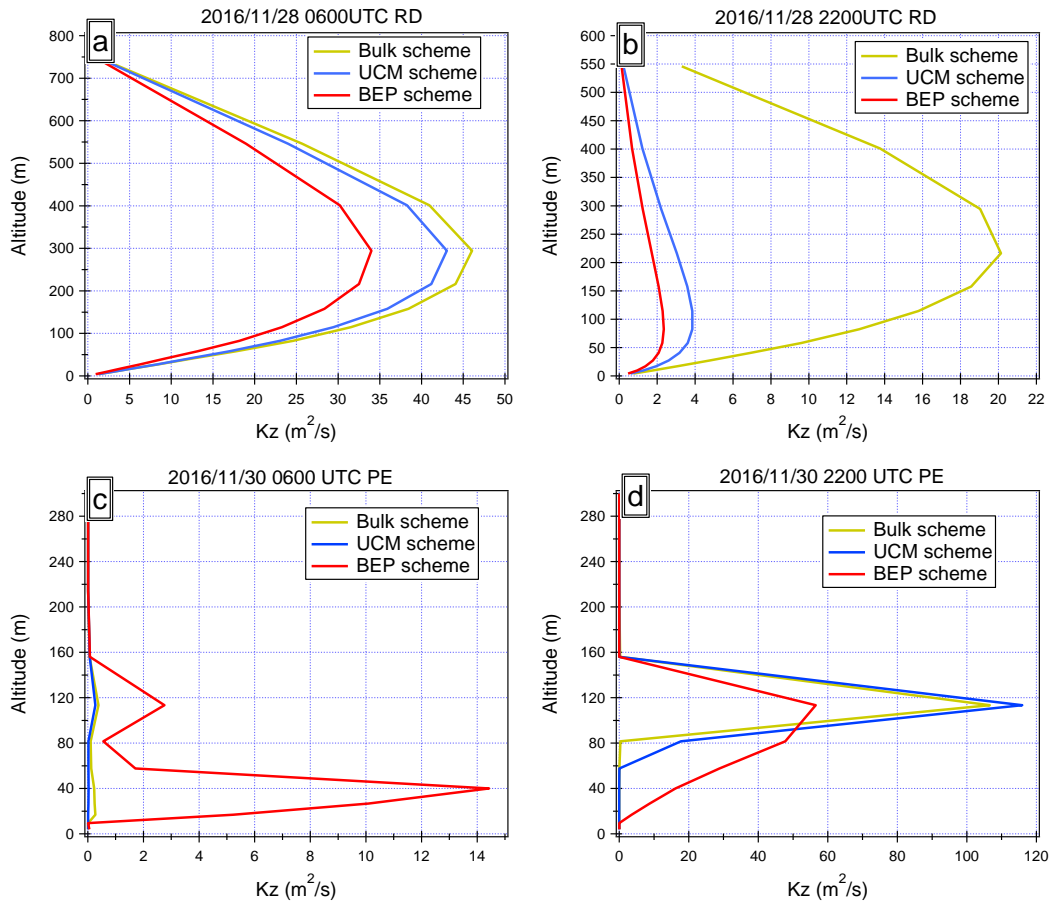


Figure 3.13 Vertical profiles of the CHIMERE K_z extracted at the FR04143 station. The profile is extracted at 06:00 and 22:00 UTC for both Regular Days (RD) and the Particulate Episode (PE).

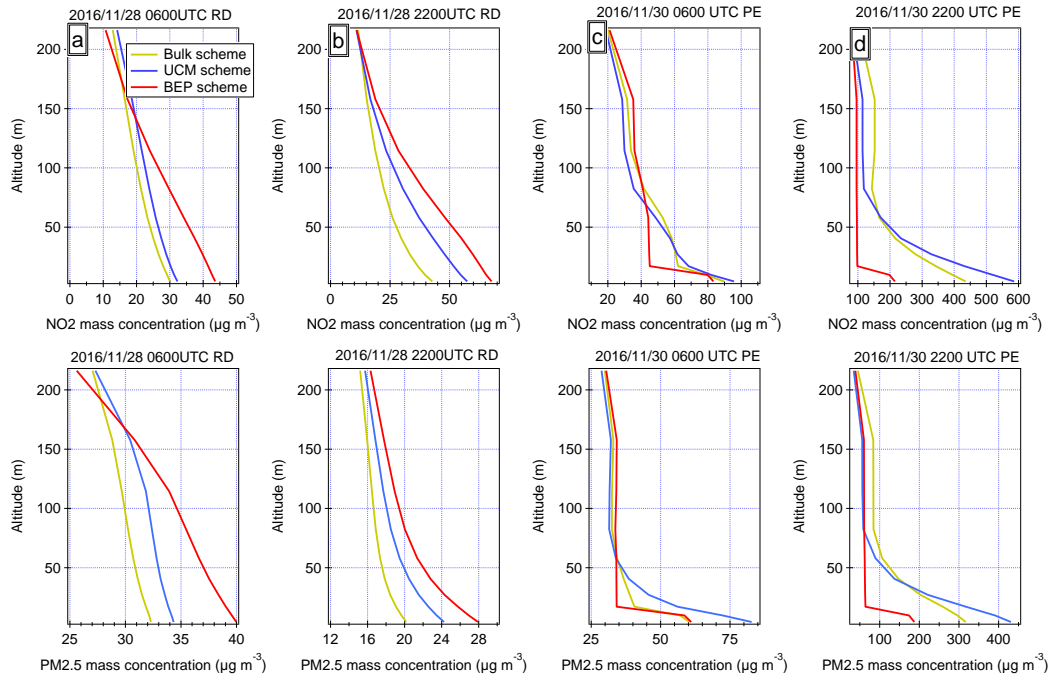


Figure 3.14 Vertical profiles of the NO_2 and $\text{PM}_{2.5}$ mass concentration ($\mu\text{g}/\text{m}^3$) at the FR04143 station. The profiles are extracted at 06:00 and 22:00 UTC for both Regular Days (RD) and the Particulate Episode (PE). Columns (a), (b), (c), and (d) represent the vertical mass NO_2 and $\text{PM}_{2.5}$ concentration of at 28th November 06:00, 28th November 22:00, 30th November 06:00, and 30th November 22:00 UTC, respectively.

3.3.3 Impact of Mixing Boundary Layer Height

3.3.3.1. PBL Height

WRF version 3.9.1 provides 14 options for the PBL scheme, following the approach of LeMoine et al. Briefly, they can be categorized as TKE schemes and non-TKE schemes (LeMone et al., 2006; LeMone et al., 2013). Two TKE-based schemes and one non-TKE-based PBL scheme are selected for these PBL sensitivity simulations. The TKE schemes chosen in this assessment are the MYJ and Boulac schemes, and the non-TKE scheme is the YSU scheme. Unified PBL sensitivities are not possible in this section with the canopy schemes from the previous section, because the BEP urban canopy scheme requires the simultaneous use of a TKE scheme and the Boulac PBL scheme is designed for coupling with the multi-urban canopy model. Regarding the configuration of the canopy models in Section 3.3.2, each canopy scheme will be coupled with two PBL schemes, giving the YSU–Bulk and MYJ–Bulk schemes, the YSU–UCM and MYJ–UCM schemes, and the Boulac–BEP and MYJ–BEP schemes. All the other physics options are the same. For the observed PBL height, we have the complete dataset for Roissy station and the last four days data for Sirta station. Figure 3.15 displays a comparison between the observed Lidar data and the 15

min averaged modeled output of PBL height. Generally, all the PBL schemes systematically underestimate PBL height for the whole time series, especially during the PE and the beginning of RD (from 27th November 00:00 UTC). This explains the strong overestimations of pollutants during the PE in Section 3.3.2 and is consistent with the positive biases of pollutant concentrations at the beginning of the RD in Figure3.11. If we consider the simulation of PBL during the PE, the average observed PBL height was around 110m and is only relatively well reproduced by the Boulac–BEP, scheme even though it still underestimates the PBL height by around 40m on average. The other PBL schemes reach the minimum PBL height (set up to 20m in the model) during the whole PE and strongly underestimate PBL height, especially at night and early in the morning. In general, the Boulac–BEP scheme gives the best performance, and it is the only option which can effectively estimate the evolution of the PBL height during the PE in this sensitivity test. For the other PBL schemes, the agreement between the simulations and observations is poor. MYJ displays the poorest correlation compared to the observed soundings, regardless of other parameter settings.

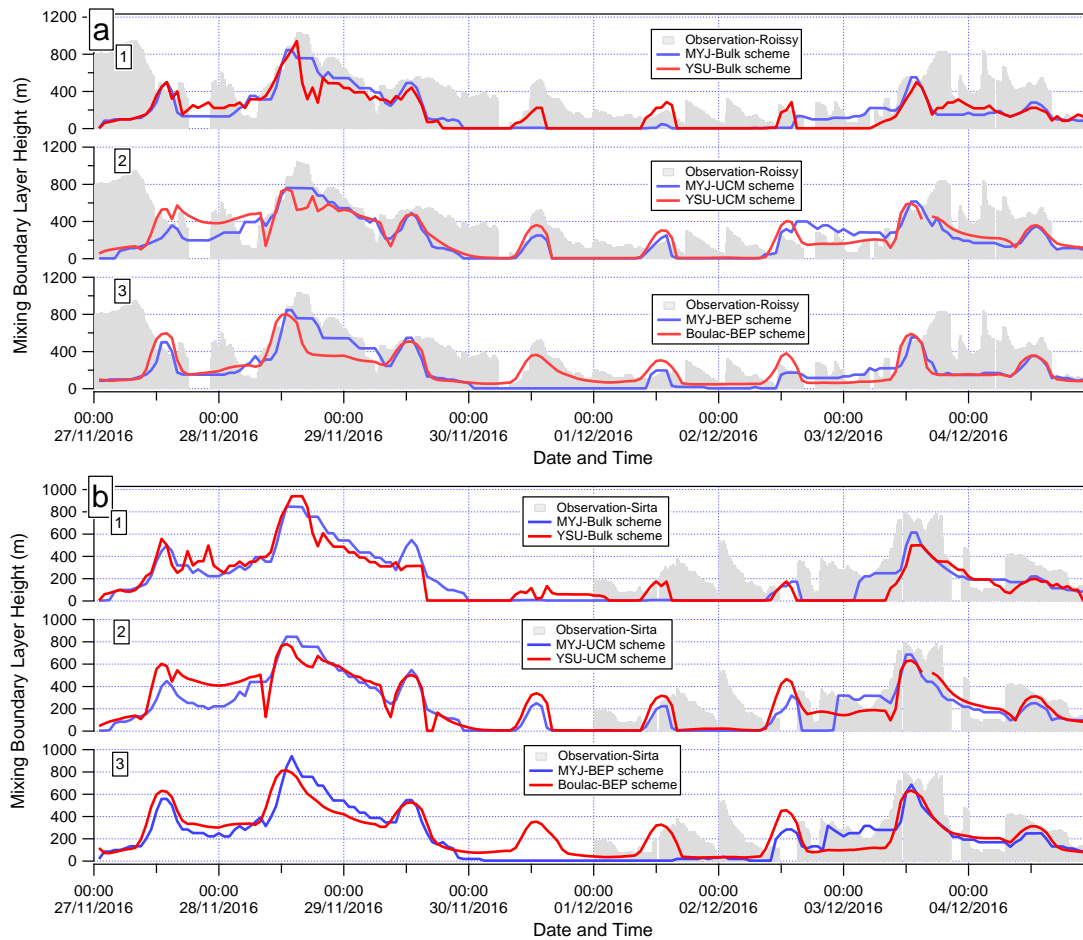


Figure 3.15 Time series of the observed and modelled mixing boundary layer height: (a) and (b) represent Roissy and Sirta station, respectively; 1, 2, and 3 represent each PBL scheme coupled with each urban canopy scheme.

3.3.3.2. Ground Meteorological Variables

A comparison of the performances of various PBL schemes in simulating the surface meteorological variables (T2 and W10) is presented in this section. Figure 3.16 and Figure 3.17 shows the time series of T2 and W10 based on several PBL schemes. The YSU–Bulk and Boulac–BEP have a slight positive bias compared to MYJ, but the YSU–UCM scheme had a cooling effect compared to the MYJ–UCM scheme during the PE. In the MYJ–BEP and Boulac–BEP schemes, it can be observed that the models always underestimate the wind speed compared to the observations in this period. The Boulac–BEP scheme produces a lower W10 than MYJ–BEP throughout the whole period, especially during RD. In contrast, W10 does not show significant differences between the MYJ and YSU schemes coupled with the other two Bulk and UCM canopy models. Table 3.3 summarizes the performances of the models, including the mean bias (MB) and mean linear correlation coefficient (R) of meteorological variables. These schemes display a high correlation which approximately

reproduces the measured trend. The three experiments with the MYJ boundary layer scheme display a negative bias in W10 in Roissy and a negative bias in T2 in both Roissy and Sirta stations. A less negative bias is noticed with the simulations using the Boulac–BEP scheme compared with the others for the whole period, but it still produces a positive bias during nighttime in the PE. The reason could be that the Boulac PBL scheme takes the turbulent exchange affected by complex terrain into account in the calculation of the turbulent diffusion coefficient, leading to a smaller bias in T2 prediction (Li et al., 2006). The Boulac–BEP scheme slightly improves the results with respect to the MYJ–BEP scheme for the W10, but still strongly underestimates by 1.53m/s at Roissy station. The correlation indicates the PBL schemes coupled with the urban canopy schemes (MYJ–UCM, YSU–UCM, MYJ–BEP, and Boulac–BEP) are more accurate than those with no urban canopy scheme (MYJ–Bulk and YSU–Bulk). In contrast to the PBL height results, the model performances for T2 and W10 based on various PBL schemes are mixed. Therefore, it is not straightforward to agree on a definitive best choice for the PBL scheme.

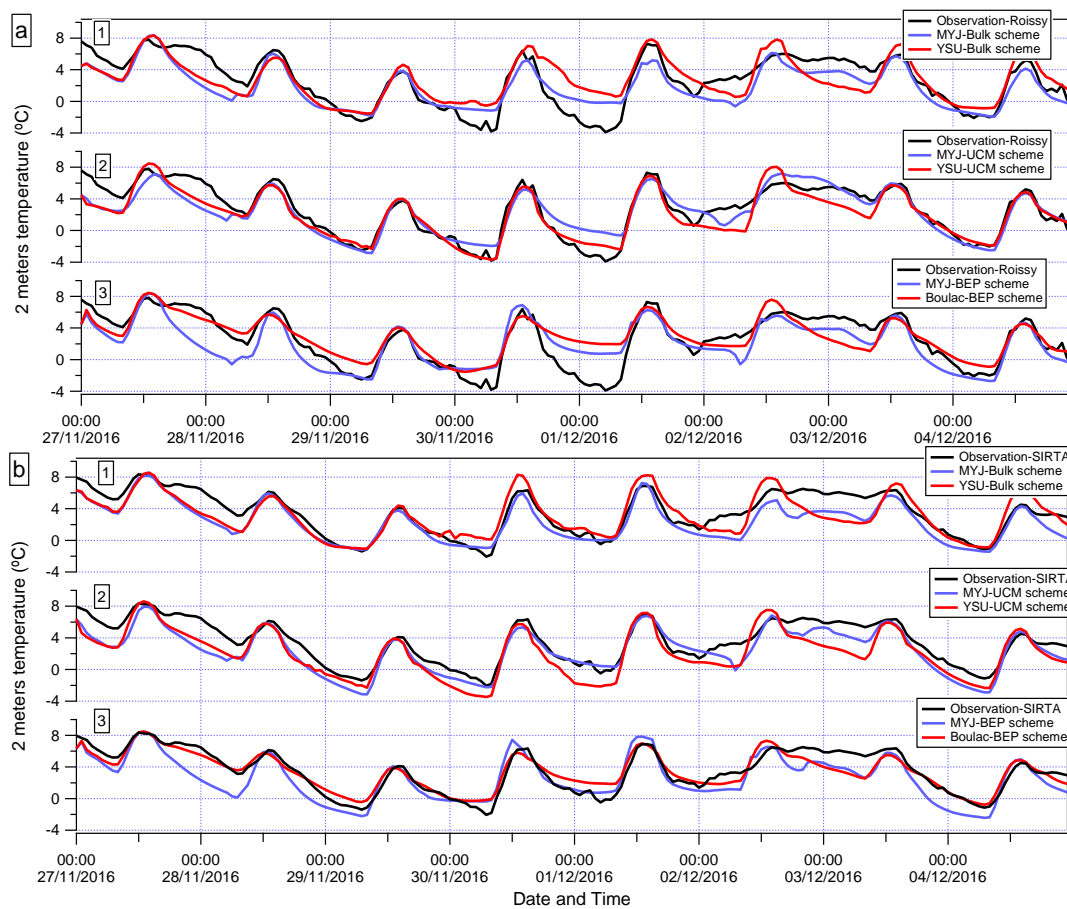


Figure 3.16 Time series between the observed and modelled T2: (a) and (b) represent Roissy and Sirta station, respectively; 1, 2, and 3 represent each PBL scheme coupled with each urban canopy scheme.

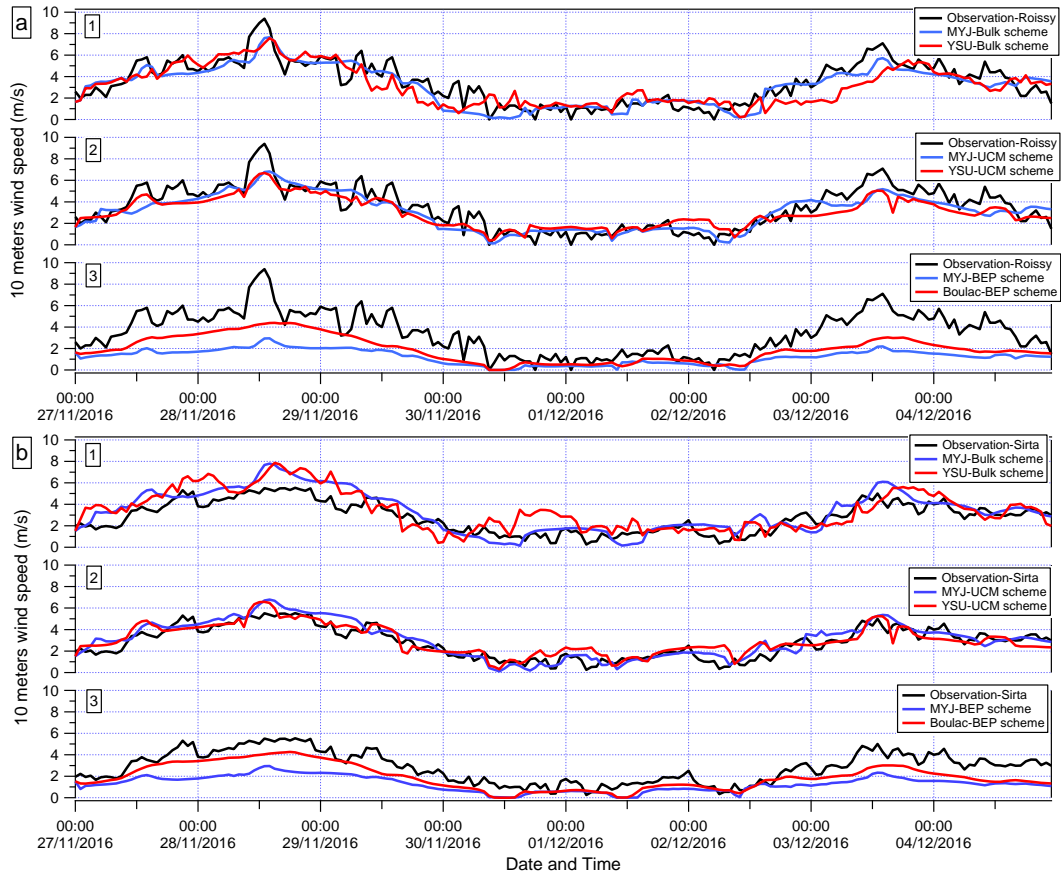


Figure 3.17 Time series between the observed and modelled W10: (a) and (b) represent Roissy and Sirta station, respectively; 1, 2, and 3 represent each PBL scheme coupled with each urban canopy scheme.

Table 3.3 Statistics of surface variables: mean bias (MB) and mean linear correlation coefficient (R) between the simulations and observations of 2 m temperature (T2) and 10 m wind speed (W10) at Roissy and Sirta stations.

	Roissy				Sirta			
	T2		W10		T2		W10	
	MB	R	MB	R	MB	R	MB	R
MYJ-Bulk	-0.69	0.83	-0.29	0.86	-1.13	0.88	0.53	0.84
YSU-Bulk	0.23	0.77	-0.30	0.78	0.20	0.82	0.62	0.74
MYJ-UCM	-0.22	0.90	-0.38	0.87	-1.08	0.90	0.24	0.91
YSU-UCM	-0.51	0.92	-0.46	0.90	-1.31	0.93	0.18	0.88
MYJ-BEP	-0.56	0.82	-2.23	0.89	-0.89	0.86	-1.52	0.90
Boulac-BEP	0.40	0.84	-1.53	0.88	-0.03	0.90	-0.90	0.92

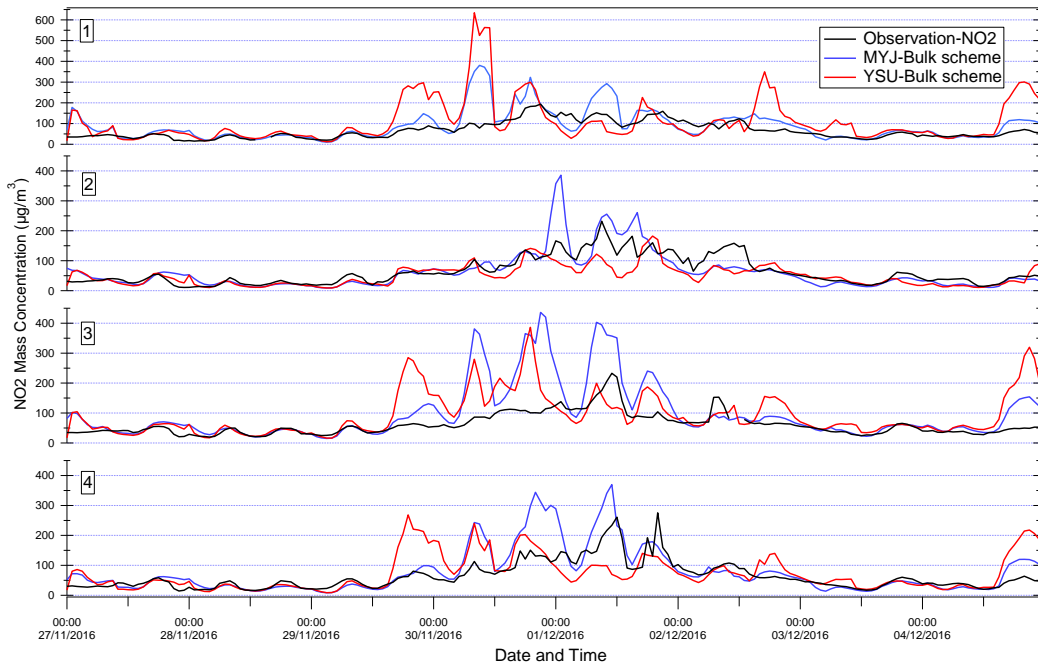
3.3.3.3. Air Quality Simulations

The impacts of the PBL schemes on air quality are analyzed in this section. The time series of the model predictions of the NO₂, PM_{2.5}, PM₁₀ concentrations for all the schemes are compared with the observations (the NO₂ can be found in Figure 3.18; the PM_{2.5} and PM₁₀ can be found in Figures S4 and S5). In general, all the schemes have a better performance for the RD than the PE period, and almost all the schemes strongly overestimate pollutant concentrations at the beginning of the PE, except the Boulac–BEP scheme. The bias between the modelled and observed pollutant concentrations can be found in Figures S6, Figure S7, and Figure S8. All the schemes give a worse performance for NO₂ and PM_{2.5} prediction than for PM₁₀. The PBL height reaches the minimum value at 18:00 UTC on 29th November, with the YSU–Bulk scheme corresponding to an underestimation of 500 m; such a difference creates a large bias in air pollutant concentrations. The same phenomenon occurs for the MYJ–Bulk, MYJ–UCM, YSU–UCM, and MYJ–BEP schemes at 00:00 UTC on 30th November. However, the overestimation of pollutant concentrations does not occur at this time but at 06:00 UTC on 1st December, because this episode is largely influenced by local sources (road traffic and residential heating). On 1st December 2016 at 06:00 UTC (a weekday), the morning rush hour leads to a lag effect in the bias, explaining why all the schemes have their worst performance for the NO₂ and PM_{2.5} predictions. The averaged statistics for the four air quality monitoring stations are summarized in Table 3.4. Figure 3.19 gives the scatterplot between the observed and modelled NO₂; the scatterplot for the PM_{2.5} and PM₁₀ can be found in Figure S9. Overall, the MYJ scheme overestimates the mass concentrations of all pollutants, whatever the selected urban canopy model. The Boulac–BEP scheme has a significantly better performance than other schemes for all the evaluated variables. The YSU–Bulk scheme has the lowest mean bias ($-1.3 \mu\text{g}/\text{m}^3$) in PM₁₀ prediction, but its mean linear correlation coefficients of NO₂, PM_{2.5}, and PM₁₀ were 0.52, 0.40, and 0.53, respectively. The mean biases for the NO₂ and PM_{2.5} prediction were $17.63 \mu\text{g}/\text{m}^3$ and $46.0 \mu\text{g}/\text{m}^3$, respectively. The low correlation for all the analyzed variables, positive biases for NO₂ and PM_{2.5} prediction, and negative bias for PM₁₀ prediction indicate that this scheme under and over-estimates the concentrations simultaneously, which means that the YSU–Bulk scheme cannot be performed effectively for the prediction of short-term PE in urban regions. The Boulac–BEP scheme was better for all the analyzed variables, both in terms of bias and correlation statistics; its mean biases for NO₂, PM_{2.5}, and PM₁₀ prediction were $-5.13 \mu\text{g}/\text{m}^3$,

$1.23 \mu\text{g}/\text{m}^3$, and $-8.63 \mu\text{g}/\text{m}^3$, respectively. This indicates that both the urban canopy and PBL schemes play an important role in the PE forecast for urban regions.

Table 3.4 Statistics of surface variables: mean bias (MB), root mean square error (RMSE), and mean linear correlation coefficient (R) between the simulations and observations of NO₂, PM_{2.5}, PM₁₀.

	NO ₂			PM _{2.5}			PM ₁₀		
	MB	R	RMSE	MB	R	RMSE	MB	R	RMSE
MYJ-Bulk	19.1	0.77	3.40	21.9	0.74	2.37	12.5	0.77	2.39
YSU-Bulk	17.6	0.52	1.28	46.0	0.40	1.12	-1.3	0.53	2.34
MYJ-UCM	29.6	0.73	2.21	24.9	0.60	2.07	15.2	0.64	2.01
YSU-UCM	14.6	0.76	2.03	15.2	0.64	1.88	5.6	0.68	1.93
MYJ-BEP	20.0	0.80	2.35	19.2	0.72	1.91	10.1	0.76	1.93
Boulac-BEP	-5.1	0.79	2.93	1.2	0.74	1.70	-8.6	0.76	1.71



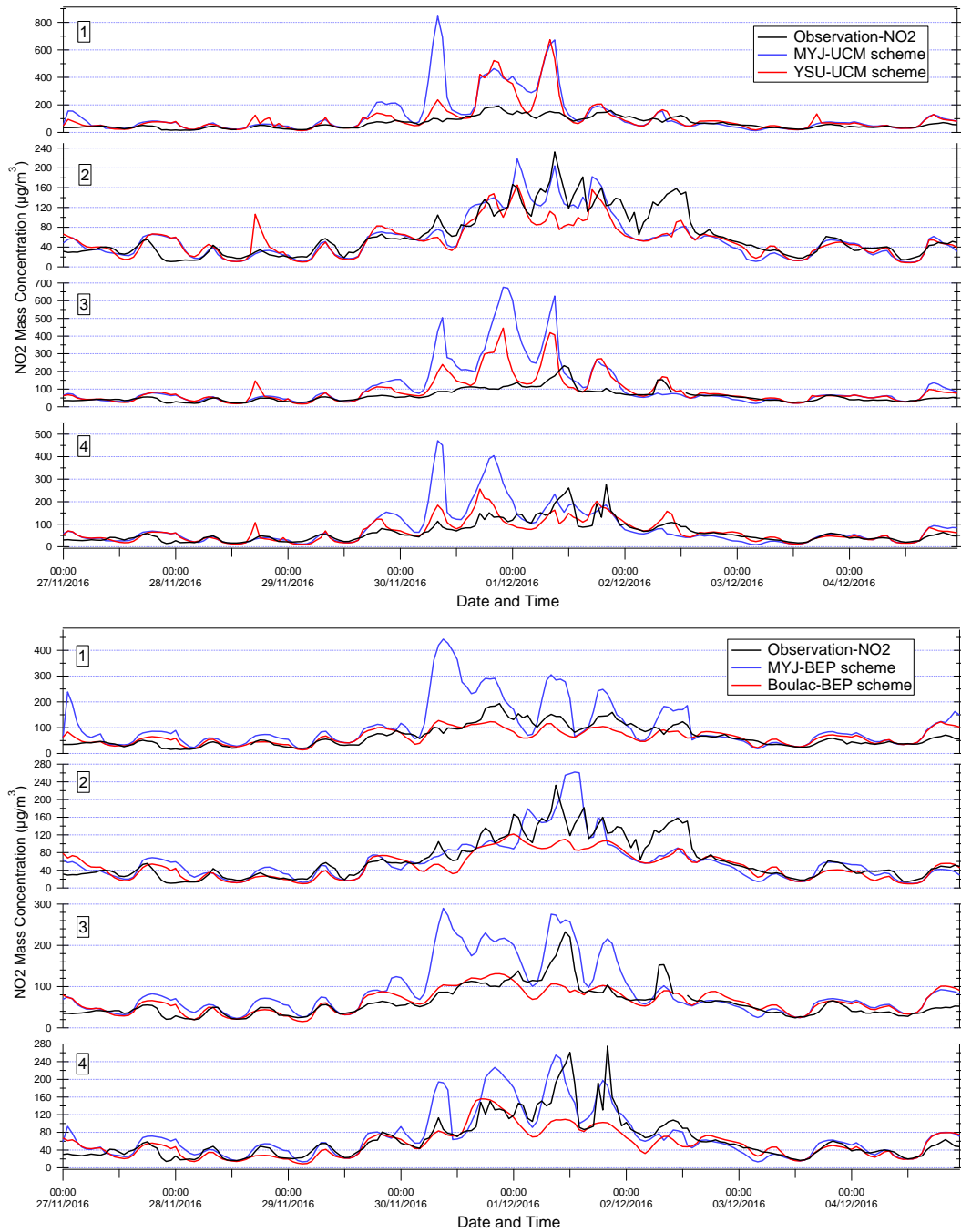


Figure 3.18 Time series of NO₂ mass concentrations: No 1, 2, 3, and 4 represent station FR04002, FR04034, FR04143, and FR04156, respectively.

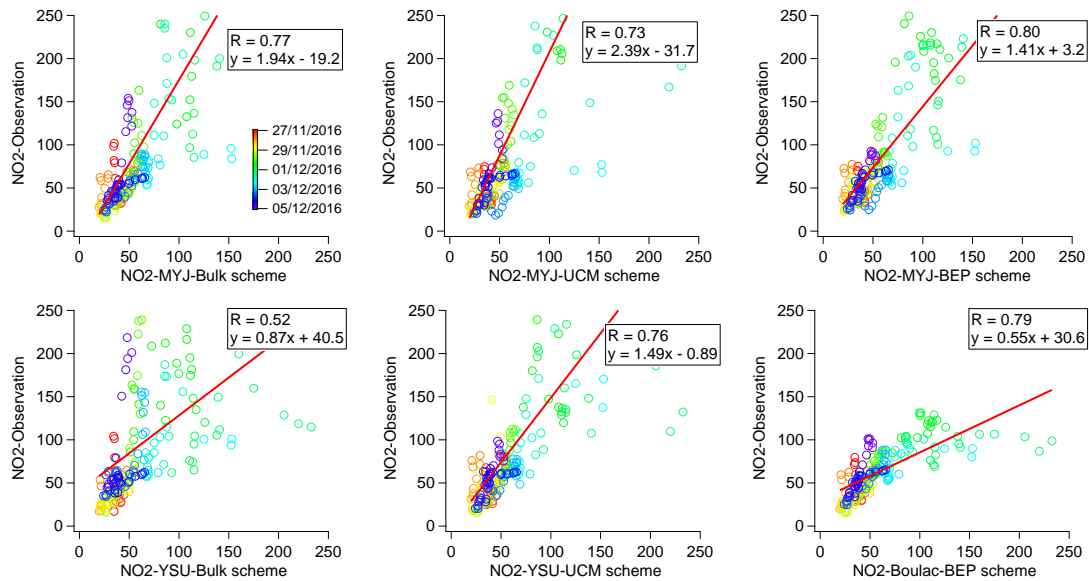


Figure 3.19 Liner fit between the observed and modelled NO₂.

3.3.4 Impact of Land surface model

In order to understand the impact of land surface model (LSM), a widely used Noah LSM scheme (version 3.0) and an advanced LSM model (Noah-mp) are analyzed in this section. Compared with Noah, Noah-mp separating the vegetation canopy from the ground surface which could solve the critical problems such as overestimation of runoff, too dry deep soil, too impermeable frozen soil, and too rapid ablation of snow, etc. Other physical parameterizations were based on the formal study which means BEP urban canopy model and Boulac PBL model (Bou-BEP) are selected in this section.

We evaluated the modelled T₂ and W₁₀ against observations in three stations. As illustrated by Figure 3.20, Noah-mp scheme gives a warmer surface skin temperature compared to the Noah scheme and its improved T₂ simulation in the nighttime during the PE. Some researches (Niu et al., 2011; Salamanca et al., 2018) reported that Noah-mp produces a weaker surface exchange coefficient that Noah scheme leads a higher heating of the land surface during the midday hours.

Modeled mean 10m wind speed across the three stations is shown in Figure 3.21. The results show Noah-mp almost had no effect in the W₁₀. The possible reason is the Noah-mp improve the vegetation canopy from the surface which could be more efficient in vegetated areas through plant stomata and root uptakes of soil water then better account for the surface energy balance. The surface wind speed in urban region mainly influenced by the city clusters and

diffusion conditions, the use of the Noah - mp scheme makes negligible differences in W10 simulation.

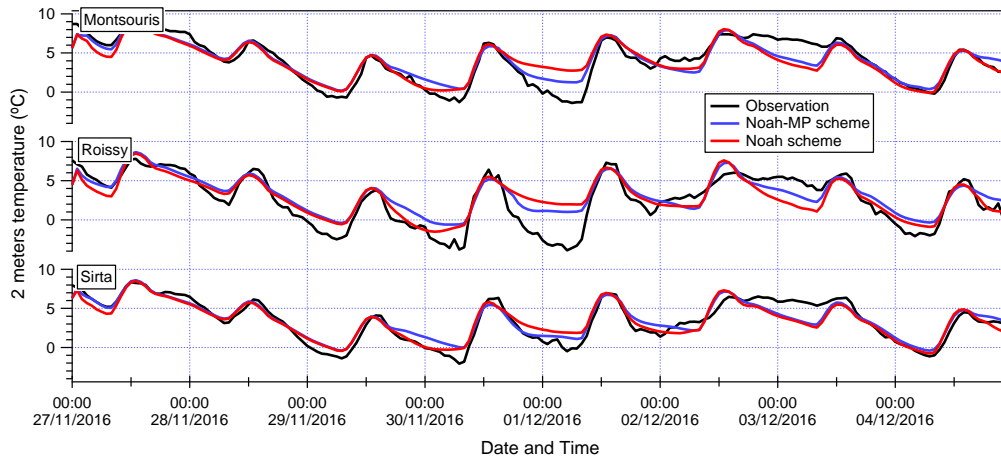


Figure 3.20 Time series of 2m temperature (°C) between observations and different urban schemes at Montsouris, Roissy, and Sirta stations.

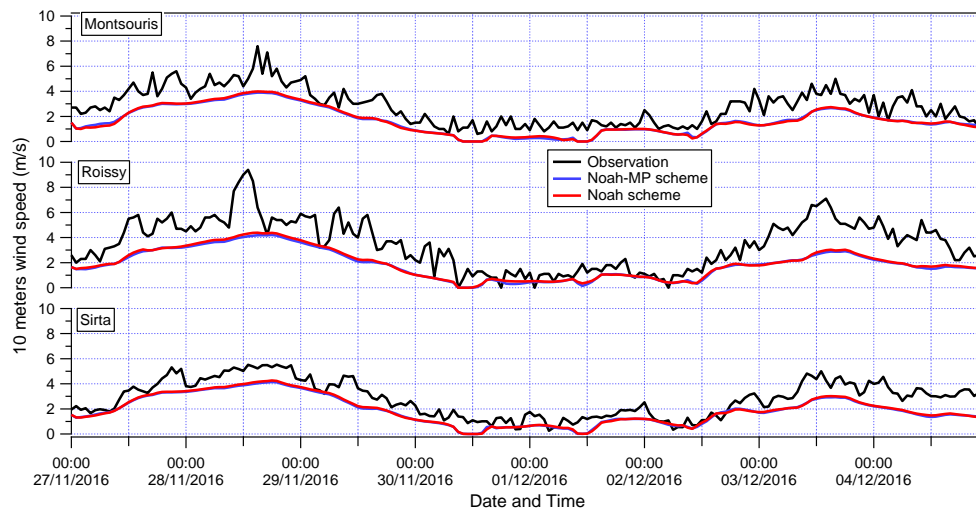


Figure 3.21 Comparison of the time series of 10m wind speed (m/s) between the observations and different urban schemes at Montsouris, Roissy and Sirta stations.

The impacts of the LSM on NO_2 and $\text{PM}_{2.5}$ simulation is illustrating in Figure 3.22 (The PM_{10} can be found in Figure S10). The results show a very slight difference during regular days in all four station for both NO_2 and $\text{PM}_{2.5}$ simulation but gives some differences at the PE in FR04034 and FR04143 station. The possible reason could be the Noah-mp model produces stronger amplitude of ground heat flux by removing the exponential decay of the surface soil thermal conductivity with vegetation cover fraction (Niu et al., 2011). Overall, Noah - mp is demonstrated to be a viable research tool through which the role of a specific

process in controlling surface temperature and fluxes. But for the air quality simulation and forecast, Urban canopy and PBL schemes may play a more important role than LSM.

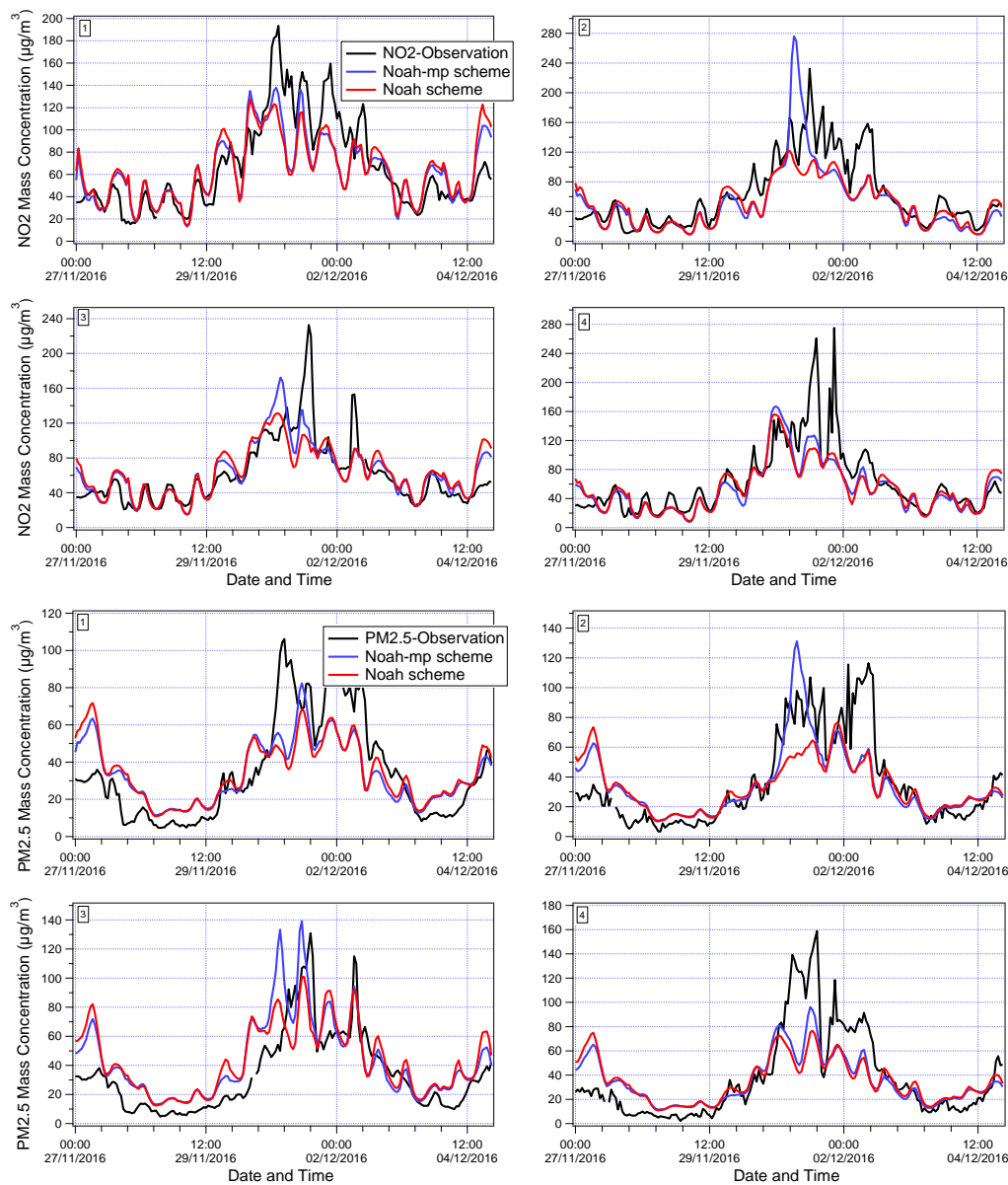


Figure 3.22 Time series of NO_2 and $\text{PM}_{2.5}$ mass concentrations: No 1, 2, 3, and 4 represent station FR04002, FR04034, FR04143, and FR04156, respectively.

3.4 Conclusions

This study evaluates the impact of three urban canopy parametrization schemes (Bulk, UCM, and BEP) and three boundary layer parametrization schemes coupled with urban canopy schemes (MYJ–Bulk, YSU–Bulk, MYJ–UCM, YSU–UCM, MYJ–BEP, and Boulac–BEP) from the Weather Research and Forecasting (WRF Version 3.9.1) mesoscale model on the simulations of meteorological variables and predicted pollutant concentrations issued from the

CHIMERE chemical transport model. This study aims at understanding those impacts on the short-term pollution episode in the Paris region, France.

For the first time, chemistry transport models have been used with a first layer at 4m to better account for physical processes within the suburban layer in relation to ground emissions such as road traffic. Clearly, the sharp gradient of concentrations shows the added value of using such a low level in urban areas. This study shows the high sensitivity of air quality simulation to meteorological model outputs during stable conditions favorable to the occurrence of PM episodes.

Three urban canopy models could reproduce the T2 effectively in the daytime; the Bulk and UCM model reproduced the W10 well, but the BEP model underestimates W10 for the whole episode, indicating an important impact of buildings on the diffusion rate for this scheme. The UCM scheme overestimates the surface heat index in rural areas, leading to a slight negative bias for T2 in rural versus urban areas. T2 displays ambiguous results, while all schemes reproduced results well at Sirta station but overestimated during nighttime at Montsouris and Roissy during a pollution episode. This could be due to the use of a single urban category in this study, which leads to a discrepancy that causes more spatial variability in urban parameters. NO₂, PM_{2.5}, and PM₁₀ were selected to evaluate the effect of physics parameterizations on air quality simulation. Large differences were found in the simulation of pollutant concentrations, with an overall overestimation during the pollution episode.

The six PBL sensitivity tests display an underestimation of the PBL height when compared with the observations issued from the Lidar. All the sensitivity tests, except Boulac–BEP, could not effectively simulate the PBL height during the pollution episode. The two PBL schemes coupled with the BEP scheme still underestimated the W10 for the whole period, but the Boulac–BEP scheme improved the simulations compared with the MYJ–BEP scheme. The Boulac–BEP scheme had a significantly better performance than the other schemes for the simulation of pollutant concentrations, indicating that both the canopy parametrization and PBL schemes have a positive effect on air quality simulation in urban regions, especially during pollution episodes. The Noah-mp land surface scheme has slightly impact for both meteorological and air quality simulation. An advanced urban category could improve air quality prediction in urban regions.

References

- Allen, L.; Lindberg, F.; Grimmond, C.S.B. Global to city scale urban anthropogenic heat flux: Model and variability. *Int. J. Clim.* 2010, *31*, 1990–2005.
- Anderson, W.; Meneveau, C. A Large-Eddy Simulation Model for Boundary-Layer Flow over Surfaces with Horizontally Resolved but Vertically Unresolved Roughness Elements. *Bound. Layer Meteorol.* 2010, *137*, 397–415.
- Baklanov, A.; Mestayer, P.G.; Clappier, A.; Zilitinkevich, S.; Joffre, S.; Mahura, A.; Nielsen, N.W. Towards improving the simulation of meteorological fields in urban areas through updated/advanced surface fluxes description. *Atmos. Chem. Phys. Discuss.* 2008, *8*, 523–543.
- Barlage, M.; Miao, S.; Chen, F. Impact of physics parameterizations on high-resolution weather prediction over two Chinese megacities. *J. Geophys. Res. Atmos.* 2016, *121*, 4487–4498.
- Best, M. Representing urban areas within operational numerical weather prediction models. *Bound. Layer Meteorol.* 2005, *114*, 91–109.
- Bessagnet, B.; Hodzic, A.; Vautard, R.; Beekmann, M.; Cheinet, S.; Honoré C.; Liousse, C.; Rouil, L. Aerosol modeling with CHIMERE—preliminary evaluation at the continental scale. *Atmos. Environ.* 2004, *38*, 2803–2817.
- Bessagnet, B.; Beauchamp, M.; Guerreiro, C.; De Leeuw, F.; Tsyro, S.; Colette, A.; Meleux, F.; Rouil, L.; Ruysenaars, P.; Sauter, F.; et al. Can further mitigation of ammonia emissions reduce exceedances of particulate matter air quality standards? *Environ. Sci. Policy* 2014, *44*, 149–163.
- Bessagnet, B.; Menut, L.; Colette, A.; Couvidat, F.; Dan, M.; Mailler, S.; L'Éinois, L.; Pont, V.; Rouil, L. An Evaluation of the CHIMERE Chemistry Transport Model to Simulate Dust Outbreaks across the Northern Hemisphere in March 2014. *Atmosphere* 2017, *8*, 251.
- Borrego, C.; Souto, J.A.; Monteiro, A.; Dios, M.; Rodriguez, A.; Ferreira, J.; Saavedra, S.; Casares, J.J.; Miranda, A.I. The role of transboundary air pollution over Galicia and North Portugal area. *Environ. Sci. Pollut. Res.* 2013, *20*, 2924–2936.
- Bougeault, P.; Lacarrère, P. Parameterization of orographic induced turbulence in a meso beta scale model. *Mon. Weather Rev.* 1989, *117*, 1872–1890.
- Bowden, J.H.; Otte, T.L.; Nolte, C.G.; Otte, M. Examining Interior Grid Nudging Techniques Using Two-Way Nesting in the WRF Model for Regional Climate Modeling. *J. Clim.* 2012, *25*, 2805–2823.
- Coseo, L. Larsen Cooling the heat island in compact urban environments: The effectiveness of Chicago's green alley program. *Procedia Eng.* 2015, *118*, 691–710.
- Couvidat, F.; Bessagnet, B.; Garcia-Vivanco, M.; Real, E.; Menut, L.; and Colette, A. Development of an inorganic and organic aerosol model (Chimere2017b2 v1.0): Seasonal and spatial evaluation over Europe. *Geosci. Model. Dev.* 2018, *11*, 165–194.

EEA. *Air Quality in Europe—2018 Report*; EEA Report No 13/2018; European Environment Agency: Copenhagen, Denmark, 2018.

Falasca, S.; Catalano, F.; Moroni, M. Numerical Study of the Daytime Planetary Boundary Layer over an Idealized Urban Area: Influence of Surface Properties, Anthropogenic Heat Flux, and Geostrophic Wind Intensity. *J. Appl. Meteorol. Clim.* 2016, *55*, 1021–1039.

Falasca, S.; Catalano, F. Impact of Highly Reflective Materials on Meteorology, PM10 and Ozone in Urban Areas: A Modeling Study with WRF-CHIMERE at High Resolution over Milan (Italy). *Urban Sci.* 2018, *2*, 18.

Fan, S.; Guo, Y.R.; Chen, M.; Zhong, J.; Chu, Y.; Wang, W.; Huang, X.Y.; Wang, Y.; Guo, Y.H. Application of WRF 3D Var to a high-resolution model over Beijing area. *Plateau Meteorol.* 2008, *27*, 1181–1188.

Flaounas, E.; Bastin, S.; Janicot, S. Regional climate modelling of the 2006 West African monsoon: sensitivity to convection and planetary boundary layer parameterisation using WRF. *Clim. Dyn.* 2010, *36*, 1083–1105.

Gedzelman, S.D.; Austin, S.; Cermak, R.; Stefano, N.; Partridge, S.; Quesenberry, S.; Robinson, D.A. Mesoscale aspects of the Urban Heat Island around New York City. *Theor. Appl. Clim.* 2003, *75*, 29–42.

Glisan, J.M.; Gutowski, W.J.; Cassano, J.J.; Higgins, M.E. Effects of Spectral Nudging in WRF on Arctic Temperature and Precipitation Simulations. *J. Clim.* 2013, *26*, 3985–3999.

Hamaoui-Laguel, L.; Meleux, F.; Beekmann, M.; Bessagnet, B.; G nermont, S.; Cellier, P.; L inois, L. Improving ammonia emissions in air quality modelling for France Atmospheric Environment, 92 (2014), pp. 584-595

Hariprasad, K.B.R.R.; Srinivas, C.V.; Singh, A.B.; Rao, S.V.B.; Baskaran, R.; Venkatraman, B. Numerical simulation and inter comparison of boundary layer structure with different PBL schemes in WRF using experimental observations at a tropical site. *Atmos. Res.* 2014, *145*, 27–44.

He, Q.; Zhao, X.; Lu, J.; Zhou, G.; Yang, H.; Gao, W.; Yu, W.; Cheng, T. Impacts of biomass-burning on aerosol properties of a severe haze event over Shanghai. *Particuology* 2015, *20*, 52–60.

Hu, X.-M.; Nielsen-Gammon, J.W.; Zhang, F. Evaluation of Three Planetary Boundary Layer Schemes in the WRF Model. *J. Appl. Meteorol. Clim.* 2010, *49*, 1831–1844.

Janjic, Z. *Nonsingular Implementation of the Mellor-Yamada Level 2.5 Scheme in the NCEP Meso Model*; NCEP Office Note, No. 437; National Centers for Environmental Prediction: College Park, MD, USA, 2002; p. 61.

Janjić, Z.I. The Step-Mountain Coordinate: Physical Package. *Mon. Weather. Rev.* 1990, *118*, 1429–1443.

Hong, S.-Y.; Noh, Y.; Dudhia, J. A New Vertical Diffusion Package with an Explicit Treatment of Entrainment Processes. *Mon. Weather. Rev.* 2006, *134*, 2318–2341.

- Kim, Y.; Sartelet, K.; Raut, J.-C.; Chazette, P. Evaluation of the Weather Research and Forecast/Urban Model Over Greater Paris. *Bound. Layer Meteorol.* 2013, *149*, 105–132, doi:10.1007/s10546-013-9838-6.
- Kim, Y.; Sartelet, K.; Raut, J.-C.; Chazette, P. Influence of an urban canopy model and PBL schemes on vertical mixing for air quality modeling over Greater Paris. *Atmos. Environ.* 2015, *107*, 289–306.
- Kleczek, M.A.; Steeneveld, G.-J.; Holtslag, A. Evaluation of the Weather Research and Forecasting Mesoscale Model for GABLS3: Impact of Boundary-Layer Schemes, Boundary Conditions and Spin-Up. *Bound. Layer Meteorol.* 2014, *152*, 213–243.
- Kusaka, H.; Kondo, K.; Kikegawa, Y.; Kimura, F. A simple single-layer urban canopy model for atmospheric models: Comparison with multi-layer and slab models. *Bound. Layer Meteorol.* 2001, *101*, 329–358.
- Kusaka, H.; Kimura, F. Coupling a Single-Layer Urban Canopy Model with a Simple Atmospheric Model: Impact on Urban Heat Island Simulation for an Idealized Case. *J. Meteorol. Soc. Jpn.* 2004, *82*, 67–80.
- Lai, L.-W.; Cheng, W.-L. Air quality influenced by urban heat island coupled with synoptic weather patterns. *Sci. Total. Environ.* 2009, *407*, 2724–2733.
- LeMone, M.; Tewari, M.; Chen, F.; Dudhia, J. Objectively-determined fair-weather convective boundary layer depths in the ARW-WRF NWP model and their comparison to CASES-97 observations. *Mon. Weather Rev.* 2013, *141*, 30–54.
- LeMone, M.; Tewari, M.; Chen, F.; Dudhia, J. Objectively-determined fair-weather NBL features in the ARW-WRF model and their comparison to CASES-97 observations. *Mon. Weather Rev.* 2014, *142*, 2709–2732.
- Li, M.; Ma, Y.; Ma, W.; Hu, Z.; Ishikawa, H.; Su, Z.; Sun, F. Analysis of turbulence characteristics over the northern Tibetan Plateau area. *Adv. Atmos. Sci.* 2006, *23*, 579–585.
- Lin, C.-Y.; Chen, F.; Huang, J.-C.; Chen, W.-C.; Liou, Y.-A.; Chen, W.-N.; Liu, S.-C. Urban heat island effect and its impact on boundary layer development and land–sea circulation over northern Taiwan. *Atmos. Environ.* 2008a, *42*, 5635–5649.
- Lin, C.-Y.; Chen, W.-C.; Liu, S.C.; Liou, Y.A.; Liu, G.; Lin, T. Numerical study of the impact of urbanization on the precipitation over Taiwan. *Atmos. Environ.* 2008b, *42*, 2934–2947.
- Liu, Y.; Chen, F.; Warner, T.; Basara, J.B. Verification of a Mesoscale Data-Assimilation and Forecasting System for the Oklahoma City Area during the Joint Urban 2003 Field Project. *J. Appl. Meteorol. Clim.* 2006, *45*, 912–929.
- Liu, M.; Chen, M. Evaluation of BJ-RUC system for the forecast quality of planetary boundary layer in Beijing area. *J. Appl. Meteorol. Sci.* 2014, *25*, 212–221.
- Mailler, S.; Menut, L.; Khvorostyanov, D.; Valari, M.; Couvidat, F.; Siour, G.; Turquety, S.; Briant, R.; Tuccella, P.; Bessagnet, B.; et al. CHIMERE-2017: From urban to hemispheric chemistry-transport modeling. *Geosci. Model Dev.* 2017, *10*, 2397–2423.

- Markakis, K.; Valari, M.; Engardt, M.; Lacressonniere, G.; Vautard, R.; Andersson, C. Mid-21st century air quality at the urban scale under the influence of changed climate and emissions case studies for Paris and Stockholm. *Atmos. Chem. Phys.* 2016, *16*, 1877–1894.
- Martilli, A.; Clappier, A.; Rotach, M. An urban surface exchange parameterization for mesoscale models. *Bound. Layer Meteorol.* 2002, *104*, 261–304.
- Mellor, G.L.; Yamada, T. Development of a turbulence closure model for geophysical fluid problems. *Rev. Geophys.* 1982, *20*, 851–875.
- Menut, L.; Goussebaile, A.; Bessagnet, B.; Khvorostiyarov, D.; Ung, A. Impact of realistic hourly emissions profiles on air pollutants concentrations modelled with CHIMERE. *Atmos. Environ.* 2012, *49*, 233–244.
- Menut, L.; Bessagnet, B.; Khvorostyanov, D.; Beekmann, M.; Blond, N.; Colette, A.; Coll, I.; Curci, G.; Forêt, G.; Hodzic, A.; et al. CHIMERE 2013: A model for regional atmospheric composition modelling. *Geosci. Model Dev.* 2013, *6*, 981–1028.
- Miao, S.; Chen, F.; Li, Q.; Fan, S. Impacts of urban processes and urbanization on summer precipitation: A case study of heavy rainfall in Beijing on 1 Aug 2006. *J. Appl. Meteorol. Climatol.* 2010, *50*, 806–825.
- Molteni, F.; Buizza, R.; Palmer, T.N.; Petroliagis, T. The ECMWF ensemble prediction system: Methodology and validation. *Quart. J. R. Meteor. Soc.* 1996, *122*, 73–119.
- Niu, G.-Y., Yang, Z. L., Mitchell, K. E., Chen, F., Ek, M. B., Barlage, M., et al. The community Noah land surface model with multiparameterization options (Noah-MP): 1. Model description and evaluation with local-scale measurements. *Journal of Geophysical Research.* 2011, *116*, D12109.
- Oke, T. K. *Boundary Layer Climates* (2nd ed.), Rutledge, New York, 1988. p. 464
- Patricola, C.M.; Li, M.; Xu, Z.; Chang, P.; Saravanan, R.; Hsieh, J.-S. An investigation of tropical Atlantic bias in a high-resolution coupled regional climate model. *Clim. Dyn.* 2012, *39*, 2443–2463.
- Salamanca, F.; Krpo, A.; Martilli, A.; Clappier, A. A new building energy model coupled with an urban canopy parameterization for urban climate simulations—Part I. formulation, verification, and sensitivity analysis of the model. *Theor. Appl. Clim.* 2009a, *99*, 331–344.
- Salamanca, F.; Martilli, A. A new Building Energy Model coupled with an Urban Canopy Parameterization for urban climate simulations—Part II. Validation with one-dimension off-line simulations. *Theor. Appl. Clim.* 2009a, *99*, 345–356.
- Sarrat, C.; Lemonsu, A.; Masson, V.; Guedalia, D. Impact of urban heat island on regional atmospheric pollution. *Atmos. Environ.* 2006, *40*, 1743–1758.
- Toll, I.; Baldasano, J.M. Modeling of photochemical air pollution in the Barcelona area with highly disaggregated anthropogenic and biogenic emissions. *Atmos. Environ.* 2000, *34*, 3069–3084.

- Troen, I.B.; Mahrt, L. A simple model of the atmospheric boundary layer; sensitivity to surface evaporation. *Bound. Layer Meteorol.* 1986, *37*, 129–148.
- Tuccella, P.; Curci, G.; Visconti, G.; Bessagnet, B.; Menut, L.; Park, R.J. Modeling of gas and aerosol with WRF/Chem over Europe: Evaluation and sensitivity study. *J. Geophys. Res. Space Phys.* 2012, *117*, D03303.
- Tyagi, B.; Magliulo, V.; Finardi, S.; Gasbarra, D.; Carlucci, P.; Toscano, P.; Zaldei, A.; Riccio, A.; Calori, G.; D’Allura, A.; et al. Performance Analysis of Planetary Boundary Layer Parameterization Schemes in WRF Modeling Set Up over Southern Italy. *Atmosphere* 2018, *9*, 272.
- Valari, M.; Menut, L. Transferring the heterogeneity of surface emissions to variability in pollutant concentrations over urban areas through a chemistry-transport model. *Atmos. Environ.* 2014, *44*, 3229–3238.
- Vigaud, N.; Roucou, P.; Fontaine, B.; Sijikumar, S.; Tyteca, S. WRF/ARPEGE-CLIMAT simulated climate trends over West Africa. *Clim. Dyn.* 2009, *36*, 925–944.
- Wang, L.T.; Wei, Z.; Yang, J.; Zhang, Y.; Zhang, F.F.; Su, J.; Meng, C.C.; Zhang, Q. The 2013 severe haze over southern Hebei, China: model evaluation, source apportionment, and policy implications. *Atmos. Chem. Phys. Discuss.* 2014, *14*, 3151–3173.
- Wang, L.; Liu, J.; Gao, Z.; Li, Y.; Huang, M.; Fan, S.; Zhang, X.; Yang, Y.; Miao, S.; Zou, H.; et al. Vertical observations of the atmospheric boundary layer structure over Beijing urban area during air pollution episodes. *Atmos. Chem. Phys. Discuss.* 2019, *19*, 6949–6967, doi:10.5194/acp-19-6949-2019.
- Wu, J.; Zha, J.L.; Zhao, D.M.; Yang, Q.D. Changes in terrestrial near-surface wind speed and their possible causes: An overview. *Clim. Dyn.* 2017, *51*, 2039–207

Chapter IV: On the impact of WRF-CHIMERE vertical grid resolution and first layer height on mesoscale meteorological and chemistry transport modelling

This chapter has been designed to be considered for publication.

Chapter IV: On the impact of WRF-CHIMERE vertical grid resolution and first layer height on mesoscale meteorological and chemistry transport modelling

Lei Jiang^{1,2,*}, Bertrand Bessagnet^{1,†}, Frederik Meleux¹, Frederic Tognet¹, Florian Couvidat¹

¹ INERIS, National Institute for Industrial Environment and Risks, Parc Technologique ALATA, 60550 Verneuil-en-Halatte, France

² Sorbonne University, UPMC Univ Paris 06, DE129, 75005 Paris, France

[†] Now at European Commission, Joint Research Centre (JRC), 21027 Ispra, Italy.

Abstract

The mesoscale Weather Research and Forecasting (WRF) and chemistry transport model (CTM) CHIMERE models were used to evaluate the impact of vertical grid resolution and first layer height in meteorological and chemistry transport modelling. Three model configuration (L4, L12 and L40) were investigated: (i) **L4**: 53 vertical layers in WRF and 20 vertical levels in CHIMERE are defined, the first layer height is about 4m; (ii) **L12**: 51 vertical layers in WRF and 20 vertical levels in CHIMERE, the first layer height approximately at 12m; (iii) **L40**: 36 vertical layer in WRF and 9 vertical levels in CHIMERE, the first layer height is approximately at 40m. A fifteen days simulation including a three-day heavy pollution episode (PE) illustrates the impact of vertical grid resolution. The first layer height has a relatively small impact on meteorological simulation and the main differences of meteorological variables were observed at nighttime. However, a consistent improvement in chemistry transport modelling were displayed with refined vertical resolutions and the first layer height, compared to L12 and L40, the average improvement from L4 case in terms of RMSE are 23.26% and 25.09% on regular days (RD) defined as “without pollution episodes” and 62% and 129% during PE respectively. In general, the ability of the model with low vertical grid resolution to correctly predict air quality is reasonable on RD or light pollution events, while it fails to predict correctly the pollutant concentrations for heavy polluted situations. The performances were improved with refined vertical resolutions particularly with extra fine first layer height at 4m.

Résumé

Les modèles à méso-échelle CHIMERE et Weather Research and Forecasting (WRF) ont été utilisés pour évaluer l'impact de la résolution de la grille verticale et de la hauteur de la première couche dans la modélisation chimie transport. Trois configurations de modèles (L4, L12 et L40) ont été étudiées : (i) L4 : 53 couches verticales dans WRF et 20 niveaux verticaux dans CHIMERE sont définis, la hauteur de la première couche est d'environ 4m ; (ii) L12 : 51 couches verticales dans WRF et 20 niveaux verticaux dans CHIMERE, la hauteur de la première couche est d'environ 12m ; (iii) L40 : 36 couches verticales dans WRF et 9 niveaux verticaux dans CHIMERE, la hauteur de la première couche est d'environ 40m. Une simulation sur quinze jours en hiver incluant un épisode de forte pollution (PE) de trois jours illustre l'impact de la résolution de la grille verticale. La hauteur de la première couche a un impact relativement faible sur la simulation météorologique et les principales différences de variables météorologiques ont été observées la nuit. Cependant, une amélioration significative de la modélisation du transport des polluants a été constatée avec des résolutions verticales raffinées et la hauteur de la première couche. Ainsi, l'amélioration moyenne du cas L4 par rapport à L12 et L40 en termes de RMSE est de 23,26% et 25,09% sur les jours réguliers (RD) sans épisodes de pollution et 62% et 129% pendant PE respectivement. En général, la capacité du modèle à faible résolution verticale à reproduire correctement les concentrations de polluants est raisonnable sur les RD ou les épisodes de pollution légère, alors qu'il ne parvient pas à reproduire correctement les concentrations de polluants pour les situations de forte pollution. Les performances ont été améliorées avec une résolution verticale affinée, en particulier avec une hauteur de première couche très fine.

Keywords: air quality; vertical resolution; first layer height; diffusion; urban

4.1 Introduction

The prevention and control of environmental pollution has become an important task in the development and construction of the country, and the prevention and control of air pollution has become the top priority (Lu et al., 2020). Over the past decades, European countries deepen efforts to decouple air pollution from economic growth and the goal is to build an ecological civilization society (Ivanova, 2011; Koolen and Rothenberg, 2019b; Nam et al., 2010). Studies show many air pollutants have decreased substantially since mid-1980's (Grennfelt et al., 2020; Lelieveld et al., 2019; Renzi et al., 2017), for example, observation

data show that in Europe, the concentration of PM_{2.5} drops by 2.5µg/m³ per year over the past decades (Gozzi et al., 2017). However, some reports indicate more than 400,000 people die prematurely due to air pollution each year in Europe and this number is one million in 1990 (Guerreiro et al., 2015). Air pollution is still one of the biggest threats to the health of Europeans. In many European cities, the concentration of main pollutants still exceeds the reference value of European Union (Barsova et al., 2019; Xu et al., 2017) and over the hemispherical background concentrations (Vautard et al., 2009). Therefore, regional joint prevention and control play an important role in improving air quality. At region and urban scale, mesoscale chemistry transport model (CTM) are widely used to assess the efficiency of such policies in controlling air pollution (Ma et al., 2020). With the continuous improvement of pollution sources and meteorological knowledge, many studies have proved the important role of horizontal resolution in improving model capabilities (Jensen et al., 2017; Martins, 2012; Russell et al., 2019; Thunis et al., 2016b). However, there is still a lack of research on the effect of vertical grid resolution on the chemical transport processes. Accurate simulations of near-surface parameters particularly the representation of turbulence is difficult but very important on vertical mixing of meteorological and chemistry transport modelling. A spatial resolution increase enhances the variability of the concentrations, but also the amplitude of the errors due to meteorology, vertical resolution, land use or other factors (Aligo et al., 2009; Vautard et al., 2007). Since human activities are mainly concentrated within 50 meters from the ground, it is particularly important to improve the model's representation of pollutants in low boundary height. Research found that adding an extra vertical layer close to the surface is important for high nocturnal concentrations under stable boundary layers (Menut et al., 2013b).

In this chapter, an evaluation of three vertical grid resolution configurations and a first layer height, used to simulate a winter period including a short heavy pollution event in Paris region is proposed.

4.2 Method

The mesoscale Weather Research and Forecasting (WRF) model in Version3.9.1 and CTM model CHIMERE in Version2013 are used to simulate the meteorological parameters and pollutant concentrations over Paris. The horizontal domain setting is same as that of in Chapter II, with four nested-grid domains over Europe, France, the north of France, and Ile-de-France, with horizontal resolutions of 45km, 15km, 5km, and 1.67km, respectively.

The horizontal resolution of CHIMERE is consistent with WRF. Details can be found in Chapter III. A winter pollution event occurred between 30th November to 1st December 2016. In Chapter III, we analyzed the impact of physical parameterizations on high resolution meteorological and chemistry transport modelling and summarized the best parameter settings. Which means the rapid radiative transfer model for GCMs (RRTMG) shortwave and longwave radiation scheme; Monin–Obukhov (MO) similarity surface layer scheme; multi-layer urban canopy (BEP) scheme and Bougeault and Lacarrere (Boulac) boundary layer scheme are used as the physical parameter settings in this study. In order to better evaluate the impact of the vertical grid resolution and the first layer height on the air quality prediction on Regular days (RD) and Pollution episode (PE), the time series has been extended from eight days to fifteen days (from 20th November to 4th December) compared to the Chapter III, including 12 days RD from 20th November to 29th November and 3rd December to 4th December, and a three days heavy winter PE from 30th November to 2nd December .

The vertical resolution of WRF is projected over CHIMERE. WRF having more vertical layers than CHIMERE. Therefore, three different vertical resolutions are defined for CHIMERE and WRF individually, and the configurations of the first layer height of the two models remain the same:

- L4: 53 vertical layers are defined in WRF and 20 vertical layers are defined in CHIMERE. The first layer of the two model is at 999.5 hPa (approximately 4m) up to over 500hPa.
- L12: 51 vertical layers are defined in WRF and 20 vertical layers are defined in CHIMERE, with the first layer at 998.5 hPa (approximately 12m) up to over 500hPa..
- L40: 36 vertical layers are defined in WRF and 9 vertical layers are defined in CHIMERE, the vertical layers are from 995 hPa (approximately 40m) up to over 500hPa. This is the low vertical grid resolution test with a high first layer height, a similar configuration of vertical resolution and first layer height used in the national air quality forecasting platform PREV’AIR.

To assess the model abilities in simulating the vertical profiles of meteorological parameters and pollutant concentrations, two types of observation datasets including three meteorological observation stations operated by METEO FRANCE and SIRTA and four air quality

monitoring stations issued from AIRPARIF were used. Those stations are urban or sub-urban background stations, the locations of stations can be found in Figure4.1.

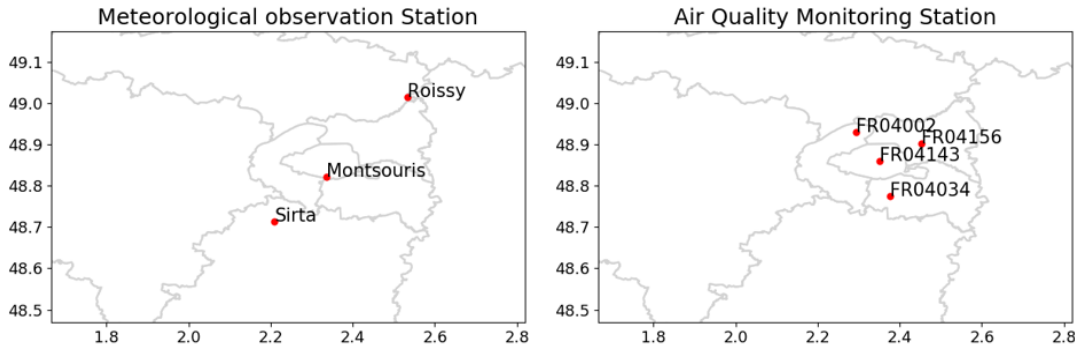


Figure4.1 Locations of the meteorological and air quality monitoring stations.

Here, taking the relative change in % of the RMSE as the evaluation criteria of the model performances which defined as (4.1):

$$Imp(\%) = \frac{RMSE_{tes} - RMSE_{ref}}{RMSE_{ref}} * 100 \quad (4.1)$$

Where $RMSE_{tes}$ refers to the RMSE of the test case and $RMSE_{ref}$ refers to the RMSE of the reference case.

4.3. Results and Discussion

4.3.1 Surface meteorological and pollutants concentration

4.3.1.1 Meteorology

The aim of this study is to assess the ability of the WRF-CHIMERE suite in simulating meteorological parameters and the main pollutant concentrations with different vertical grid resolution. In Figure4.2, the maps of 2m temperature (T2), 10m wind speed (W10) and surface relative humidity (RH) are displayed for the finest domain over the whole period. Although the absolute values are different, the regional patterns are similar for the three cases. For the simulation of T2, all three cases show obvious urban heat island effects of the domain, the absolute values in urban regions are approximately 2 °C higher than the surroundings, and proportional to the height of the first layer ($T2_{L40} > T2_{L12} > T2_{L4}$). The W10 values increase with an increasing first layer height in rural areas. However, in urban areas, L12 displays the highest W10, and L4 trends to produce the lowest W10 in cities. The momentum sinks depend on urban morphology in BEP urban canopy scheme, this indicates that an ultra-fine

first layer height could overestimate the drag effect of the realistic urban morphologies. The regional pattern of surface RH is inversely proportional to T2, with the highest RH simulation both in urban and rural region for L4 and lowest for L40. Table 4.1 lists the range and average values of meteorological parameters for the three cases. The relative bias (RB) of L12 and L40 compared to the reference case (L12-L4 and L40-L4) are 2.17% and 22.95% for T2, 4.01% and -12.69% for W10, -0.12% and -2.72% for RH, respectively. The RB of L40-L4 clearly shows that vertical grid resolution has a strong impact of meteorology particularly for T2 simulation, but there is no obvious impact on meteorological parameters simulations by refining fine first layer according to the results of L12-L4.

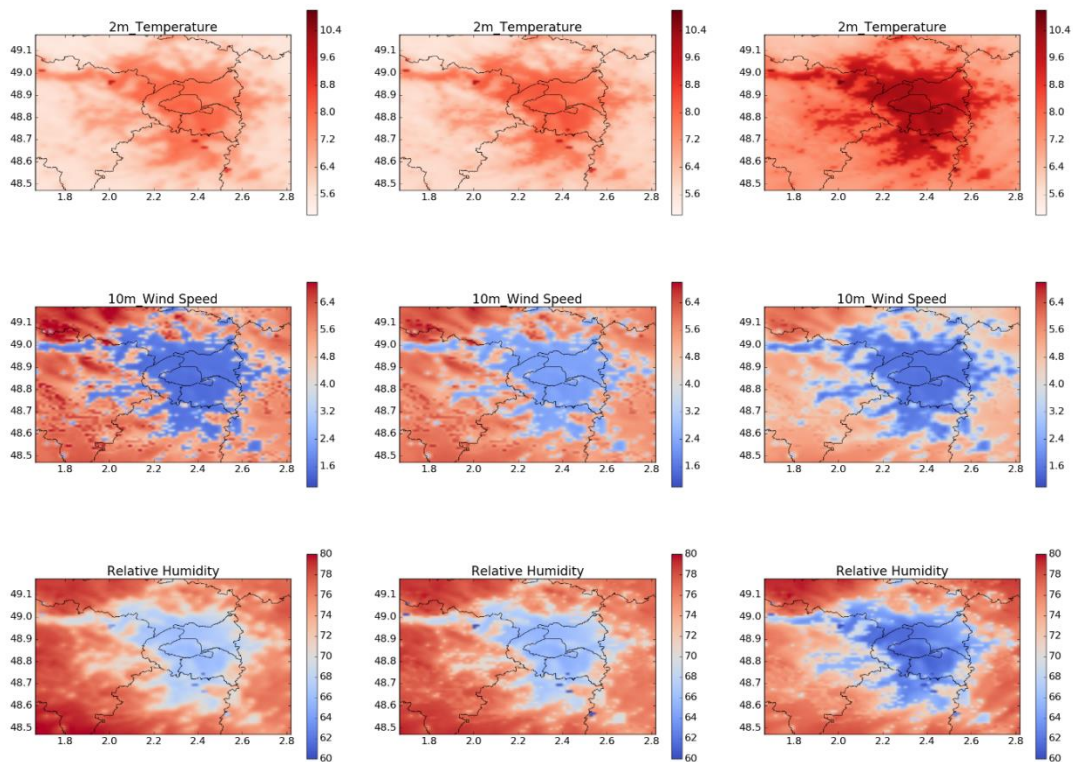


Figure 4.2 Maps of the mean 2m temperature (°C); mean 10m wind speed (m/s) and mean surface relative humidity (%) over the period from 20th November to 4th December. Left column: results from L4; Middle column: results from L12; Right column: results from L40.

Table 4.1 Range and average values of 2m temperature (°C); 10m wind speed (m/s) and surface relative humidity (%) over the period

	L4		L12		L40	
	Range	Avg	Range	Avg	Range	Avg
T2	5.35 – 9.78	6.45	5.41 – 10.10	6.59	6.11 – 11.54	7.93
W10	1.38 – 8.79	4.49	2.08 – 7.57	4.67	1.44 – 6.73	3.92
RH	61.06 – 80.52	73.88	55.87 – 79.72	73.79	56.50 – 79.99	71.87

4.3.1.2 Surface pollutant concentrations

NO₂, PM_{2.5} and PM₁₀ concentrations are considered as the main pollutants to evaluate model performances on air quality simulations in this winter case study. Figure 4.3 shows the maps of simulated surface NO₂, PM_{2.5} and PM₁₀ concentrations. As expected and similarly with the performances of meteorological parameters simulation, all three cases display gradient concentrations between the urban and rural areas. In the case of NO₂, the surface concentrations in urban area and near the traffic lines are much higher. Table 4.2 shows that unlike the vertical grid resolution has a relatively small impact on meteorology, RB in L12-L4 and L40-L4 are both substantial in air quality simulations. The RB are -10.68% and -39.34%, respectively. In the case of PM_{2.5} and PM₁₀, surface concentrations from the individual cases again displays large differences. The RB of L12-L4 and L40-L4 are -4.61% and -36.98% for PM_{2.5}, -4.01% and -35.85% for PM₁₀, respectively. The dispersion of the particulate matters away from the cities are uneven. Regional patterns show the lowest surface particulate matters in near urban surroundings and southwest regions, this because those areas are mainly covered by broad-leaf forests. The range of pollutants provide by the individual cases are also worth noting. Taking NO₂ as an example, the maximum concentrations values from L4, L12 and L40 are 136.34µg/m³, 82.56µg/m³ and 62.87µg/m³ respectively. The value of the L4 case is 1.65 time than L12 and more than twice value of the L40. This indicates the potential improvement of the model's ability on pollution events prediction through an improvement of the vertical grid resolution.

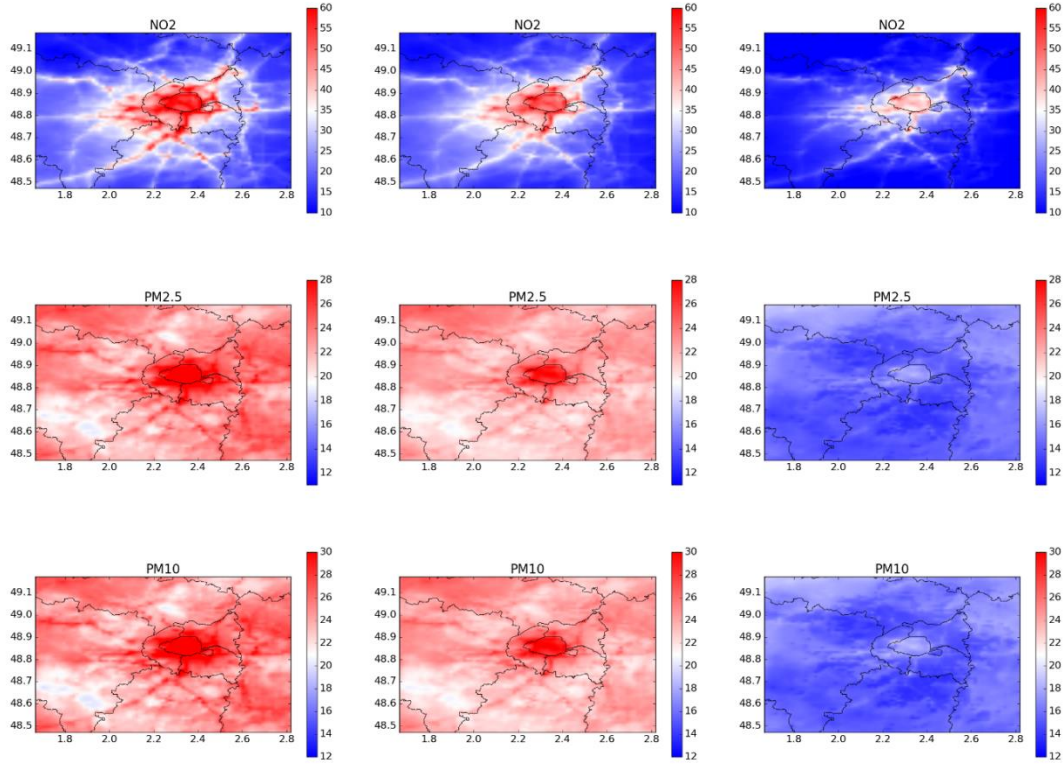


Figure 4.3 Maps of the mean NO_2 ($\mu\text{g}/\text{m}^3$); mean $\text{PM}_{2.5}$ ($\mu\text{g}/\text{m}^3$) and mean PM_{10} ($\mu\text{g}/\text{m}^3$) mass concentrations over the period from 20th November to 4th December. Left column: results from L4; Middle column: results from L12; Right column: results from L40.

Table 4.2 Range and average values NO_2 ($\mu\text{g}/\text{m}^3$); $\text{PM}_{2.5}$ ($\mu\text{g}/\text{m}^3$) and PM_{10} ($\mu\text{g}/\text{m}^3$) over the period

	L4		L12		L40	
	Range	Avg	Range	Avg	Range	Avg
NO₂	10.01 - 136.34	25.65	10.40 - 82.56	22.91	7.16 - 62.87	15.56
PM_{2.5}	18.65 - 47.51	23.33	19.04 - 34.93	22.16	12.35 - 20.78	14.64
PM₁₀	19.82 - 51.96	24.94	20.42 - 38.32	23.94	13.51 - 22.95	16.00

4.3.2 Vertical profiles

The averaged vertical profiles of vertical diffusion coefficient K_z , NO_2 , $\text{PM}_{2.5}$ and PM_{10} concentrations for the corresponding first layer height to 1000m for the Paris region are displayed in Figure 4.4. The vertical K_z profile shows similar shapes but different order of magnitudes from surface to the top. For all cases the K_z displays an inverse concentration-like distribution within the first 400m, low vertical grid resolution trend to produce stronger vertical mixing. The values of K_z at first layer are $1.48\text{m}^2/\text{s}$, $4.25\text{m}^2/\text{s}$ and $15.37\text{m}^2/\text{s}$ for L4,

L12 and L40 respectively, showing the model would generate a very poor mixing close to the surface. The pollutants profiles decrease with altitude. The vertical K_z in L12 is generally higher than L40, and the vertical distribution of pollutants is inversely proportional to K_z , which indicates that the main effect of increasing the vertical resolution is to increase the concentration of pollutants. Vertical profiles showing maximum concentrations of all pollutants at surface and decreasing faster with increasing altitude, this feature shows that adding an extra fine layer near surface may have an important impact on chemistry transport modelling.

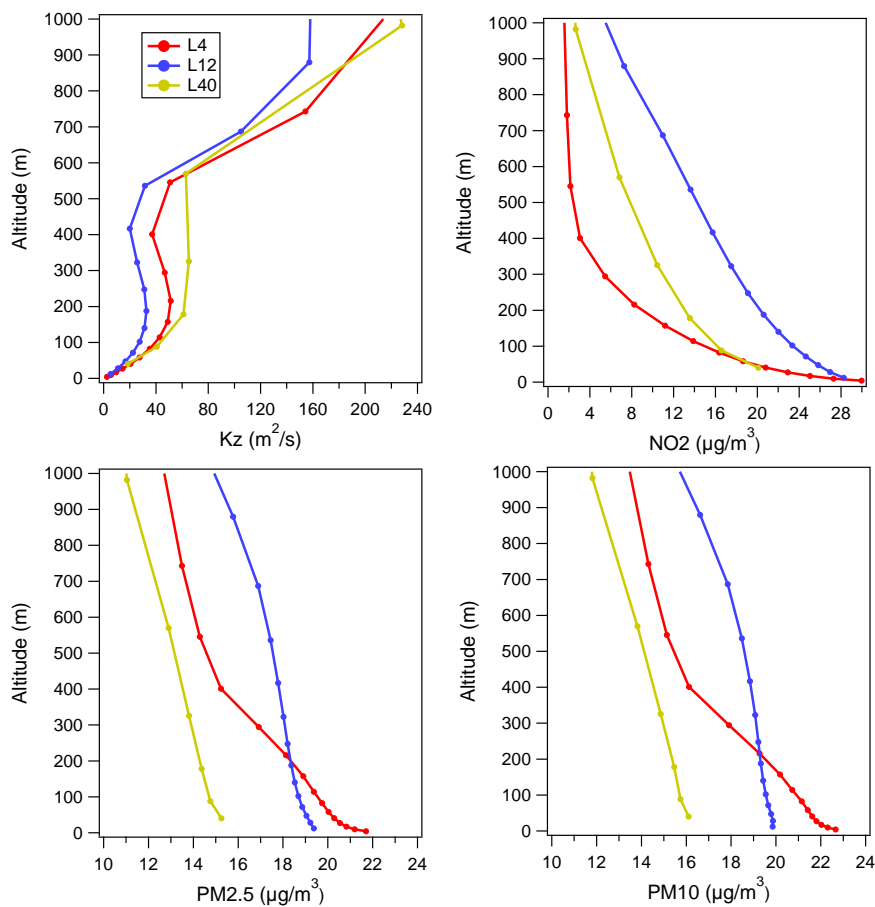


Figure 4.4 Vertical profiles of K_z (m^2/s), NO_2 , $PM_{2.5}$ and PM_{10} ($\mu g/m^3$) from 20th November to 4th December over Paris region.

4.3.3 Comparison of model results with observations

4.3.3.1 Meteorological simulations

The comparison of model simulated and observed T2 and W10, as well as planetary boundary layer height (PBLH) are presented in Figure 4.5. During this period, a PE from 30th November to 2nd December was reported according to the PREV'AIR system. For L4 and L12 cases, the model reproduces well T2 on RD and overestimated T2 on PE by up to 3.08 °C for L4 and

4.73 °C for L12. The statistical evaluation (Table4.3) shows that differences of model performance for T2 between L4 and L12 are small, both with high correlation (0.97 and 0.96) and low root mean square error (RMSE) shows that those two cases results reproduced realistic T2 fields. However, there is an overall overestimation of T2 for L40 case up to 9.08 °C at night of 1st December. Table4.3 shows that the mean bias (MB) for L40 case are 4 and 3.49 times compared with L4 and L12. The second example of predictions refers to the simulation of W10. The L12 case simulated the highest W10 most of the time, three meteorological observation stations are all urban background stations. These results match with the maps of W10 in the urban region. All three cases underestimate W10 during the whole period, the negative biases are 1.95m/s, 1.23m/s and 1.96m/s respectively. The L12 shows better performance on W10 prediction than other two cases. The observed Planetary Boundary Layer Height (PBLH) is very often below 200m, leading to a weak mixing of pollutants and therefore an accumulation of pollutants closes to the surface. For the PBLH, the model performance is poor, the highest correlation coefficient was found in L40, however, this case overestimated PBLH approximately 160m on PE, this will cause an overestimated mixing rate and thus underestimate the pollutant concentration.

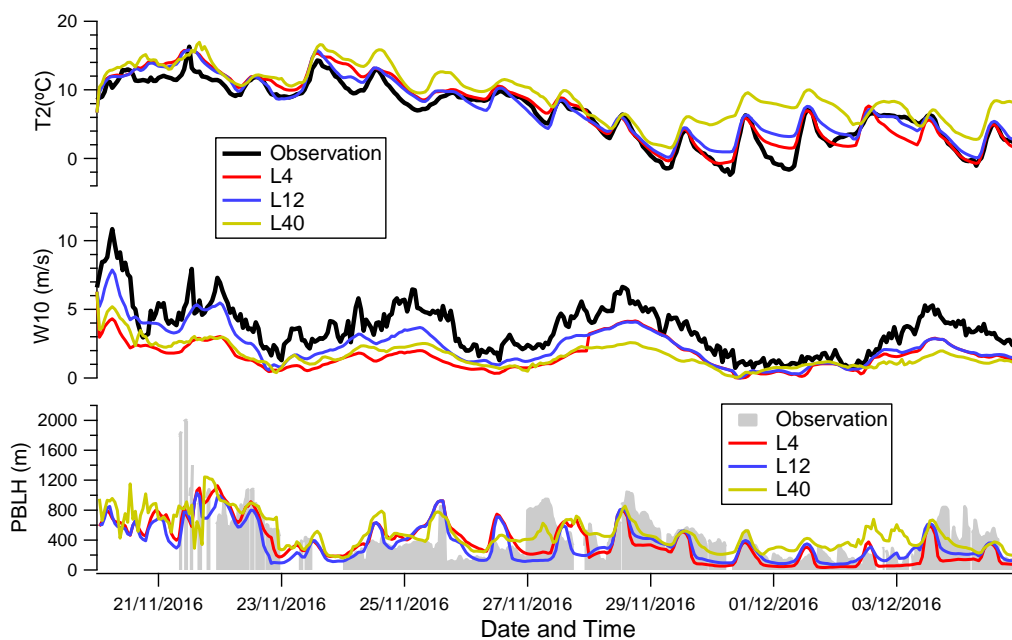


Figure4.5 Time series between the observed and modelled 2m temperature (°C); mean 10m wind speed (m/s) and planetary boundary layer height (PBLH)

Table4.3 Statistics of surface variables: mean bias (MB), mean linear correlation coefficient (R) and root mean square error (RMSE) between the simulations and

observations of 2m temperature (°C); mean 10m wind speed (m/s) and planetary boundary layer height (PBLH)

	L4			L12			L40		
	R	MB	RMSE	R	MB	RMSE	R	MB	RMSE
T2	0.97	0.68	1.45	0.96	0.78	1.43	0.89	2.72	3.35
W10	0.81	-1.95	2.25	0.92	-1.23	1.42	0.88	-1.96	2.23
PBLH	0.66	-36.17	262.51	0.70	-54.91	238.03	0.77	81.8	213.92

In order to better understand the main differences, diurnal cycles are presented in Figure4.6. The model tends to overestimate T2 all over the day, usually more overestimated at night compared to the daytime. The diurnal cycle of W10 is relatively flat and all three cases strongly underestimate W10. L12 shows good results compare with others regarding the MB throughout the day. Due to missing part of the observation data, the diurnal cycle of observed PBLH does not have absolute accuracy. Based on existing data, we can find that L40 tends to overestimate and L4, L12 tends to underestimate PBLH at night and the diurnal variation of L40 significantly smaller than the other two cases. The diurnal cycles of meteorological parameters indicate that the vertical grid resolution is important on meteorology. Refining the levels thicknesses near the surface mostly affect the wind speed calculation.

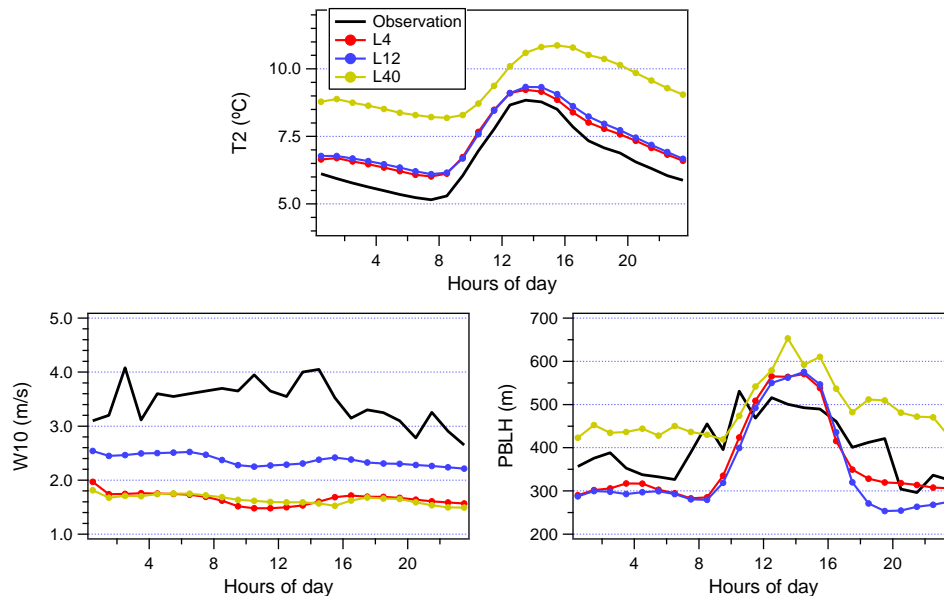


Figure4.6 Diurnal cycles for surface 2m temperature (°C); mean 10m wind speed (m/s) and planetary boundary layer height (PBLH) from 20th November to 4th December.

4.3.3.2 Evaluation of main pollutants simulations

The time evolution of hourly-averaged NO₂, PM_{2.5} and PM₁₀ between observation and three cases involved in the inter-comparison is provided in Figure 4.7. The results show that all three cases captured fairly well the day-to-day variability of the surface pollutants concentrations on RD but generally underestimated the intensity during the PE days. A relatively small differences between cases can be found from 20th to 29th November. While refining the first layer height has not a very sensitive impact on meteorology, it has a significant beneficial impact on air quality simulation. As shown in Table 4.4, L4 case gives a clear best performance for of pollutants. The agreement with observations is generally better than for the other two cases, the correlations are 0.87, 0.90 and 0.91 in the cases of NO₂, PM_{2.5} and PM₁₀ respectively. Compared to the observations, the peak of pollutants corresponding to the PE is well modeled in L4 simulation, although it still underestimates surface concentrations on PE. The changes of pollutants concentrations are small between RD and PE in L40, which indicates low vertical resolution can hardly predict the PE effectively. The model comparison in Figure 4.8 presents the differences between cases. Positive biases are found in L12-L4 and negative biases are found in L40-L4 from 20th to 28th November. On reason is the relatively low PBLH of L12 and relatively high PBLH of L40 compare with L4 over this period. Since 29th November, the surface pollutants concentrations obtained from L4 are mostly higher than other two cases. While the average PM_{2.5} and PM₁₀ surface concentrations are 25.64 μg/m³ and 36.25 μg/m³ in the observations, in the simulations, the values are 27.42 μg/m³ and 29.67 μg/m³ from L4, 24.45 μg/m³ and 26.69 μg/m³ from L12, 14.82 μg/m³ and 16.24 μg/m³ from L40 respectively. This result is consistent with our one-year simulation over French region in Chapter II, the ratio of PM_{2.5}/PM₁₀ generally over 90% in the model. The reason could originate from the overestimation of fine mode emissions, as well as the lack of natural coarse emissions (Im et al., 2010; Vautard et al., 2009). In general, emission inventory needs improvement.

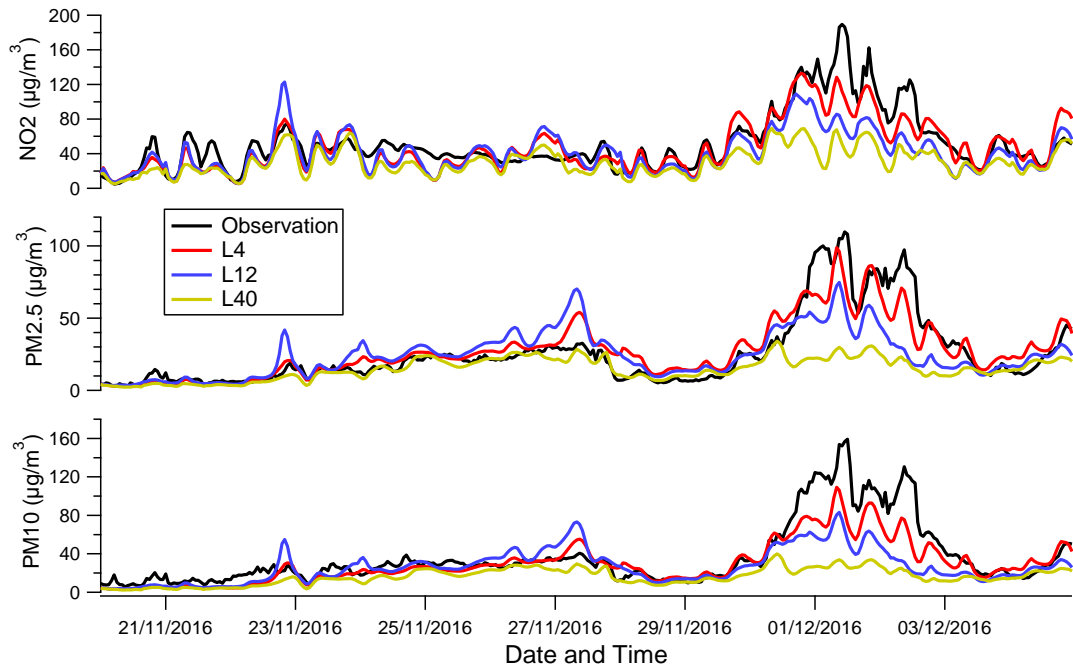


Figure 4.7 Time series between the observed and modelled NO_2 , $PM_{2.5}$, PM_{10} ($\mu\text{g}/\text{m}^3$).

Table 4.4 Statistics of surface variables: mean bias (MB), mean linear correlation coefficient (R) and root mean square error (RMSE) between the simulations and observations of NO_2 , $PM_{2.5}$, PM_{10} .

	L4			L12			L40		
	R	MB	RMSE	R	MB	RMSE	R	MB	RMSE
NO₂	0.87	-4.30	17.18	0.75	-10.35	24.90	0.69	-21.12	33.33
PM_{2.5}	0.90	1.78	10.99	0.70	-1.19	17.53	0.62	-10.82	23.05
PM₁₀	0.91	-6.58	17.05	0.70	-9.56	25.42	0.63	-20.01	34.10

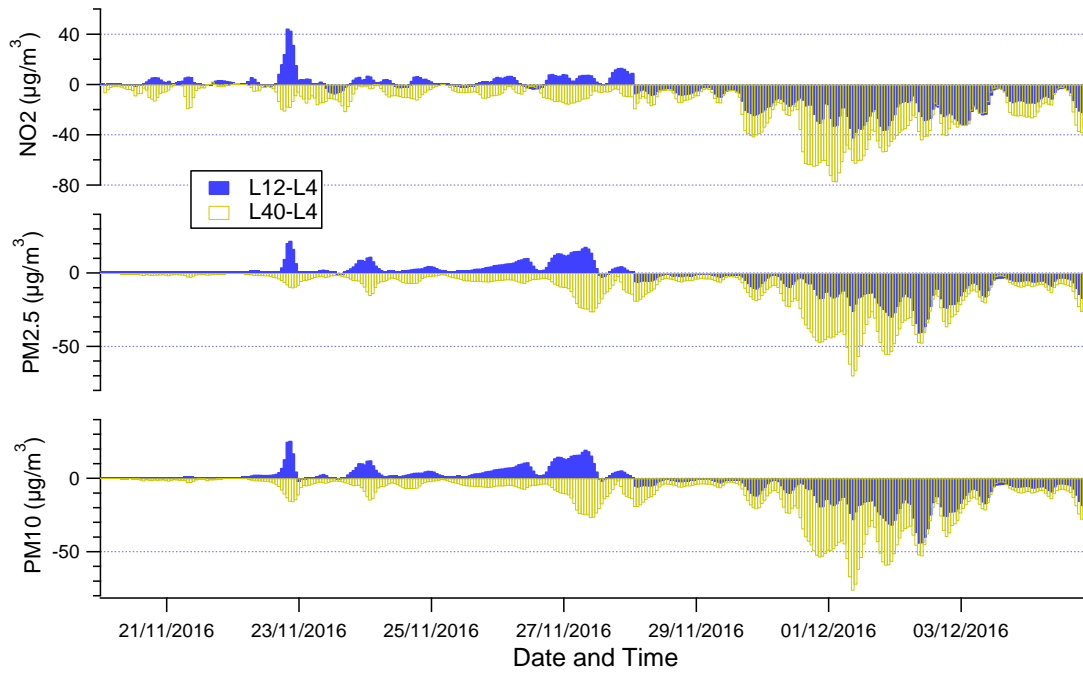


Figure 4.8 Time series of bias between L12 to L4 (L12-L4) and L40 to L4 (L40-L4).

In order to better evaluate the model performance during the PE, statistics of individual cases can be found in Table 4.5. On RD, the RB of L12 to L4 is small, the values are -4.79%, 2.43% and 3.84% for NO₂, PM_{2.5} and PM₁₀ respectively. However, such values are large in L40-L4, which are -28.25%, -34.51% and -33.74%. The reason is the vertical mixing is much stronger in L40 than for L4 and L12 leading to more dispersion. Taking RMSE as the evaluation criteria of the model performances, L4 case improves the model ability by 23.26% and 25.09% on average compare with L12 and L40 on RD. Therefore, it also means the differences between L12 and L40 are relatively small. The average RMSE is 5.09% in L40-L12. This indicates that improving vertical grid resolution has relatively small impact during RD, but a fine first layer height is important for air quality simulation. Interestingly, during PE days, surface concentration of pollutants is much strongly influenced by the vertical resolution and first layer heights. The average NO₂, PM_{2.5} and PM₁₀ concentrations from L4 are respectively 1.92, 2.64, 2.56 time than L40. The correlations in the case of L40 are reasonable on RD but poor on PE. Those results show that model configurations with low vertical grid resolutions and first layer height can reproduce pollutants well on RD, while for PE days the reproduction of amplitudes and variabilities will remain difficult. For the cases of L4, the simulation of all pollutants shows good agreement with observations. However, the amplitudes of pollutants remain underestimated, NO₂ concentrations are underestimated on average by 15.98%, for PM_{2.5} by 12.68% and for PM₁₀ by 30.45%. The improvement of the model performance on PE by increasing the vertical resolution and refining first layer height is rather clear. Compare with

L12 and L40 cases, L4 improved model ability by 62.10% and 129.02% on average. The improvement is significantly higher than for RD.

Table 4.5 Statistics of surface variables: average mass concentration ($\mu\text{g}/\text{m}^3$), mean bias (MB), mean linear correlation coefficient (R) and root mean square error (RMSE) between the simulations and observations of NO_2 , $\text{PM}_{2.5}$, PM_{10} on regular days (RD) and pollution episode (PE).

		RD			PE		
		NO_2	$\text{PM}_{2.5}$	PM_{10}	NO_2	$\text{PM}_{2.5}$	PM_{10}
L4	Avg	36.57	20.08	21.34	88.97	56.61	62.80
	R	0.72	0.85	0.81	0.75	0.73	0.79
	MB	-1.28	4.24	-1.40	-16.92	-8.22	-27.50
	RMSE	12.97	7.32	7.14	28.32	19.74	35.34
L12	Avg	34.82	20.58	22.16	66.02	39.93	44.82
	R	0.69	0.74	0.70	0.62	0.50	0.57
	MB	-3.03	4.74	-0.58	-39.87	-24.90	-45.40
	RMSE	13.98	9.99	9.84	48.15	33.71	53.33
L40	Avg	26.24	13.15	14.14	46.39	21.43	24.52
	R	0.69	0.82	0.78	0.38	0.26	0.29
	MB	-11.61	-2.69	-8.60	-59.50	-43.40	-65.78
	RMSE	15.83	9.25	10.45	67.46	50.21	73.33

All the analysis results indicate the model configuration of L4 is significantly better than the other two in the simulation of the chemical transport process during this period, but it is difficult to state that L4 is the best model setting in all cases.

Table 4.6 reports the operational time consumed by the three cases for simulating a single day meteorological and chemical transport processes for all domains. The operating processes of WRF and CHIMERE both consist of two steps: a pre-processing step and a main operating step. The pre-processing step takes a very short time, ranging from tens of seconds to several minutes. Here, a single-day operational time often refers to the total time taken to complete these two steps. The difference between the L4 and L12 cases for meteorological modelling is small, only 3 minutes but L40 can save 14 minutes compare with L4. For chemistry transport modelling, the difference between the L4 and L2 cases is similar with their meteorological process, while the difference for operational uses of the L40 case is more straightforward. Compared with the L4 case, 44 minutes are saved, the CPU time is divided at least by a factor 2.

Results show acceptable model ability at low vertical grid resolution on RD. Therefore, for the high-resolution small domain cases, it is obvious that high vertical grid resolution is a better setting. In particular, the reasonable first layer height may greatly improve the simulation results. For a long-term and large-scale simulation, considering the cost of computing resources, a low vertical resolution configuration should be a more suitable solution for practical use.

Table 4.6 Operational time (minutes) for a single day simulation in meteorological and chemistry transport modelling

	WRF	CHIMERE	TOTAL
L4	70	84	154
L12	67	82	149
L40	56	40	96

4.4 Conclusions

This study presents a sensitivity analysis of the impact of vertical grid resolution and the first layer height in meteorological and chemistry transport modelling during a pollution episode at urban scale. The simulations are carried out over a fifteen days winter period from 20th November to 4th December 2016 including a pollution episode (PE) from 30th November to 1st December and the rest of days is defined as regular days (RD).

The maps of meteorological parameters and main pollutants show similar regional patterns for the three cases. The differences between the different model configurations are relatively small on meteorological parameters. The relative bias (RB) of L12 and L40 compare with L4 (L12-L4 and L40-L4) are 2.17% and 22.95% for 2m temperature (T2), 4.01% and -12.69% for 10m wind speed (W10), -0.12% and -2.72% for surface relative humidity (RH), respectively. The differences between three configurations in chemistry transport modelling are more obvious. The RB of L12-L4 and L40-L4 are -10.68% and -39.34% for NO₂, -4.61% and -36.98% for PM_{2.5} and -4.01% and -35.85% for PM₁₀, respectively.

However, for the planetary boundary layer height (PBLH), L40 case reproduces higher PBLH than others in most of the time of this period and overestimated PBLH about 160m on PE, leading to a stronger vertical mixing than for L12 and L4 simulations. The differences between the three configurations in meteorological parameters simulations are larger during nighttime than that for daytime.

The comparisons between observed and modelled surface main pollutants concentrations were performed. Although the model performances are uneven, all three configurations demonstrate the ability of chemistry transport modelling on RD. The impact of vertical grid resolution and first layer height is moderate. Taking the root mean square error as the evaluation criteria, L4 improves the model ability by 23.26% and 25.09% than L12 and L40 respectively. However, on PE, improving vertical grid resolution and first layer height results clearly improves the air quality prediction, average improvements are 62.10% and 129.02% from L12 to L4 and from L40 to L4 respectively.

This study highlights the model ability both in meteorological and chemistry transport modelling with low vertical resolution on RD, but such a model configuration displays discrepancies in representing the amplitudes of pollutants concentrations on PE and increasing the vertical resolution and refining first layer height leads to clear improvement during pollution episodes.

References

- Allen, L.; Lindberg, F.; Grimmond, C.S.B. Global to city scale urban anthropogenic heat flux: Model and variability. *Int. J. Clim.* 2010, *31*, 1990–2005.
- Anderson, W.; Meneveau, C. A Large-Eddy Simulation Model for Boundary-Layer Flow over Surfaces with Horizontally Resolved but Vertically Unresolved Roughness Elements. *Bound. Layer Meteorol.* 2010, *137*, 397–415.
- Baklanov, A.; Mestayer, P.G.; Clappier, A.; Zilitinkevich, S.; Joffre, S.; Mahura, A.; Nielsen, N.W. Towards improving the simulation of meteorological fields in urban areas through updated/advanced surface fluxes description. *Atmos. Chem. Phys. Discuss.* 2008, *8*, 523–543.
- Barlage, M.; Miao, S.; Chen, F. Impact of physics parameterizations on high-resolution weather prediction over two Chinese megacities. *J. Geophys. Res. Atmos.* 2016, *121*, 4487–4498.
- Best, M. Representing urban areas within operational numerical weather prediction models. *Bound. Layer Meteorol.* 2005, *114*, 91–109.
- Bessagnet, B.; Hodzic, A.; Vautard, R.; Beekmann, M.; Cheinet, S.; Honoré C.; Liousse, C.; Rouil, L. Aerosol modeling with CHIMERE—preliminary evaluation at the continental scale. *Atmos. Environ.* 2004, *38*, 2803–2817.
- Bessagnet, B.; Beauchamp, M.; Guerreiro, C.; De Leeuw, F.; Tsyro, S.; Colette, A.; Meleux, F.; Rouil, L.; Ruysenaars, P.; Sauter, F.; et al. Can further mitigation of ammonia emissions reduce exceedances of particulate matter air quality standards? *Environ. Sci. Policy* 2014, *44*, 149–163.
- Bessagnet, B.; Menut, L.; Colette, A.; Couvidat, F.; Dan, M.; Mailler, S.; L'Éinois, L.; Pont, V.; Rouil, L. An Evaluation of the CHIMERE Chemistry Transport Model to Simulate Dust Outbreaks across the Northern Hemisphere in March 2014. *Atmosphere* 2017, *8*, 251.
- Borrego, C.; Souto, J.A.; Monteiro, A.; Dios, M.; Rodriguez, A.; Ferreira, J.; Saavedra, S.; Casares, J.J.; Miranda, A.I. The role of transboundary air pollution over Galicia and North Portugal area. *Environ. Sci. Pollut. Res.* 2013, *20*, 2924–2936.
- Bougeault, P.; Lacarrère, P. Parameterization of orographic induced turbulence in a meso beta scale model. *Mon. Weather Rev.* 1989, *117*, 1872–1890.
- Bowden, J.H.; Otte, T.L.; Nolte, C.G.; Otte, M. Examining Interior Grid Nudging Techniques Using Two-Way Nesting in the WRF Model for Regional Climate Modeling. *J. Clim.* 2012, *25*, 2805–2823.
- Coseo, L. Larsen Cooling the heat island in compact urban environments: The effectiveness of Chicago's green alley program. *Procedia Eng.* 2015, *118*, 691–710.
- Couvidat, F.; Bessagnet, B.; Garcia-Vivanco, M.; Real, E.; Menut, L.; and Colette, A. Development of an inorganic and organic aerosol model (Chimere2017b2 v1.0): Seasonal and spatial evaluation over Europe. *Geosci. Model. Dev.* 2018, *11*, 165–194.

- EEA. *Air Quality in Europe—2018 Report*; EEA Report No 13/2018; European Environment Agency: Copenhagen, Denmark, 2018.
- Falasca, S.; Catalano, F.; Moroni, M. Numerical Study of the Daytime Planetary Boundary Layer over an Idealized Urban Area: Influence of Surface Properties, Anthropogenic Heat Flux, and Geostrophic Wind Intensity. *J. Appl. Meteorol. Clim.* 2016, *55*, 1021–1039.
- Falasca, S.; Catalano, F. Impact of Highly Reflective Materials on Meteorology, PM10 and Ozone in Urban Areas: A Modeling Study with WRF-CHIMERE at High Resolution over Milan (Italy). *Urban Sci.* 2018, *2*, 18.
- Fan, S.; Guo, Y.R.; Chen, M.; Zhong, J.; Chu, Y.; Wang, W.; Huang, X.Y.; Wang, Y.; Guo, Y.H. Application of WRF 3D Var to a high-resolution model over Beijing area. *Plateau Meteorol.* 2008, *27*, 1181–1188.
- Flaounas, E.; Bastin, S.; Janicot, S. Regional climate modelling of the 2006 West African monsoon: sensitivity to convection and planetary boundary layer parameterisation using WRF. *Clim. Dyn.* 2010, *36*, 1083–1105.
- Gedzelman, S.D.; Austin, S.; Cermak, R.; Stefano, N.; Partridge, S.; Quesenberry, S.; Robinson, D.A. Mesoscale aspects of the Urban Heat Island around New York City. *Theor. Appl. Clim.* 2003, *75*, 29–42.
- Glisan, J.M.; Gutowski, W.J.; Cassano, J.J.; Higgins, M.E. Effects of Spectral Nudging in WRF on Arctic Temperature and Precipitation Simulations. *J. Clim.* 2013, *26*, 3985–3999.
- Hamaoui-Laguel, L.; Meleux, F.; Beekmann, M.; Bessagnet, B.; Générumont, S.; Cellier, P.; L'Éinois, L. Improving ammonia emissions in air quality modelling for France Atmospheric Environment, 92 (2014), pp. 584-595
- Hariprasad, K.B.R.R.; Srinivas, C.V.; Singh, A.B.; Rao, S.V.B.; Baskaran, R.; Venkatraman, B. Numerical simulation and inter comparison of boundary layer structure with different PBL schemes in WRF using experimental observations at a tropical site. *Atmos. Res.* 2014, *145*, 27–44.
- He, Q.; Zhao, X.; Lu, J.; Zhou, G.; Yang, H.; Gao, W.; Yu, W.; Cheng, T. Impacts of biomass-burning on aerosol properties of a severe haze event over Shanghai. *Particuology* 2015, *20*, 52–60.
- Hu, X.-M.; Nielsen-Gammon, J.W.; Zhang, F. Evaluation of Three Planetary Boundary Layer Schemes in the WRF Model. *J. Appl. Meteorol. Clim.* 2010, *49*, 1831–1844.
- Janjic, Z. *Nonsingular Implementation of the Mellor-Yamada Level 2.5 Scheme in the NCEP Meso Model*; NCEP Office Note, No. 437; National Centers for Environmental Prediction: College Park, MD, USA, 2002; p. 61.
- Janjić, Z.I. The Step-Mountain Coordinate: Physical Package. *Mon. Weather. Rev.* 1990, *118*, 1429–1443.
- Hong, S.-Y.; Noh, Y.; Dudhia, J. A New Vertical Diffusion Package with an Explicit Treatment of Entrainment Processes. *Mon. Weather. Rev.* 2006, *134*, 2318–2341.

- Kim, Y.; Sartelet, K.; Raut, J.-C.; Chazette, P. Evaluation of the Weather Research and Forecast/Urban Model Over Greater Paris. *Bound. Layer Meteorol.* 2013, *149*, 105–132, doi:10.1007/s10546-013-9838-6.
- Kim, Y.; Sartelet, K.; Raut, J.-C.; Chazette, P. Influence of an urban canopy model and PBL schemes on vertical mixing for air quality modeling over Greater Paris. *Atmos. Environ.* 2015, *107*, 289–306.
- Kleczek, M.A.; Steeneveld, G.-J.; Holtslag, A. Evaluation of the Weather Research and Forecasting Mesoscale Model for GABLS3: Impact of Boundary-Layer Schemes, Boundary Conditions and Spin-Up. *Bound. Layer Meteorol.* 2014, *152*, 213–243.
- Kusaka, H.; Kondo, K.; Kikegawa, Y.; Kimura, F. A simple single-layer urban canopy model for atmospheric models: Comparison with multi-layer and slab models. *Bound. Layer Meteorol.* 2001, *101*, 329–358.
- Kusaka, H.; Kimura, F. Coupling a Single-Layer Urban Canopy Model with a Simple Atmospheric Model: Impact on Urban Heat Island Simulation for an Idealized Case. *J. Meteorol. Soc. Jpn.* 2004, *82*, 67–80.
- Lai, L.-W.; Cheng, W.-L. Air quality influenced by urban heat island coupled with synoptic weather patterns. *Sci. Total. Environ.* 2009, *407*, 2724–2733.
- LeMone, M.; Tewari, M.; Chen, F.; Dudhia, J. Objectively-determined fair-weather convective boundary layer depths in the ARW-WRF NWP model and their comparison to CASES-97 observations. *Mon. Weather Rev.* 2013, *141*, 30–54.
- LeMone, M.; Tewari, M.; Chen, F.; Dudhia, J. Objectively-determined fair-weather NBL features in the ARW-WRF model and their comparison to CASES-97 observations. *Mon. Weather Rev.* 2014, *142*, 2709–2732.
- Li, M.; Ma, Y.; Ma, W.; Hu, Z.; Ishikawa, H.; Su, Z.; Sun, F. Analysis of turbulence characteristics over the northern Tibetan Plateau area. *Adv. Atmos. Sci.* 2006, *23*, 579–585.
- Lin, C.-Y.; Chen, F.; Huang, J.-C.; Chen, W.-C.; Liou, Y.-A.; Chen, W.-N.; Liu, S.-C. Urban heat island effect and its impact on boundary layer development and land–sea circulation over northern Taiwan. *Atmos. Environ.* 2008a, *42*, 5635–5649.
- Lin, C.-Y.; Chen, W.-C.; Liu, S.C.; Liou, Y.A.; Liu, G.; Lin, T. Numerical study of the impact of urbanization on the precipitation over Taiwan. *Atmos. Environ.* 2008b, *42*, 2934–2947.
- Liu, Y.; Chen, F.; Warner, T.; Basara, J.B. Verification of a Mesoscale Data-Assimilation and Forecasting System for the Oklahoma City Area during the Joint Urban 2003 Field Project. *J. Appl. Meteorol. Clim.* 2006, *45*, 912–929.
- Liu, M.; Chen, M. Evaluation of BJ-RUC system for the forecast quality of planetary boundary layer in Beijing area. *J. Appl. Meteorol. Sci.* 2014, *25*, 212–221.
- Mailler, S.; Menut, L.; Khvorostyanov, D.; Valari, M.; Couvidat, F.; Siour, G.; Turquety, S.; Briant, R.; Tuccella, P.; Bessagnet, B.; et al. CHIMERE-2017: From urban to hemispheric chemistry-transport modeling. *Geosci. Model Dev.* 2017, *10*, 2397–2423.

- Markakis, K.; Valari, M.; Engardt, M.; Lacressonniere, G.; Vautard, R.; Andersson, C. Mid-21st century air quality at the urban scale under the influence of changed climate and emissions case studies for Paris and Stockholm. *Atmos. Chem. Phys.* 2016, *16*, 1877–1894.
- Martilli, A.; Clappier, A.; Rotach, M. An urban surface exchange parameterization for mesoscale models. *Bound. Layer Meteorol.* 2002, *104*, 261–304.
- Mellor, G.L.; Yamada, T. Development of a turbulence closure model for geophysical fluid problems. *Rev. Geophys.* 1982, *20*, 851–875.
- Menut, L.; Goussebaile, A.; Bessagnet, B.; Khvorostiyarov, D.; Ung, A. Impact of realistic hourly emissions profiles on air pollutants concentrations modelled with CHIMERE. *Atmos. Environ.* 2012, *49*, 233–244.
- Menut, L.; Bessagnet, B.; Khvorostyanov, D.; Beekmann, M.; Blond, N.; Colette, A.; Coll, I.; Curci, G.; Forêt, G.; Hodzic, A.; et al. CHIMERE 2013: A model for regional atmospheric composition modelling. *Geosci. Model Dev.* 2013, *6*, 981–1028.
- Miao, S.; Chen, F.; Li, Q.; Fan, S. Impacts of urban processes and urbanization on summer precipitation: A case study of heavy rainfall in Beijing on 1 Aug 2006. *J. Appl. Meteorol. Climatol.* 2010, *50*, 806–825.
- Molteni, F.; Buizza, R.; Palmer, T.N.; Petroliagis, T. The ECMWF ensemble prediction system: Methodology and validation. *Quart. J. R. Meteor. Soc.* 1996, *122*, 73–119.
- Niu, G.-Y., Yang, Z. L., Mitchell, K. E., Chen, F., Ek, M. B., Barlage, M., et al. The community Noah land surface model with multiparameterization options (Noah-MP): 1. Model description and evaluation with local-scale measurements. *Journal of Geophysical Research.* 2011, *116*, D12109.
- Oke, T. K. *Boundary Layer Climates* (2nd ed.), Rutledge, New York, 1988. p. 464
- Patricola, C.M.; Li, M.; Xu, Z.; Chang, P.; Saravanan, R.; Hsieh, J.-S. An investigation of tropical Atlantic bias in a high-resolution coupled regional climate model. *Clim. Dyn.* 2012, *39*, 2443–2463.
- Salamanca, F.; Krpo, A.; Martilli, A.; Clappier, A. A new building energy model coupled with an urban canopy parameterization for urban climate simulations—Part I. formulation, verification, and sensitivity analysis of the model. *Theor. Appl. Clim.* 2009a, *99*, 331–344.
- Salamanca, F.; Martilli, A. A new Building Energy Model coupled with an Urban Canopy Parameterization for urban climate simulations—Part II. Validation with one-dimension off-line simulations. *Theor. Appl. Clim.* 2009a, *99*, 345–356.
- Sarrat, C.; Lemonsu, A.; Masson, V.; Guedalia, D. Impact of urban heat island on regional atmospheric pollution. *Atmos. Environ.* 2006, *40*, 1743–1758.
- Toll, I.; Baldasano, J.M. Modeling of photochemical air pollution in the Barcelona area with highly disaggregated anthropogenic and biogenic emissions. *Atmos. Environ.* 2000, *34*, 3069–3084.

- Troen, I.B.; Mahrt, L. A simple model of the atmospheric boundary layer; sensitivity to surface evaporation. *Bound. Layer Meteorol.* 1986, *37*, 129–148.
- Tuccella, P.; Curci, G.; Visconti, G.; Bessagnet, B.; Menut, L.; Park, R.J. Modeling of gas and aerosol with WRF/Chem over Europe: Evaluation and sensitivity study. *J. Geophys. Res. Space Phys.* 2012, *117*, D03303.
- Tyagi, B.; Magliulo, V.; Finardi, S.; Gasbarra, D.; Carlucci, P.; Toscano, P.; Zaldei, A.; Riccio, A.; Calori, G.; D’Allura, A.; et al. Performance Analysis of Planetary Boundary Layer Parameterization Schemes in WRF Modeling Set Up over Southern Italy. *Atmosphere* 2018, *9*, 272.
- Valari, M.; Menut, L. Transferring the heterogeneity of surface emissions to variability in pollutant concentrations over urban areas through a chemistry-transport model. *Atmos. Environ.* 2014, *44*, 3229–3238.
- Vigaud, N.; Roucou, P.; Fontaine, B.; Sijikumar, S.; Tyteca, S. WRF/ARPEGE-CLIMAT simulated climate trends over West Africa. *Clim. Dyn.* 2009, *36*, 925–944.
- Wang, L.T.; Wei, Z.; Yang, J.; Zhang, Y.; Zhang, F.F.; Su, J.; Meng, C.C.; Zhang, Q. The 2013 severe haze over southern Hebei, China: model evaluation, source apportionment, and policy implications. *Atmos. Chem. Phys. Discuss.* 2014, *14*, 3151–3173.
- Wang, L.; Liu, J.; Gao, Z.; Li, Y.; Huang, M.; Fan, S.; Zhang, X.; Yang, Y.; Miao, S.; Zou, H.; et al. Vertical observations of the atmospheric boundary layer structure over Beijing urban area during air pollution episodes. *Atmos. Chem. Phys. Discuss.* 2019, *19*, 6949–6967, doi:10.5194/acp-19-6949-2019.
- Wu, J.; Zha, J.L.; Zhao, D.M.; Yang, Q.D. Changes in terrestrial near-surface wind speed and their possible causes: An overview. *Clim. Dyn.* 2017, *51*, 2039–207

Chapter V: Improvement of the vertical mixing in chemistry transport modelling based on a 1.5 order turbulence kinetic energy-based eddy diffusivity closure scheme

This chapter has been designed to be considered for publication.

Improvement of the vertical mixing in chemistry transport modelling based on a 1.5-order turbulence kinetic energy-based eddy diffusivity closure scheme

Lei Jiang^{1,2,*}, **Bertrand Bessagnet**^{1,†}, **Frederik Meleux**¹, **Frederic Tognet**¹, **Florian Couvidat**¹

¹ INERIS, National Institute for Industrial Environment and Risks, Parc Technologique ALATA, 60550 Verneuil-en-Halatte, France

² Sorbonne University, UPMC Univ Paris 06, DE129, 75005 Paris, France

[†] **Now at** European Commission, Joint Research Centre (JRC), 21027 Ispra, Italy.

Abstract

In this study, a 1.5-order turbulence kinetic energy-based eddy diffusivity closure scheme called as the new eddy diffusion (NED) is embedded in the chemical transport model CHIMERE to describe more realistic diffusion processes near the surface for urban pollution applications. A 15 days simulation including a winter pollution episode were simulated for three major French cities with fine horizontal resolution of 1.67km and first layer height 12m respectively. The NED scheme improved NO₂ simulations in every urban site compare with the initial K diffusion scheme (IKD). Taking the root mean square error as the evaluation criteria, the average improvements are 18.77%, 24.51% and 9.52% in Paris, Lyon and Bordeaux respectively for the whole period. PM_{2.5} and PM₁₀ simulation achieved same results with NO₂, a 13.47% and 19.08% improvement were found in the urban area of Paris respectively. However, the model performance for Particulate Matter in Lyon and Bordeaux probably indicate a huge underestimation of biomass burning emissions in wintertime. Sensitivity test shows that the model results are sensitive to changes of first layer height, over-refined first layer height will lead to unreasonable TKE simulations. Overall, preliminary outcomes of this study are encouraging. The simulation with more sophisticated and realistic eddy viscosities are better than IKD based on *K-theory* that is widely used in CTMs.

Résumé

Dans cette étude, un schéma de fermeture d'ordre 1.5 de la diffusion turbulente basé sur l'énergie cinétique de la turbulence, défini comme la «new eddy diffusion »(NED), est intégré dans le modèle de transport chimique CHIMERE pour décrire des processus de diffusion plus réalistes près de la surface pour étudier pollution urbaine. Une simulation de 15 jours incluant un épisode de pollution hivernale a été réalisée pour trois grandes villes françaises avec une résolution horizontale fine de 1,67km et une hauteur de première couche de 12m. Le schéma NED améliore les simulations des concentrations de NO₂ pour chaque site urbain par rapport au schéma de diffusion K initialement implante dans CHIMERE (IKD). En prenant l'erreur quadratique moyenne comme critère d'évaluation, les améliorations moyennes sont de 18,77%, 24,51% et 9,52% à Paris, Lyon et Bordeaux respectivement pour toute la période. La simulation des PM_{2.5} et PM₁₀ a donné les mêmes résultats que celle du NO₂, avec une amélioration de 13,47% et 19,08% respectivement dans la zone urbaine de Paris. Cependant, les performances du modèle pour les particules à Lyon et Bordeaux indiquent probablement une énorme sous-estimation des émissions de la combustion de la biomasse en hiver. Le test de sensibilité montre que les résultats du modèle sont sensibles aux changements de la hauteur de la première couche, une hauteur de première couche trop raffinée conduira à des simulations TKE déraisonnables. Dans l'ensemble, les résultats préliminaires sont encourageants dans cette étude. La représentation de schémas de turbulence plus sophistiqués et réalistes semble améliorer les simulations de chimie transport.

Keywords: turbulence; urban; air quality; vertical diffusion; winter episode

5.1 Introduction

Air pollution is one of the biggest public health hazards worldwide responsible for over 6 million deaths every year (Forouzanfar et al., 2016; Lim et al., 2012; Valari et al., 2020). In cities, air quality is a major concern for citizens and city managers (Baklanov et al., 2007). With the development of computer performance and a better knowledge of the meteorology and pollution sources, meteorological and air quality modelling has been widely used in the last

decades, particularly in urbanized and industrialized areas (Mailler et al., 2013). Today, High resolution mesoscale chemistry–transport models (CTM) such as CMAQ, CAMx or CHIMERE have achieved sufficient accuracy to be considered for urban air quality predictions (Byun and Schere, 2006b; Fillingham, 2019; Sokhi et al., 2018; Terrenoire et al., 2015). However, patterns of urban air pollution are rather variable and spatially heterogeneous (Wolf et al., 2020), the interactions between urban and the atmosphere remains challenges (Letzel et al., 2008), especially on modelling airflow and dispersion within the urban canopy (Baker et al., 2004). Turbulence plays an important role on the vertical mixing of pollutants and other physical parameters (Laurent Menut et al., 2013a; Pierce et al., 2010), but the representation of turbulence is difficult to predict particularly close to the ground levels. All CTMs must account the problem of turbulence, even if turbulent processes are still not fully understood: for example the statistical approaches of turbulence closure schemes used to solve the Navier-Stokes equations are not fully mature or are not always relevant for all scales due to the nonlinearity of these equations (Argyropoulos and Markatos, 2015; Novati et al., 2021). For mesoscale CTM models, the turbulent diffusion is mainly based on the gradient transport theory (*K-theory*) which is a first order turbulence closure. It defines the turbulence fluxes as analogous to molecular transport, assuming that the turbulence is a fluid cluster, which has the same properties as the molecular transport model, and a linear relationship between the gradient and the flux is thus obtained (Huang, 2019; Klimontovich, 1985). This local turbulence closure approach assumes that turbulence consists of only small eddies, causing diffusion-like transport. For example, the vertical kinematic flux $\overline{w'c'}$ of a pollutant can be modeled as being equal to an eddy thermal diffusivity K times the vertical gradient of mean concentrations \bar{c} .

$$\overline{w'c'} = -K \frac{\partial \bar{c}}{\partial z}$$

Also, the near-surface flow is complex process to simulate, the nature of turbulent transport is far from a simple linear relationship, it changes with the spatial scale of the atmospheric turbulence field and this notion of scale for turbulence is of major importance (He et al., 2019). In mesoscale model, the grid size Δ is considerably larger than the energy containing turbulence scale l , the turbulent energy is clearly in the unresolvable sub- scale. Therefore, the turbulence only needs to be parameterized instead of directly resolved. Currently, the most mainstream

turbulence parameterization method is based on the first-order local closure scheme. In Chapter II, three parameterizations were analyzed based on the first-order local closure scheme, and the results show that this concise method is feasible. However, the high pollutants concentrations are frequently found under stable atmospheric and cold weather conditions, such conditions are characterized by a stably stratified lower atmosphere and very low turbulent diffusion (Wolf-Grosse et al., 2017; Zilitinkevich and Esau, 2005). In cities, traffic and local industrial emissions have a significant share of the local pollutants, those emissions can accumulate and have longer residence times near the ground level due to low transport and mixing (Kurppa et al., 2018) which makes harder to provide an accurate prediction of pollution level and the early warning of pollution episode (PE). A way to improve the turbulence parameterization is to increase the order of the closure (Stull, 1988).

In this study we use the eddy diffusion from the 1.5-order closure TKE embedded in the Weather Research and Forecasting (WRF) model as a new vertical diffusion coefficient (K_z) in the CTM CHIMERE to describe more realistic diffusion processes near the surface for urban pollution applications. Two schemes are defined: one as the initial *K-theory* diffusion scheme in CHIMERE (IKD) and one as the new eddy diffusion (NED) scheme from WRF respectively. A high spatial resolution simulation, which is conducted for a winter period from November 20th to December 4th, 2016 over three major cities (Paris, Lyon and Bordeaux) in France was performed with the WRF / CHIMERE suite. Based on our work presented in the previous chapters, the grid resolution of the models has strong influence on pollutants prediction (Punger and West, 2013). The first step of the study is to understand the impact of vertical grid resolution on the NED simulation and find the finest vertical resolution for the following steps. Second, examples of IKD and NED simulations are investigated for the different urban environments. The results are presented in terms of model performances between the configurations for the usual criteria pollutants. The final goal of this study is to propose a more advanced diffusion scheme to improve air quality simulations and forecast over urban and peri-urban area especially on the short-term pollution events.

5.2 Model Description and Experiment Design

5.2.1 WRF and CHIMERE Model Description

As the first step of this experiment, the WRF model (Version 3.9.1) is used to provide the meteorological input data for the CTM. The initial and boundary conditions of WRF are issued from the Global Forecasting System (GFS) analysis data from the National Centers for Environmental Prediction (NCEP), available at a $0.25^\circ \times 0.25^\circ$ resolution at six-hourly time steps. In order to calculate realistic meteorological input variables and pollutant concentrations, the system is configured with four nested-grid domains in Paris, Lyon and Bordeaux (as shown in Figure 5.1) include 106×91 , 118×115 , 115×103 and 85×79 grid points, with cell sizes of 45 (d01), 15 (d02), 5 (d03), and 1.67km (d04) horizontal resolution, respectively. The domain size and resolution are the same in the three areas. Parameters setting come from the best case in Chapter III for the WRF simulation. It means: the rapid radiative transfer model for GCMs longwave radiation scheme, the rapid radiative transfer model for GCMs shortwave radiation scheme, Monin–Obukhov surface layer scheme, Noah land surface scheme, multi-layer urban canopy scheme and Bougeault and Lacarrere (Boulac) boundary layer scheme.

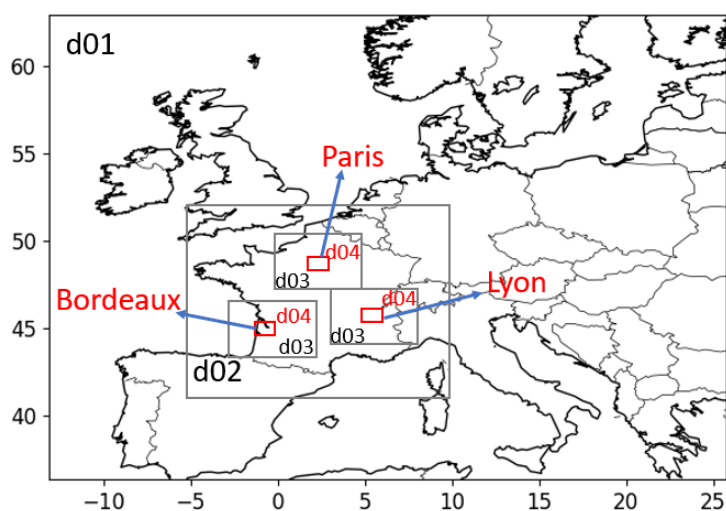


Figure 5.1 Four nested domains—from d01, the largest one, at a low resolution to d04, the finest one, at a high resolution.

The CTM model CHIMERE (Version 2013) (Menut et al., 2013) is used for air quality modeling in the present study. CHIMERE is a state-of-the-art Eulerian offline CTM model

use a mass conservative approach to reproduce pollutant chemical transformations and transport. The initial vertical diffusion of CHIMERE defined as IKD in this study is based on first order closure scheme, it is mostly controlled by the PBL height. The horizontal diffusion is neglected in CHIMERE. The PBL height is directly read from WRF and capped at a minimal value of 20m to avoid unrealistic simulations. In CHIMERE, the vertical movement diffusion is calculated using the parameterization of Troen and Mahrt (1986) but without counter-gradient term in Equation (5.1):

$$K_z = kw_s z \left(1 - \frac{z}{h}\right)^2 \quad (5.1)$$

where k is the von Karman constant set to 0.41, z is the altitude, h is the boundary layer height, and w_s is the vertical scale given by the similarity formulae, detailed explanation can be found in Chapter II. In this scheme, it can clearly see that the boundary layer height plays a crucial role in the vertical mixing, and have a direct impact on the mixing depth, height of maximum mixing and magnitude of mixing. Many studies indicate this first order closure K -theory is appropriate for mesoscale modeling particularly for neutral to weakly stable conditions. However, our previous studies have shown that during heavy pollution periods, there are huge differences in the boundary heights simulations according to different planetary boundary layer (PBL) schemes. Some of the PBL schemes cannot effectively simulate the height of the boundary layer during the pollution period, resulting in the simulation of pollutants concentrations several times the observation (Jiang et al., 2020). There are generally two ways to improve the mesoscale vertical mixing. The first is to use a higher-order local closure scheme to replace the first-order local closure. Second, the unknown quantity on the grid point can be determined by the known quantity on the grid point farther away in the vertical direction, which is called non-local closure scheme (Warner, 2010).

In WRF, the commonly used 1.5 order local mixing PBL schemes including Mellor-Yamada-Janjic (MYJ), Mellor-Yamada Nakanishi and Niino Level 2.5 (MYNN2) and Boulac scheme, the nonlocal mixing PBL schemes including Yonsei University (YSU) and asymmetric convective model V2 (ACM2) PBL schemes. The TKE order-1.5 model was

calculated from Boulac PBL scheme defined as NED scheme in this study. Figure5.2 shows the general principle of the NED simulation. The computation strategy of NED can be separated into the following sequential steps:

- i. Activation of the vertical eddy viscosity in the WRF code as is not the default output variable of the model;
- ii. Calculate K_z of NED in WRF simulation based on Boulac PBL scheme;
- iii. Pre-processing in CHIMERE: Interpolate NED to CHIMERE;
- iv. Initialization phase of CHIMERE simulation, replacing IKD with NED;
- v. Launch the main step of CHIMERE simulation and get all output variables based on NED.

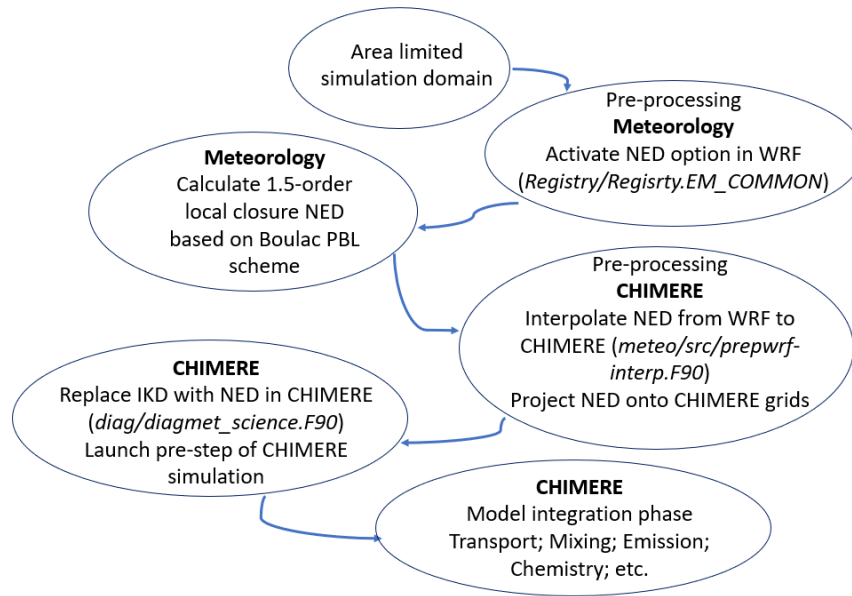


Figure5.2 General principle of the NED simulation

The Reynolds decomposition prognostic equation for TKE e under the assumptions of horizontal homogeneity can be written as (5.2):

$$\frac{\partial e}{\partial t} = -\frac{\partial}{\partial z} \left(\overline{w'e} + \frac{\overline{w'p'}}{\rho_0} \right) + \frac{g}{\theta_{v0}} \overline{w'\theta_v} - \left(\overline{w'u'} \frac{\partial v}{\partial z} + \overline{w'v'} \frac{\partial u}{\partial z} \right) + \varepsilon \quad (5.2)$$

Where u , v , w are the wind components, θ_v is the mean virtual potential temperature, p is the pressure, ρ_0 is the density, g is the gravitational acceleration and ε is the viscous dissipation of TKE (Stull, 1988).

The TKE order-1.5 is also constructed upon the gradient transport theory as (5.3):

$$\overline{w\phi} = -K \frac{\partial \phi}{\partial z} \quad (5.3)$$

The left side represents the Reynolds-average operator, the vertical turbulent flux $\overline{w\phi}$ is parameterized as the product of local gradient of analytical variable ϕ and eddy diffusivity K . In Boulac scheme, vertical eddy diffusivity defined as (5.4):

$$K_z = C_k l \sqrt{e} \quad (5.4)$$

Where C_k is a constant set up to 0.7, l is the vertical length scale (Deardorff, 1980), and e is the TKE defined as (5.5):

$$e = \frac{1}{2} (\overline{u'^2} + \overline{v'^2} + \overline{w'^2}) \quad (5.5)$$

In the Boulac scheme, it is assumed that at individual level in the atmosphere, the length scale l may be related to the distance that the parcel originating from the corresponding level and having the initial kinetic energy equal to the average TKE of the layer which can move up and down before being prevented by the buoyancy effect. The l_{up} and l_{down} is defined as (5.6):

$$\begin{aligned} \int_Z^{Z+l_{up}} \beta(\theta(Z) - \theta(Z')) dZ' &= e(Z) \\ \int_{Z+l_{down}}^Z \beta(\theta(Z) - \theta(Z')) dZ' &= e(Z) \end{aligned} \quad (5.6)$$

Thus, the length scale l must be related to some value between l_{up} and l_{down} . In Boulac scheme, the l is written as (5.7):

$$l = \sqrt{l_{up} l_{down}} \quad (5.7)$$

The advantage of this scheme is to allow for remote effects of stable zones to define the turbulence mixing length scale (Bougeault and Lacarrere, 1989). This scheme solves a prognostic TKE equation which includes TKE advection and parameterizes sources and sinks from shear production, buoyancy, mixing and dissipation (Simon et al., 2019). The model physical parameterizations remain the same as Boulac-BEP scheme detailed in Chapter III, (see Table3.1 of Chapter III).

5.2.2 Domains Setup and Observations Data

Previous Chapter indicates the first layer height plays an important role in chemistry transport modelling. In order to understand the impact of the first layer height on TKE prediction, for the first step of this study, the WRF vertical grid is discretized vertically on 53, 51 and 49 vertical levels from 999.5hPa, 998.5hPa and 995hPa to the top in Paris region. The three model configurations are defined:

- (i) H4: 53 vertical layers are defined in WRF and 20 vertical layers are defined in CHIMERE. The first layer of the two model is at 999.5hPa (approximately 4m) up to over 500hPa;
- (ii) H12: 51 vertical levels are defined in WRF and 20 levels are defined in CHIMERE, starting with the first vertical height at about 12 meters above the ground;
- (iii) H40: 49 vertical levels are defined in WRF and 20 vertical layers are defined in CHIMERE from 995hPa to 500hPa, starting with the first vertical height at about 40 meters above the ground;

To take full advantage of the physical parameterizations, the CHIMERE simulation is performed with the same horizontal resolution as the WRF; the vertical levels from the WRF simulation are projected onto 20 levels in CHIMERE the namelist can be found in Annex B List.1.

Two types of observation data are used in the present study: (i) the meteorological observation stations (MOS) operated by METEO FRANCE were used to evaluate the simulated meteorological variables from the model; and (ii) the hourly surface concentrations of criteria pollutants (NO_2 , O_3 , $\text{PM}_{2.5}$, and PM_{10}) issued from AIRPARIF, the official Paris air quality monitoring network. It is not usual to discuss O_3 during wintertime, but O_3 can reacts with nitrogen oxide (NO) to form NO_2 , this will be insightful to better understand the chemical regimes. The location of the meteorological observation stations and the air quality monitoring stations (AQS) can be found in Figure5.3.

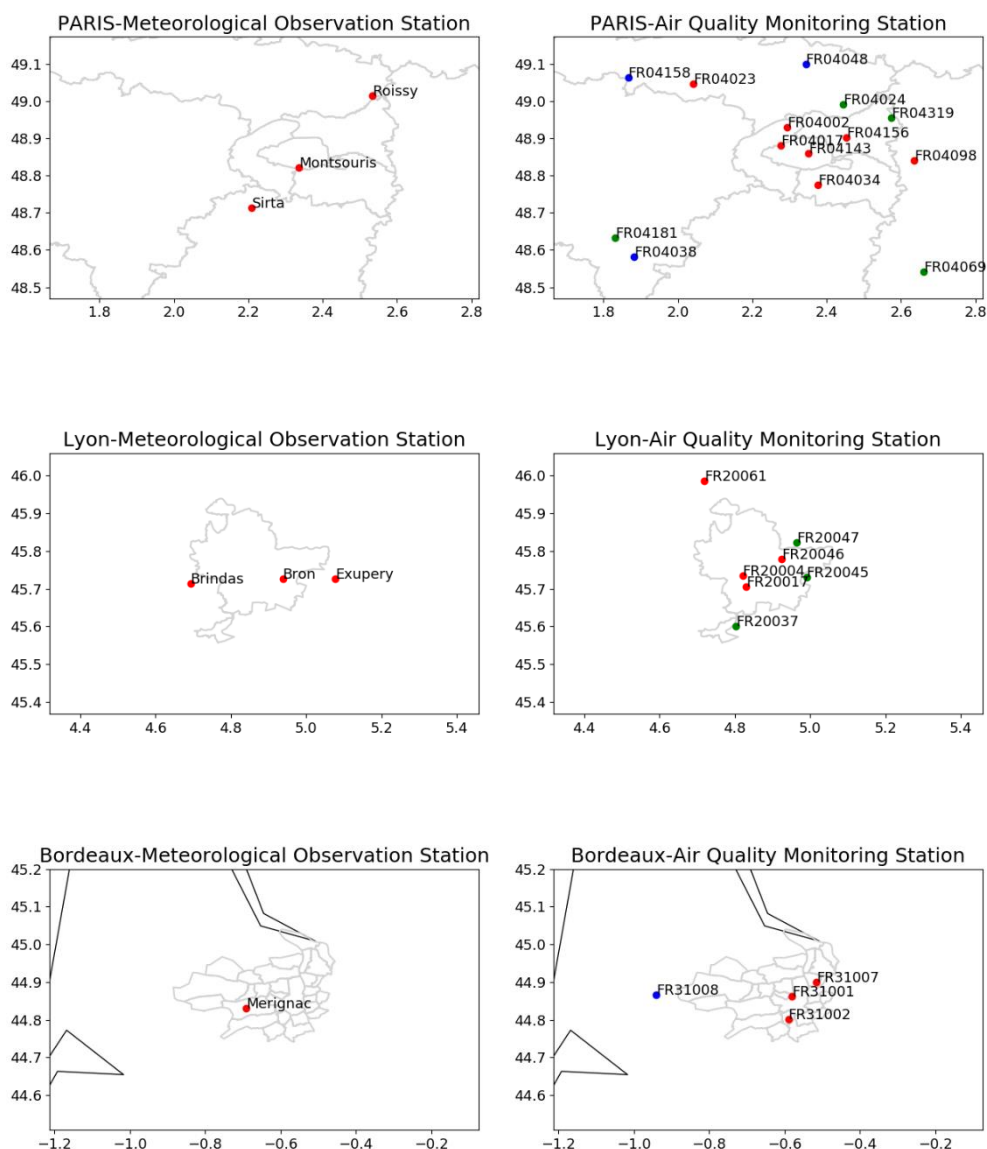


Figure 5.3 Maps of the meteorological and air quality monitoring stations. Red dots represent urban background station; green dots represent suburban background station and blue dots represent rural background station.

5.3 Results and Discussions

5.3.1 Impact of the first layer height on NED modelling

Three vertical grids are tested to study the sensitivity and impact of the first layer height performed with the WRF and CHIMERE, from 27th November to 4th December 2016 over Paris region.

The aim is to quantify the variability in the surface pollutants concentrations results by implementing the NED scheme in the mesoscale CTM which would be more representative to the simulation of air flow and pollutant dispersion in urban atmosphere particularly on the PE.

Figure5.4 gives the vertical diffusion coefficient in urban and rural area. The K_z profiles show different shapes and magnitudes between H4, H12 and H40. The values of diffusivity are relatively poor at low levels from H4 scheme and do not exceed $0.12\text{m}^2/\text{s}$ on the first layer in both urban and rural area. H12 gives $0.71\text{m}^2/\text{s}$ and $0.25\text{m}^2/\text{s}$ in urban and rural area with is approximately 7 and 2 times than H4. H40 reaches the maximum diffusion rate since the first layer and decreasing with the increasing altitudes. For all schemes and regions, the most important differences are in the low layers, showing that the point close to the surface generates a complex mixing under different first layer height.

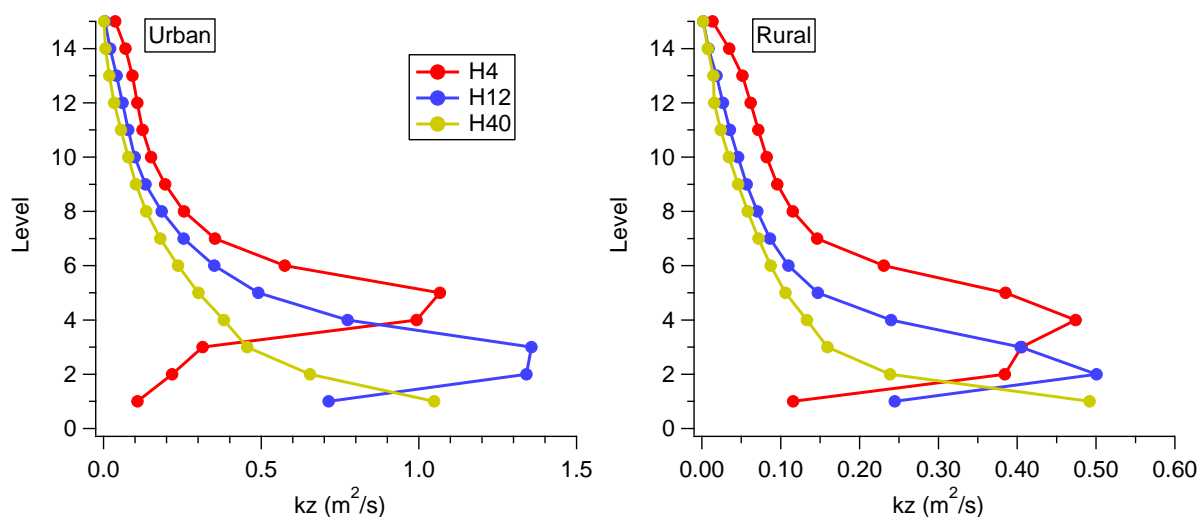


Figure5.4 Vertical profiles of the CHIMERE K_z from NED scheme extracted at the FR04143 station.

Taking NO_2 as the reference pollutant, Figure5.5 gives the surface NO_2 mass concentrations in urban and rural background station between observation and three sensitivity simulations. It is noteworthy that the models capture well the evolution of NO_2 concentrations over the urban and rural stations, these first results show that implementing a more advanced scheme is feasible. H4 strongly overestimates NO_2 concentrations for the whole period in the urban regions, the reason is the strong underestimation of K_z at lower levels. Table5.1 lists the correlation (R), mean bias (MB) and root mean square error (RMSE) of each sensitivity

studies. H12 displays a more reasonable behavior of NO_2 than the two other grid and will be used as the model configuration of vertical grid resolution for the following steps. This sensitivity test indicates the first layer height is crucial on TKE parameterization, an extra fine first layer height at 4m does not produce better simulation results.

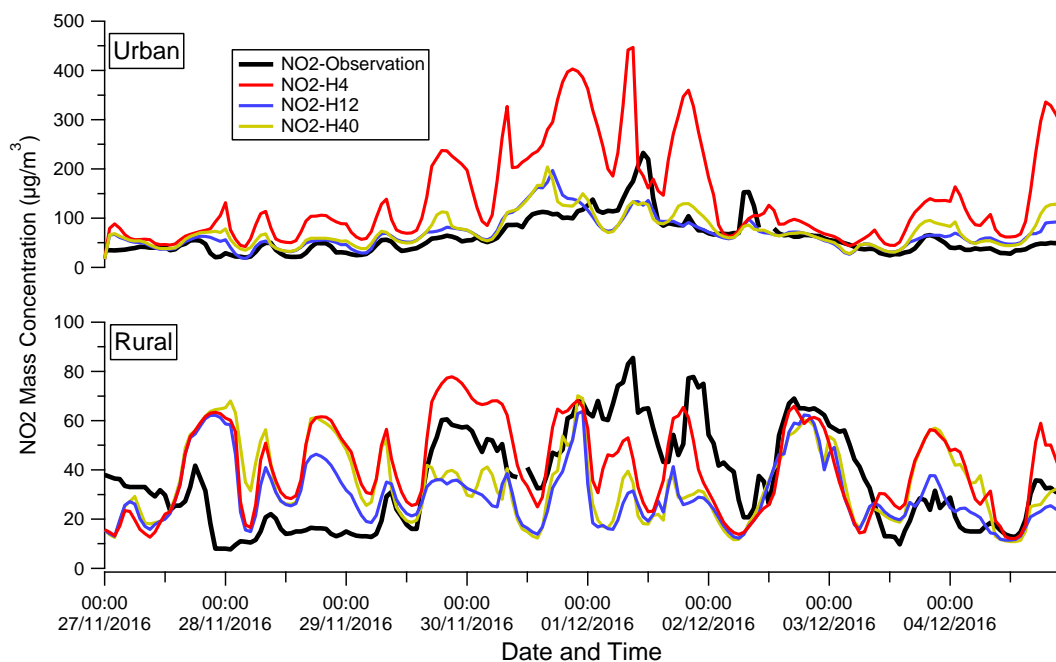


Figure 5.5 Time series between observed and modelled NO_2 mass concentrations ($\mu\text{g}/\text{m}^3$) from NED scheme in urban and rural background stations in Paris region.

Table 5.1 The correlation (R); mean bias (MB) and root mean square error ($RMSE$) between Observation and simulation of NO_2 in four urban and rural background stations over Paris region.

	L4			L12			L40		
	R	MB	RMSE	R	MB	RMSE	R	MB	RMSE
Urban	0.62	78.71	112.87	0.77	7.89	25.89	0.70	13.21	31.14
Rural	0.37	5.40	21.90	0.44	-6.21	21.84	0.33	-1.73	24.31

5.3.2 NO_2 and O_3 Simulations over Paris region

5.3.2.1 NO_2 and O_3 simulations in urban background stations

Road traffic emission is the largest contribution to NO_2 concentrations in urban areas (Dragomir et al., 2015; Lee et al., 2014; Palmgren et al., 1996). The mean first layer NO_2 and O_3 mass concentrations and K_z over the period are shown in Figure 5.6. The results show that the absolute values are different between the IKD and NED scheme, the regional patterns are

similar for the K_z and the two pollutants. It is clear that the results over urban areas exhibit the role NO_2 emissions on NO_2 concentrations. The K_z simulated by the NED method is significantly lower than the IKD scheme in the entire region. The average surface K_z from NED scheme is $1.13\text{m}^2/\text{s}$ in the urban region with is approximately half of the IKD scheme ($2.50\text{m}^2/\text{s}$), this value is similar to our plan of dividing K_z by 2 in urban areas since the Version-2017 of CHIMERE. Consequently, the NED scheme runs generates remarkably higher surface NO_2 concentration by $6.93\mu\text{g}/\text{m}^3$ on average in urban area. The spatial differences for O_3 mass concentration between IKD scheme and NED scheme are more substantial than for NO_2 . The O_3 and NO_2 maps show that the area with maximum NO_2 increase coincide well with that of sharp O_3 reduction due to the titration effect. (Yao et al., 2005) indicated that the contribution of direct NO_2 emissions to the atmospheric NO_2 concentration is low, the NO_2 concentrations mainly comes from the oxidation of NO . The chemical reaction involving NO with O_3 plays an important role in the formation of NO_2 (Song et al., 2011), even in winter.

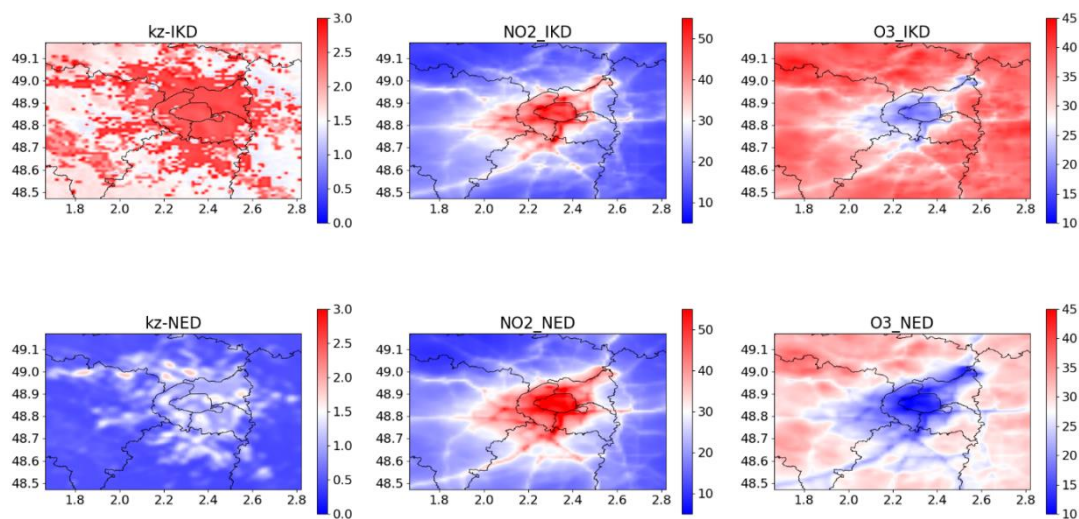


Figure 5.6 Maps of the mean vertical diffusion coefficient (m^2/s) at first layer; mean surface NO_2 mass concentration ($\mu\text{g}/\text{m}^3$) and mean surface O_3 mass concentration ($\mu\text{g}/\text{m}^3$) over the period from 20th November to 4th December. The first line: results from IKD scheme; the second line: results from NED scheme.

Figure 5.7 shows the time series of hourly averaged mass concentrations of NO_2 and O_3 , from all urban background stations from November 20th to December 4th 2016. The index of

agreement between observed and modelled NO_2 can be found in Annex B Figure S5.1. Relatively high NO_2 concentrations were observed in all four urban background stations, with a mean concentration of $53.45 \mu\text{g}/\text{m}^3$; $50.05 \mu\text{g}/\text{m}^3$; $52.47 \mu\text{g}/\text{m}^3$; $49.66 \mu\text{g}/\text{m}^3$ in FR04002; FR04034; FR04143; FR04156 station, respectively. Table 5.2 lists the performances of NO_2 simulation for both schemes with their average mass concentration (Avg); correlation (R); mean bias (MB) and root mean square error (RMSE) at each station. The results show that the period is well modelled by the IKD scheme with the correlation from 0.62 to 0.74 among stations. However, this scheme seems underestimated NO_2 concentration in all stations, this is mainly because of the underestimation during the PE. The performance of NED scheme is very satisfactory and improves NO_2 simulations for most of stations. Taking the relative changes in RMSE as the evaluation criteria, the largest improvements occur for FR04034 station (the improvement is of 19.22%). The averaged time series and statistics for the urban background stations are summarized in Figure S5.2 and Table S5.1. The two schemes capture quite well the evolution of NO_2 concentration over the urban region, the R and MB are 0.74 and $-10.40 \mu\text{g}/\text{m}^3$ for IKD scheme and 0.80 and $-3.80 \mu\text{g}/\text{m}^3$ for NED scheme with the improvement is of 18.77% in the urban area. It is noteworthy that both schemes give a better performance in the city center station (FR40143) than others, it may indicate categories of urban area are not enough detailed in the model, which might help assessing the urban categories and roughness length for the model in the urban area. The performances of O_3 simulation from IKD and NED schemes are quite different according to their performances of NO_2 simulation. The IKD scheme gives a clearly better performance in the first three days of the period. Subsequently, both schemes significantly overestimate the O_3 concentration at all urban background stations until 27th November. Previous researches reported that surface O_3 concentrations in wintertime are highly correlated to reduced photochemical activity (Chen et al., 2020; Peshin et al., 2017). Therefore, the overestimation of O_3 may be due to underestimation of cloud thickness in this period. Table 5.3 provides an overall evaluation for IKD and NED schemes for the urban stations. O_3 concentrations are on average overestimated particularly for the IKD scheme. However, the time series shows that the O_3 concentration is strongly overestimated in some days, therefore the MB cannot well represent the simulation accuracy of two schemes for O_3 . Unlike the results of NO_2 simulation, the IKD scheme gives

a better correlation and RMSE in all stations than NED scheme. The NED scheme resulted in 4.05%, 9.12%, 1.27% and 13.86% drops in O₃ simulation accuracy in four urban stations.

Figure 5.7 also shows the ability of the model to locate the pattern of the PE but also a clear underestimation of NO₂ concentrations during the PE for all stations. At most of the sites, the peak NO₂ concentration occurred during the daytime on December 1st, the NO₂ exceeded 200 µg/m³ in the observations but the model does not effectively capture this moment with both schemes. The average mean bias in urban background stations for IKD and NED schemes during the PE are -39.88 µg/m³ and -24.16 µg/m³ respectively, showing a better ability of the NED simulation to reproduce primary pollutant concentrations

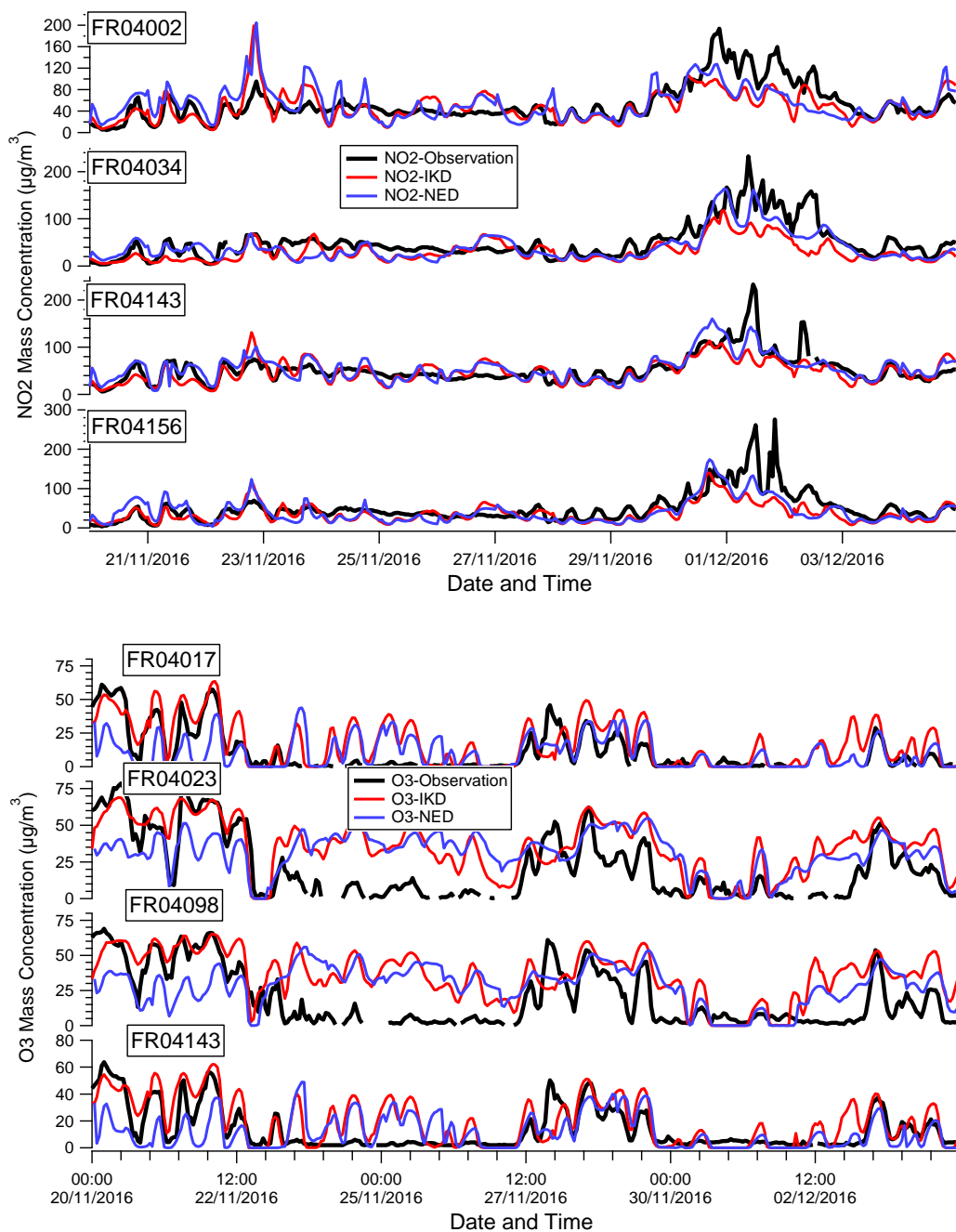


Figure 5.7 Time series between observed and modelled NO₂ and O₃ mass concentrations (µg/m³) in urban background stations.

Table5.2 Average modelled NO₂ mass concentrations (Avg); the correlation (R); mean bias (MB) and root mean square error (RMSE) between Observation and simulation of NO₂ in four urban background stations over Paris region.

	IKD				NED				improvement ^a
	Avg	R	MB	RMSE	Avg	R	MB	RMSE	
FR04002	48.34	0.62	-5.11	28.09	54.39	0.57	0.94	30.29	-7.83%
FR04034	31.12	0.74	-18.93	32.05	40.04	0.78	-10.01	25.89	19.22%
FR04143	47.98	0.67	-4.49	23.68	55.38	0.78	2.91	20.21	14.65%
FR04156	36.79	0.69	-12.87	30.68	40.81	0.72	-8.85	28.23	7.99%

a: The “improvement” is the relative change in % of the RMSE by using the initial Kz diffusion (IKD) coefficient and by using the new eddy diffusion (NED) coefficient.

Table5.3 Average modelled O₃ mass concentrations (Avg); the correlation (R); mean bias (MB) and root mean square error (RMSE) between Observation and simulation of O₃ in four urban background stations over Paris region.

	IKD				NED				improvement
	Avg	R	MB	RMSE	Avg	R	MB	RMSE	
FR04017	17.45	0.73	5.30	13.82	10.33	0.67	-1.82	14.38	-4.05%
FR04023	35.81	0.70	14.05	22.25	31.16	0.64	9.40	24.28	-9.12%
FR04098	35.81	0.63	16.23	23.64	28.62	0.54	9.04	23.94	-1.27%
FR04143	19.25	0.73	5.83	13.35	11.59	0.66	-1.83	15.20	-13.86%

5.3.2.2. Diurnal cycles of the surface K_z, NO₂ and O₃

In order to deeply investigate the differences between the schemes, the diurnal cycles are calculated for K_z, NO₂ and O₃ for the corresponding surface observations at the urban background stations over the Paris region. Figure5.8(a) illustrates the mean diurnal K_z on urban regions. The diurnal variation of the surface K_z throughout the schemes shows similarities, K_z remains flat in the morning and nighttime and a peak is simulated around 12:00. The average K_z on the unstable condition from IKD scheme is approximately 1.7 times than NED scheme and approximately three times higher on the stable condition. The bimodal distribution of the surface NO₂ concentration are observed and simulated during this period, with the morning peak around 8:00–9:00 and the evening peak around 18:00–19:00. Both schemes capture the fluctuations quite well, but IKD scheme strongly underestimates NO₂ concentrations in the early morning. The results of the Chapter II prove that the IKD scheme overestimates the vertical diffusion rate in urban areas. This section further demonstrates that

the overestimation of vertical diffusion under stable conditions is higher than under unstable conditions in IKD. The NED scheme simulation overestimates NO_2 concentration at nighttime, the reason should be the overestimation of K_z drop after 14:00. Figure 5.8(c) displays the diurnal cycles of surface O_3 concentrations, both schemes well predicts the diurnal evolution of O_3 but with an overestimate all the day long. Due to the overestimation of the O_3 diurnal cycles, the time series illustrates that the model strongly overestimates O_3 concentrations from 23rd November to 27th November. There is a positive correlation between peak values of NO_2 and low values of O_3 concentrations, this result once again confirmed that O_3 take part in the oxidation reaction of NO .

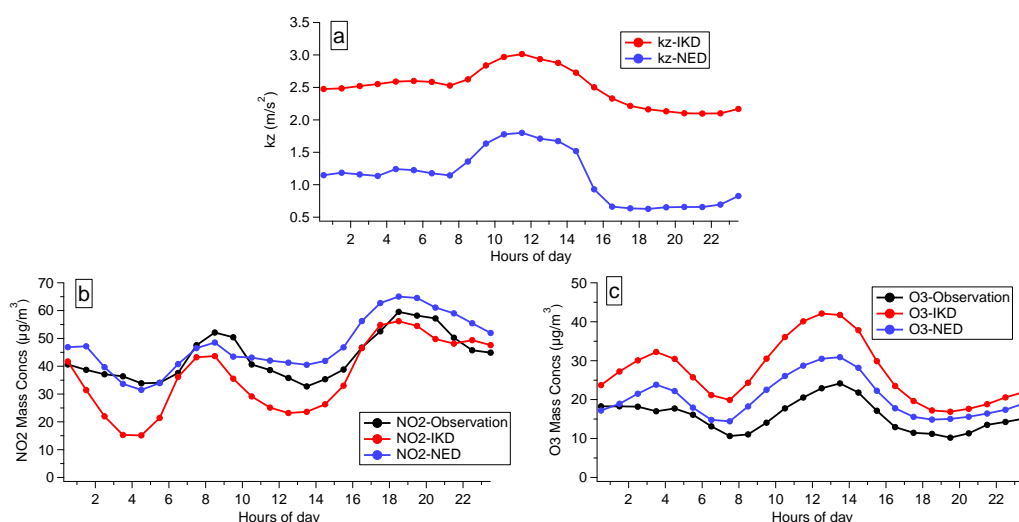


Figure 5.8 Diurnal cycles for surface K_z and surface concentrations of O_3 and NO_2 ($\mu\text{g}/\text{m}^3$) from 20th November to 4th December in urban background stations.

5.3.2.3. NO_2 Simulations in suburban and rural background stations

Figure 5.9(a) and Figure 5.9(b) gives the time series of hourly averaged mass concentrations of surface NO_2 and O_3 in background suburban stations and background rural stations respectively. The surface NO_2 concentration in suburban and rural sites are the average data from two background suburban stations (FR04024 and FR04319) and one background rural station (FR04038). The surface O_3 concentration in suburban and rural sites are the average data from two background suburban stations (FR04181 and FR04319) and three background rural

stations (FR04038; FR04048 and FR04158). Overall, both schemes show their ability capture the majority of fluctuations for NO_2 . The performance of O_3 prediction in suburban and rural sites are similar with urban areas, both schemes significantly overestimates the O_3 concentration during daytime of 23rd November to 27th November. The NED scheme underestimates O_3 concentration for the first three days. Table 5.4 reports the average concentration, R, MB and RMSE for both schemes and the improvement by using the NED scheme compared with the IKD in suburban and rural sites over the Paris region. The NED scheme slightly improved the NO_2 and O_3 prediction in suburban area but displays a poor performance in rural areas. Figure 5.6 indicates that average K_z from NED scheme is around $0.3 \text{ m}^2/\text{s}$ in rural areas, this value is underestimated in NED scheme. However, there is only one background rural station of NO_2 in this region, therefore the result could be not robust enough.

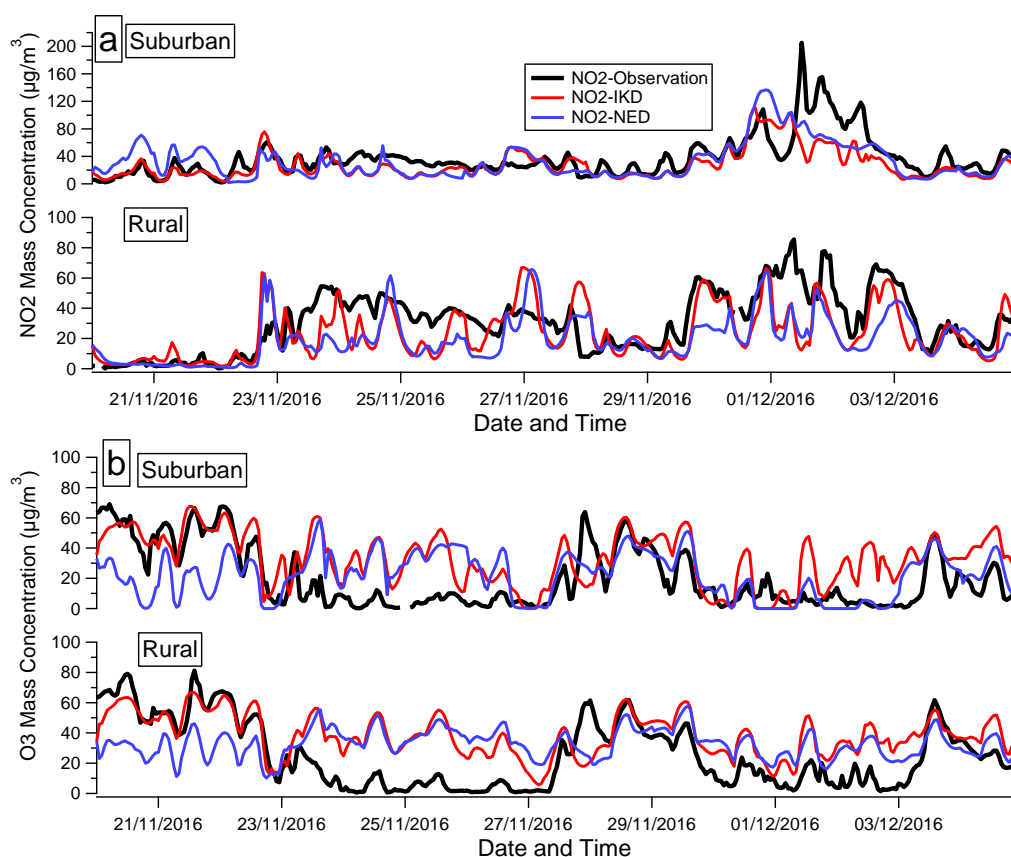


Figure 5.9 Time series between observed and modelled NO_2 and O_3 mass concentrations ($\mu\text{g}/\text{m}^3$) suburban background stations and rural background stations.

Table 5.4 Average modelled NO₂ and O₃ mass concentrations (Avg); the correlation (R); mean bias (MB) and root mean square error (RMSE) between Observation and simulation of NO₂ and O₃ in suburban and rural background stations over Paris region.

	IKD				NED				improvement
	Avg	R	MB	RMSE	Avg	R	MB	RMSE	
Suburban-NO₂	27.58	0.71	-10.40	24.95	32.76	0.69	-3.80	24.56	1.56%
Rural-NO₂	23.62	0.64	-9.62	17.13	19.50	0.61	-4.44	19.07	-11.33%
Suburban-O₃	37.77	0.61	17.65	21.33	21.80	0.45	1.68	20.97	1.69%
Rural-O₃	38.36	0.68	13.19	20.85	32.85	0.34	7.68	24.02	-15.02%

5.3.3 PM2.5 and PM10 Simulations over Paris region

In Figure 5.10, surface PM2.5 and PM10 concentrations are illustrated for IKD and NED schemes. The surface concentration fields show a gradient between the urbanized area surroundings in both schemes but not as strong as for NO₂ surface distributions, this result is expected because PM2.5 and PM10 is much more influenced by regional transport and peri-urban and rural emissions from biomass burning. The PM2.5 and PM10 surface concentrations from NED scheme is approximately 4.4 $\mu\text{g}/\text{m}^3$ and 4.2 $\mu\text{g}/\text{m}^3$ higher on average than the IKD scheme.

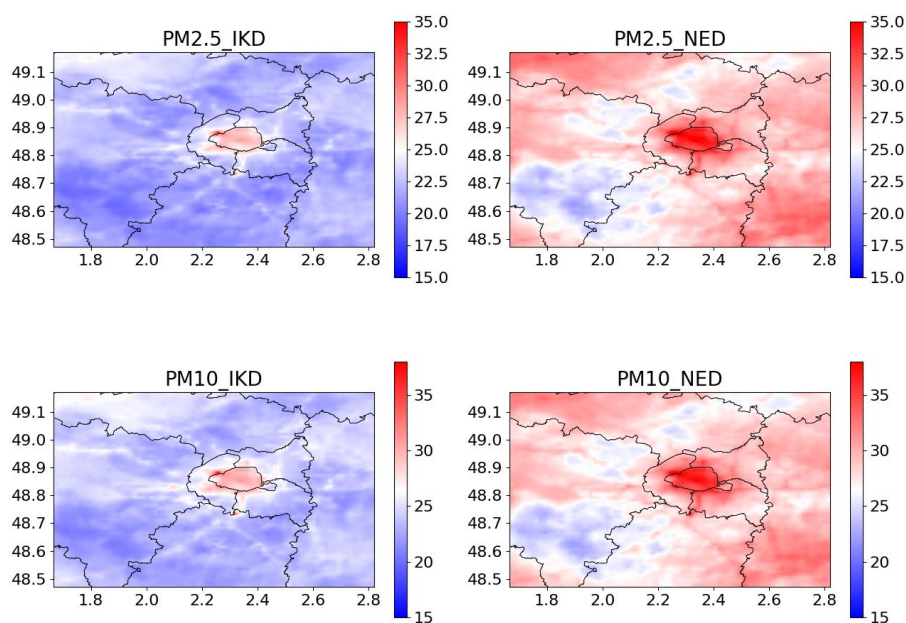


Figure 5.10 Maps of the mean surface PM2.5 and PM10 mass concentration ($\mu\text{g}/\text{m}^3$); over the period from 20th November to 4th December.

Figure 5.11 displays a comparison between the observed and modeled surface PM_{2.5} and PM₁₀ at urban sites. The linear regression of PM_{2.5} and PM₁₀ concentrations between observation and simulation can be found in Figure S5.3 and Figure S5.4 respectively. The direct comparison shows a fair reproduction of PM_{2.5} and PM₁₀ concentrations during the RD but the models underestimate the concentrations on the PE. The fluctuations of PM_{2.5} and PM₁₀ at Paris center station (FR04143) is obviously different with others which indicate that the emissions of PM at the center of the city is different with other sites, traffic emissions should be the major source of the FR04143 station. This also can be confirmed throughout the comparison between the fluctuations of NO₂ and PM in the corresponding station. Both schemes display similar behavior for the simulated period and display a reasonable representation of PM_{2.5} and PM₁₀ observations. The simulation of PM₁₀ is good on regular days but the model tends to slightly overestimate PM_{2.5} concentration at the same time. It indicates the slight overestimation of fine particles in the model. Two schemes underestimated PM concentration during the PE, the NED scheme gives a higher PM_{2.5} and PM₁₀ concentrations than IKD scheme, which tends to be closer to the observations on the PE and the peaks of PM_{2.5} and PM₁₀ are also enhanced from NED. As shows in Table 5.5 and

Table 5.6, the striking result is that the NED scheme impressively improves the PM_{2.5} and PM₁₀ simulation at urban sites. Based on RMSE indicator, the improvements are almost more than 10% in every urban background station and the correlation are also significantly improved in the urban sites. At suburban sites, NED scheme slightly improved both PM_{2.5} and PM₁₀ simulation compared to the IKD scheme but IKD had slightly better performances in the rural areas.

We also notice that the underestimation of PM₁₀ is obviously higher than PM_{2.5} during the PE. Table 5.7 reports the ratio between PM_{2.5} and PM₁₀ during the whole period (WP) and PE in urban, suburban and rural areas. The location of suburban and rural PM_{2.5} monitoring stations are not completely matched with PM₁₀ monitoring stations. Thus, the ratio PM_{2.5}/PM₁₀ for suburban and rural sites are given for guidance, we focus here on urban sites only. There is no evident variation of this ratio on the PE for both observation and simulations,

but the ratio is approximately 70% for the observation and around 90% for both simulations. Considering the overestimation of fine particles concentrations, this result shows that model have a strong underestimation of PM with particles exceeding $2.5\ \mu\text{m}$. The model displays a reasonable behavior for both $\text{PM}_{2.5}$ and PM_{10} on the PE, this indicates that the underestimation of pollutants on the PE is due to the underestimation of local urban pollutions sources, vehicle emission and other local sources should play important roles on this period.

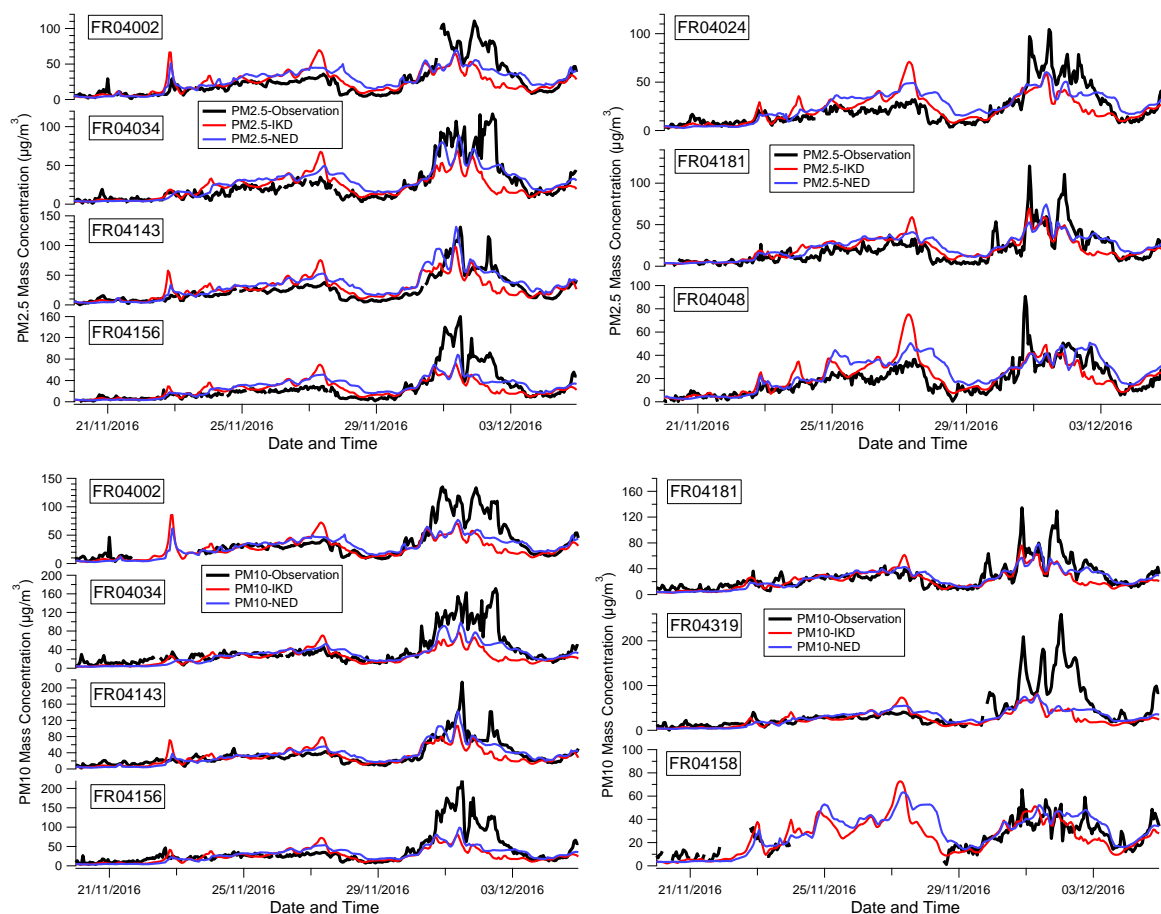


Figure 5.11 Time series between observed and modelled $\text{PM}_{2.5}$ and PM_{10} mass ($\mu\text{g}/\text{m}^3$) in urban; suburban and rural background stations. Urban background stations: FR04002; FR04034; FR04143 and FR04156. Suburban background stations: FR04024 and FR04181 for $\text{PM}_{2.5}$ simulation and observation; FR04181 and FR04319 for PM_{10} simulation and observation. Rural background stations: FR04048 for $\text{PM}_{2.5}$ simulation and observation; FR04158 PM_{10} simulation and observation.

Table5.5 Average modelled PM_{2.5} mass concentrations (Avg); the correlation (R); mean bias (MB) and root mean square error (RMSE) between Observation and simulation of PM_{2.5} in urban, suburban and rural background stations over Paris regions.

		IKD				NED				improvement
		Avg	R	MB	RMSE	Avg	R	MB	RMSE	
Urban	FR04002	24.17	0.63	-1.35	18.23	27.69	0.74	2.17	16.22	11.03%
	FR04034	22.18	0.62	-3.34	20.27	27.28	0.81	1.76	15.59	23.09%
	FR04143	27.93	0.72	2.41	16.26	32.66	0.86	7.13	14.38	11.56%
	FR04156	23.53	0.66	-2.77	22.74	27.42	0.74	1.12	20.88	8.18%
Suburban	FR04024	21.82	0.64	-0.51	14.72	25.70	0.73	3.38	13.46	8.56%
	FR04181	20.98	0.75	1.10	12.27	23.66	0.77	3.78	12.02	2.04%
Rural	FR04048	21.61	0.70	2.82	10.96	24.71	0.84	5.92	11.51	-4.78%

Table5.6 Average modelled PM₁₀ mass concentrations (Avg); the correlation (R); mean bias (MB) and root mean square error (RMSE) between Observation and simulation of PM₁₀ in urban, suburban and rural background stations over Paris regions.

		IKD				NED				improvement
		Avg	R	MB	RMSE	Avg	R	MB	RMS	
Urban	FR04002	26.56	0.66	-10.98	25.76	29.7	0.76	-7.82		14.29%
	FR04034	24.15	0.62	-13.42	30.38	29.26	0.80	-8.31	23.44	22.84%
	FR04143	30.34	0.70	-4.50	21.38	34.91	0.86	0.07	15.19	28.95%
	FR04156	25.70	0.70	-12.16	33.55	29.38	0.77	-8.48	30.11	10.25%
Suburban	FR04181	22.55	0.76	-4.76	14.35	24.86	0.78	-2.45	13.18	8.88%
	FR04319	25.34	0.57	-15.92	39.58	29.39	0.66	-11.87	36.60	7.53%
Rural	FR04158	24.91	0.81	-3.20	24.57	28.60	0.84	0.37	22.44	-8.07%

Table5.7 Proportion between PM_{2.5} and PM₁₀ in urban, suburban and rural background stations for the whole period (WP) and pollution episode (PE) over Paris regions.

	Obs	WP		Obs	PE	
		IKD	NED		IKD	NED
Urban	70.73%	91.61%	93.31%	71.27%	88.35%	90.49%
Suburban	61.73%	89.35%	90.96%	59.22%	85.04%	86.22%
Rural	78.24%	86.75%	86.40%	86.19%	89.56%	92.29%

5.3.4 Study in Lyon and Bordeaux regions

The IKD and NED schemes are also applied in Bordeaux and Lyon areas in order to understand whether the NED scheme can be used in other areas. Lyon is in the southeast of France and is located in the Rhone valley where the wind is meridional and often strong particularly in winter and is the second largest city in France. Bordeaux is close to the sea that is often influenced by oceanic flows and located in the southwest part of France. The period of interest remains the same from 20th November to 4th December.

5.3.4.1. Ground Meteorological Variables

Here, we compared observation of 2 meters temperature (T2) and 10 meters wind speed (W10) from four meteorological observation sites (three in Lyon and one in Bordeaux) to the simulations from WRF. The comparison is of hourly average values from observation sites with hourly average values from the nearest of each site location. Figure 5.12 presents the maps of averaged T2 and W10 simulated in Lyon and Bordeaux over the period. Both regions show a UHI effect in the urban region, which gives positive bias of up to 3 °C over the period in Lyon and 2.5 °C in Bordeaux respectively compared to the rural areas. The maps of W10 presents a higher surface wind speed in rural areas than in urban regions with a negative bias for 3.2m/s in Lyon and 3.5m/s in Bordeaux respectively. The City of Lyon is formed by the core city of Lyon and its 58 suburban municipalities, so the UHI effect is more widespread than Bordeaux.

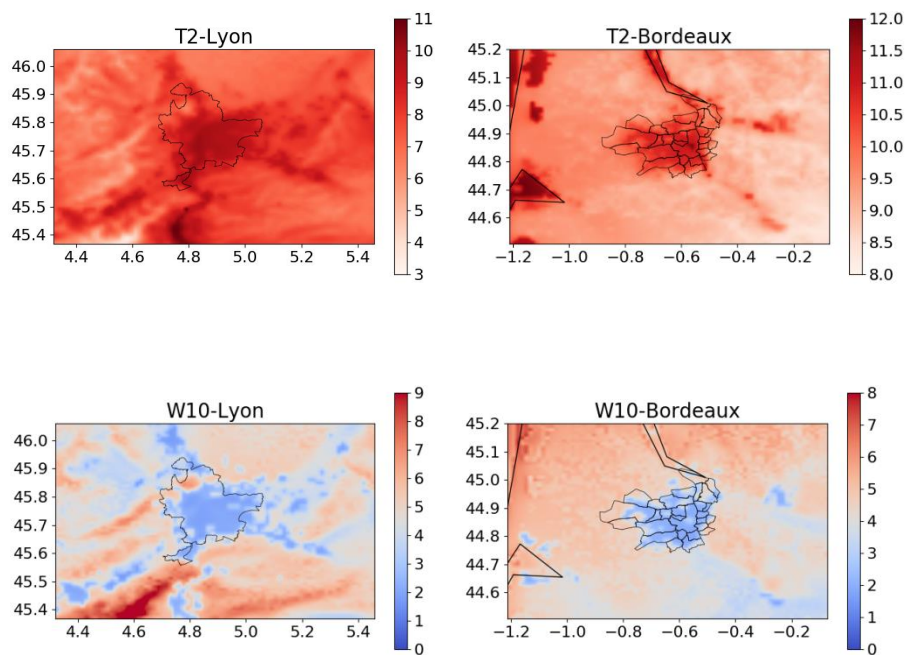


Figure 5.12 Maps of the mean 2m temperature ($^{\circ}\text{C}$) and 10m wind speed (m/s) over the period from 27th November to 4th December.

Figure 5.13 presents the time series of hourly-averaged T2 and W10 for the whole period. T2 overall shows a decreased tendency throughout the period and the model effectively captures this trend. Compared with the observations, the model tends to overestimate the T2 for all stations, with a positive bias for 2.36°C in Lyon and 2.16°C in Bordeaux during this period and a positive bias for 3.09°C in Lyon and 2.70°C in Bordeaux on the PE. The diurnal differences for W10 are relatively low in Lyon, the models overestimate the wind speed in Lyon, with a positive bias for 2.76m/s for the whole period and 0.77m/s on the PE, the main bias of W10 simulation come from the overestimation from the first four days of the period. In Bordeaux, W10 simulation is closed to the observation, with a negative bias for -0.48m/s for the whole period and 0.33m/s on the PE.

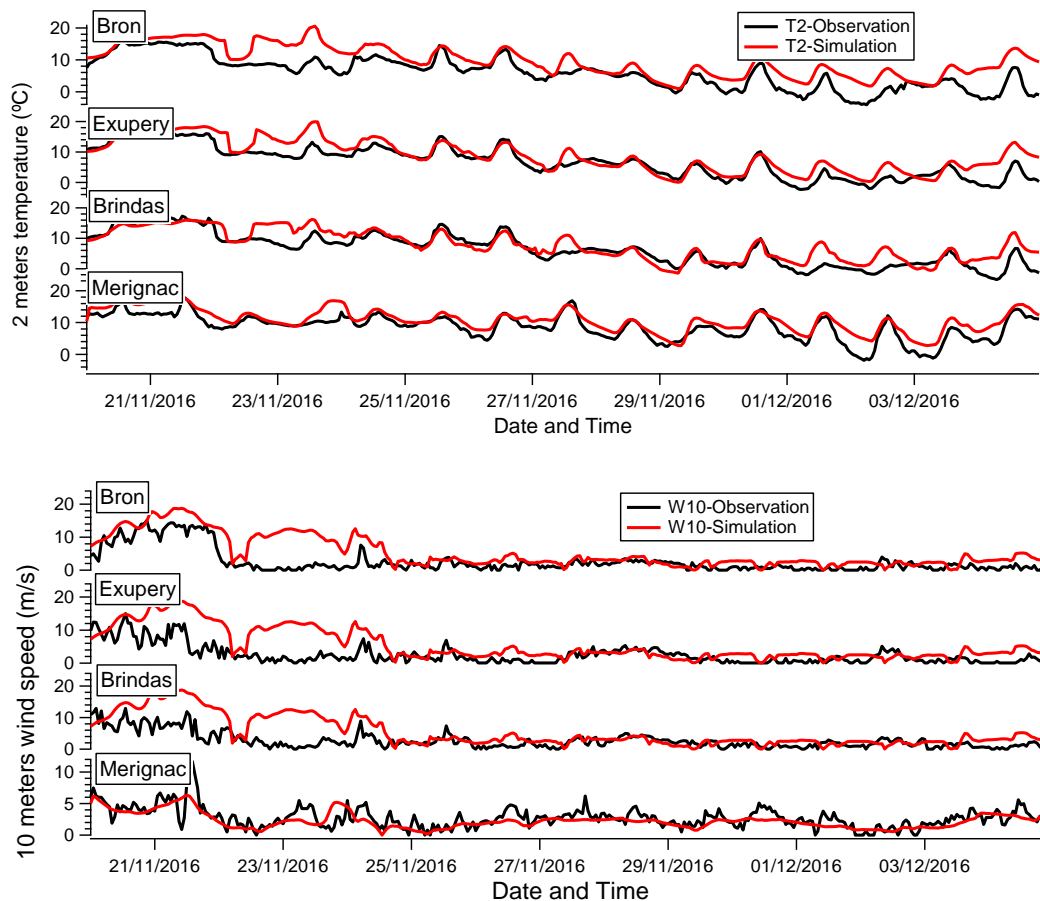


Figure 5.13 Comparison of the time series of 2m temperature (°C) and 10m wind speed (m/s) between the observations and different urban schemes at Bron, Exupery, Brindas and Merignac stations. The Bron, Exupery and Brindas stations are located in Lyon region and Merignac station is located in Bordeaux region.

5.3.4.2 NO₂ Simulations over Lyon and Bordeaux regions

5.3.4.2.1 Focus on urban areas

The mean first layer Kz and NO₂ mass concentrations for Lyon and Bordeaux domains over the period are displayed in Figure 5.14 and Figure 5.15 respectively. Both domains present similar regional distribution when compared to the Paris domain. The NO₂ concentrations are higher within the urban area and become patchier in the suburban and rural area, these concentrations are higher near the traffic routes.

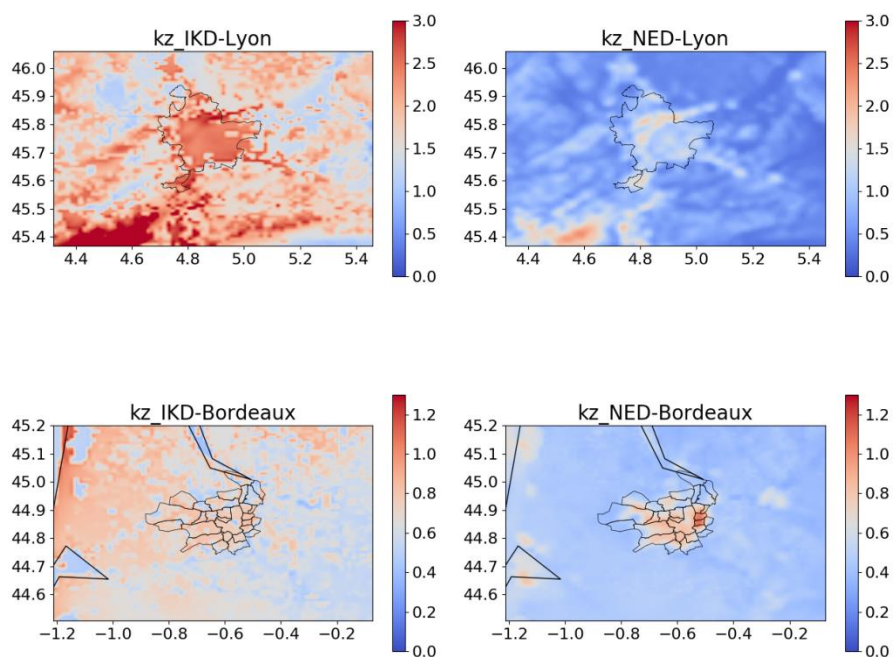


Figure5.14 Maps of the mean vertical diffusion coefficient (m^2/s); over the period from 20th November to 4th December. The first line: results from Lyon domain; the second line: results from Bordeaux domain.

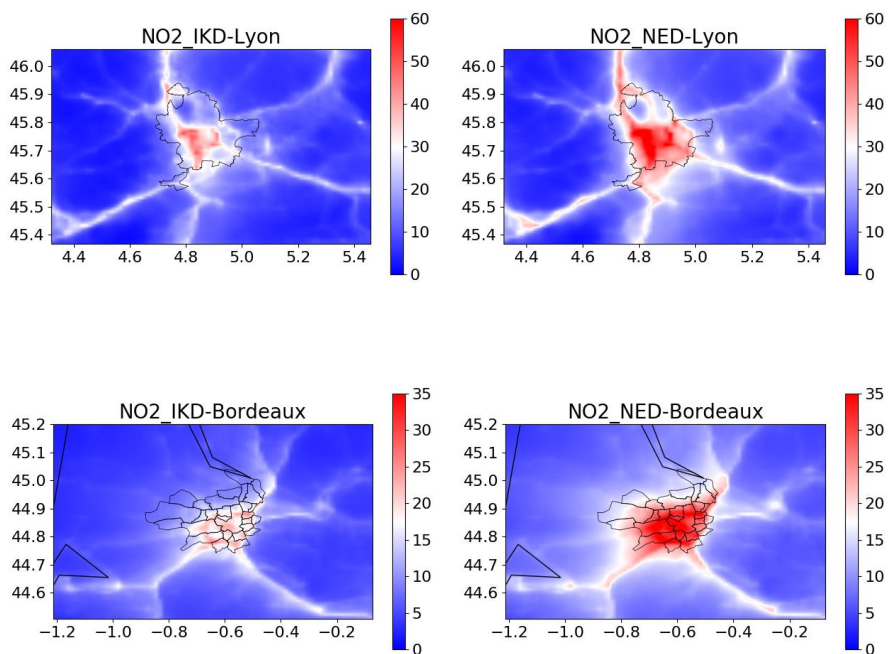


Figure5.15 Maps of the mean surface NO_2 mass concentration ($\mu g/m^3$); over the period from 20th November to 4th December. The first line: results from Lyon domain; the second line: results from Bordeaux domain.

The time series of the model predictions of the NO₂ mass concentrations compared to the observations for all urban background stations over Lyon and Bordeaux region can be found in Figure 5.16. The Linear fit between observed and modelled NO₂ can be found in Figure S5.5. *The correction between observed and modelled NO₂ in urban background stations over Lyon and Bordeaux regions. FR20XXX represents the station in Lyon region and FR31XXX represents the station in Bordeaux region.* In general, the increase in NO₂ mass concentrations during PE in Lyon and Bordeaux region are not as pronounced as the case in Paris. This demonstrates that the PE in Lyon and Bordeaux were not primarily caused by local sources. In Lyon, it seems that there are two slight NO₂ pollution episodes during this period. One from 22nd November to 26th November and another from 30th November to 3rd December. Overall, both schemes capture the majority of fluctuations quite well in both two regions. In particular, the NED scheme almost perfectly captures the first peak of NO₂, the 22nd December. However, despite the IKD scheme captures the fluctuations of NO₂, the second light peak in Lyon since the nighttime of 30th November in the observations and the IKD scheme underestimated NO₂ concentration at this period.

Table 5.8 reports a detailed evaluation of NO₂ simulation for both schemes at each urban background station. Similarly, to the focus in Paris, the IKD scheme underestimates NO₂ concentrations at all urban sites especially on the period of 30th November to 3rd December. Taking the RSME as the criterion, the use of the NED scheme improves NO₂ simulation in every urban site especially in the three urban sites in the Lyon region with an average improvement of 24.51%. In general, the model has a better performance for NO₂ simulation in Bordeaux than Lyon, that because the terrain of Lyon is more complex than in Bordeaux, the city is close to the Alps in a hilly region with sharp terrain gradients and the distribution of urban land use that is more scattered than Bordeaux.

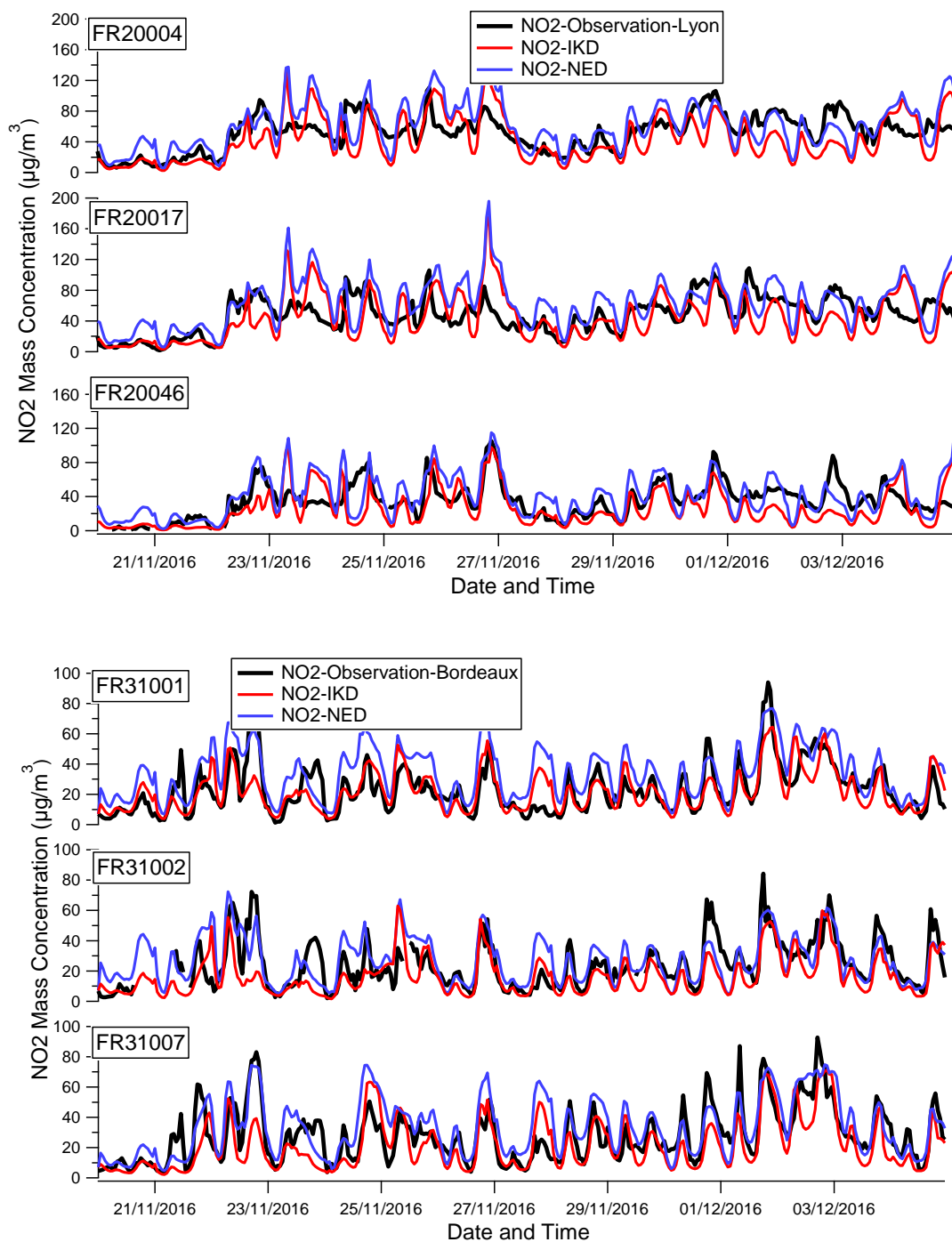


Figure 5.16 Time series between observed and modelled NO_2 mass concentrations ($\mu\text{g}/\text{m}^3$) in urban background stations. FR20XXX represents the station in Lyon region and FR31XXX represents the station in Bordeaux region.

Table 5.8 Average modelled NO₂ mass concentrations (Avg); the correlation (R); mean bias (MB) and root mean square error (RMSE) between Observation and simulation of NO₂ in four urban background stations over Paris region.

	IKD				NED				improvement
	Avg	R	MB	RMSE	Avg	R	MB	RMSE	
FR20004	43.75	0.55	-7.81	26.85	61.06	0.60	9.40	19.24	28.34%
FR20017	44.52	0.44	-3.10	29.00	62.93	0.53	15.31	20.64	28.83%
FR20046	25.70	0.57	-12.55	20.79	40.58	0.63	2.34	17.39	16.35%
FR31001	21.92	0.71	-1.23	13.78	34.10	0.74	7.94	11.34	17.70%
FR31002	21.51	0.72	-6.27	14.30	33.52	0.77	5.12	14.29	0.01%
FR31007	16.88	0.65	-7.22	14.18	27.06	0.66	2.96	12.64	10.86%

Figure 5.17 illustrates the diurnal cycles for surface K_z and surface concentrations of NO₂ during this period in urban sites for Lyon and Bordeaux domains. The diurnal variations of the surface K_z throughout both schemes shows similarities in Lyon but are very different in Bordeaux. In Bordeaux, the K_z from NED scheme remains stable only in the early morning and nighttime but K_z from IKD scheme had small changes throughout the day. Figure 5.16(c) and Figure 5.16(d) displays the diurnal cycles of surface NO₂ concentrations in Lyon and Bordeaux respectively. Both schemes capture the fluctuations well in both regions, displaying a bimodal distribution with the morning peak around 8:00–9:00 and the evening peak around 18:00–19:00 for observations and simulation. The IKD scheme tends to underestimate and the NED scheme tends to overestimate the surface NO₂ concentrations all day long in urban areas of those three cities (Paris, Lyon and Bordeaux).

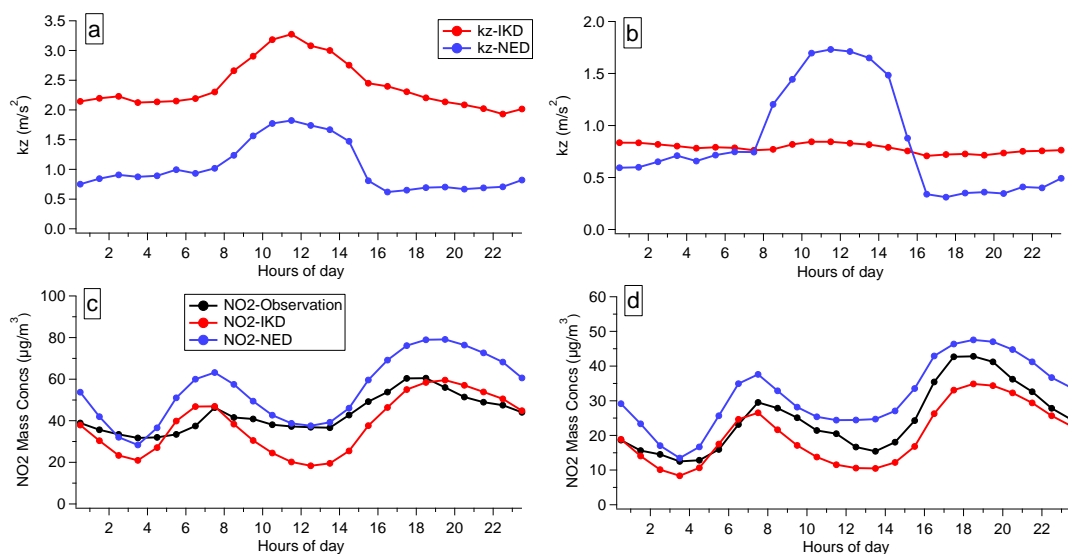


Figure 5.17 Diurnal cycles for surface K_z and surface concentrations of NO_2 ($\mu\text{g}/\text{m}^3$) from 20th November to 4th December in urban background stations. Left side are the diurnal cycles of K_z and NO_2 in Lyon region and right side are the diurnal cycles of K_z and NO_2 in Bordeaux region.

5.3.4.2.2 NO_2 simulations in suburban and rural areas

The mean NO_2 ground concentrations in suburban and rural area for Lyon and Bordeaux regions over the period are displayed in Figure 5.18. Unfortunately, no observation data was available for background rural station in Lyon and for background suburban station in Bordeaux. Thus, the suburban site in this section only represents the average data from three background suburban stations (FR20037; FR20045 and FR20047) in Lyon domain and the rural site only represent the data from one background rural station (FR31008) in Bordeaux. Both schemes capture well the main variability in the suburban area of Lyon and rural area of Bordeaux. Similar performances are displayed in urban area of Lyon, the model captures the first NO_2 peak value quite well by the NED scheme, the IKD tends to underestimate NO_2 since the 1st December. Table 5.9 reports that NED gives a better performance in both suburban sites of Lyon and rural sites of Bordeaux, with an improvement of 13.84% and 3.26% respectively. Even the performance of the model in suburban of Lyon cannot be compared with the rural of Bordeaux directly, the model should give better performances in the suburban and rural area in Bordeaux than Lyon.

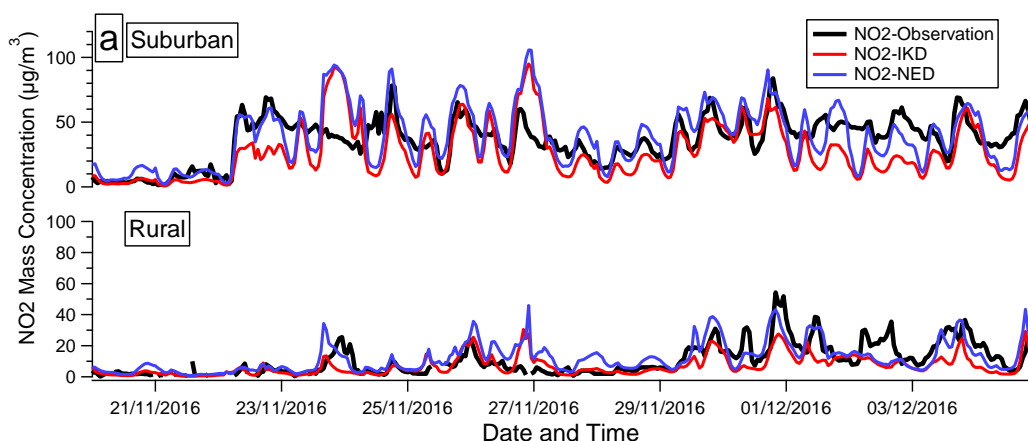


Figure 5.18 Time series between observed and modelled NO_2 and O_3 mass concentrations ($\mu\text{g m}^{-3}$) suburban background stations and rural background station in Lyon and Bordeaux region. Suburban represents the average data from three background suburban stations (FR20037; FR20045 and FR20047) in Lyon domain and the rural site only represent the data from one background rural station (FR31008) in Bordeaux.

Table 5.9 Average modelled NO_2 mass concentrations (Avg); the correlation (R); mean bias (MB) and root mean square error ($RMSE$) between Observation and simulation of NO_2 in suburban background station over Lyon region and rural background station over Bordeaux region.

	IKD				NED				improvement
	Avg	R	MB	RMSE	Avg	R	MB	RMSE	
Suburban	27.12	0.57	-9.18	20.23	39.33	0.66	3.03	17.77	13.84%
Rural	7.04	0.61	-3.93	8.60	12.13	0.67	1.16	8.32	3.26%

5.3.4.3. PM_{2.5} and PM₁₀ simulations over Lyon and Bordeaux

The first layer PM_{2.5} and PM₁₀ mean concentrations in Lyon and Bordeaux domains over the period are displayed in Figure 5.19 and Figure 5.20 respectively. It represents the surface concentrations of pollutants that are usually compared to the observation stations to test the accuracy of the model. Results show the regional patterns of PM_{2.5} and PM₁₀ are similar for both schemes. The simulated surface PM_{2.5} concentrations from NED scheme is approximately $1.6 \mu\text{g}/\text{m}^3$ and $1.4 \mu\text{g}/\text{m}^3$ higher on average than for the IKD scheme in Lyon and Bordeaux region respectively and gives approximately $1.6 \mu\text{g}/\text{m}^3$ and $1.2 \mu\text{g}/\text{m}^3$ higher PM₁₀ surface concentration than IKD scheme in Lyon and Bordeaux respectively. The

differences mainly occurred on the urban sites with slight differences in rural areas for both Lyon and Bordeaux domains.

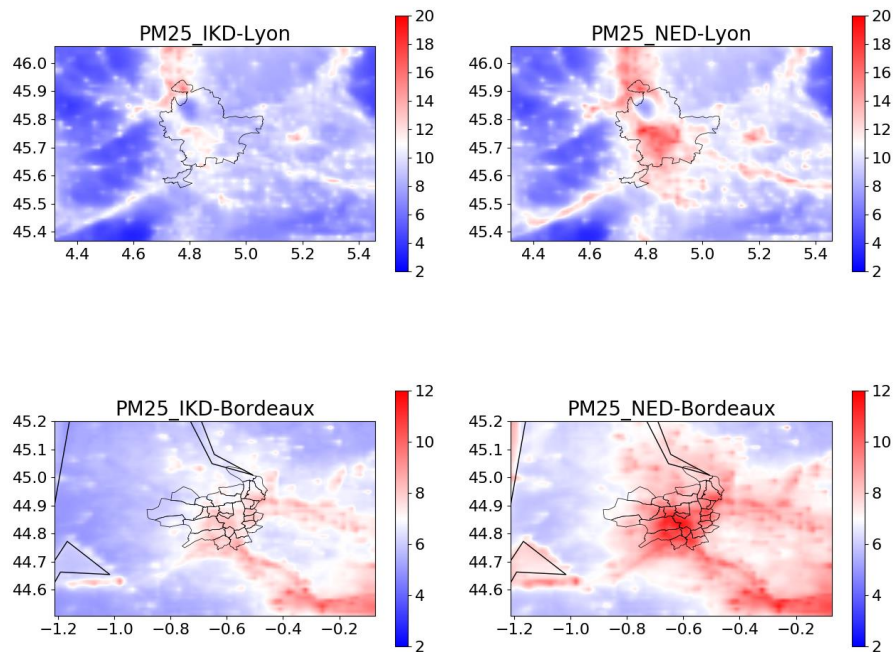


Figure 5.19 Maps of the mean surface PM_{2.5} mass concentration (μg/m³); over the period from 20th November to 4th December. The first line: results from Lyon domain; the second line: results from Bordeaux domain.

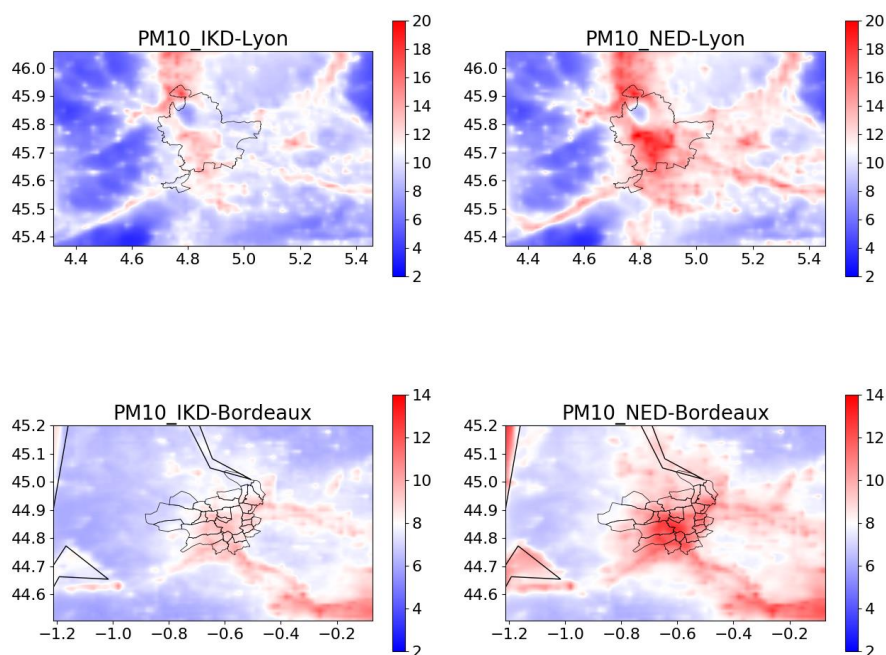


Figure 5.20 Maps of the mean surface PM₁₀ mass concentration ($\mu\text{g}/\text{m}^3$); over the period from 20th November to 4th December. The first line: results from Lyon domain; the second line: results from Bordeaux domain.

The comparison of simulated PM_{2.5} and PM₁₀ concentrations by the IKD and NED schemes in Lyon and Bordeaux regions with observational data are presented in Figure 5.21. The results show that the model could fairly capture the time variability of PM_{2.5} and PM₁₀ on the regular days of Lyon domain but strongly underestimates the concentrations during the PE. In Bordeaux, the model could not reproduce the PM_{2.5} and PM₁₀ well for the whole period, a huge underestimation occurred at all station. Previous study (Lanzafame, 2019) indicates that the biomass burning emissions are strongly underestimated in the model over the western cities of France, especially for the city of Bordeaux. The Alps region are also often submitted to pollution episodes in wintertime with a large contribution of wood burning (Bessagnet et al., 2020). Thus, the underestimation of the biomass burning emissions over Lyon regions should be a likely explanation of the issue on the PE. The specific quantitative analysis on the model performance of PM simulation is not confirmed in this section due to large uncertainties associated to emissions mainly. The model provides satisfactory results for NO₂ simulations but cannot give a reasonable behavior of PM_{2.5} and PM₁₀ when compared to the observations. This indicates the issue of PM simulation in Lyon and Bordeaux regions

should not be due to the model configuration. Improvements on the emission inventories are required first in those regions.

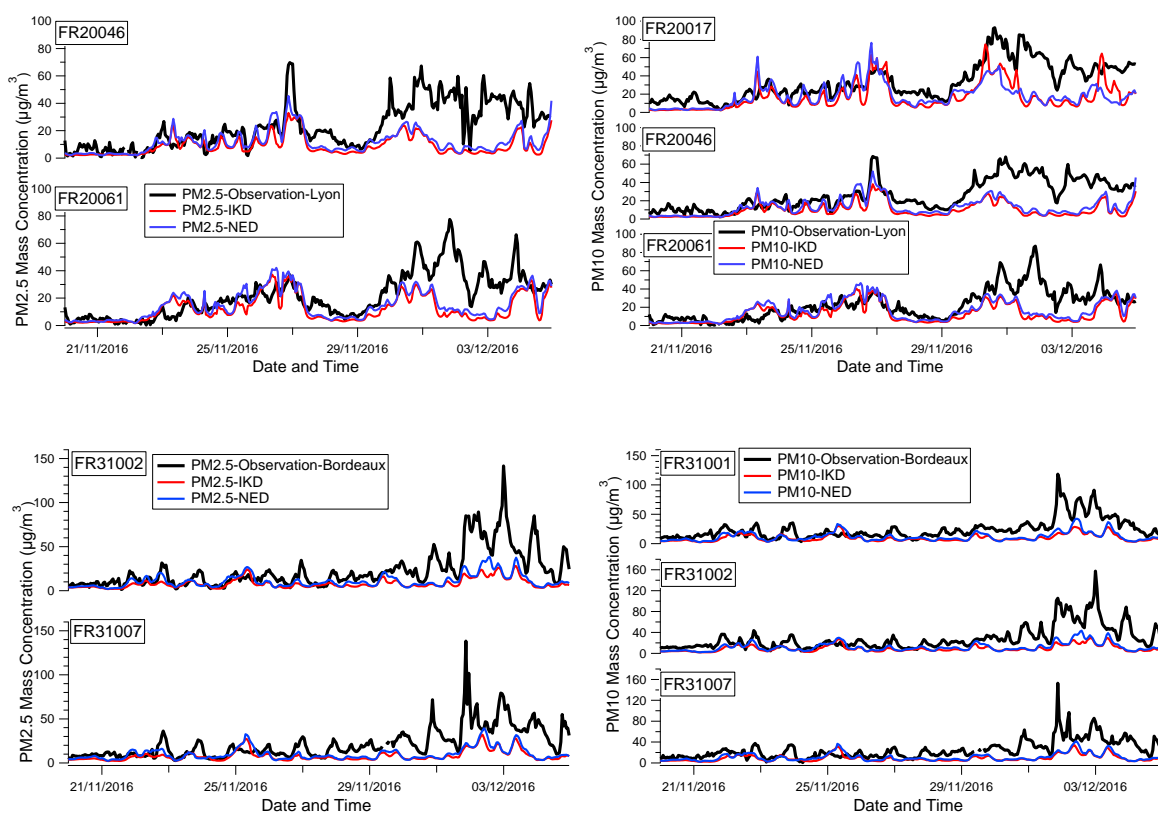


Figure 5.21 Time series between observed and modelled PM_{2.5} and PM₁₀ mass concentrations ($\mu\text{g m}^{-3}$) in urban background stations. FR20XXX represents the station in Lyon region and FR31XXX represents the station in Bordeaux region.

5.4 Conclusions

The flow characteristics and dispersion mechanisms of pollutants are important for air quality predictions particularly over urban areas. However, the representation of turbulent diffusion in mesoscale models remains a challenge especially for transport chemistry models. This study used a 1.5-order turbulence kinetic energy-based eddy diffusivity closure scheme from WRF defined as NED on the urban air quality context to assess consequences of surface-level emission of nitrogen dioxide (NO_2) and particulate matter (PM_{2.5} and PM₁₀) in Paris, Lyon and Bordeaux and Ozone (O_3) only in Paris. The performances of the NED and initial K_z diffusion (IKD) scheme were evaluated by ground observations both temporally and spatially.

The study in Paris indicates both two schemes can capture the evolution of the NO₂, O₃, PM_{2.5} and PM₁₀ concentrations in urban, suburban, and rural areas even if some constitutive species are underestimated on the pollution episode (PE). The NED scheme shows a better ability on PE prediction and displays a better performance in urban areas for NO₂, PM_{2.5} and PM₁₀ simulation with an average improvement at 18.77%, 13.47% and 19.08% respectively. In suburban areas, the NED scheme improves the simulation, but the degree of improvement was not as strong as in the urban areas. The NED scheme is not performing as well as IKD in rural areas. Diurnal cycles indicate average vertical diffusion rate (K_z) based on IKD is approximately 2.5 times than the NED, the IKD scheme overall overestimates K_z in urban region and the NED scheme slightly underestimates K_z during nighttime.

The model performance in Lyon and Bordeaux confirm the results obtained in Paris. The NED scheme improves the NO₂ simulation approximately by 24.51% and 9.52% in the urban areas of Lyon and Bordeaux respectively. Due to data limitations, model performances are only evaluated in the suburban areas of Lyon and rural areas of Bordeaux. Differently to Paris, the NED scheme better captures the fluctuations of NO₂ in the suburban of Lyon and Rural of Bordeaux than IKD scheme, with an average improvement at 13.84% and 3.26% respectively. However, PM simulations in Lyon and Bordeaux indicate that a strong underestimation of biomass burning emissions in wintertime could be the main reasons. The NED scheme gradually improves the air quality simulation from rural to urban areas. Although the overall performance of the proposed method is better than initial model configuration, the NED scheme still slightly overestimates the concentration of major pollutants on RD. The underestimation of K_z of NED is more pronounced in the nighttime than the daytime. Further improvements are necessary particularly under stables boundary conditions. In general, the 1.5-order turbulence kinetic energy-based eddy diffusivity closure scheme is an effective way to improve the CTM ability particularly under low stagnant conditions. It can be expected further improvement of the model ability through a higher-order turbulent closure calculation.

References

- Baker, J., Walker, H. L. and Cai, X.: A study of the dispersion and transport of reactive pollutants in and above street canyons—a large eddy simulation, *Atmospheric Environment*, 38(39), 6883–6892, doi:10.1016/j.atmosenv.2004.08.051, 2004.
- Baklanov, A., Hänninen, O., Slørdal, L. H., Kukkonen, J., Bjergene, N., Fay, B., Finardi, S., Hoe, S. C., Jantunen, M., Karppinen, A., Rasmussen, A., Skouloudis, A., Sokhi, R. S., Sørensen, J. H. and Ødegaard, V.: Integrated systems for forecasting urban meteorology, air pollution and population exposure, *Atmospheric Chemistry and Physics*, 7(3), 855–874, doi:https://doi.org/10.5194/acp-7-855-2007, 2007.
- Bessagnet, B., Menut, L., Lapere, R., Couvidat, F., Jaffrezo, J.-L., Mailler, S., Favez, O., Pennel, R. and Siour, G.: High Resolution Chemistry Transport Modeling with the On-Line CHIMERE-WRF Model over the French Alps—Analysis of a Feedback of Surface Particulate Matter Concentrations on Mountain Meteorology, *Atmosphere*, 11(6), 565, doi:10.3390/atmos11060565, 2020.
- Chen, Q., Li, X.-B., Song, R., Wang, H.-W., Li, B., He, H.-D. and Peng, Z.-R.: Development and utilization of hexacopter unmanned aerial vehicle platform to characterize vertical distribution of boundary layer ozone in wintertime, *Atmospheric Pollution Research*, 11(7), 1073–1083, doi:10.1016/j.apr.2020.04.002, 2020.
- Deardorff, J. W.: Stratocumulus-capped mixed layers derived from a three-dimensional model, *Boundary-Layer Meteorol*, 18(4), 495–527, doi:10.1007/BF00119502, 1980.
- Dragomir, C. M., Constantin, D.-E., Voiculescu, M., Georgescu, L. P., Merlaud, A. and Roozendaal, M. V.: Modeling results of atmospheric dispersion of NO₂ in an urban area using METI-LIS and comparison with coincident mobile DOAS measurements, *Atmospheric Pollution Research*, 6(3), 503–510, doi:10.5094/APR.2015.056, 2015.
- Forouzanfar, M. H., Afshin, A., Alexander, L. T., Anderson, H. R., Bhutta, Z. A., Biryukov, S., Brauer, M., Burnett, R., Cercy, K., Charlson, F. J., Cohen, A. J., Dandona, L., Estep, K., Ferrari, A. J., Frostad, J. J., Fullman, N., Gething, P. W., Godwin, W. W., Griswold, M., Hay, S. I., Kinfu, Y., Kyu, H. H., Larson, H. J., Liang, X., Lim, S. S., Liu, P. Y., Lopez, A. D., Lozano, R., Marczak, L., Mensah, G. A., Mokdad, A. H., Moradi-Lakeh, M., Naghavi, M., Neal, B., Reitsma, M. B., Roth, G. A., Salomon, J. A., Sur, P. J., Vos, T., Wagner, J. A., Wang, H., Zhao, Y., Zhou, M., Aasvang, G. M., Abajobir, A. A., Abate, K. H., Abbafati, C., Abbas, K. M., Abd-Allah, F., Abdulle, A. M., Abera, S. F., Abraham, B., Abu-Raddad, L. J., Abyu, G. Y., Adebisi, A. O., Adedeji, I. A., Ademi, Z., Adou, A. K., Adsuar, J. C., Agardh, E. E., Agarwal, A., Agrawal, A., Kiadaliri, A. A., Ajala, O. N., Akinyemiju, T. F., Al-Aly, Z., Alam, K., Alam, N. K. M., Aldhahri, S. F., Aldridge, R. W., Alemu, Z. A., Ali, R., Alkerwi, A., Alla, F., Allebeck, P., Alsharif, U., Altirkawi, K. A., Martin, E. A., Alvis-Guzman, N.,

- Amare, A. T., Amberbir, A., Amegah, A. K., Amini, H., Ammar, W., Amrock, S. M., Andersen, H. H., Anderson, B. O., Antonio, C. A. T., Anwari, P., Ärnlov, J., Artaman, A., Asayesh, H., Asghar, R. J., Assadi, R., Atique, S., Avokpaho, E. F. G. A., Awasthi, A., Quintanilla, B. P. A., Azzopardi, P., et al.: Global, regional, and national comparative risk assessment of 79 behavioural, environmental and occupational, and metabolic risks or clusters of risks, 1990–2015: a systematic analysis for the Global Burden of Disease Study 2015, *The Lancet*, 388(10053), 1659–1724, doi:10.1016/S0140-6736(16)31679-8, 2016.
- Johnson, G. T. and Hunter, L. J.: Urban wind flows: wind tunnel and numerical simulations—a preliminary comparison, *Environmental Modelling & Software*, 13(3–4), 279–286, doi:10.1016/S1364-8152(98)00028-0, 1998.
- Kirkil, G., Mirocha, J., Bou-Zeid, E., Chow, F. K. and Kosović, B.: Implementation and Evaluation of Dynamic Subfilter-Scale Stress Models for Large-Eddy Simulation Using WRF*, *Monthly Weather Review*, 140(1), 266–284, doi:10.1175/MWR-D-11-00037.1, 2012.
- Kurppa, M., Hellsten, A., Auvinen, M., Raasch, S., Vesala, T. and Järvi, L.: Ventilation and Air Quality in City Blocks Using Large-Eddy Simulation—Urban Planning Perspective, *Atmosphere*, 9(2), 65, doi:10.3390/atmos9020065, 2018.
- Lee, J.-H., Wu, C.-F., Hoek, G., de Hoogh, K., Beelen, R., Brunekreef, B. and Chan, C.-C.: Land use regression models for estimating individual NO_x and NO₂ exposures in a metropolis with a high density of traffic roads and population, *Science of The Total Environment*, 472, 1163–1171, doi:10.1016/j.scitotenv.2013.11.064, 2014.
- Letzel, M. O., Krane, M. and Raasch, S.: High resolution urban large-eddy simulation studies from street canyon to neighbourhood scale, *Atmospheric Environment*, 42(38), 8770–8784, doi:10.1016/j.atmosenv.2008.08.001, 2008.
- Lim, S., Kim, J., Kim, T., Lee, K., Yang, W., Jun, S. and Yu, S.: Personal exposures to PM_{2.5} and their relationships with microenvironmental concentrations, *Atmospheric Environment*, 47, 407–412, doi:10.1016/j.atmosenv.2011.10.043, 2012.
- Mailler, S., Khvorostyanov, D. and Menut, L.: Impact of the vertical emission profiles on background gas-phase pollution simulated from the EMEP emissions over Europe, *Atmos. Chem. Phys.*, 13(12), 5987–5998, doi:10.5194/acp-13-5987-2013, 2013.
- Menut, L., Bessagnet, B., Khvorostyanov, D., Beekmann, M., Blond, N., Colette, A., Coll, I., Curci, G., Foret, G., Hodzic, A., Mailler, S., Meleux, F., Monge, J.-L., Pison, I., Siour, G., Turquety, S., Valari, M., Vautard, R. and Vivanco, M. G.: CHIMERE 2013: a model for regional atmospheric composition modelling, *Geosci. Model Dev.*, 6(4), 981–1028, doi:10.5194/gmd-6-981-2013, 2013a.
- Menut, L., Bessagnet, B., Colette, A. and Khvorostyanov, D.: On the impact of the vertical resolution on chemistry-transport modelling, *Atmospheric Environment*, 67, 370–384, doi:10.1016/j.atmosenv.2012.11.026, 2013b.

- Palmgren, F., Berkowicz, R., Hertel, O. and Vignati, E.: Effects of reduction of NO_x on the NO₂ levels in urban streets, *Science of The Total Environment*, 189–190, 409–415, doi:10.1016/0048-9697(96)05238-2, 1996.
- Peshin, S. K., Sharma, A., Sharma, S. K., Naja, M. and Mandal, T. K.: Spatio-temporal variation of air pollutants and the impact of anthropogenic effects on the photochemical buildup of ozone across Delhi-NCR, *Sustainable Cities and Society*, 35, 740–751, doi:10.1016/j.scs.2017.09.024, 2017.
- Pierce, T., Hogrefe, C., Trivikrama Rao, S., Porter, P. S. and Ku, J.-Y.: Dynamic evaluation of a regional air quality model: Assessing the emissions-induced weekly ozone cycle, *Atmospheric Environment*, 44(29), 3583–3596, doi:10.1016/j.atmosenv.2010.05.046, 2010.
- Punger, E. M. and West, J. J.: The effect of grid resolution on estimates of the burden of ozone and fine particulate matter on premature mortality in the USA, *Air Qual Atmos Health*, 6(3), 563–573, doi:10.1007/s11869-013-0197-8, 2013.
- Song, F., Young Shin, J., Jusino-Atresino, R. and Gao, Y.: Relationships among the springtime ground-level NO_x, O₃ and NO₃ in the vicinity of highways in the US East Coast, *Atmospheric Pollution Research*, 2(3), 374–383, doi:10.5094/APR.2011.042, 2011.
- Valari, M., Markakis, K., Powaga, E., Collignan, B. and Perrussel, O.: EXPLUME v1.0: a model for personal exposure to ambient O₃ and PM_{2.5}, *Geosci. Model Dev.*, 13(3), 1075–1094, doi:10.5194/gmd-13-1075-2020, 2020.
- Walton, A. and Cheng, A. Y. S.: Large-eddy simulation of pollution dispersion in an urban street canyon—Part II: idealised canyon simulation, *Atmospheric Environment*, 36(22), 3615–3627, doi:10.1016/S1352-2310(02)00260-1, 2002.
- Warner, T.T., 2011. Numerical weather and climate prediction. Cambridge Univ. Press, Cambridge
- Wolf, T., Pettersson, L. H. and Esau, I.: A very high-resolution assessment and modelling of urban air quality, *Atmos. Chem. Phys.*, 20(2), 625–647, doi:10.5194/acp-20-625-2020, 2020.
- Wolf-Grosse, T., Esau, I. and Reuder, J.: Sensitivity of local air quality to the interplay between small- and large-scale circulations: a large-eddy simulation study, *Atmos. Chem. Phys.*, 17(11), 7261–7276, doi:10.5194/acp-17-7261-2017, 2017.
- Wyngaard, J.C., 2004. Toward Numerical Modeling in the “Terra Incognita.” *Journal of the Atmospheric Sciences* 61, 1816–1826. [https://doi.org/10.1175/1520-0469\(2004\)061<1816:TNMITT>2.0.CO;2](https://doi.org/10.1175/1520-0469(2004)061<1816:TNMITT>2.0.CO;2)
- Yao, X., Lau, N. T., Chan, C. K. and Fang, M.: The use of tunnel concentration profile data to determine the ratio of NO₂/NO_x;

directly emitted from vehicles, *Atmos. Chem. Phys. Discuss.*, 5(6), 12723–12740, doi:10.5194/acpd-5-12723-2005, 2005.

Zilitinkevich, S. S. and Esau, I. N.: Resistance and heat-transfer laws for stable and neutral planetary boundary layers: Old theory advanced and re-evaluated, *Q. J. R. Meteorol. Soc.*, 131(609), 1863–1892, doi:10.1256/qj.04.143, 2005.

Conclusions and Perspectives

- The first order K-theory is **an effective way** to reproduce the dispersion of pollutants in mesoscale chemistry transport model **in most of time**. However, this method sometimes **lacks the ability** to predict vertical mixing **under a very low turbulent diffusion**.
- The urban canopy and boundary layer height plays a crucial role in the mesoscale chemistry transport modelling simulation, especially for **the boundary layer height**, it plays a key role **in the early warning of pollution episode**.
- **Geographical condition is also important** in regional transport and dispersion of pollutants. Pollutant's dispersion processes over the valley-basin city are much more complicated than over flat areas.
- Our study indicates the **1.5 order TKE-based** eddy diffusivity closure scheme improved the CTM in every urban site. A way to **improve the turbulence parameterization** is to **increase the order of the closure**.

With an increasing number of humans now living in urban areas, there are needs of investigating the role of urbanization on air pollution, local meteorology and climate change. With the increasing computing capacities, numerical tools have become attractive tools for simulating transport and dispersion of airborne materials in the urban canopy. The present thesis work uses mesoscale models for meteorological and air quality simulations, representative of background air quality in urban region and its surroundings. The main goal of the thesis is to evaluate and improve the ability of models to simulate and forecast air quality and in France over urban regions.

Initially, three vertical diffusion schemes which have been used in multiple mesoscale chemical transport models (CTM) were tested over a one-year simulation covering the whole France. Those schemes are all based on first order local closure scheme, but the expressions differ. All three schemes present a fair reproduction of pollutant concentrations both in urban and rural areas, indicating it is an effective way to reproduce the dispersion of pollutants in chemistry transport modelling. However, the differences between test results are weak.

Therefore, it cannot be expected to significantly improve the vertical mixing in CTM under the first order closure scheme.

In the second part of the study, the impact of physical parameterizations was evaluated through couple the CTM model CHIMERE with the Weather Research and Forecasting (WRF) mesoscale model. Three canopy schemes, including a single layer urban canopy scheme (UCM); a multiple layer urban canopy scheme (BEP) and a reference case (Bulk). Three boundary layer parametrization schemes coupled with urban canopy schemes (MYJ–Bulk, YSU–Bulk, MYJ–UCM, YSU–UCM, MYJ–BEP, and Boulac–BEP) and two land surface schemes (Noah and Noah-mp) has been tested in this part. This study aims at understanding their impacts on air quality simulation with focus on a short-term pollution episode (PE) in the Paris region. CTM have been used with a first layer at 4m to better account for physical processes within the suburban layer in relation to ground emissions. The results indicate three canopy schemes could reproduce the 2m temperature (T2) effectively in the daytime; the Bulk and UCM model reproduced the 10m windspeed (W10) well, but the BEP model underestimates W10 for the whole episode. The UCM scheme overestimates the surface heat index in rural areas, leading to a slight negative bias for T2 in rural versus urban areas. NO₂, PM_{2.5}, and PM₁₀ were selected to evaluate the effect of physics parameterizations on air quality simulation. Large differences were found in the simulation of pollutant concentrations, with an overall overestimation during the pollution episode. The overall boundary layer schemes display an underestimation of the PBL height practically during PE. The Boulac–BEP is the only scheme that could relative effectively reproduce the PBL height during PE. The Boulac–BEP scheme gives a significantly better performance on air quality simulation than the rest, indicating that both the canopy parameterization and boundary layer schemes have a significantly positive effect on air quality simulation in urban regions. The study on the land surface scheme shows it has slightly impact for both meteorological and air quality simulation. An advanced urban category could improve air quality prediction in urban regions.

Fifteen days sensitivity tests with multiple vertical grid resolution and first layer height defined as (i) L4: 53 vertical layers are defined in WRF and 20 vertical layers are defined in CHIMERE. The first layer of the two model is at 999.5hPa (approximately 4m) up to over 500hPa; (ii) L12: 51 vertical levels are defined in WRF and 20 levels are defined in CHIMERE, starting with the first vertical height at about 12 meters above the ground; (iii)

L40: 49 vertical levels are defined in WRF and 20 vertical layers are defined in CHIMERE from 995hPa to 500hPa, the first layer is about 40m. Results show the impact is relatively small in meteorological simulations. The relative bias (RB) of L12 and L40 compare with L4 (L12-L4 and L40-L4) are 2.17% and 22.95% for 2m temperature (T2), 4.01% and -12.69% for 10m wind speed (W10), -0.12% and -2.72% for surface relative humidity (RH), respectively. On regular days, all three configurations demonstrate the ability of chemistry transport modelling. L4 improved model ability of 23.26% and 25.09% compare with L12 and L40 respectively. During pollution episodes, refined vertical grid resolution and first layer height produces a significant improvement in chemistry transport modeling, improvements are 62.10% and 129.02% in L4 compare with L12 and L40.

The flow characteristics and dispersion mechanisms of pollutants are important for air quality simulation and forecast. The first part of the study illustrates the difficulties to improve the ability of the model through the simplest first order local closure schemes.

In the last part of the study, a 1.5-order turbulence-resolve scheme defined as NED has been applied in the CHIMERE model on the urban air quality context to assess consequences of low-level emission of pollutants in Paris, Lyon and Bordeaux. The performances of NED and initial K_z diffusion scheme (IKD) were evaluated against ground observations both temporally and spatially. The study in Paris shows both two schemes can capture the evolution of the NO_2 , O_3 , $\text{PM}_{2.5}$ and PM_{10} concentrations in urban, suburban, and rural areas even if some constitutive species are underestimated on the pollution episode (PE). Taking the relative change in % of the RMSE as the evaluation criteria, the NED scheme improved the ability of models to assess air quality with an average improvement at 18.77%, 13.47% and 19.08% of NO_2 , $\text{PM}_{2.5}$ and PM_{10} respectively. However, the IKD scheme reproduces the O_3 more effectively than NED. In suburban areas, NED scheme improved the simulation, but the degree of improvement was not as strong as in the urban areas. The NED scheme is not performing as well as IKD in rural areas. Diurnal cycles between the vertical diffusion coefficient and pollutants indicate the IKD scheme overall overestimate diffusion rate in urban region and NED scheme slightly underestimated it during the nighttime. The model performances in Lyon and Bordeaux are rather good over Paris, NED scheme improved the

NO₂ simulation approximately 24.51% and 9.52% in the urban areas of Lyon and Bordeaux respectively. However, PM simulation results over those two latter areas could indicate a huge underestimation of biomass burning emissions in wintertime., Both schemes can capture the evolution of PM_{2.5} and PM₁₀, the average concentrations are strongly underestimated particularly in Bordeaux and on the PE of Lyon. The NED scheme gradually improves the air quality simulation as it approaches the city center. Sensitivity tests to grid resolution showed that the model results are sensitive to the vertical resolution and do not tend to improve with increasing resolution, there configuration of parameters are weak under the displacement height, the aspect ratio is curial on eddy simulation. Overall, surface turbulent motions were better preserved by a 1.5-order turbulence kinetic energy-based eddy diffusivity closure scheme than those with the simplest ones.

Since the 1970s, the CTMs have developed from the initial simple box model to today's complex third generation CTM models. The configurations of CTM should be combined with the characteristics of the research problem, the time and space scale of the simulation, data availability, technical complexity, software and hardware platform requirements, etc. Not all simulations have to choose the highest model configuration. Advanced configurations generally have very strict requirements on basic data, hardware platform, professional threshold, etc., and the cost will be several times compared with the basic configurations. Therefore, choosing an appropriate model configuration is the key to achieving the goals with the lowest cost. From the perspective of air quality model application practice, it is often difficult for users to accurately grasp the applicable conditions of the model or simplify complex issues.

With the rapid development of high-performance computers, high resolution numerical simulation has achieved great success. However, most high-resolution simulations are still at the research stage, the time span is usually from days to a month. Although computer resources are not extravagant, long time series high-resolution simulation is still difficult to achieve. Thus, a technique that could pass the costly high simulation is important. The uncertainty of the CTM mainly comes from five parts: chemical mechanism; chemical reaction rate; boundary layer; emission inventory and meteorological data. Take the model performance of particulate matter as an example, the ratio of PM_{2.5} to PM₁₀ is above 90% in

every studies of this research, however, the value is approximately 70% in the real atmospheric. In coastal cities, the modeled particulate matter concentrations are far from the observation. The lack of emissions directly leads to the poor performance of models. The completeness of emission inventories particularly on residential emissions remains challenging for the air quality community.

Urban-induced atmospheric circulations, though typically small scale, can have a significant impact on mesoscale dynamics. Many studies indicate that refining urban landuse categories helps improving the model's ability to simulate the processes in the urban canopy. However, it could present notable challenges for mesoscale models due to the tremendous horizontal and vertical variability of the urban landscape and the variety of surface forcing. A lower first model layer could better reproduce the transport and diffusion of pollutants in a real urban environment. However, urban canopy is an open canopy, a refined urban category could increase the displacement height in the cities leads a very weak configuration of parameters at low level, it requires more studies. Future works should also focus on the comparison of pollutant concentrations over the vertical within the urban canopy to better evaluate the performance of models.

In recent years, due to the improvement of computing power, the interdisciplinary field of machine learning-statistics and computer science has flourished. At present, the application of Artificial Intelligence (AI) techniques to air quality simulation has been initially applied but is still in the exploratory stage. For example, use wavelet transform to split the pollutant time series into more regular sub-sequences, then use the artificial neural network to train independent models for them to further improve the accuracy. Or using AI techniques could be used to calculate higher-order turbulent kinetic energy makes it possible to apply direct numerical simulation to mesoscale models. How to combine CTM and AI techniques for air quality prediction will be a very active field in the future to allow fast high-resolution simulations at urban scale to monitor air quality. At last, let us remind that using neural network is complementary of developing more and more complex physical models with more layers and accurate urban schemes. They are good instruments to simplify complex models by developping surrogate associated models for operational uses at high resolution (by catching the main patterns) and offering the possibility to develop more and more sophisticated deterministic models representing the "real world".

List of Figures

Figure1.1 Typical sources, formation, removal pathways and size distributions of atmospheric aerosol.

Figure1.2 Direct, semi-direct and indirect effects of aerosols on climate.

Figure1.3 Change in RF effects caused by atmospheric pollutants for the period 1750–2011, associated with individual confidence range.

Figure1.4 MODIS aerosol optical depth averaged over the 10-year period 2001–2010Pie charts shows the contribution of different aerosols to the total aerosol optical depth for different regions.

Figure1.5 Emission trends in the EU28 on the basis of fuel sold.

Figure1.6 Urban heat island in cities.

Figure2.1 General principle of the air quality simulation system

Figure2.2 The main linkages between megacities, air quality and climate.

Figure2.3 Example of mass conservation.

Figure2.4 Typical diurnal variation of the boundary layer structure. Sunrise (SR), Sunset (SS).

Figure2.5 Sensitivity test of vertical profile of kz (m^2/s) in stable and unstable conditions.

Figure2.6 Vertical profiles of kz (m^2/s); NO_2 ($\mu g/m^3$); O_3 ($\mu g/m^3$) $PM_{2.5}$ ($\mu g/m^3$) and PM_{10} ($\mu g/m^3$) over the France domain. The profiles are averaged from January 1st to December 31st, 2016.

Figure2.7 Maps of the seasonal mean vertical diffusion coefficient (m^2/s) over the France domain.

Figure2.7 Seasonal changes between observed and modelled NO_2 , $PM_{2.5}$ and PM_{10} mass concentrations ($\mu g/m^3$) in France domain.

Figure2.9 Time series between observed and modelled NO_2 , $PM_{2.5}$ and PM_{10} mass concentrations ($\mu g/m^3$) in Urban and Rural areas.

Figure2.10 Diurnal cycles for surface concentrations ($\mu g/m^3$) of NO_2 , $PM_{2.5}$ and PM_{10} in the year 2016

Figure3.1 The structure diagram of UCM(left) and BEP(right) urban canopy scheme. Ta: Atmospheric temperature at Za meters height; Tg: Pavement temperature; H : Sensible heat exchange; Tr: Temperature of the roof; Tw: Temperature of the wall; Tg: Temperature of the street; Ts: Atmospheric temperature at Zs meters height; Ha: Sensible heat flux from street

canyon to atmosphere; Hw: Sensible heat flux from wall to street canyon; Hg: Sensible heat flux from road to street canyon; Hr: Sensible heat flux from roof to atmosphere.

Figure3.2 Four nested domains—from d01, the largest one, at a low resolution to d04, the finest one, at a high resolution.

Figure3.3 Maps of the meteorological and air quality monitoring stations.

Figure3.4 Time series of 2m temperature and 10m wind speed at Sirta station.

Figure3.5 Time series of 2m temperature and 10m wind speed at Montsouris station.

Figure3.6 Maps of the mean 2m temperature (°C) over the period from 27th November to 4th December

Figure3.7 Maps of the mean surface heat flux (W m^{-2}) over the period from 27th November to 4th December.

Figure3.8 Time series of 2m temperature (°C) between observations and different urban schemes at Montsouris, Roissy, and Sirta stations.

Figure3.9 Maps of the mean 10m wind speed (m s^{-1}) over the period from 27th November to 4th December.

Figure3.10 Comparison of the time series of 10 m wind speed (m s^{-1}) between the observations and different urban schemes at Montsouris, Roissy and Sirta stations.

Figure3.11 The differences in the daily averaged NO_2 ($\mu\text{g m}^{-3}$), $\text{PM}_{2.5}$ ($\mu\text{g m}^{-3}$), and PM_{10} ($\mu\text{g m}^{-3}$) between different schemes from 27th November to 4th December 2016.

Figure3.12 Time series of NO_2 mass concentrations ($\mu\text{g m}^{-3}$). No1, 2, 3, 4 represent station FR04002, FR04034, FR04143, and FR04156, respectively.

Figure3.13 Vertical profiles of the CHIMERE Kz extracted at the FR04143 station. The profile is extracted at 06:00 and 22:00 UTC for both Regular Days (RD) and the Particulate Episode (PE).

Figure3.14 Vertical profiles of the NO_2 and $\text{PM}_{2.5}$ mass concentration ($\mu\text{g m}^{-3}$) at the FR04143 station. The profiles are extracted at 06:00 and 22:00 UTC for both Regular Days (RD) and the Particulate Episode (PE). Columns (a), (b), (c), and (d) represent the vertical mass NO_2 and $\text{PM}_{2.5}$ concentration at 28th November 06:00, 28th November 22:00, 30th November 06:00, and 30th November 22:00 UTC, respectively.

Figure3.15 Time series of the observed and modelled mixing boundary layer height: (a) and (b) represent Roissy and Sirta station, respectively; 1, 2, and 3 represent each PBL scheme coupled with each urban canopy scheme.

Figure3.16 Time series between the observed and modelled T2: (a) and (b) represent Roissy and Sirta station, respectively; 1, 2, and 3 represent each PBL scheme coupled with each urban canopy scheme.

Figure3.17 Time series between the observed and modelled W10: (a) and (b) represent Roissy and Sirta station, respectively; 1, 2, and 3 represent each PBL scheme coupled with each urban canopy scheme.

Figure3.18 Time series of NO₂ mass concentrations: No 1, 2, 3, and 4 represent station FR04002, FR04034, FR04143, and FR04156, respectively.

Figure3.19 Liner fit between the observed and modelled NO₂.

Figure3.20 Time series of 2m temperature (°C) between observations and different urban schemes at Montsouris, Roissy, and Sirta stations.

Figure3.21 Comparison of the time series of 10m wind speed (m s⁻¹) between the observations and different urban schemes at Montsouris, Roissy and Sirta stations.

Figure3.22 Time series of NO₂ and PM_{2.5} mass concentrations: No 1, 2, 3, and 4 represent station FR04002, FR04034, FR04143, and FR04156, respectively.

Figure4.1 Locations of the meteorological and air quality monitoring stations.

Figure4.2 Maps of the mean 2m temperature (°C); mean 10m wind speed (m/s) and mean surface relative humidity (%) over the period from 20th November to 4th December. Left column: results from L4; Middle column: results from L12; Right column: results from L40.

Figure4.3 Maps of the mean NO₂ (µg/m³); mean PM_{2.5} (µg/m³) and mean PM₁₀ (µg/m³) mass concentrations over the period from 20th November to 4th December. Left column: results from L4; Middle column: results from L12; Right column: results from L40.

Figure4.4 Vertical profiles of Kz(m²/s), NO₂, PM_{2.5} and PM₁₀ (µg/m³) from 20th November to 4th December over Paris region.

Figure4.5 Time series between the observed and modelled 2m temperature (°C); mean 10m wind speed (m/s) and planetary boundary layer height (PBLH)

Figure4.6 Diurnal cycles for surface 2m temperature (°C); mean 10m wind speed (m/s) and planetary boundary layer height (PBLH) from 20th November to 4th December.

Figure4.7 Time series between the observed and modelled NO₂, PM_{2.5}, PM₁₀ (µg/m³).

Figure4.8 Time series of bias between L12 to L4 (L12-L4) and L40 to L4 (L40-L4).

Figure5.1 Schematic of a turbulent-energy spectrum. l is the scale of the energy-containing turbulence, Δ is the horizontal grid size; ϕ is turbulent energy, and λ is wavelength(Warner, 2011).

Figure5.2 Maps of the meteorological and air quality monitoring stations. Red represent urban background station; green represent suburban background station and blue represent rural background station.

Figure5.3 Vertical profiles of the CHIMERE Kz extracted at the FR04143 station. The profile is extracted at 06:00 and 22:00 UTC for both Regular Days (RD) and the Particulate Episode (PE).

Figure5.4 Time series between observed and modelled NO₂ mass concentrations ($\mu\text{g m}^{-3}$) in urban and rural background stations.

Figure5.5 Maps of the mean vertical diffusion coefficient (m s^2); mean surface NO₂ mass concentration ($\mu\text{g m}^{-3}$) and surface mean O₃ mass concentration ($\mu\text{g m}^{-3}$) over the period from 20th November to 4th December. The first line: results from IKD scheme; the second line: results from NED scheme.

Figure5.6 Time series between observed and modelled NO₂ and O₃ mass concentrations ($\mu\text{g m}^{-3}$) in urban background stations.

Figure5.7 Diurnal cycles for surface kz and surface concentrations of O₃ and NO₂ ($\mu\text{g m}^{-3}$) from 20th November to 4th December in urban background stations.

Figure5.8 Time series between observed and modelled NO₂ and O₃ mass concentrations ($\mu\text{g m}^{-3}$) suburban background stations and rural background stations.

Figure5.9 Maps of the mean surface PM_{2.5} and PM₁₀ mass concentration ($\mu\text{g m}^{-3}$); over the period from 20th November to 4th December.

Figure5.10 Time series between observed and modelled PM_{2.5} and PM₁₀ mass concentrations ($\mu\text{g m}^{-3}$) in urban; suburban and rural background stations. Urban background stations: FR04002; FR04034; FR04143 and FR04156. Suburban background stations: FR04024 and FR04181 for PM_{2.5} simulation and observation; FR04181 and FR04319 for PM₁₀ simulation and observation. Rural background stations: FR04048 for PM_{2.5} simulation and observation; FR04158 PM₁₀ simulation and observation.

Figure5.11 Maps of the mean 2m temperature ($^{\circ}\text{C}$) and 10m wind speed (m s^{-1}) over the period from 27th November to 4th December.

Figure5.12 Comparison of the time series of 2m temperature ($^{\circ}\text{C}$) and 10 m wind speed (m s^{-1}) between the observations and different urban schemes at Bron, Exupery, Brindas and Merignac

stations. The Bron, Exupery and Brindas stations are located in Lyon region and Merignac station is located in Bordeaux region.

Figure5.13 Maps of the mean vertical diffusion coefficient ($\text{m}^2 \text{s}^{-1}$); over the period from 20th November to 4th December. The first line: results from Lyon domain; the second line: results from Bordeaux domain.

Figure5.14 Maps of the mean surface NO_2 mass concentration ($\mu\text{g m}^{-3}$); over the period from 20th November to 4th December. The first line: results from Lyon domain; the second line: results from Bordeaux domain.

Figure5.15 Time series between observed and modelled NO_2 mass concentrations ($\mu\text{g m}^{-3}$) in urban background stations. FR20XXX represents the station in Lyon region and FR31XXX represents the station in Bordeaux region.

Figure5.16 Diurnal cycles for surface k_z and surface concentrations of NO_2 ($\mu\text{g m}^{-3}$) from 20th November to 4th December in urban background stations. Left side are the diurnal cycles of k_z and NO_2 in Lyon region and right side are the diurnal cycles of k_z and NO_2 in Bordeaux region.

Figure5.17 Time series between observed and modelled NO_2 and O_3 mass concentrations ($\mu\text{g m}^{-3}$) suburban background stations and rural background station in Lyon and Bordeaux region. Suburban represents the average data from three background suburban stations (FR20037; FR20045 and FR20047) in Lyon domain and the rural site only represent the data from one background rural station (FR31008) in Bordeaux.

Figure5.18 Maps of the mean surface $\text{PM}_{2.5}$ mass concentration ($\mu\text{g m}^{-3}$); over the period from 20th November to 4th December. The first line: results from Lyon domain; the second line: results from Bordeaux domain.

Figure5.19 Maps of the mean surface PM_{10} mass concentration ($\mu\text{g m}^{-3}$); over the period from 20th November to 4th December. The first line: results from Lyon domain; the second line: results from Bordeaux domain.

Figure5.20 Time series between observed and modelled $\text{PM}_{2.5}$ and PM_{10} mass concentrations ($\mu\text{g m}^{-3}$) in urban background stations. FR20XXX represents the station in Lyon region and FR31XXX represents the station in Bordeaux region.

List of Tables

Table2.1 The kz (m^2/s) values within 10 levels

Table2.2 Seasonal average mass concentration of NO_2 , $PM_{2.5}$ and PM_{10} ($\mu g/m^3$) between observation and three schemes.

Table2.3 Statistics of surface variables: mean linear correlation coefficient (R); mean bias (MB) and root mean square error (RMSE) between the simulations and observations of NO_2 , $PM_{2.5}$ and PM_{10} in Urban and Rural areas.

Table3.1 Summary of the physics parameterizations used.

Table3.2 Statistics of surface pollutants: mean bias between the simulations and observations of NO_2 , $PM_{2.5}$, and PM_{10} during Whole Period (WP) and Pollution Episode (PE).

Table3.3 Statistics of surface variables: mean bias (MB) and mean linear correlation coefficient (R) between the simulations and observations of 2 m temperature (T2) and 10 m wind speed (W10) at Roissy and Sirta stations.

Table3.4 Statistics of surface variables: mean bias (MB), root mean square error (RMSE), and mean linear correlation coefficient (R) between the simulations and observations of NO_2 , $PM_{2.5}$, PM_{10} .

Table4.1 Range and average values of 2m temperature ($^{\circ}C$); 10m wind speed (m/s) and surface relative humidity (%) over the period

Table4.2 Range and average values NO_2 ($\mu g/m^3$); $PM_{2.5}$ ($\mu g/m^3$) and PM_{10} ($\mu g/m^3$) over the period

Table4.3 Statistics of surface variables: mean bias (MB), mean linear correlation coefficient (R) and root mean square error (RMSE) between the simulations and observations of 2m temperature ($^{\circ}C$); mean 10m wind speed (m/s) and planetary boundary layer height (PBLH)

Table4.4 Statistics of surface variables: mean bias (MB), mean linear correlation coefficient (R) and root mean square error (RMSE) between the simulations and observations of NO_2 , $PM_{2.5}$, PM_{10} .

Table4.5 Statistics of surface variables: average mass concentration ($\mu g/m^3$), mean bias (MB), mean linear correlation coefficient (R) and root mean square error (RMSE) between the simulations and observations of NO_2 , $PM_{2.5}$, PM_{10} on regular days (RD) and pollution episode (PE).

Table4.6 Operation time (minutes) of single day simulation in meteorological and chemistry transport modeling

Table5.1 The correlation (R); mean bias (MB) and root mean square error (RMSE) between Observation and simulation of NO_2 in four urban and rural background stations over Paris region.

Table5.2 Average modelled NO₂ mass concentrations (Avg); the correlation (R); mean bias (MB) and root mean square error (RMSE) between Observation and simulation of NO₂ in four urban background stations over Paris region.

Table5.3 Average modelled O₃ mass concentrations (Avg); the correlation (R); mean bias (MB) and root mean square error (RMSE) between Observation and simulation of O₃ in four urban background stations over Paris region.

Table5.4 Average modelled NO₂ and O₃ mass concentrations (Avg); the correlation (R); mean bias (MB) and root mean square error (RMSE) between Observation and simulation of NO₂ and O₃ in suburban and rural background stations over Paris region.

Table5.5 Average modelled PM_{2.5} mass concentrations (Avg); the correlation (R); mean bias (MB) and root mean square error (RMSE) between Observation and simulation of PM_{2.5} in urban, suburban and rural background stations over Paris regions.

Table5.6 Average modelled PM₁₀ mass concentrations (Avg); the correlation (R); mean bias (MB) and root mean square error (RMSE) between Observation and simulation of PM₁₀ in urban, suburban and rural background stations over Paris regions.

Table5.7 Proportion between PM_{2.5} and PM₁₀ in urban, suburban and rural background stations for the whole period (WP) and pollution episode (PE) over Paris regions.

Table5.8 Average modelled NO₂ mass concentrations (Avg); the correlation (R); mean bias (MB) and root mean square error (RMSE) between Observation and simulation of NO₂ in four urban background stations over Paris region.

Table5.9 Average modelled NO₂ mass concentrations (Avg); the correlation (R); mean bias (MB) and root mean square error (RMSE) between Observation and simulation of NO₂ in suburban background station over Lyon region and rural background station over Bordeaux region.

Annex A

Supplementary Material of Chapter III

Impact of Physics Parameterizations on High-Resolution Air Quality Simulations over the Urban Region

Lei Jiang^{1,2,*}, Bertrand Bessagnet^{1,†}, Frederik Meleux¹, Frederic Tognet¹, Florian Couvidat¹

¹ INERIS, National Institute for Industrial Environment and Risks, Parc Technologique ALATA, 60550 Verneuil-en-Halatte, France; bertrand.bessagnet@citepa.org (B.B.); Frederik.MELEUX@ineris.fr (F.M.); Frederic.TOGNET@ineris.fr (F.T.); Florian.COUIDAT@ineris.fr (F.C.)

² Sorbonne University, UPMC Univ Paris 06, DE129, 75005 Paris, France

[†] Now at Citepa: Technical Reference Center for Air Pollution and Climate Change, 42, rue de Paradis, 75010 Paris, France.

LIST OF TABLES AND FIGURES

Table S3.1. The urban parameters for the urban canopy model.

Figure S3.1. Time series of PM_{2.5}, PM₁₀ mass concentrations: No1, 2, 3, 4 represent station FR04002, FR04034, FR04143, FR04156, respectively.

Figure S3.2. Time series of bias of NO₂, PM_{2.5}, PM₁₀ mass concentrations: No1, 2, 3, 4 represent station FR002, FR034, FR143, FR156, respectively.

Figure S3.3. Time series between observed and modelled NO₂ with the first height of about 4 m, 18m and 40 m, respectively. Both observation and simulations are the average of Station FR04002, FR04034, FR04143, FR04156, respectively.

Figure S3.4. Time series between observed and modelled PM_{2.5}: a, b and c represent each PBL schemes coupled with each urban canopy schemes respectively; 1, 2, 3, and 4 represent Station FR04002, FR04034, FR04143, FR04156, respectively.

Figure S3.5. Time series between observed and modelled PM10: a, b and c represent each PBL schemes coupled with each urban canopy schemes respectively; 1, 2, 3, and 4 represent Station FR04002, FR04034, FR04143, FR04156, respectively.

Figure S3.6. Time series of bias between observed and modelled NO₂: a, b and c represent each PBL schemes coupled with each urban canopy schemes respectively; 1, 2, 3, and 4 represent Station FR04002, FR04034, FR04143, FR04156, respectively.

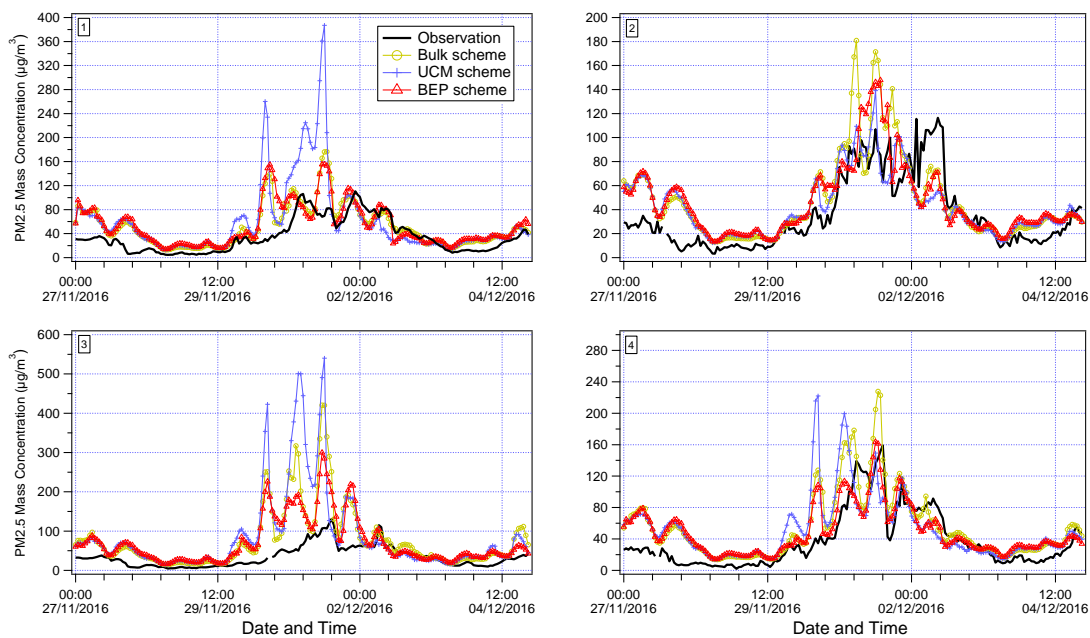
Figure S3.7. Time series of bias between observed and modelled PM2.5: a, b and c represent each PBL schemes coupled with each urban canopy schemes respectively; 1, 2, 3, and 4 represent Station FR04002, FR04034, FR04143, FR04156, respectively.

Figure S3.8. Time series of bias between observed and modelled PM10: a, b and c represent each PBL schemes coupled with each urban canopy schemes respectively; 1, 2, 3, and 4 represent Station FR04002, FR04034, FR04143, FR04156, respectively.

Figure. S3.9. Liner fit between observed and modelled PM2.5 and PM10.

Table.S3.1. The urban parameters for the urban canopy model

Parameters	URBAN-PAM1	URBAN-PAM2
Buliding height	12 m	16.3 m
Roof width	3.75 m	25 m
Road width	11.25 m	16.6 m
Urban area ratio for a grid	0.95	0.95
Vegetation area ratio for a grid	0.95	0.95
Diurnal maximum of anthropogenic heat	50 w m ⁻²	50 w m ⁻²



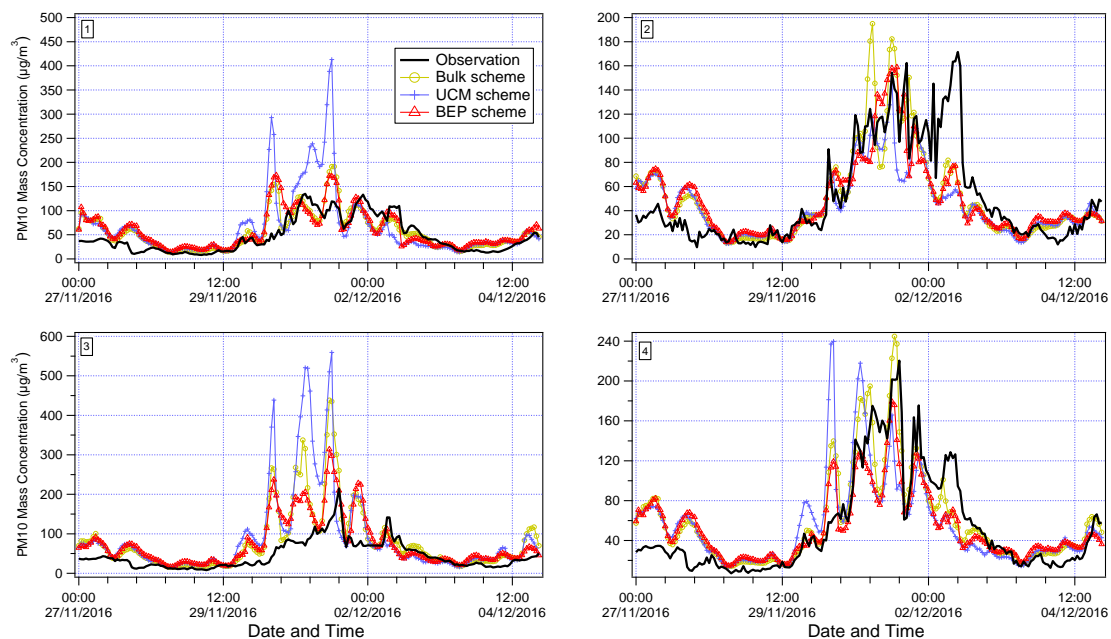


Figure S3.1. Time series of PM_{2.5}, PM₁₀ mass concentrations ($\mu\text{g m}^{-3}$): No1, 2, 3, 4 represent station FR04002, FR04034, FR04143, FR04156, respectively.

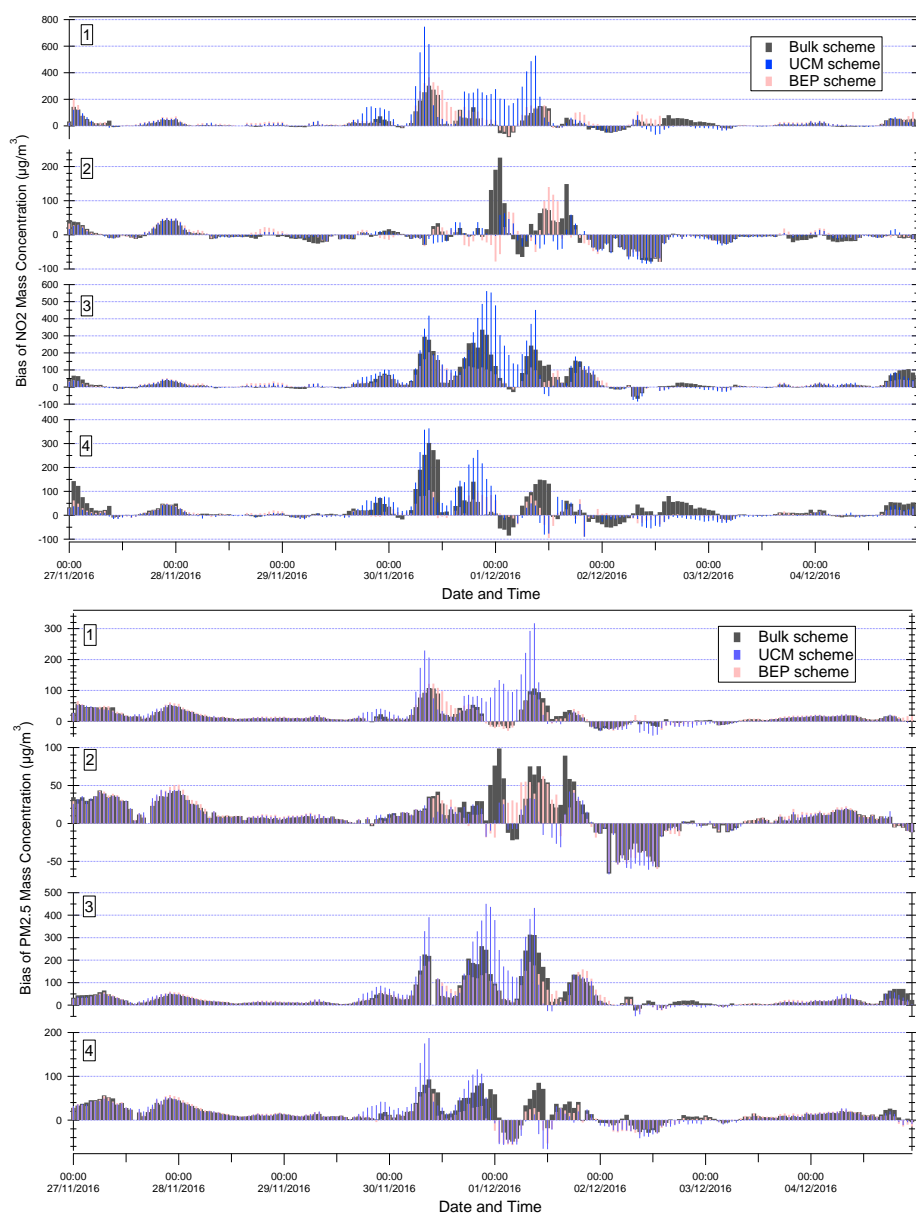


Figure S3.2. Time series of bias of NO_2 , $\text{PM}_{2.5}$, PM_{10} mass concentrations: No1, 2, 3, 4 represent station FR002, FR034, FR143, FR156, respectively.

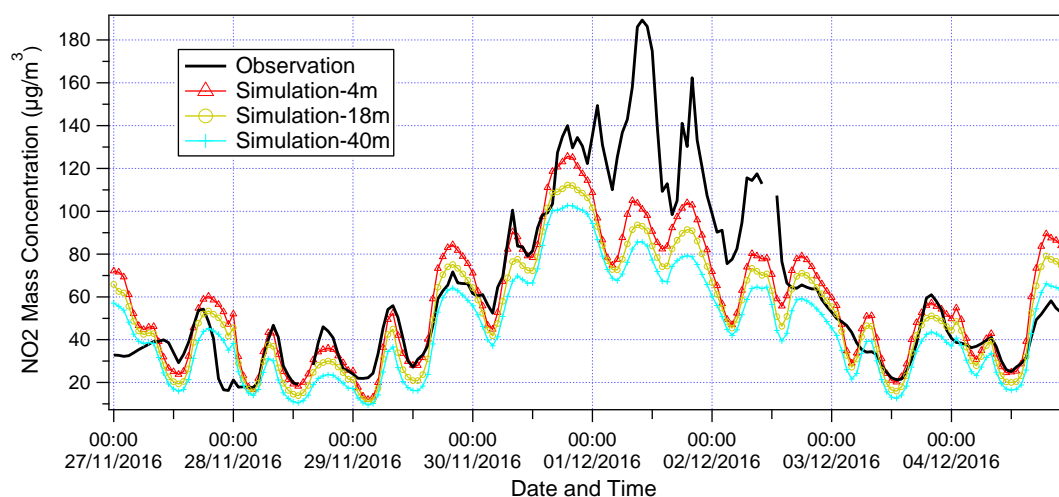
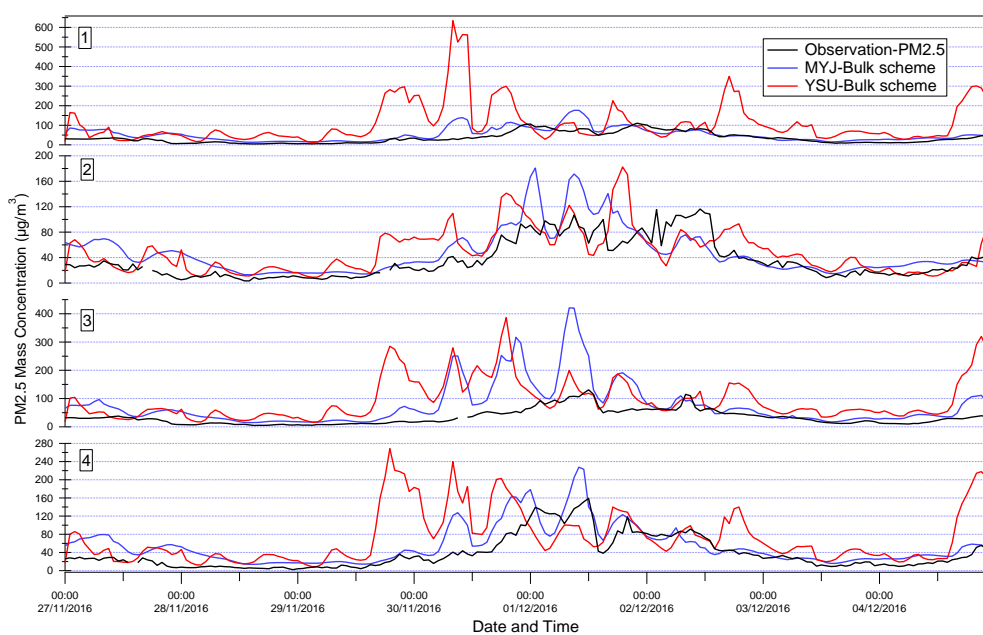


Figure S3.3. Time series between observed and modelled NO_2 with the first height of about 4 m, 18m and 40 m, respectively. Both observation and simulations are the average of Station FR04002, FR04034, FR04143, FR04156, respectively.



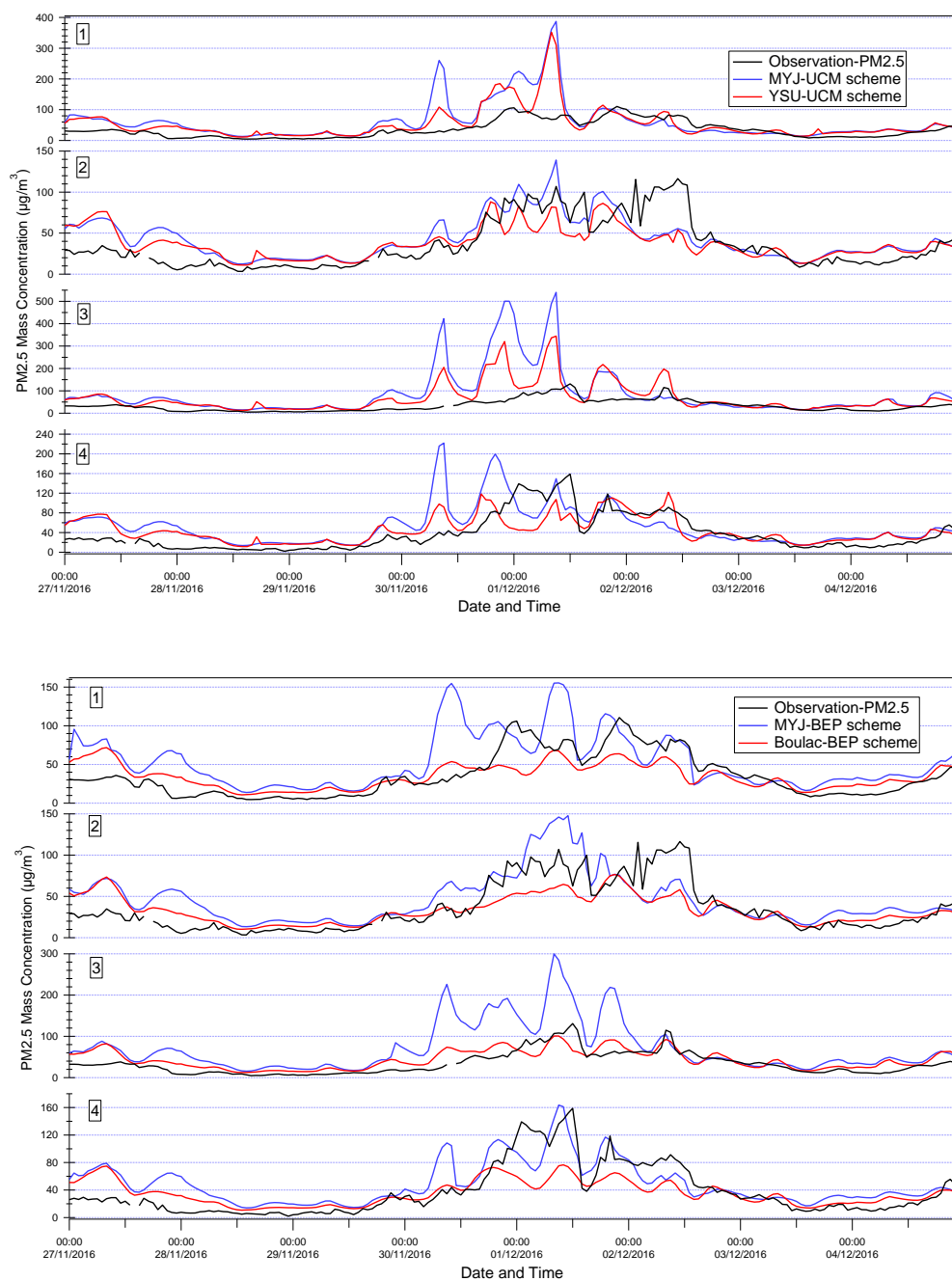


Figure S3.4. Time series between observed and modelled PM2.5: a, b and c represent each PBL schemes coupled with each urban canopy schemes respectively; 1, 2, 3, and 4 represent Station FR04002, FR04034, FR04143, FR04156, respectively

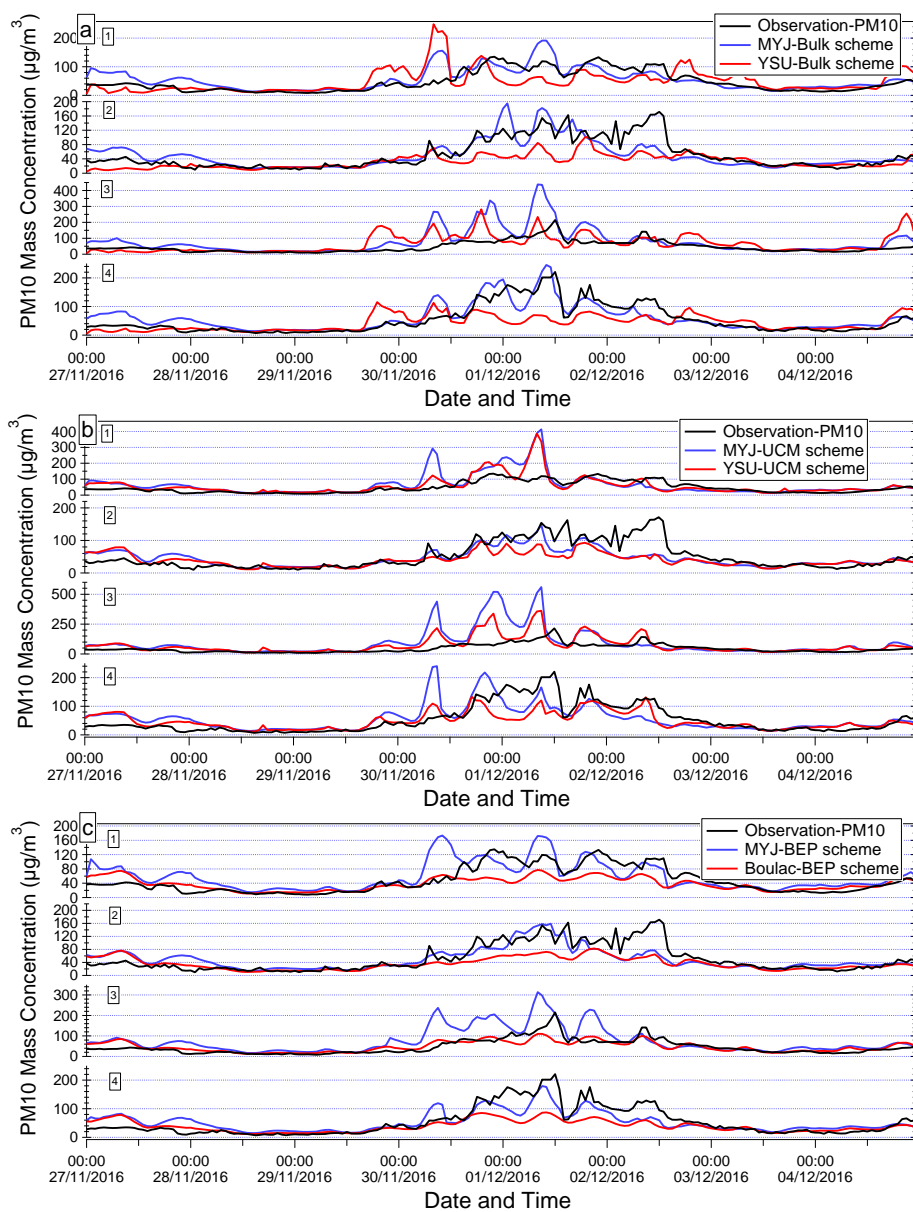


Figure S3.5. Time series between observed and modelled PM10: a, b and c represent each PBL schemes coupled with each urban canopy schemes respectively; 1, 2, 3, and 4 represent Station FR04002, FR04034, FR04143, FR04156, respectively.

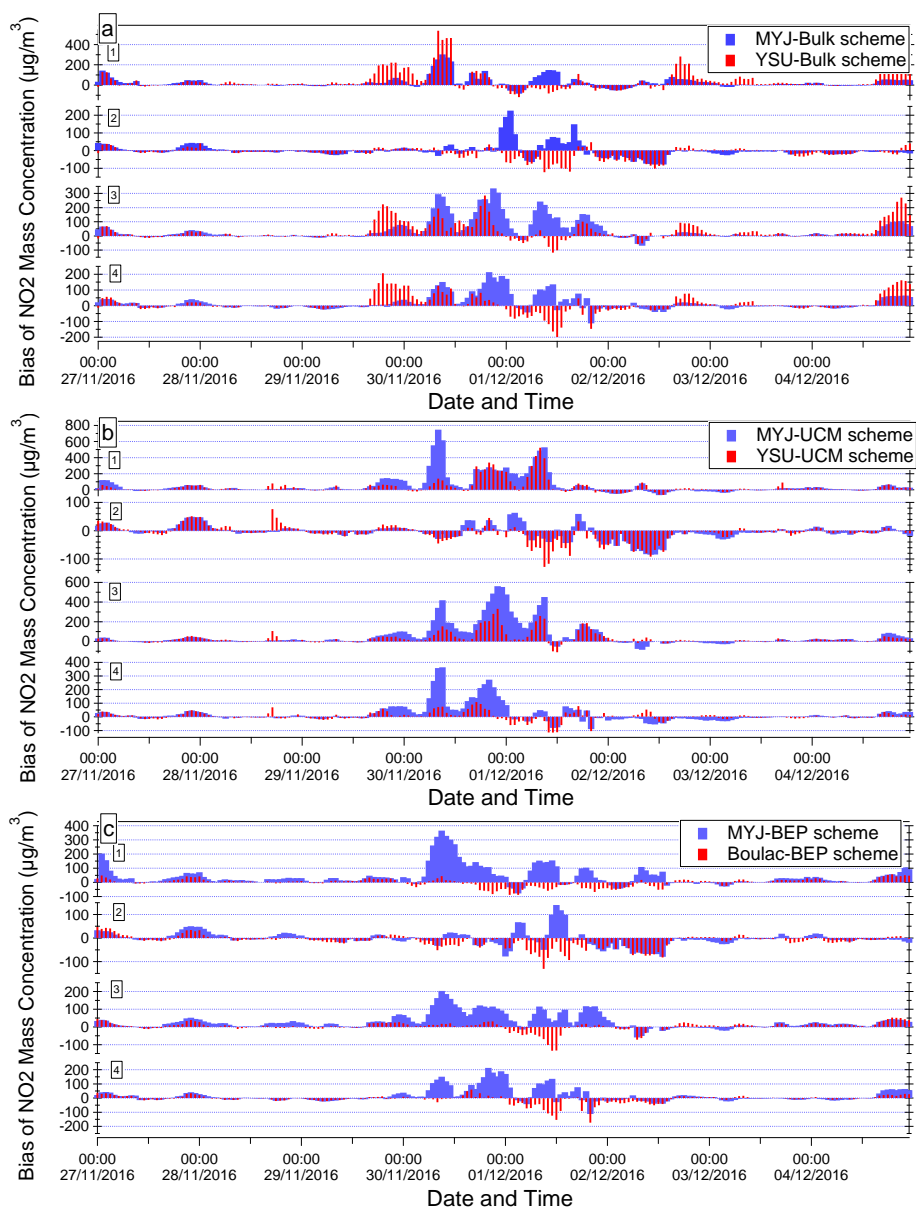


Figure S3.6. Time series of bias between observed and modelled NO_2 : a, b and c represent each PBL schemes coupled with each urban canopy schemes respectively; 1, 2, 3, and 4 represent Station FR04002, FR04034, FR04143, FR04156, respectively.

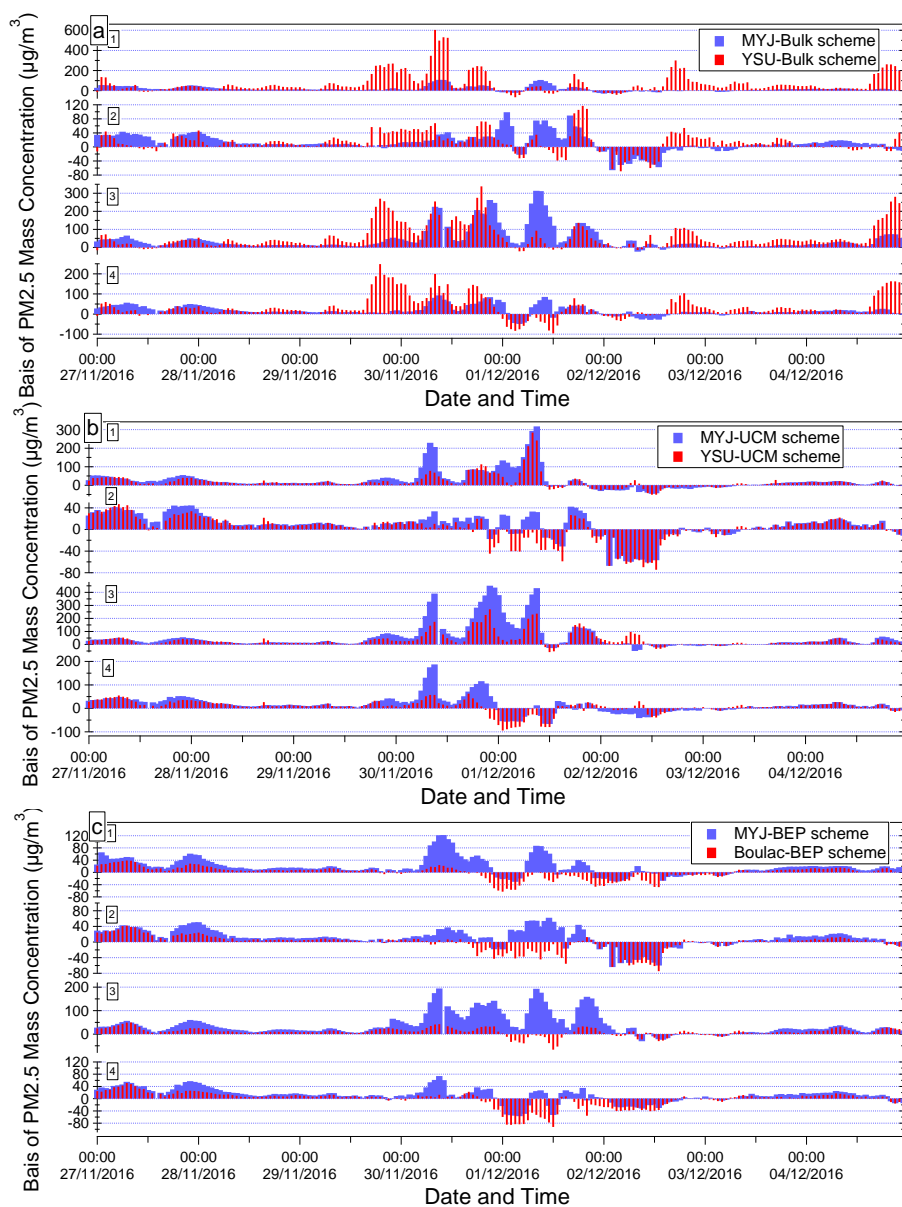


Figure S3.7. Time series of bias between observed and modelled PM_{2.5}: a, b and c represent each PBL schemes coupled with each urban canopy schemes respectively; 1, 2, 3, and 4 represent Station FR04002, FR04034, FR04143, FR04156, respectively.

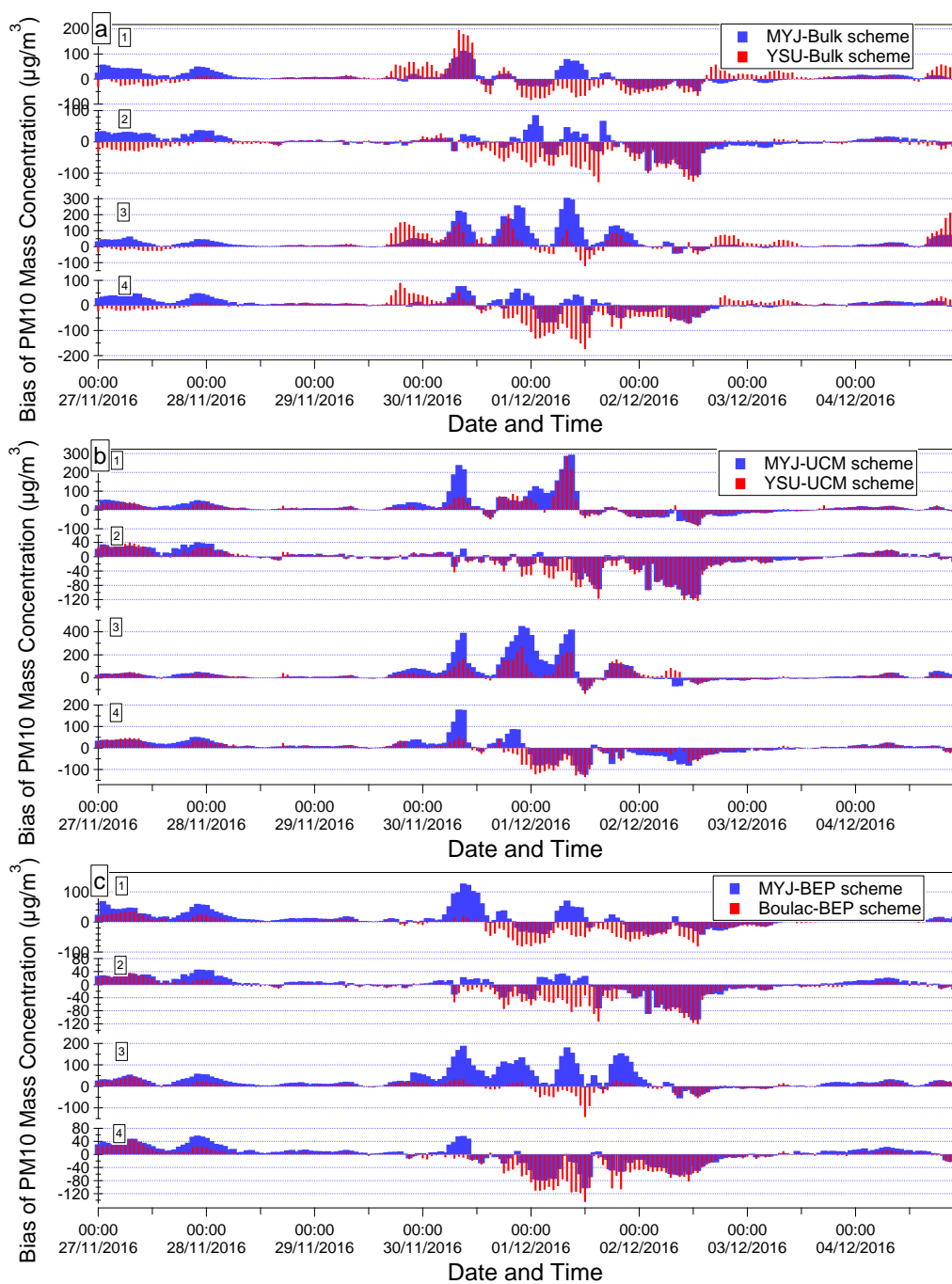


Figure S3.8. Time series of bias between observed and modelled PM10: a, b and c represent each PBL schemes coupled with each urban canopy schemes respectively; 1, 2, 3, and 4 represent Station FR04002, FR04034, FR04143, FR04156, respectively.

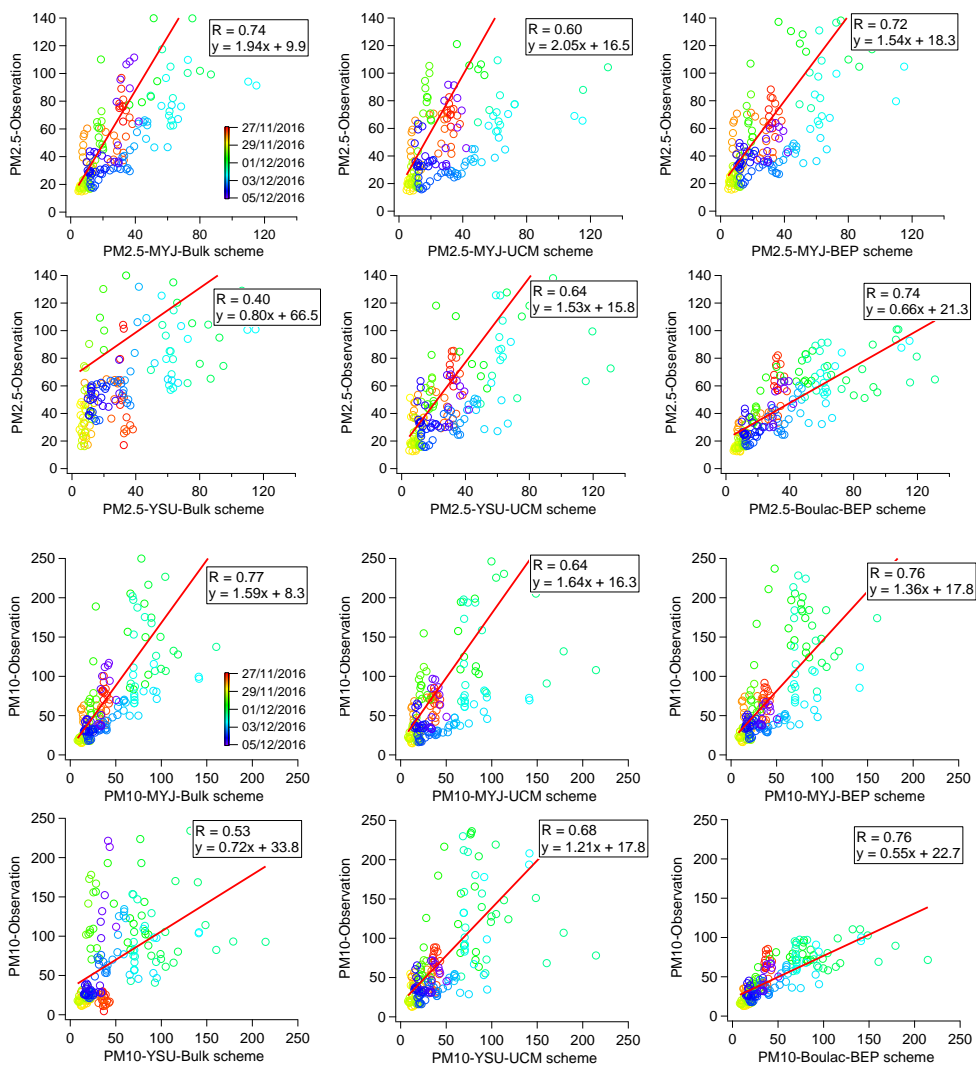


Figure. S3.9. Liner fit between observed and modelled PM2.5 and PM10

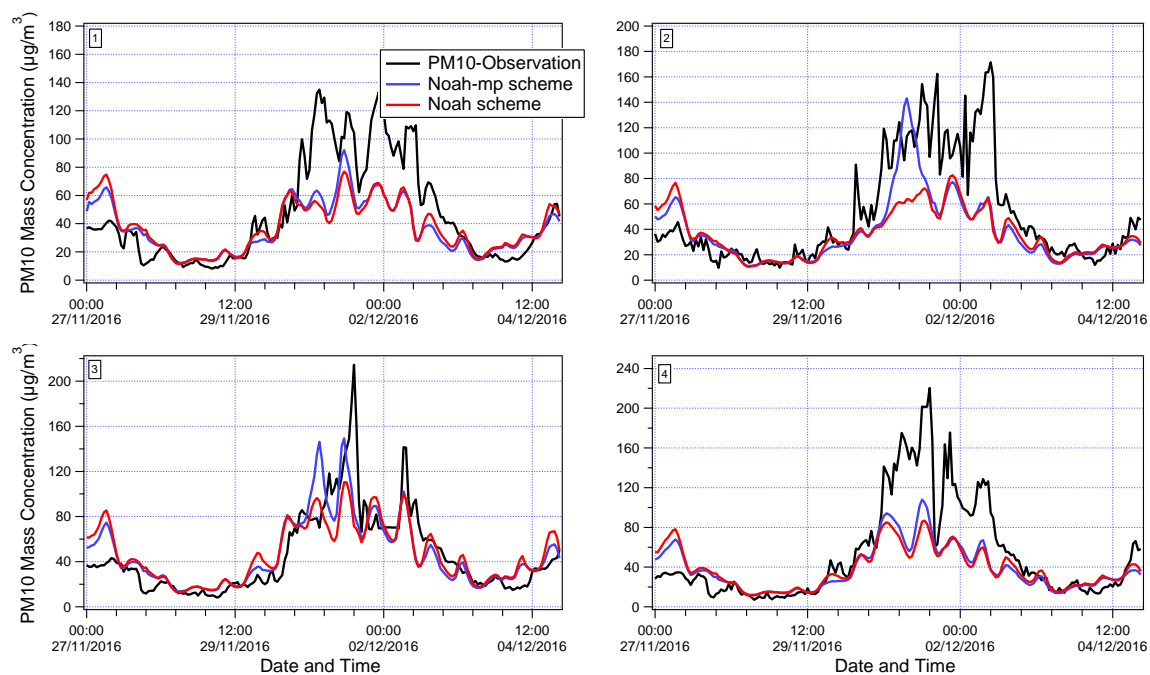


Figure s3.10. Time series of PM10 mass concentrations: No 1, 2, 3, and 4 represent station FR04002, FR04034, FR04143, and FR04156, respectively.

Annex B

Supplementary Material of Chapter V

Improvement of vertical mixing in chemistry transport modelling based on a 1.5-order turbulence kinetic energy-based eddy diffusivity closure scheme

Lei Jiang^{1,2,*}, **Bertrand Bessagnet**^{1,†}, **Frederik Meleux**¹, **Frederic Tognet**¹, **Florian Couvidat**¹

¹ INERIS, National Institute for Industrial Environment and Risks, Parc Technologique ALATA, 60550 Verneuil-en-Halatte, France; bertrand.bessagnet@citepa.org (B.B.); Frederik.MELEUX@ineris.fr (F.M.); Frederic.TOGNET@ineris.fr (F.T.); Florian.COUIDAT@ineris.fr (F.C.)

² Sorbonne University, UPMC Univ Paris 06, DE129, 75005 Paris, France

[†] Now at Citepa: Technical Reference Center for Air Pollution and Climate Change, 42, rue de Paradis, 75010 Paris, France.

List.S1. Name list of WRF model

```

&time_control
run_days           = 0,
run_hours          = 24,
run_minutes        = 0,
run_seconds        = 0,
start_year         = _Y1_,_Y1_,_Y1_,_Y1_,
start_month        = _M1_,_M1_,_M1_,_M1_,
start_day          = _D1_,_D1_,_D1_,_D1_,
start_hour         = 00, 00, 00, 00,
start_minute       = 00, 00, 00, 00,
start_second       = 00, 00, 00, 00,
end_year           = _Y2_,_Y2_,_Y2_,_Y2_,
end_month          = _M2_,_M2_,_M2_,_M2_,
end_day            = _D2_,_D2_,_D2_,_D2_,
end_hour           = 00, 00, 00, 00,
end_minute         = 00, 00, 00, 00,
end_second         = 00, 00, 00, 00,
interval_seconds   = 21600
input_from_file    = .true.,.true.,.true.,.true.,
history_interval   = 60, 60, 60, 60,
frames_per_outfile = 1000,1000,1000,1000,
restart            = ._THIS_RST_,
restart_interval   = 1440,
write_hist_at_0h_rst = ._THIS_RST_,

```

```

io_form_history           = 2
io_form_restart          = 102
io_form_input            = 2
io_form_boundary         = 2
debug_level              = 0
use_netcdf_classic       = .true.

&domains
time_step                = 60,
time_step_fract_num      = 0,
time_step_fract_den      = 1,
max_dom                  = 2,
s_we                     = 1,   1,   1,   1,
e_we                     = 106, 118, 115, 85,
s_sn                     = 1,   1,   1,   1,
e_sn                     = 91,  115, 103, 79,
s_vert                   = 1,   1,   1,   1,
e_vert                   = 53,  53,  53,  53,
p_top_requested          = 5000,
num_metgrid_levels       = 32,
num_metgrid_soil_levels = 4,
dx                       = 45000, 15000, 5000, 1666.6667,
dy                       = 45000, 15000, 5000, 1666.6667,
grid_id                  = 1,   2,   3,   4,
parent_id                = 1,   1,   2,   3,
i_parent_start           = 1,   24,  39,  44,
j_parent_start           = 1,   20,  66,  38,
parent_grid_ratio        = 1,   3,   3,   3,
parent_time_step_ratio   = 1,   3,   3,   3,
feedback                 = 1,
smooth_option            = 0,
eta_levels for H4
= 1., 0.9995, 0.999, 0.9985, 0.9975,
0.996230185, 0.9949736, 0.993716955, 0.992334723,
0.990814209, 0.989141703, 0.987301886, 0.98527813,
0.983051956, 0.980603218, 0.977909565, 0.974946558,
0.971687257, 0.968101978, 0.964158237, 0.959820092,
0.955048144, 0.949799001, 0.94402492, 0.937673509,
0.930686891, 0.923001587, 0.914547801, 0.905248582,
0.895019472, 0.883767486, 0.871390283, 0.857775331,
0.842798889, 0.826324821, 0.80820334, 0.788269699,
0.7663427, 0.742223024, 0.715691328, 0.68650645,
0.65440315, 0.619089544, 0.580244482, 0.537514985,
0.49051252, 0.438809812, 0.381936818, 0.319376528,
0.250560224, 0.17486228, 0.0915945247, 0.0000,

eta_levels for H12
= 1., 0.9985, 0.9975,
0.996230185, 0.9949736, 0.993716955, 0.992334723,
0.990814209, 0.989141703, 0.987301886, 0.98527813,
0.983051956, 0.980603218, 0.977909565, 0.974946558,
0.971687257, 0.968101978, 0.964158237, 0.959820092,
0.955048144, 0.949799001, 0.94402492, 0.937673509,

```

```

0.930686891, 0.923001587, 0.914547801, 0.905248582,
0.895019472, 0.883767486, 0.871390283, 0.857775331,
0.842798889, 0.826324821, 0.80820334, 0.788269699,
0.7663427, 0.742223024, 0.715691328, 0.68650645,
0.65440315, 0.619089544, 0.580244482, 0.537514985,
0.49051252, 0.438809812, 0.381936818, 0.319376528,
0.250560224, 0.17486228, 0.0915945247, 0.0000,

eta_levels for H40
= 1., 0.9949736, 0.993716955, 0.992334723,
0.990814209, 0.989141703, 0.987301886, 0.98527813,
0.983051956, 0.980603218, 0.977909565, 0.974946558,
0.971687257, 0.968101978, 0.964158237, 0.959820092,
0.955048144, 0.949799001, 0.94402492, 0.937673509,
0.930686891, 0.923001587, 0.914547801, 0.905248582,
0.895019472, 0.883767486, 0.871390283, 0.857775331,
0.842798889, 0.826324821, 0.80820334, 0.788269699,
0.7663427, 0.742223024, 0.715691328, 0.68650645,
0.65440315, 0.619089544, 0.580244482, 0.537514985,
0.49051252, 0.438809812, 0.381936818, 0.319376528,
0.250560224, 0.17486228, 0.0915945247, 0.0000,

/
&physics
mp_physics = 6, 6, 6, 6,
ra_lw_physics = 4, 4, 4, 4,
ra_sw_physics = 4, 4, 4, 4,
radt = 30, 30, 30, 30,
bldt = 0, 0, 0, 0,
cu_physics = 1, 1, 1, 0,
cudt = 5, 5, 5, 5,
isfflx = 1,
ifsnow = 1,
icloud = 1,
surface_input_source = 3,
num_soil_layers = 4,
num_land_cat = 21,
maxiens = 1,
maxens = 3,
maxens2 = 3,
maxens3 = 16,
ensdim = 144,
sf_sfclay_physics = 2, 2, 2, 2,
sf_surface_physics = 2, 2, 2, 2,
sf_urban_physics = ( 0 for Bulk; 1 for UCM; 2 for BEP)
bl_pbl_physics = ( 1 for YSU; 2 for MYJ; 8 for Boulac)
num_urban_layers = 6400
/
&fdda
grid_fdda = 1, 1, 0, 0,
gfdda_inname = "wrffdda_d<domain>",

```

```

gfdda_end_h           = 10000, 10000, 255, 255,
gfdda_interval_m     = 360, 360, 360, 360,
io_form_gfdda        = 2,
fgdt                  = 1, 1, 1, 1,
if_no_pbl_nudging_uv = 0, 0, 0, 0,
if_no_pbl_nudging_t  = 0, 0, 0, 0,
if_no_pbl_nudging_q  = 0, 0, 0, 0,
if_zfac_uv           = 1, 1, 1, 1,
k_zfac_uv            = 12, 12, 12, 12,
if_zfac_t            = 1, 1, 1, 1,
k_zfac_t             = 12, 12, 12, 12,
if_zfac_q            = 1, 1, 1, 1,
k_zfac_q             = 12, 12, 12, 12,
if_zfac_ph           = 1, 1, 1, 1,
k_zfac_ph            = 12, 12, 12, 12,
guv                  = 0.0003, 0.0003, 0.0003, 0.0003,
gt                   = 0.0003, 0.0003, 0.0003, 0.0003,
gq                   = 0.0003, 0.0003, 0.0003, 0.0003,
gph                  = 0.0003, 0.0003, 0.0003, 0.0003,
xwavenum             = 5, 5, 5, 5,
ywavenum             = 5, 5, 5, 5,
if_ramping           = 0,
dtramp_min           = 60.0,
/
&dynamics
w_damping            = 1,
rk_ord               = 3,
diff_opt             = 1, 1, 1, 2,
km_opt               = 4, 4, 4, 2,
diff_6th_opt         = 2, 2, 2, 2,
diff_6th_factor      = 0.12, 0.12, 0.12, 0.12,
base_temp            = 290,
damp_opt             = 1,
zdamp                = 5000., 5000., 5000., 5000.,
dampcoef             = 0.01, 0.01, 0.01, 0.01,
khdif                = 0, 0, 0, 0,
kvdif                = 0, 0, 0, 0,
smdiv = 0.1, 0.1, 0.1,
emdiv = 0.01, 0.01, 0.01,
epssm = 0.1, 0.1, 0.1,
non_hydrostatic     = .true., .true., .true., .true.,
moist_adv_opt        = 1, 1, 1, 2,
scalar_adv_opt        = 1, 1, 1, 2,
tke_adv_opt          = 1, 1, 1, 2,
time_step_sound      = 4, 4, 4, 4,
h_mom_adv_order      = 5, 5, 5, 5,
v_mom_adv_order      = 3, 3, 3, 3,
h_sca_adv_order      = 5, 5, 5, 5,
v_sca_adv_order      = 3, 3, 3, 3,
/

```

```

&bdy_control
spec_bdy_width           = 5,
spec_zone                = 1,
relax_zone               = 4,
specified                = .true., .false., .false., .false.,
nested                  = .false., .true., .true., .true.,
/

&grib2
&namelist_quilt
nio_tasks_per_group = 0,
nio_groups = 1,

```

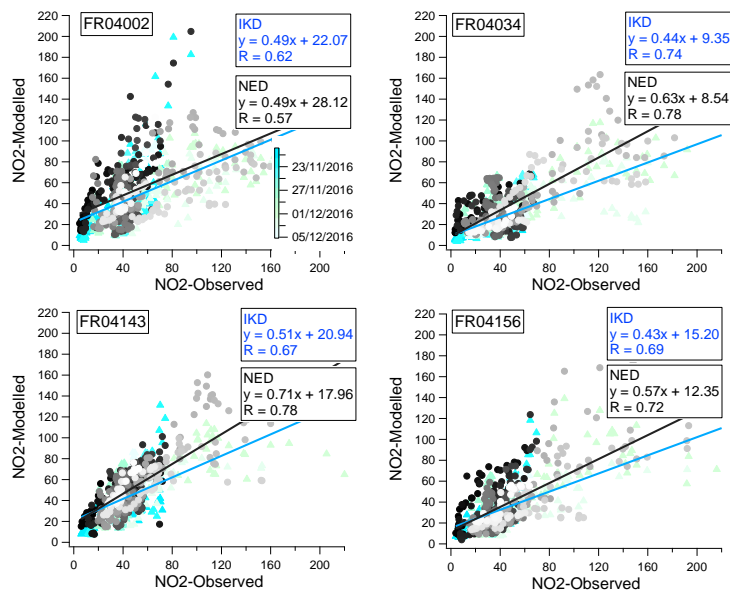


Figure S5.1. The correction between observed and modelled NO₂ in urban background stations over Paris region.

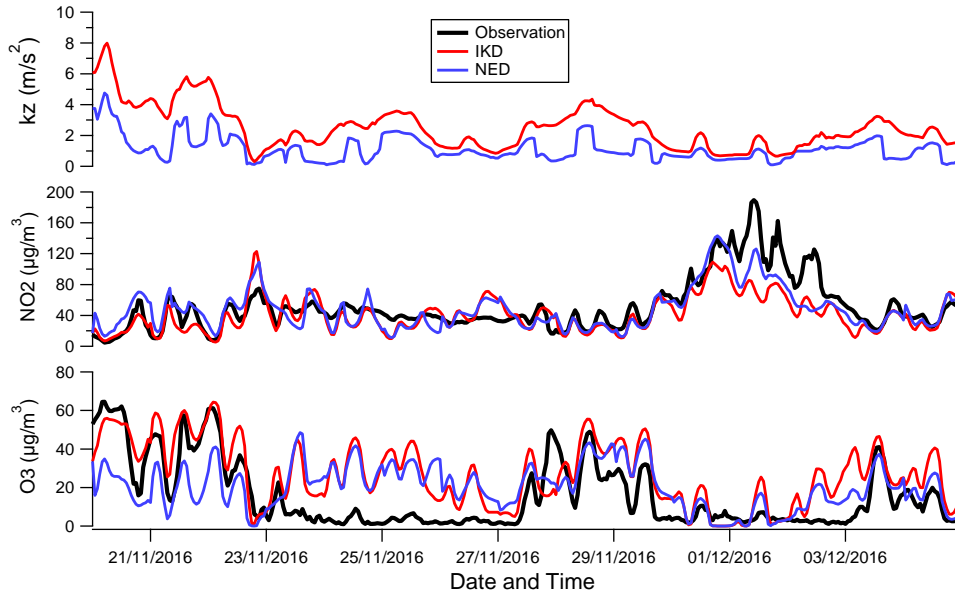


Figure S5.2. Time series between observed and modelled k_z , NO_2 and O_3 mass concentrations in urban background station over Paris region.

Table S5.1. Average modelled NO_2 and O_3 mass concentrations (Avg); the correlation (R); mean bias (MB) and root mean square error (RMSE) between Observation and simulation of NO_2 and O_3 in urban background stations over Paris region

	IKD				NED				improvement ^a
	Avg	R	MB	RMSE	Avg	R	MB	RMSE	
Urban-NO₂	41.06	0,74	-10.40	24.90	47.99	0.80	-3.80	20.40	18.77%
Urban-O₃	27.08	0.74	11.29	16.65	20.41	0.64	4.63	17.47	-4.80%

a: The “improvement” is the relative change in % of the RMSE by using the initial k_z diffusion coefficient and by using the new eddy diffusion coefficient.

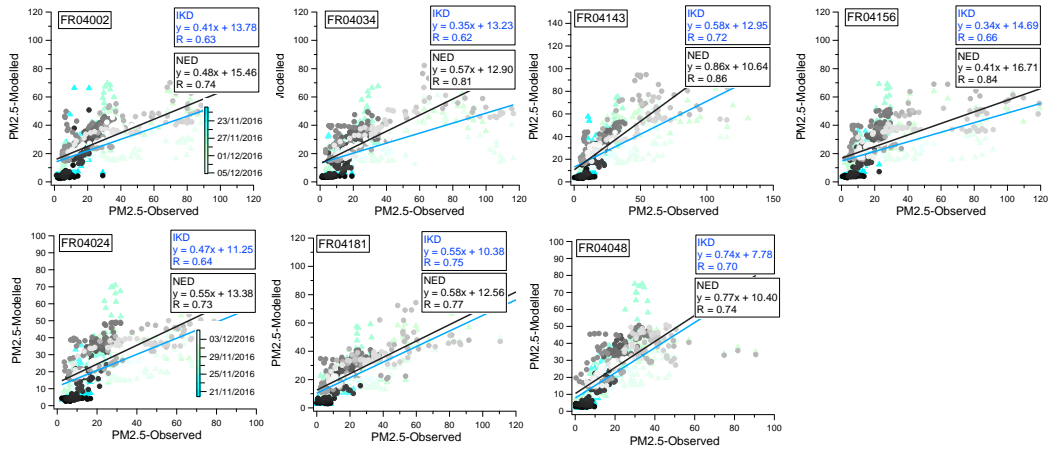


Figure S5.3. The correction between observed and modelled PM_{2.5} in urban, suburban and rural background stations over Paris region.

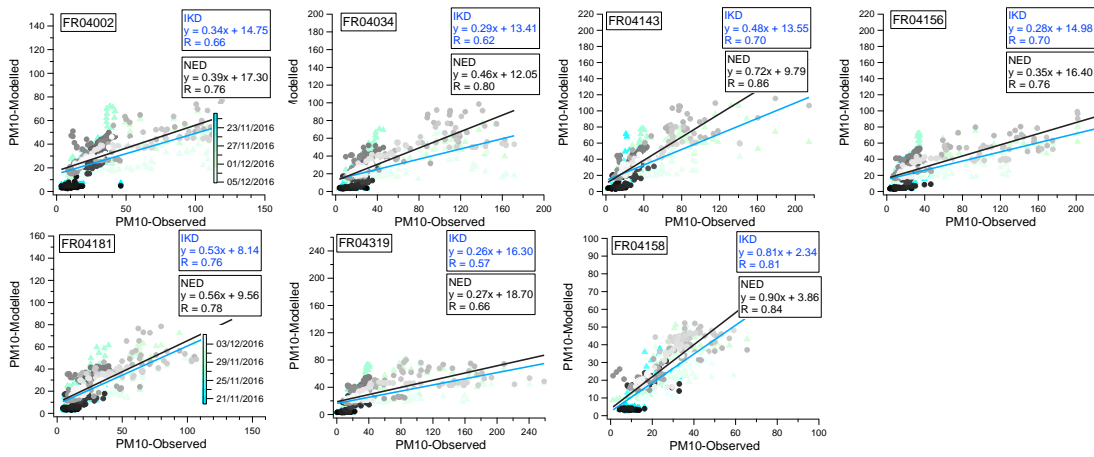
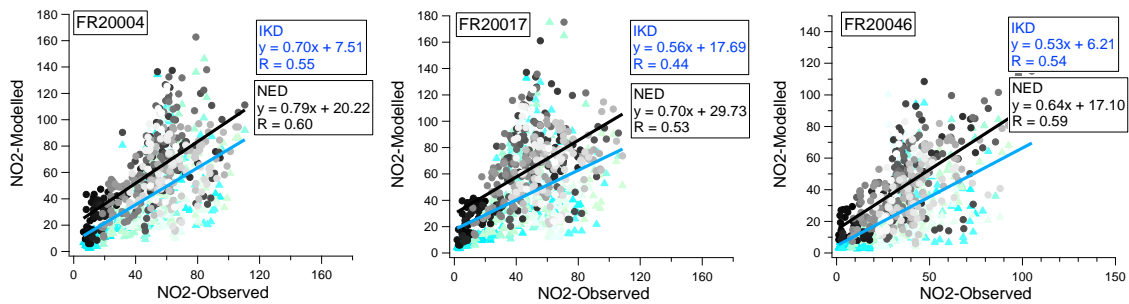


Figure S5.4. The correction between observed and modelled PM₁₀ in urban, suburban and rural background stations over Paris region.



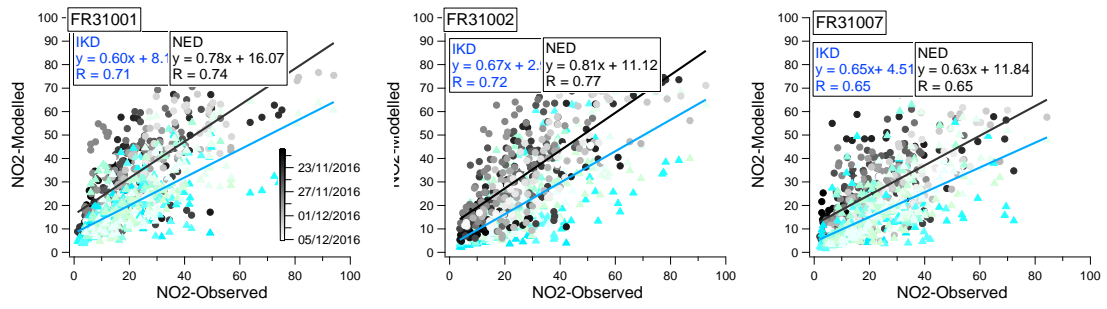


Figure S5.5. The correction between observed and modelled NO₂ in urban background stations over Lyon and Bordeaux regions. FR20XXX represents the station in Lyon region and FR31XXX represents the station in Bordeaux region.